Non-Destructive Passive Magnetic and Ultrasonic Inspection Methods for Condition Assessment of Reinforced Concrete

by

SeyedBijan Mahbaz

A thesis
presented to University of Waterloo
in fulfillment of the
thesis requirement for the degree of
Doctor of Philosophy
in
Civil Engineering

Waterloo, Ontario, Canada, 2016

Author's Declaration

I hereby declare that I am the sole author of this thesis. This is a true copy of the thesis, including any required final revisions, as accepted by my examiners.

I understand that my thesis may be made electronically available to the public.

SeyedBijan Mahbaz

Abstract

Sustainability, reliability, and safety of complex industrial infrastructure are crucial worldwide issues. Long-term sustainable life quality, services and economic growth provided by modern life is dependent on the quality of the civil infrastructure. Highways, bridges, water networks, waste treatment facilities, and energy supplies are examples of vital civil infrastructure. Substantial investment is necessary for developing and maintaining these complex systems, which affect all parts of our modern life. Corrosion is a key problem now pursuing the life-span of infrastructures and its effects are visible in most infrastructural systems.

This thesis describes two complementary quantitative non-destructive testing methods for corrosion assessment of reinforced concrete structures. One based on the magnetic properties of the medium and the second one based on the acoustic properties of the medium. The first testing method use a novel passive magnetic developed for corrosion assessment of rebar within concrete structures. A prototype of a magnetic inspection device was designed and built in the NDT lab at the University of Waterloo, using magneto-inductive sensors. The prototype can scan reinforcement by moving it on the concrete surface to assess corrosion state without damaging the structure. This method is passive; meaning that there is no electrical current passing through the rebar. Different corroded rebars were scanned with the new device. Using signal processing methods, raw (not processed data) magnetic data were analyzed and results show that the scanning device and analysis method have potential for industrial application. The complete calibration of the prototype will be performed as a continuation of this research.

By using the developed prototype, three different types of samples were tested. First tests were performed on a rebar with three holes at different locations and positions (top, bottom, and center). Experimental tests were done at two different locations in the lab. At each location, tests were repeated 10 times and averaged to account for local variability in the magnetic field. The maximum standard deviations of experimental results for tests set at Location 1 and Location 2 are 13.6% and 21.4%, respectively. Numerical simulations were also performed for this experimental test data. Using signal processing techniques, hole locations were detected using this passive magnetic method. Also, different patterns were observed for each hole. This experimental test program was done as prove of concept.

The second set of tests was done on six rebars with different corrosion levels (metal loss). Penetration depth for the prototype and its ability to distinguish corroded bar from sound bar were tested first. Generally, increasing thickness of concrete (cover) decreases the detectability. However, the scanning prototype was able to detect corrosion for a concrete cover of 11 cm. Wavelet energy analysis was used as a signal processing method for analyzing experimental test data. Two trends were extracted in order to predict the percentage of metal loss in rebar by using the wavelet energy analysis. Although coefficient of correlation was 0.67 and 0.62 for X and Z direction respectively, two equations were developed and can be used as a general indicator for general metal loss prediction. Minimum and maximum level of detected corrosion was %4.7 and %14.3 respectively with ± %1 error.

The last set of tests using the magnetometer device was done on three different rebars, which had local corrosion spots. These tests were done using a second version of the scanning prototype. In this version two parallel sensors were used to cover more area. A rotary encoder sensor was added to wheel in order to take the positioning and a memory card board was added to record raw data. The maximum standard deviations for each test were below 1.1%, considered to be an excellent result. Continuous wavelet transform was used to extract features from the raw data. The technique not only detected corrosion, but some inferences could be made about the type of corrosion as well.

For the second testing methodology, ultrasonic surface waves were used as a complementary method to detect corrosion de-bonding in rebars. Reinforcement de-bonding from concrete is a major consequence of corrosion. A high frequency transducer (1MHz) and a laser vibrometer device were used to capture displacements at the end of rebar specimens. Surface wave analysis and numerical simulations have been done to detect reinforcement de-bonding. Results show that the peak-to-peak amplitude was in the range up to 4.7 times larger for a de-bonded bar compared to a perfectly bonded bar, because of leaking energy from rebar to the concrete in a perfectly bonded sample compare to de-bonded one. Also, the peak to peak amplitude was 6.2 times more for the de-bonded rebar compared to the perfectly bonded rebar. These differences were clear in their Fourier transform results as well.

This thesis describes the development of a novel passive magnetic method and a new approach using ultrasonic waves to detect corrosion of rebars. A new prototype was designed and constructed and its final calibration is under development. Although each method measures different physic approaches, there are some quantified results from each to show the percentage of corrosion. Therefore, data fusion of the passive magnetic method with an ultrasonic method can increase the accuracy of corrosion detection as these methods are perfected and applied in the field.

Acknowledgement

I would like to express my sincere appreciation to my supervisors Professor Maurice Dusseault, and Professor Giovanni Cascante. Prof. Dusseault gave me an opportunity to study at a great university with wonderful people in a great and welcoming country. His support from the first day, his valuable insights, suggestions and guidance eased this complicated path of PhD for me. Prof. Cascante opened a new window in my view through the non-destructive testing industry. His patience was great for me during the process of learning new fields in my studies. Also his valuable suggestions and guidance brightened the path of my PhD. Also, I would like to thank Betty A. Dusseault who encouraged me all the time during these years. My sincere thanks to Professor P. Vanheeghe, his collaboration helped me a lot through the signal processing part of this study.

I would like to thank my thesis committee: Professor M.A. Polak, Professor K. Ponnambalam, Professor S. Walbridge, and Professor D. Fratta for their valuable feedback and suggestions.

This work was funded partially by NSERC (National Sciences and Engineering Research Council of Canada) and by the MITACS program for graduate students. Thanks to both organizations for preparing this great opportunity. Also, thanks to Speir Hunter Ltd. for their financial support in first year of this project in collaboration with MITACS.

I would also like to thank Professors Carolyn Hansson from Mechanical Engineering and Professor Rania Al-Hammoud from Civil and Environmental Engineering for giving me some of their samples. Special thanks to Prof. Dipanjan Basu for his consultations about my simulation problems. Thank to Professor Carl T. Hass and his post-doctorate fellow Mohammad Nahangi for letting me to use the surface laser scanning device. Also thanks to Professor Adil Al-Mayah and his Dr. Magdy Shaheen for their help to take X-ray images from ultrasonic transducer work. To the late Professor Khaled Soudki for letting me do some preliminary experimental tests.

I would also like to thank Civil and Environmental Engineering Administrative and technical staff specifically Structural Laboratory Richard Morrison, Douglas Hirst, and Rob Sluban. Thank to T. Ridgway and Anne M. Allen for all your helps during these years. My special thanks also goes to Engineering Machine Shop staffs; Rick Forgett, Jorge A. Cruz, Charlie G. Boyle, Andrew Urschel, Graeme Adair, Phil Laycock, Karl Janzen, and Ashley Kropf. Thanks to all staff members of the Civil and Environmental Engineering Department for providing continuous support during these years.

Profound thanks to my love, Roja Mosharrafy for being patience in all these years, supporting me throughout this entire process, and providing a peaceful place at home to study better. These past four years have been very tough both financially and academically, but she stood beside me without complaint, just so that I could focus on my research and thesis. I thank my older Son, SeyedMohamadMehdi, for understanding his father and all his patience to me and making my life full of joy. Profound thanks to my mother, Tahereh Tavvafzadeh, for being both father and mother to me, and more important, being a great model in my life. Thanks to my younger son, Radmehr, who came recently into my life and brought happiness with him. Special thanks to my father in law, Alireza Mosharrafy, and to my mother in law, Batool Parvizi which without their help I couldn't make my PhD. I would like to express my gratitude and appreciation to Dr. Katayoun Adab and Dr. Hossein Shahrasbi for their financial and kind emotional support to me and my family during my PhD program. They have been like sister and brother to me. A special thank you to my Aunt, Touran Farivar, for your support during my Master's program and PhD as well. I will be grateful forever for your love.

My strong appreciation to my friends in NDT and geotechnical groups, especially Hassan Ali, Sina Varamini, Maria Jose Rodrigez, Mathieu Finas, M. Irfan, F.A. Diaz, and Sabah Hassan who were always being there to help me when I needed them. Thanks to all my friends in the Civil and Environmental Engineering Department, and other departments of the University of Waterloo for making this place such a delightful place for study.

Dedication

To

My mother Tahereh,

Loving wife Roja,

My sons (MohamadMehdi and Radmehr),

And to my father Ali

Table of Contents

LIST OF TABLES

LIST OF FIGURES

Chapter 1

1.1. Problem definition

Reinforced concrete is one of the main construction materials for buildings, bridges, and platforms as well as for underground structures such as concrete pipelines and tunnels [1]. Generally, the durability and reliability of reinforced concrete requires being high in harsh environmental conditions such as those encountered in marine, cold weather climate, and industrial situations. However, instead of benefiting from long-term durability of high quality materials leading to good performance, the majority of concrete structures fail due to reinforcement corrosion [2]. Although there are specified lifetimes for concrete based on standards, there are numerous reasons, which cause exposure leading to the chemical or electrochemical attack of the steel reinforcement [3]. Hence, corrosion is a primary cause of reducing the durability of reinforcement concrete [4].

From an economic point of view, the first known annual estimation of cost of corrosion was $5.5 billion or 2.1 percent of 1949 GNP in the United States [5]. Corrosion damage just for reinforced concrete bridges in the United States is estimated between $325 and $1000 million per year in 1991 [6, 7]. Also, based on the NACE Corrosion Costs Study, corrosion costs increased more than $1 trillion in 2012 [8]. Understanding the various types of corrosion helps in selecting an appropriate detection method. Corrosion types and characteristics are summarized in Table 1.1 [9].

Table 1.1. Types and characteristics of most common corrosion processes [9].

Corrosion type	Cause	Appearance	By-products
Uniform attack	Exposure to corrosive environment	Irregular roughening of the exposed surface	Scale, metallic salts
Pitting	Impurity or chemical discontinuity in the paint or protective coating	Localized pits or holes with cylindrical shape and hemispherical bottom	Rapid dissolution of the base metal
Inter-granular or Exfoliation	Presence of strong potential differences in grain or phase boundaries	Appears at the grain or phase boundaries as uniform damage	Produces scale type indications at smaller magnitude than stress corrosion
Crevice	Afflicts mechanical joints, such as coupled pipes or threaded connections. Triggered by local difference in environment composition (Oxygen concentration)	Localized damage in the form of scale and pitting	Same as scale and pitting
Filiform	High humidity around fasteners, skin joints or breaks in coating cause an electrolytic process	Fine, meandering, thread-like trenches that spread from the source	Similar to scale. Lifting of the coating.
Galvanic Corrosion	Corrosive condition that results from contact of different metals	Uniform damage, scale, surface fogging or tarnishing	Emission of mostly molecular hydrogen gas in a diffused form
Stress Corrosion Cracking	Mechanical tensile stresses combined with chemical susceptibility	Micro-macro-cracks located at shielded or concealed areas	Initially produces scale type indications. Ultimately leads to cracking.

1.2. Major limitations in current technologies

Several technologies can be used for detection, characterization, and quantification of corrosion damage in reinforced concrete structures. These technologies are part of the methods of Non

Destructive Testing methods (NDT). Table 1.2 shows the primary corrosion detection methods and their strengths and weaknesses [9].

The most vital point in corrosion detection is assessing the health state of an inspected object and determining its remaining lifetime. This means that if a method accurately determines the corrosion level within a concrete structure and can give an estimate of condition before the structure is torn down prematurely, large operation costs could be avoided.

Table 1.2. Conventional corrosion detection methods [11, 12].

Method	Strength	Weakness
Visual	• Relatively inexpensive • Large area coverage • Portability	• Highly subjective • Measurements not precise • Limited to surface inspection • Labor intensive
Enhanced Visual	• Large area coverage • Very fast • Very sensitive to lap joint corrosion • Multi-layer	• Quantification difficult • Subjective - requires experience • Requires surface preparation
Eddy Current	• Relatively inexpensive • Good resolution • Multiple layer capability • Portability	• Low throughput • Interpretation of output • Operator training • Human factors
Ultrasonic	• Good resolution • Can detect material loss and thickness	• Single-sided • Requires coupling • Cannot assess multiple layers • Low throughput • Scattering problems
Radiography	• Best resolution (~1%) • Image interpretation	• Expensive • Radiation safety • Bulky equipment
Infrared Thermography	• Large area scan • Relatively high throughput • “Macro view” of structures	• Complex equipment • Layered structures are a problem • Precision of measurements

Visual inspection is one of the most common inspection methods, it is cheap and quick, but it is highly dependent on the operator's experience and is not suitable for detecting hidden corrosion [10].

Although some weaknesses are resolved using enhanced visual method, certain disadvantages remain, including:

- Proper quantifying of inspection remains challenging.
- A large effect of the operator's experience.
- Surface preparation for good imaging.

The Eddy current method is precise, but the main problems of this method include elaborate to human health and the necessity for high operator skill [11, 12].

Ultrasonic probing is a common non-destructive test applicable to concrete, ceramics, and stone. Detecting general changes in concrete conditions such as identifying weakening areas because of cracking or de-bonding is a main advantage of the ultrasonic method. However, this technique is not applicable in some conditions such as cases with rough surfaces, cases where poor coupling with concrete surface and transducers is a difficulty, and in cases requiring crack detection [13].

Using radioactive isotopes as radiation emitters in order to probe the concrete and detect the quality of concrete is another non-destructive method, which is also applicable to reinforced concrete. Gamma ray and X-ray methods are two subcategories of this method. Measuring density changes, locating voids, and detecting internal cracks are the main capacities of this method [14, 15].

Measuring emitted infrared radiation from the surface of an object that has been subjected to a temperature change is a common thermography method. Heat flow through the surface of the object can be affected by delamination or internal or external cracks cause by corrosion. Then crack and delamination are two main defects, which are commonly detected by this method. Low risk and high inspection speed are two main advantages of infrared thermography method. One main disadvantage of this technique is the effect of environment temperature changes on results [16].

1.3. Research objectives

There are some limitations in the existing methods for corrosion/crack detection of rebar. Thus, this thesis presents an investigation of the potential use of passive magnetic method for detection of corrosion in rebars. Using an ultrasonic method to complement the magnetic data is also presented in this study. Accordingly this research project was planned based on the following steps:

- Review of the theory and fundamental equations of ferromagnetic materials;
- Application of passive magnetic methods as a state of the art non-destructive testing method;
- Developing an inspection prototype for recording the intrinsic magnetic field of reinforcement steel from the surface of concrete;
- Using developed scanning device for experimental test;
- Using signal processing methods to extract features related to defects (corrosion/crack);
- Using ultrasonic experimental tests and numerical modeling as an alternative method;

1.4. Methodology

These objectives are achieved using the following items:

- A first version of scanning prototype was designed and made just to prove the concept. This version had only one magnetic sensor and a main board to receive magnetic data and transfer it to PC. The second version of prototype was designed and made with four main improvements: 1-New main board with higher processing capability, 2-Two parallel magnetic sensors, 3-positioning sensor, and 4-Memory card board. This version of device is a ready prototype. However, it needs following improvements which will be implemented for continuation of this research. Some of improvements can be following items: a) Robust positioning system, b) Wireless transfer system, c) A real time system for showing scanned data and analysis.

- By using the new prototype three holes in rebar could be detected. These holes were placed in different locations and different positions.
- Numerical simulations were done based on discrete finite element method to confirm experimental tests on rebar with three holes.
- The developed prototype was able to distinguish generally corroded rebars with different percentage of metal loss with the range of %4.7 to up.
- The penetration depth of developed device was tested. General corrosion effects on magnetic field around the rebars were detected by device while the distance between sensors and surface of rebar was 11 cm. Although, recorded magnetic field intensity was decreased by increased the distance between sensors and rebar.
- Two preliminary equations using linear regression method were extracted using wavelet energy analysis on experimental test of generally corroded rebars.
- Local corrosion of different rebars was detected by using developed device and continuous wavelet transform analysis. The depth of corrosion area was less than 0.5 mm.
- Numerical simulation of ultrasonic transducer was done by using discrete finite element method. Calibration of transducer was done for the first time by using laser vibrometer.
- Numerical simulation of longitudinal wave propagations were done for de-bonded and bonded rebar to the concrete cylinder.
- Experimental ultrasonic tests were done on different de-bonded and bonded mortar cylinders.

Numerical simulations and experimental tests were compared in all sections to confirm experimental tests.

1.5. Contributions

The main scientific and engineering contributions of this project include:

- a new prototype for corrosion/crack detection of reinforced concrete structures was developed.
- the design of a signal processing methodology for analyzing passive magnetic data from experimental tests.
- ultrasonic transducer is characterized using a laser vibrometer.
- laser vibrometer measurements for detection of de-bonding in reinforced concrete sample are performed.

1.6. Thesis organization

This thesis is divided in two main parts: Experimental tests and numerical simulations. Experimental tests are based on Passive magnetic inspection method and ultrasonic method. Passive magnetic method test was done by using developed scanning device as a part of this research project. Ultrasonic test was done by using Laser vibrometer. Numerical simulations were done for all experimental tests by using discrete finite element method. Results of experimental tests and numerical simulations were compared at the end of each section.

Eight chapters are current thesis are:

Chapter 1 motivation, objectives, and the organization of the thesis are presented.

Chapter 2 Introduction to nondestructive testing methods and methods that were used in this thesis.

Chapter 3 Review of scanning device prototype, sensors, parts and its specifications.

Chapter 4 Using developed device and signal processing methods for detection of three simples holes on rebar.

Chapter 5 De-bonding assessment of reinforcement using ultrasonic testing method and laser vibrometer.

Chapter 6 General and local corrosion assessment of reinforcement using passive magnetic method.

Chapter 7 Conclusion and recommendations.

Chapter 2

2.1.Magnetic inspection method

2.1.1. Active and passive methods

One of the most significant differences between NDT methods is the way of obtaining information from an inspected object. For example, the ultrasound method generates elastic waves, sends these waves through the specimen, and then collects the reflected and refracted wave fields to detect the shape of the defect [17]. Active methods emit external potentials (e.g., acoustic excitation) and then receive the reflections and refractions from the waves passing through the object. On the other hand, passive methods simply use self-potential fields created or altered by the object. In the case of acoustic energy, this could be, for example, the small internal acoustic events emitted during testing of the object (loading or heating). In summary, active method has a source and a receiver, but in passive methods there is just a receiver. Figure 2.1 shows a schematic of NDT principles using active and passive methods.

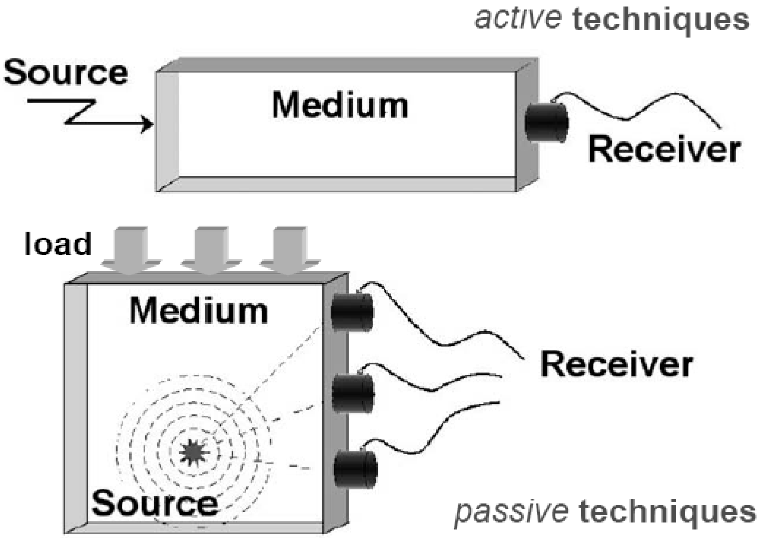

Figure 2.1. Schematic picture of active and passive methods [17].

2.1.2. Magnetic methods

Magnetic property of ferromagnetic materials is the physical basis of magnetic inspection methods. Structural and mechanical properties of ferromagnetic materials are related to their magnetic properties, so changes in structure or metal crystals such as the introduction of defects, corrosion, crack, excessive deformation, and so on, can potentially be detected by magnetic methods [18].

Ferromagnetic metals have the ability to hold an inductive magnetic field; measuring this magnetic field reveals inhomogeneity in the magnetization of metal. In a constant value of induced magnetization, non-damaged materials have uniform magnetic field, but any physical damage in the specimen causes to have a different magnetic response. This means that there is a magnetic leakage through each discontinuity in the metal such as cracks, corrosion, pitting, or any kind of crystalline changes [19]. The main active magnetic methods are:

I. Magnetic particle inspection,

II. Magnetic flux measurements,

III. Electromagnetic microwave testing

Each of these methods has advantages and disadvantages, but one main disadvantage of active magnetic methods is their repeatability. It is very hard to repeat the test for one to two years following each test depending on the magnetic properties of object, such as magnetic permeability and magnetic saturation because of the slow decay of the induced magnetization. Also, their penetration depth is not significant.

It may seem that these disadvantages are not significant, but because of them, active magnetic methods are not applicable to concrete reinforcement assessment. For example, it is necessary to access the surface of the metal object when using the magnetic particle method. In addition, both the magnetic flux technique and the electromagnetic microwave method require being very close to the object [20].

Comprehensive literature review revealed that there is a need for quick and accurate method to assess corrosion and crack conditions of reinforcement. In other hand, passive magnetic inspection method has a potential to be a proper solution to solve this industrial problem. This method has been used to assess stress concentration zones for exposed industrial metal parts and also for underground oil and gas pipelines.

2.2. Passive magnetic method

All known magnetic non-destructive inspection methods applicable to ferromagnetic materials can be classified as active or passive methods. The difference between active and passive magnetic methods is the same as for all inspection methods. In active magnetic methods, a specific magnetic field is applied from an outside source and then the response is captured by a receiver. In passive magnetic methods, residual magnetism of the system is measured. This residual magnetism can create a natural magnetic field around the object, perturb the Earth's natural magnetic field, or affect any artificial magnetic field. The residual magnetism of a ferromagnetic object is magnetic memory of object during the process of making or installing (as in the cold distortion of a reinforcing bar) [21].

The passive magnetic method is more complicated than active magnetic method. The natural residual magnetic of ferromagnetic materials which is result of magnetic field of earth or production process, is always much less than the magnetic value which is result of artificial magnetic induction methods. Therefore, a more sensitive and accurate device is needed to detect anomalies and distinguish the anomaly from the natural magnetic behavior. In addition, the passive magnetic method is directly related to stress condition of material. It is indirectly related to any kind of corrosions, defects, or cracks. Basically any changes in stress condition of materials can be detected by magnetic anomalies [21, 22].

Three physical factors cause residual magnetism in ferromagnetic materials [23]:

I. External magnetic field during measuring process;

II. Magneto-mechanical property of ferromagnetic materials; and

III. The interaction of the natural magnetic field with defects and inhomogeneity in the metal crystals and structure.

2.2.1. Fundamental definitions of magnetism

Important definitions about magnetism and ferromagnetic material properties are listed here.

Magnetic moment:

Magnetic moment is the property of ferromagnetic material to have a mechanical moment with an applied magnetic field. Magnetic moment associated with individual electrons is the main reason of macroscopic magnetic properties of materials. Magnetic moment is a positive vector quantity which shows the object tendency to align with a magnetic field. The motion of electron charges and spin angular momentum are two main sources of magnetic moment. It happens by applying a magnetic field or mechanical force. A magnetic moment which appeared because of mechanical force is called mechanical magnetic moment [24].

Magnetic induction:

Magnetization process of a ferromagnetic material like iron in a magnetic field, or under mechanical force is magnetic induction. Magnetic induction is designated by $\overline{B}$, and shows the direction and magnitude of the magnetic force's influence on the rotation direction of dipoles [24]. The total magnetic induction is the sum of the contributions of all of the current regions, and is expressed as follows [23, 24]:

$$\vec{B} = \frac{\mu_0}{4\pi} \cdot \int \frac{I}{r^3} \overrightarrow{dl} \times \vec{r} \tag{2.1}$$

Here, μ_0 is the magnetic constant ($4\pi \times 10^{-7}$ N/A^2), $\vec{r}$ is a unit vector from the basic current I to the induction point, r is the distance between basic current and induction point, l is the length of specimen and $\vec{B}$ is the magnetic induction (Figure 2.2). The mechanical force, vector $\vec{F}$, at the center of the magnetic field $\vec{B}$ can be derived from the equation below [24]:

$$\vec{F} = \int I \overrightarrow{dl} \times \vec{B} \tag{2.2}$$

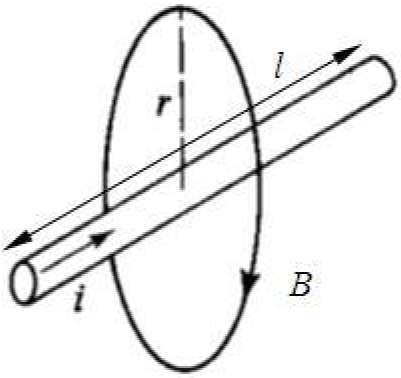

Figure 2.2. Magnetic induction.

There are several loops (magnetic flux) around permanent magnets materials which the closest loops path is called magnetic circuit. Calculating the force influencing the current circuit from the following equation is easy.

$$\vec{F} = |p_m| \cdot \frac{\overrightarrow{dB}}{dn} \tag{2.3}$$

This equation uses the circuit radius which is shorter than the distance from the field source to the circuit which was used in the previous equation (eq. 2.2) [24].

$$\frac{\overrightarrow{P_m}}{|P_m|} = \frac{\vec{n}}{|n|}$$

where n is turns per unit length and P_m is magnetic moment. The direction of the force is the same as the direction of the circuit magnetic moment $\overrightarrow{p_m}$ which induced the magnetic field [23]:

A mechanical magnetic moment is then obtained from the following equation [24]:

$$\overrightarrow{M_{Mex}} = \vec{p}_m \times \vec{B} \tag{2.4}$$

Magnetic saturation

For each ferromagnetic material, there is a maximum magnetic magnitude which by increasing the magnetic field or mechanical force, it does not increase more. In this situation the ferromagnetic material is at the magnetic saturation point [24].

2.2.2. Ferromagnetism

Some metals can have a permanent magnetic moment when there is no external field; moreover, these materials can manifest a high magnitude of magnetic susceptibility. These are characteristics of ferromagnetic materials and transition metals like iron, nickel, cobalt, and some rare metals like gadolinium (Gd). These metals have a magnetic susceptibility higher than 10^6 (Magnetization per unit volume). The permanent magnetic character of ferromagnetic materials is the result of magnetic moments of atoms. Spins of electrons in the atom result from the structure of electrons, and the orbital motion around the nucleus causes the magnetic moment. Magnetic domains are the regions of crystal in which the direction of spins in the atoms are aligned in the same orientation. A combination of all domains with aligned electrons is cause of magnetic moment in ferromagnetic material.

Ferromagnetic domain theory

Domains are small regions within which local magnetization is saturated. Each specimen is composed of these domains in which the magnetization directions are both similar and different. Figure 2.3 (a, and b) shows the schematic view of domains with zero induction magnetic field for single crystalline and polycrystalline samples, respectively [24].

There are two ways of magnetizing specimens: first by increasing the volume of domains which are oriented respectively to the magnetic field orientation and second by rotating the magnetization direction to the field direction. Figure 2.4 shows these two methods. Domain boundary displacement usually happens in weak fields while magnetization rotation usually happens in strong fields [24].

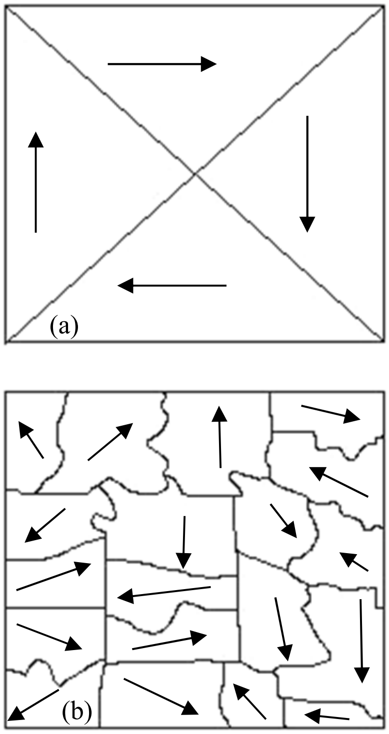

Figure 2.3. Schematic view of domains with 0 induction magnetic field. (a). Single crystal sample. (b). Polycrystalline sample [24].

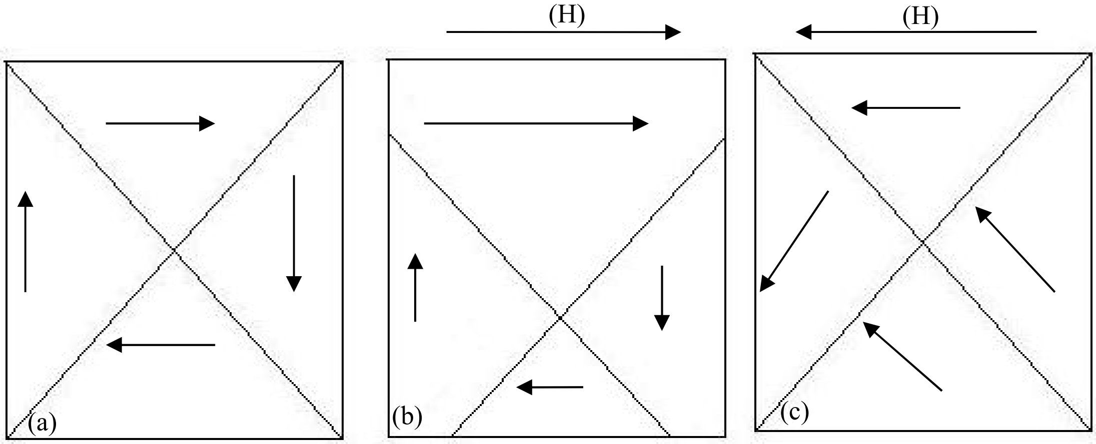

Figure 2.4. Different processes of magnetization. (a). non-magnetized crystal. (b). magnetization by domain boundary displacement. (c). Domain rotation magnetization (H arrow shows the magnetic induction direction) [24].

Five different factors must be considered in domain analysis [25]:

- Crystal anisotropy: This measure the force tending to hold magnetization of domain parallel to direction of easy magnetization.

- Block wall: In traversing a domain boundary the adjacent spins are not parallel; the forces of exchange interaction tend to make them parallel while the spin-orbit anisotropy tries to hold them parallel to a direction of easy magnetization. A force is necessary to move a wall to a position in which the anisotropy of crystal structure or strain is greater.

- Action of magnetic field: This tends to align the magnetization parallel to the field.

- Surface charge of magnetization: The occurrence of magnetic poles on the surface of the specimen, or on inter-domain boundaries is associated with a magnetic field which spreads out through space and also reacts with the magnetization of material.

- Strain anisotropy: Similar to crystal anisotropy, but organization in lattice deformation, probably through spin-spin or spin-orbit coupling.

These factors are the main components of corrosion detection based on passive magnetic method which will be further discussed in next chapters.

Domains origin

Magnetic domains are result of contributions of energy exchange (magnetic field, mechanical effect), and anisotropy of ferromagnetic materials. Two experimental methods are used to identify these domains:

1- Magnetic powder patterns method to take microphotographs of domain boundaries. Bitter (1931) has proven that shapes and sizes of domains exist as expected theoretically, and are affected by mechanical and magnetic forces [27].

2- Polarized light with an appropriate optical analyzer method in used to reveal magnetic domains. In this method the angle between the light beam and magnetization direction affects the reflection coefficient of the surface [28].

Figure 2.5 shows the simple structure of domains, representing a cross-section of a single crystal of ferromagnetic material [24].

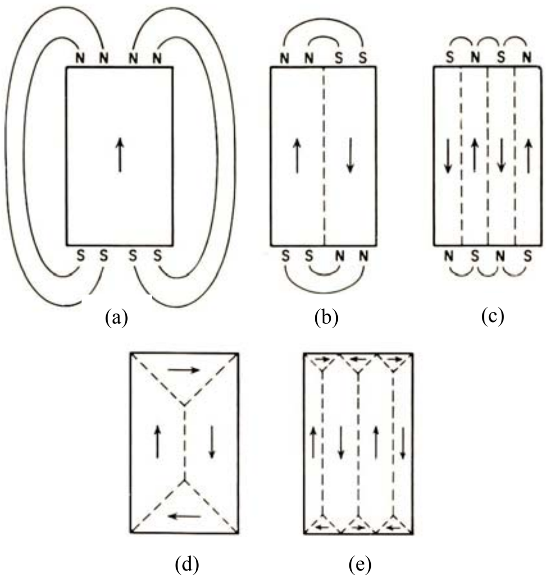

Figure 2.5. Domains origin. (a). Saturated single domain. (b). Dividing the single crystal in to two domains. (c). N number of domains. (d). Domain arrangement with zero magnetic energy. e. N numbers of domains with final zero magnetic energy [24].

Anisotropy energy of crystals is the energy required to form domains in the specimen's crystals. This energy forms magnetic domains along the specific crystallographic axes, and the preferred axis is easily magnetized. These axes differ from one specimen to another. The magnetization may be easy or difficult according to these specific crystallographic axes in each specimen [24]. Figure 2.6 shows microscope images of magnetic domains in nano-crystalline alloys with different percentage of Cobalt (0%, 20%, 40%, and 60%). There is an increase in number of domains by increase in Cobalt percentage. Also in Figures 2.6(c) and 2.6(d), the extension of domains wall are at induced magnetic anisotropy directions shown by the black arrow at the left of Figure 2.5. It can be because of the effect of Cobalt as a more magnetized metal than Iron [29].

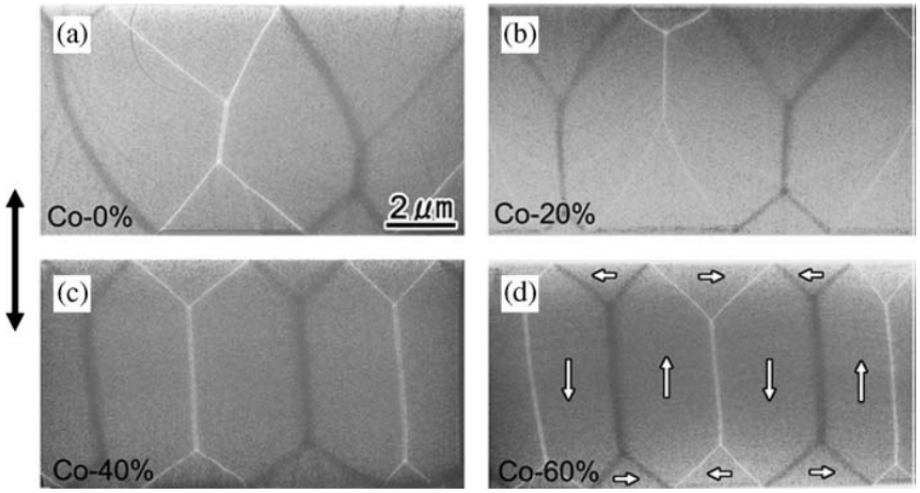

Figure 2.6. Microscope image of magnetic domain with direction of induced magnetism (black arrow) and oriented magnetic domains [29].

2.2.3. Magnetization process of ferromagnetic materials

External magnetic field

The effect of an external magnetic field on the magnetic moment vectors of atoms causes changes in the angular position of the appropriate electron's orbit. This is the magnetization process of ferromagnetic material in the external magnetic field [31, 33].

The external artificial magnetic field, while re-orienting the magnetic moment vectors of atoms, changes the direction of the proper magnetization resulting vector. Then, it changes the domain's magnetization direction. This effect cause changes in magnetic memory of specimen [34, 35].

For example, figure 2.7 shows the effect of an external magnetic field on a Pt/Co/AlO$_x$ Nano wire. The blue arrow (thick arrow) shows the direction of magnetic field and the black arrows show the changes in the domain's magnetization direction respectively from the domain wall to the end [33].

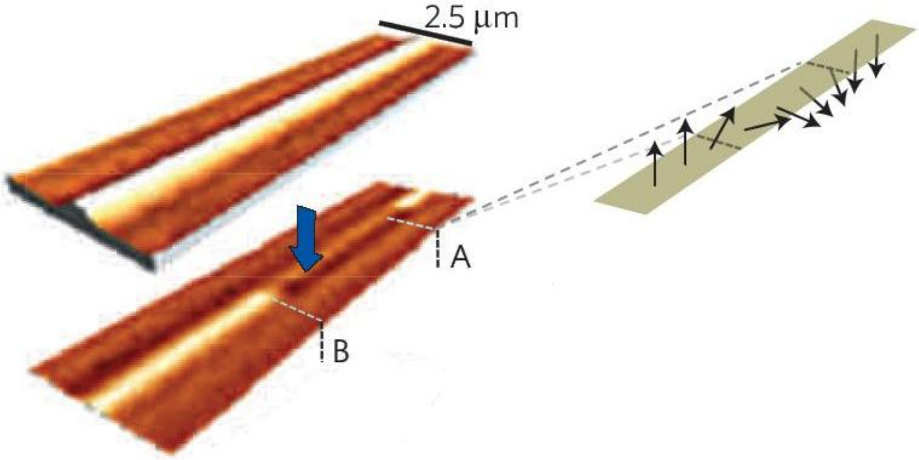

Figure 2.7. The external magnetic field and its effect on the domain magnetization direction. (Blue arrow (thick arrow) shows the applied artificial magnetic, black arrows shows the direction of dipoles in magnetic domains) [33].

Mechanical force (magneto-mechanical effect)

Shape and volume changes are the most significant effects of external force field on a ferromagnetic specimen. Atomic density is a function of lattice strain state. Therefore, any changes in the lattice geometry have an effect on atom densities, then changes in domains shape and volume. Positive dislocation of planes causes these changes and finally changes the magnetic moment of the object [24]. Changes in magnetic properties based on changes in geometry dimensions are referred to as the magneto-mechanical effect [51-53]. Stress changes the magnetism and magnetic properties of the object as a result of changes in domain structures [54]. The following equation defines magnetism as a function of applied stress:

$$\frac{dM}{d\sigma}=\frac{1}{\varepsilon^2}\sigma\left(1-c\right)\left(M_{an}-M_{irr}\right)+\frac{dM_{an}}{d\sigma} \tag{2.5}$$

where M_{an} an hysteric magnetization (A/m), M_{irr} irreversible magnetization (A/m), c ability of magnetic domains to be magnetized, σ stress, and $\varepsilon=\left(E\xi\right)^{\frac{1}{2}}$ is the material property related to the Young's modulus (E), and ξ is a coefficient with dimensions of energy per unit volume. This equation illustrates that magnetization based on stress changes also depends on the irreversible component of magnetization (M_{irr}) and losses in the magnetization curve of the material (M_{an}). Irreversible component of magnetization means the magnetic value of specimen which does not change if the mechanical effect be released, and anhysteric magnetization means the amount of magnetic value of specimen which decreases mechanical force is released [50]. The angle between applied stress and magnetization field is also important; the effect of this angle (θ) is based on strain energy (E_{σ}) resulting from the application of external stress. Therefore,

$$E_{\sigma} = -\frac{3}{2}\lambda_s \sigma \cos^2 \theta \tag{2.6}$$

where λ_s is the saturation magnetization and is therefore also the maximum possible magnetic magnitude of a ferromagnetic material [50].

A strain level affects the magnetic magnitude of ferromagnetic materials. These changes are sometimes reversible and sometimes irreversible [36]. Figure 2.8 shows the effect of tensile stress on the magnetism of an object. In this example, magnetism has a linear relationship with compression stress, but for tension it is not linear. When the stress is released from the specimen, it loses its magnetic magnitude; conversely, when it is under stress, the magnetic magnitude of an object increases [39]. In some materials, at different values of magnetization, an irreversible change of magnetization due to stress changes takes place. Figure 2.9 shows this irreversible change in a magnetic magnitude of ferromagnetic material at due to stress changes. This behavior is evidenced by all ferromagnetic materials, but the values at which an irreversible change takes place depend on the different properties of each material [37].

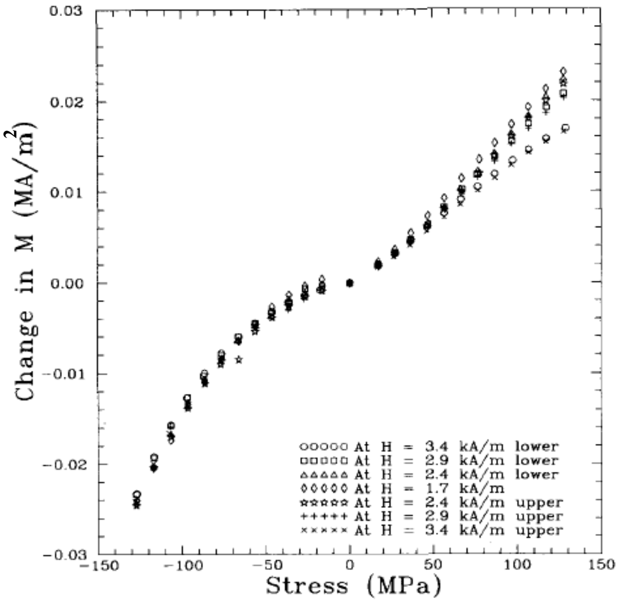

Figure 2.8. Reversible magnetization changes due to tensile stress changes in different magnetic field strengths [36].

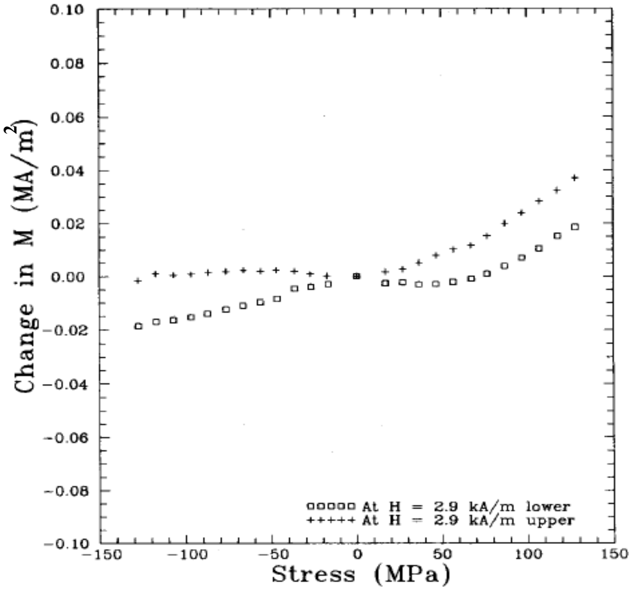

Figure 2.9. Irreversible magnetization changes due to stress changes in different magnetic field strengths [36].

Magnetic hysteresis

Magnetization in ferromagnetic materials is produced by an external magnetic field and is affected by changes in stress or temperature. The resulting magnetic value can be reversible or irreversible. Many different experiments have been performed to determine the effects of stress and temperature on the magnetization of ferromagnetic materials. Generally, with a small magnetic field or stress change, it is expected to see reversible behavior after release. While, it does not happen most of the time because there is always a small amount of magnetic field everywhere [36]. It has also been proven that cyclic stress causes irreversible changes in ferromagnetic materials [40].

Figure 2.10 shows the typical curve of magnetic hysteresis due to the applied external magnetic field. In this graph the values of the magnetization field (H) are plotted versus the intensity of magnetization (I). Clearly, the magnetization curve differs from the demagnetization curve [41], and this is the hysteresis effect.

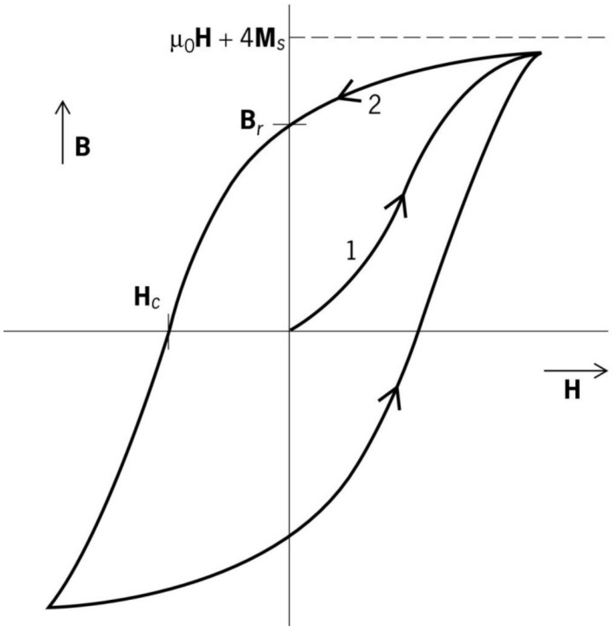

Figure 2.10. Typical hysteresis loop of ferromagnetic material [41].

2.2.4. Relative magnetic permeability as a function of external magnetic field and stress

From a practical perspective, relative magnetic permeability is an important magnetic characteristic of ferromagnetic materials. The relative magnetic permeability is a key for any analytical definition of the effect of magnetic intensity on ferromagnetic materials and the value of their magnetization [42].

The magnetic relative permeability of a ferromagnetic material is expressed by a coefficient which is related to the intensity of magnetization field and induction. There are four types of this coefficient [23]:

- static
- dynamic
- differential
- initial

Gradual changes in the intensity of the magnetic field H and its correlation with induction B characterize the static relative magnetic permeability through this linear expression: $\mu_{st} = B / (\mu_0 \cdot H)$ [23].

Magnetic viscosity or magnetic creep is magnetic relaxation or a delay of the change in magnetic value of a ferromagnetic material after releasing the external magnetic field [43].

Differential, initial, and maximum permeability terms are defined to explain the effect of nonlinear magnetic intensity of the induced field. Differential magnetic permeability is the differential value of the $B(H)$ curve at a point I; the equation is $\mu = B / (\mu_0 \cdot H)$, and the $\mu(H)$ curve is obtained from all of those points. The maximum permeability $\mu_{d\max}$ is the maximum value of the $\mu(H)$ curve. Interpolation of $\mu(H)$ curve at zero magnetic intensity gives the initial magnetic permeability. Figure 2.11 shows the difference between magnetic permeability types on the $B(H)$ curve of a ferromagnetic material [23]. Dynamic permeability is a definition for magnetic permeability which changes over a time by changes in induction magnetic field [55].

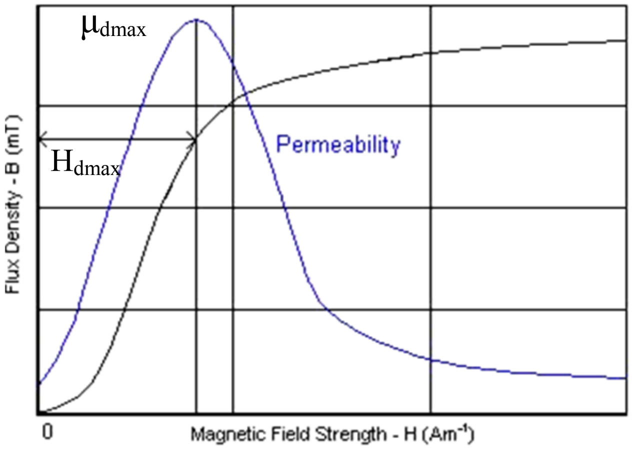

Figure 2.11. Typical $B(H)$ curve of ferromagnetic material with permeability curve and H_{dmax} [23].

Determination of $H_{d\max}$ for each type of permeability is not difficult and can be determined by the permeability versus magnetic field intensity curve. Figure 2.12 shows the static and differential permeability curves, so the $H_{d\max}$ for both curves is easy to recognize [24].

Figure 2.12 compares methods of static and differential relative magnetic permeability determination of ferromagnetic magnetization. Assessing the precise determination of $H_{d\max}$ -the intensity at which the magnetic permeability has at its maximum, is a little complicated in this case [24].

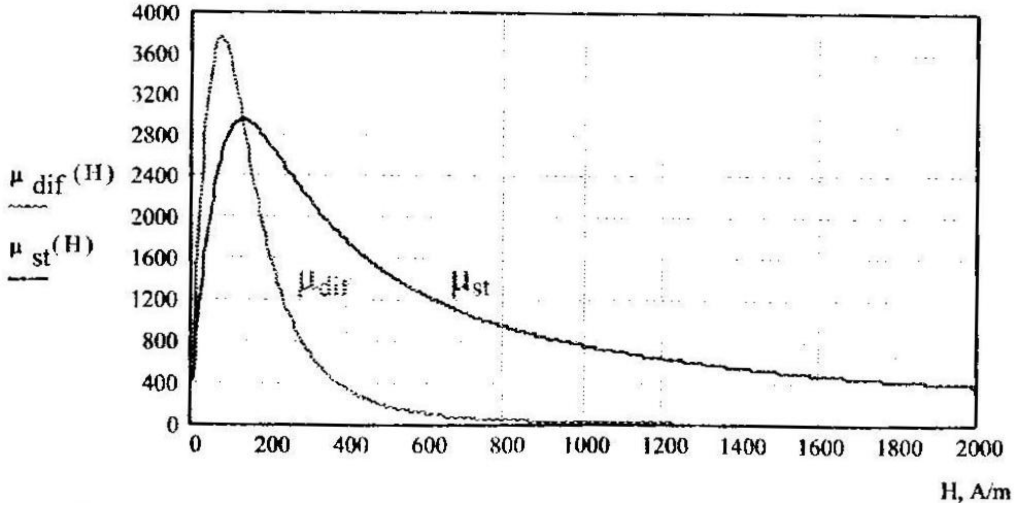

Figure 2.12. Static and differential magnetic permeability [24].

Finally, the general equation of relative magnetic permeability is defined as [24]:

$$\mu = \frac{1}{\mu_0} \cdot \left(\frac{d}{dH} B \right) \tag{2.7}$$

Where μ_0 is the magnetic permeability of free space and is equal to $4\pi \times 10^{-7}\ H/m$ [23].

Magnetic saturation process

Increase in the intensity of an external magnetic field causes an increase in ferromagnetic magnetization because of reorientation of magnetic domain vectors to the direction of the applied field. This magnetization is a non-linear curve even with a linear increase of the magnetic field, and the curve has a step-wise nature which is called the Barkhausen effect. During the displacement of domains, the shifting of domain walls increase domain volumes, and causes to change in shape, and domains dimension. Therefore the magnetization curve of the ferromagnetic material will be non-linear and shows hysteresis.

There are five typical regions on a magnetization curve which generally occur in most ferromagnetic materials during the magnetization process [43]:

Region-I: Primary magnetization region, where $B = \mu_0 \cdot \mu \cdot H$. Mainly, displacements of domain boundaries occur in this region at a constant rate with the magnetic field changes because of initial magnetic permeability. This region is also the reversible magnetization phase [24].

Region-II: In this region, called the Rayleigh region, the relative magnetic permeability increases linearly, and magnetization results from the displacement process of the magnetic domain boundaries. Part of this response in this region is reversible – linearly dependent on H – and part is irreversible – approximately dependent on H [24].

Region-III: This region consists of rapid magnetization growth accompanying irreversible displacement of domain boundaries. The highest value of relative permeability occurs in this region [24].

Region-IV: In this region, also called the transformation region, the saturation point is approached and plays an important limiting role [24] on the shape of the magnetization relationship.

Region-V: The saturated region [24].

Figure 2.13 shows the five typical regions of ferromagnetic materials magnetization process from zero magnetic value, up to the saturation point [23].

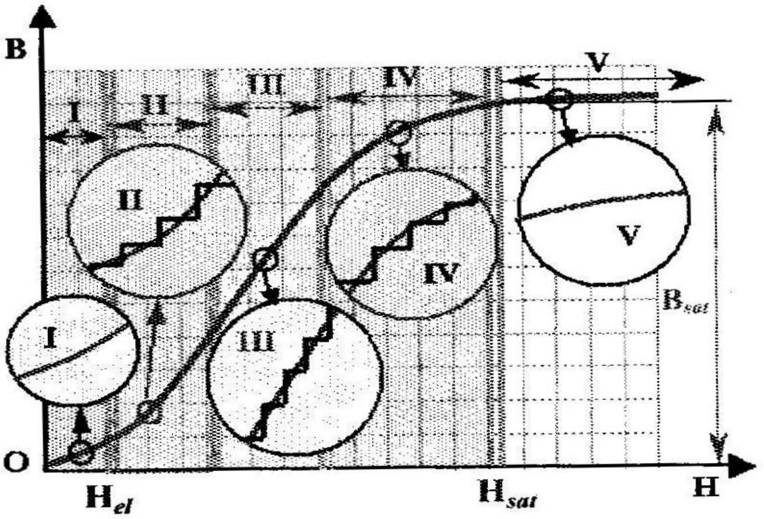

Figure 2.13. Five regions of ferromagnetic materials magnetization process [24].

Relationship between magnetism and mass

Individual electron behavior is the basic cause of magnetic moments, and leads to the macroscopic magnetic properties of materials. Magnetic moments of each electron can be generated from the orbital motion of electrons around the nucleus and the electron spin. These two motions orbit around the axis of the atom's center and around the spin axis, respectively. In this situation each electron is a small magnet with permanent orbital and spin magnetic moments [44].

The Bohr magneton μ_B with a magnitude of 9.27×10^{-24} A·m^2 is the indivisible quantum of magnetic moment. Therefore, the spin magnetic moment for each electron in an atom is $\pm\mu_B$, and the orbital magnetic moment is equal to $\mu_B m_l$, where m_l is the magnetic quantum number of the electron [44].

Orbital moments and spin moments of some electron pairs cancel each other in each individual atom. For instance, spin up cancels the spin moment of an adjacent atom with spin down. The net magnetic moment is the sum of all the magnetic moments of each of the electrons which result from both spin and orbital contributions. The response of electrons and atomic dipoles to the applied magnetic field cause material magnetism [45].

In ferromagnetic materials, atomic magnetic moment arise from sustained (permanent) electron spin as a consequence of the electron structure, and is the main reason for a permanent magnetic moment in a magnetized ferromagnetic material. The orbital magnetic moment is quite small in comparison to the spin moment, yet it still has an effect on the magnetism of ferromagnetic materials. Adjacent atoms which align with one another has non-zero net spin magnetic moments because of coupling interactions, although the origin of atomic coupling interactions is not completely understood [46].

The saturation magnetization, Ms, occurs when all dipoles are mutually aligned with the external field. This is dependent on saturation flux density *Bs*, and is equal to the sum of the net magnetic moment of each atom and the number of atoms present. For example, the net magnetic moment for iron (Fe) is 8.22 per atom, and to calculate the saturation magnetization one may say that [48]:

$$M_s = C\mu_B N \tag{2.8}$$

Here, C is the net magnetic moment per atom for the specific ferromagnetic material, μ_B is the Bohr magneton constant, and N is the number of atoms per cubic meter. The number of atoms is [47]:

$$N = \frac{\rho N_A}{A_{material}} \tag{2.9}$$

Where ρ (g/m^3) is the density of the ferromagnetic material, $A_{material}$ (g/mol) is its atomic weight, and N_A (atoms/mol) is Avogadro's number.

Therefore, for ferromagnetic materials $H << M$, magnetic flux density will be [47]:

$$B = \mu_0 H + \mu_0 M \Rightarrow B \cong \mu_0 M \tag{2.10}$$

Temperature effect on magnetic properties

Magnetic characteristics of materials can be influenced by temperature. The magnitude of thermal vibration of atoms increases with an increase in temperature, and also randomizes the direction of an atom's moment. This effect causes more and more dipoles to be misaligned as the temperature increases, thus decreasing the saturation magnetization level. The Curie temperature, T_c, defined for each ferromagnetic material, is the temperature at which the magnetic saturation becomes zero (magnetization becomes impossible. Above this temperature, the coupled spin forces remain totally disrupted and ferromagnetic materials acts as paramagnetic materials. For iron, cobalt, nickel, and Fe_3O_4, T_c values are 768˚C, 1120˚C, 335˚C, and 585˚C, respectively. Figure 2.14 shows the saturation magnetization changes based on temperature for iron and Fe_3O_4 [49]. In the case of heat works on specimen, there is a big difference between heat work area and other area and there will be an anomaly on magnetic data. This anomaly is not related to any kind of defects.

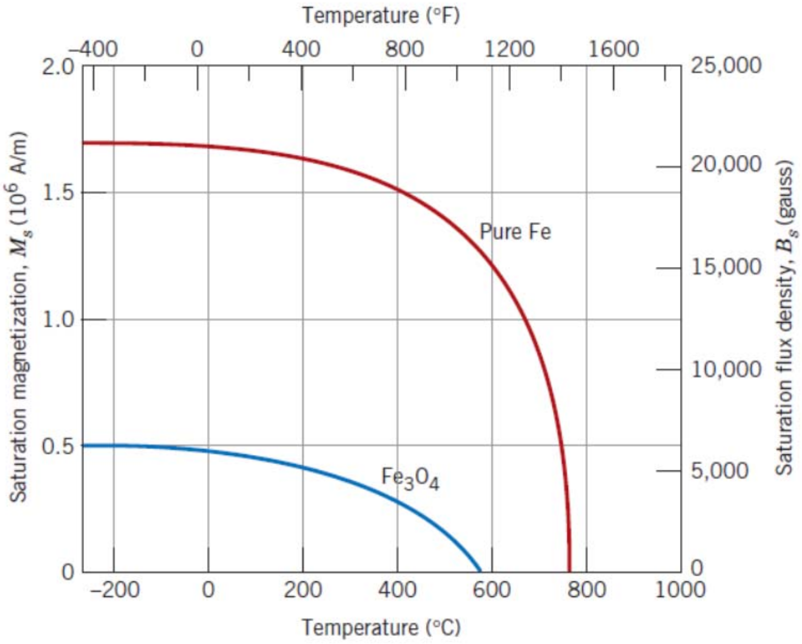

Figure 2.14. Magnetic Saturation versus temperature [49].

2.3. Ultrasonic method

One of the most essential construction materials in civil structures (e.g., buildings, bridges, platforms), and also underground structures (e.g., roadbeds, concrete pipelines and tunnels), is reinforced concrete (RC) [56]. Usually reinforced concrete is designed to be in service for more than 100 years in harsh environmental condition [57]. External environmental conditions such as exposure to corrosive industrial fluids, solutions of road salt, and service temperature, are known to considerably affect the durability and longevity of RC structures. Defects (corrosion and cracks) in steel reinforcement result from these conditions, and decrease the strength of RC structures, thus increasing their failure risk.

Recently there has been a lot of work to improve quality of concrete matrix [58], or different reinforcement protections [59, 60, and 61]. Although these attempts increased service time of RC structures, but deterioration process of reinforcement never stops. Hence, condition assessment of RC structures is still vital to assess their serviceability and their level of safety. Standard ultrasonic as a Non Destructive Testing (NDT) method has been used for more than sixty years in industrial applications. Applying 0.2-30 MHz range of bulk wave, measuring arrival time, and calculating probable discontinuities are main procedure of regular ultrasonic methods.

One of the most well-known non-destructive testing methods for underground pipelines is the ultrasonic method which is based on introducing high frequency sound waves to propagate into the inspection object. The range of frequency varies between different types of ultrasonic methods, but usually it is between 0.5 MHz to 20 MHz. Attenuation of sound waves because of mechanical properties of the inspection object, intensity of sound waves, and reflection of waves from the opposite surface of the object are the main approaches to measurement in this method [61].

Two main categories of conventional ultrasonic methods are the pulse echo method, and the transmission method. Pulse echo methods are based on reflection of sound wave from opposite surfaces. Capturing and analyzing reflected waves from the opposite surface and also from the surfaces of defects such as cracks is the main basis of this method. Arrival time and the degree of reflection depend largely on the condition of the inspection object. Capturing transmitted wave from the opposite site, measuring the arrival time, and comparing result with healthy condition are main approaches of the through-going transmission method [61].

Ultrasonic testing methods have experienced impressive developments in recent years, and now it they have become well-known methods in industry and in many different applications [62]. These developments contain applying remote operation of probes, some automatic operations, using different kind of waves, improved processing systems, using high accuracy transducers, and using newly-developed analysis software. Data processing methods of increased efficiency and reliability for ultrasonic methods now exist. These developments have allowed professionals in this area to develop new branches of ultrasonic methods such as the guided wave method [62].

Two main advantages of the guided wave method are: first, it is more appropriate for pipe inspection over a long distance, and the second one, it permits rapid inspection of the pipe's wall thickness. Comparing to the conventional point by point ultrasonic inspection method, this method can be used much more efficiently. Another advantage of this method in addition to fast inspection over a long distance is inspection capability for underground or underwater pipelines while they are in service. The possibility of inspection for different parts and joints with complex geometry is another potential advantage of this method [63, 64].

In this section, different types of elastic wave propagation and their application in the non-destructive testing area are explained. The basis of the guided wave method, its application, its advantages and disadvantages, limitations and weaknesses are the main topics addressed in this chapter. The following chapter addresses setting up different experimental tests on different types of water pipelines. These tests are the first step in applying guided wave principles, especially the use of the Lamb wave, to determine remaining wall thickness of underground water pipelines.

2.3.1. Surface waves

Being dispersive and guided in heterogeneous medium are two main properties of surface waves which cause them to be useful for NDT applications [65]. Surface waves propagate along a free surface (such as earth-air) or along an interface between materials with different elastic properties, these are called Rayleigh (1885) waves (R-wave) [66, 67 and 68]. Lamb waves (L-wave) are another type of surface waves which refer to the propagation of a strain wave as the result of the presence of two close boundaries, as in a plate. The particle displacement in Lamb waves is in two directions; there is a component of movement in the propagation direction, and another component perpendicular to the plane of the plate [69].

The major difference between R-waves and L-waves is the condition of the surface that they propagate in; R-waves propagate along one free surface like the interface of ground and air (a half-space), whereas L-waves propagate in the presence of two free surfaces like plates. When the frequency is sufficiently high so that the wavelength is much smaller than the thickness of the plate, then it is expected that L-waves behaves like R-Waves. Both of these two modes (R-wave, L-wave) are dispersive when the medium is heterogeneous, and this means that in different frequencies they have different velocities. Therefore over different distances, they have different propagation pulse shapes [70].

2.3.2. Lamb waves concept

R-waves have a small penetration depth from the free surface, but when the medium is thin enough to let the R-wave travel from the top to the bottom surface effectively, and then it becomes a flexural Lamb wave (L-wave). For this to occur, the thickness of medium should be almost equal to wavelength [70, 71]. Particle displacements occur parallel and perpendicular to the wave propagation direction, as for Rayleigh waves, and L-waves propagate in two modes: symmetrical and anti-symmetrical (Figure 2.15). L-wave velocity is related to the frequency, so it is important to make a distinction between phase and group velocity. The L-wave phase velocity depends on parameters like the order of the mode (0th, 1st, 2nd …) [72], whether the motion is symmetrical or anti-symmetrical, frequency, plate thickness, and the nature of the plate material.

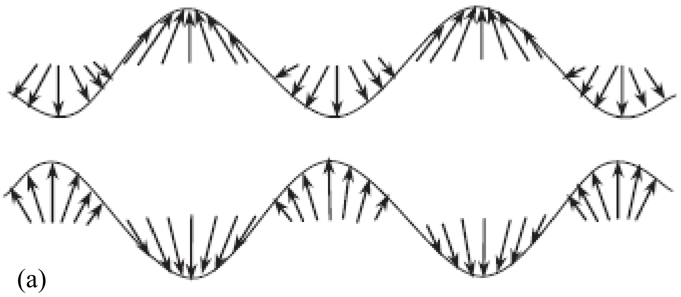

(a)

symmetric Lamb mode

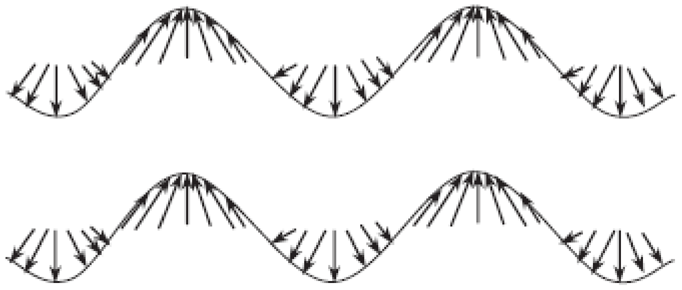

(b)

anti-symmetric Lamb mode

Figure 2.15. Lamb wave modes. (a). symmetric. (b). anti-symmetric [73].

The most important mode in L-wave studies is the fundamental mode [72]. L-waves are dispersive and their equation of motion can be expressed by the Rayleigh-Lamb frequency equation [74]. To get the equation of motion we need to start looking at Newton's second law which can be written as:

$$\left(\frac{\partial\sigma_{xx}}{\partial x}+\frac{\partial\sigma_{xy}}{\partial y}+\frac{\partial\sigma_{xz}}{\partial z}\right)\delta x\delta y\delta z=\left(\rho\delta x\delta y\delta z\right)\frac{\partial^2 u}{\partial t^2} \tag{2.11}$$

Where ρ is the density and u is the displacement. This equation can be written in x, y and z axes as well. So, for displacement in x axis:

$$\rho\frac{\partial^2 u}{\partial t^2}=\left(\frac{\partial\sigma_{xx}}{\partial x}+\frac{\partial\sigma_{xy}}{\partial y}+\frac{\partial\sigma_{xz}}{\partial z}\right) \tag{2.12}$$

From Hooke's law, the stress parameters of the equation can be replaced by elastic relations of an isotropic material:

$$\sigma_{xx}=\lambda\Delta+2\mu\varepsilon_{xx},\ \sigma_{xy}=\mu\varepsilon_{xy},\sigma_{xz}=\mu\varepsilon_{xz}$$

where λ and μ are the elastic constants (Lame's constant), $\Delta=\frac{\partial u}{\partial x}+\frac{\partial v}{\partial y}+\frac{\partial w}{\partial z}$ is the volumetric strain, v and w are displacements in axes y and z respectively.

Result from combining Hooke's law and Newton's second law is wave equation:

$$\rho\frac{\partial^2 u}{\partial t^2}=\left(\lambda+\mu\right)\frac{\partial\Delta}{\partial x}+\mu\nabla^2 u \tag{2.13}$$

where $\nabla^2=\frac{\partial^2}{\partial x^2}+\frac{\partial^2}{\partial y^2}+\frac{\partial^2}{\partial z^2}$ is Laplacian operator.

In the case of traction-free surface in xy plane with z is positive through the interior of the solid, for the 2D solution of wave equation, the potential functions are given as:

$$u=\frac{\partial\phi}{\partial x}+\frac{\partial\psi}{\partial z}\ \text{and}\ w=\frac{\partial\phi}{\partial z}-\frac{\partial\psi}{\partial x} \tag{2.14}$$

For dilation and rotation:

$$\Delta = \frac{\partial u}{\partial x} + \frac{\partial w}{\partial z} = \nabla^2 \phi \text{ and } 2w_x = \frac{\partial u}{\partial z} - \frac{\partial w}{\partial x} = \nabla^2 \psi \tag{2.15}$$

where ϕ and ψ are correspond to dilation and rotation respectively.

Using wave equations (2.13, 2.14 and 2.15):

$$\rho \frac{\partial}{\partial x}\left(\frac{\partial^2 \phi}{\partial t^2}\right) + \rho \frac{\partial}{\partial z}\left(\frac{\partial^2 \psi}{\partial t^2}\right) = (\lambda + 2\mu)\frac{\partial}{\partial x}\left(\nabla^2 \phi\right) + \frac{\partial}{\partial z}\left(\nabla^2 \psi\right) \tag{2.16.a}$$

$$\rho \frac{\partial}{\partial z}\left(\frac{\partial^2 \phi}{\partial t^2}\right) - \rho \frac{\partial}{\partial x}\left(\frac{\partial^2 \psi}{\partial t^2}\right) = (\lambda + 2\mu)\frac{\partial}{\partial z}\left(\nabla^2 \phi\right) - \frac{\partial}{\partial x}\left(\nabla^2 \psi\right) \tag{2.16.b}$$

Helmholtz equations can be achieved from these equations:

$$\frac{\partial^2 \phi}{\partial t^2} = \left(\frac{\lambda + 2\mu}{\rho}\right)\nabla^2 \phi = V_p^2 \nabla^2 \phi \tag{2.17.b}$$

$$\frac{\partial^2 \psi}{\partial t^2} = \left(\frac{\mu}{\rho}\right)\nabla^2 \psi = V_s^2 \nabla^2 \psi \tag{2.17.b}$$

where V_p and V_s are wave compressional and shear wave velocity respectively.

Harmonic solution in axis x by applying Eqs. 2.17, sinusoidal wave traveling in axis x with frequency $f = w/2\pi$ and velocity $c = w/k$:

$$\phi = F(z)e^{i(kx - wt)} \tag{2.18.b}$$

$$\psi = G(z)e^{i(kx - wt)} \tag{2.18.b}$$

where $i = \sqrt{-1}$, k is the wave number, F and G are the functions of amplitudes in axis z.

Applying V_p and V_s into Eqs. 2.18:

$$-\frac{w^2}{V_p^2}F(z) = -k^2 F(z) + \frac{d^2 F(z)}{dz^2} \tag{2.19.a}$$

$$-\frac{w^2}{V_s^2}G(z)=-k^2G(z)+\frac{d^2G(z)}{dz^2} \tag{2.19.b}$$

The general solution of Eqs. 2.19 will be:

$F(Z)=A_1e^{-\alpha z}+A_2e^{\alpha z}$ and $G(Z)=A_1e^{-\beta z}+A_2e^{\beta z}$

By using $\alpha^2=k^2-w^2/V_p^2$ and $\beta^2=k^2-w^2/V_s^2$ in the general solutions of Eqs. 2.19 we will have the potential equation of surface wave:

$$\phi = Ae^{-\alpha z}e^{i(kx-wt)} \tag{2.20.a}$$

$$\psi = Be^{-\beta z}e^{i(kx-wt)} \tag{2.20.b}$$

By applying boundary conditions $\sigma_{zz}=\sigma_{zx}=0$ and having $c = w/k = V_R$ which is basically the surface (Rayleigh) wave velocity, Rayleigh frequency equation can be achieved as below:

$$16\left[1-\left(\frac{V_R}{V_P}\right)^2\right]\left[1-\left(\frac{V_R}{V_S}\right)^2\right]=\left[2-\left(\frac{V_R}{V_S}\right)^2\right]^4 \tag{2.21}$$

Finally vertical and horizontal displacements can be derived as below:

$$u=Aki\left[-e^{-\alpha z}+\frac{2\alpha\beta}{\beta^2+k^2}e^{-\beta z}\right]e^{i(wt-kx)} \tag{2.22.a}$$

$$w=Ak\left[-\frac{\alpha}{k}e^{-\alpha z}+\frac{2\alpha\beta}{\beta^2+k^2}e^{-\beta z}\right]e^{i(wt-kx)} \tag{2.22.b}$$

The brackets present the attenuation of displacement within the depth of the medium.

To have a Lamb wave propagation equation in a plate with two traction-free surfaces, we have [69]:

$$\phi = A_s \cosh(\alpha z)e^{i\kappa x} + B_a \sinh(\alpha z)e^{i\kappa x} \tag{2.23}$$

$$\psi = C_s \cosh(\beta z)e^{i\kappa x} + D_a \sinh(\beta z)e^{i\kappa x} \tag{2.24}$$

The factor $e^{-i\omega t}$ is dropped for briefness. So, if we consider that the stresses σ_{xz} and σ_{zz} are equal to 0 at the plate boundaries $z = \pm d$, then we have:

These equations are satisfied only when the following are also satisfied:

$$\begin{cases} \left(\kappa^2 + \beta^2\right)\cosh \alpha d A_s + 2i\kappa\beta \cosh \beta d D_s = 0 \\ 2i\kappa\alpha \sinh \alpha d A_s - \left(\kappa^2 + \beta^2\right)\sinh \beta d D_s = 0 \end{cases} \tag{2.25}$$

$$\begin{cases} \left(\kappa^2 + \beta^2\right)\sinh \alpha d B_a + 2i\kappa\beta \sinh \beta d C_a = 0 \\ 2i\kappa\alpha \sinh \alpha d B_a - \left(\kappa^2 + \beta^2\right)\sinh \beta d C_a = 0 \end{cases} \tag{2.26}$$

The Rayleigh-Lamb frequency equation will be the determinants of Eq. 2.25 and Eq. 2.26 which correspond to the Eigen values of κ (wave number). The Rayleigh-Lamb wave frequency equation for symmetrical and anti-symmetrical waves can then be written as:

$$\frac{\tanh\left(\beta d\right)}{\tanh\left(\alpha d\right)} + \frac{4\alpha\beta\kappa^2}{\left(\kappa^2 - \beta^2\right)^2} = 0 \qquad \text{(Symmetrical)} \tag{2.27}$$

$$\frac{\tanh\left(\beta d\right)}{\tanh\left(\alpha d\right)} + \frac{\left(\kappa^2 - \beta^2\right)^2}{4\alpha\beta\kappa^2} = 0 \qquad \text{(Anti-symmetrical)} \tag{2.28}$$

Considering only real roots of these equations and noting that $\tanh\left(\alpha d\right) = i\tan\left(i\alpha d\right)$ and for $\kappa^2 < \omega^2/V_p^2$, and $\kappa^2 < \omega^2/V_s^2$, Eq. 2.27 and Eq. 2.28 can be written as:

$$\frac{\tan\left(\beta d\right)}{\tan\left(\alpha d\right)} + \left[\frac{4\alpha\beta\kappa^2}{\left(\kappa^2 - \beta^2\right)^2}\right]^{\pm 1} = 0, \qquad \begin{cases} +1 = \text{symmetrical} \\ -1 = \text{anti-symmetrical} \end{cases} \tag{2.29}$$

A limited number of symmetrical and anti-symmetrical L-waves can occur at different frequencies at which their phase and group velocities will be different. As frequency tends to zero, the order of the L-wave is fundamental or 0th mode, and by increasing frequency, higher L-wave modes appears. The total number of symmetrical and anti-symmetrical L-waves with critical frequencies at which higher Lamb modes appear can be expressed by following equations [69]:

$$N_s = 1 + round\left[\frac{2d}{\lambda_s}\right] + round\left[\frac{2d}{\lambda_p} + \frac{1}{2}\right] \qquad \text{(round = integer value)} \tag{2.30}$$

$$N_a = 1 + round\left[\frac{2d}{\lambda_p}\right] + round\left[\frac{2d}{\lambda_s} + \frac{1}{2}\right] \tag{2.31}$$

By solving Eq. 2.29 numerically, the dispersion curves can be obtained. Dispersion curves show the changes in phase or group velocities base on changes in frequency for different Lamb wave modes. Dispersive curves can be plotted by using different variables like frequency or velocity.

Figures 2.16(a) and 2.16(b) present normalized phase (a) and group velocity (b) of L-wave modes in an aluminum plate. Velocities were normalized to the shear velocity and frequency is normalized to $\kappa_s d$, and numbers refer to L-wave modes (e.g. s0 and a0 for fundamental mode, s1 and a1for 1st mode, and so on) [69].

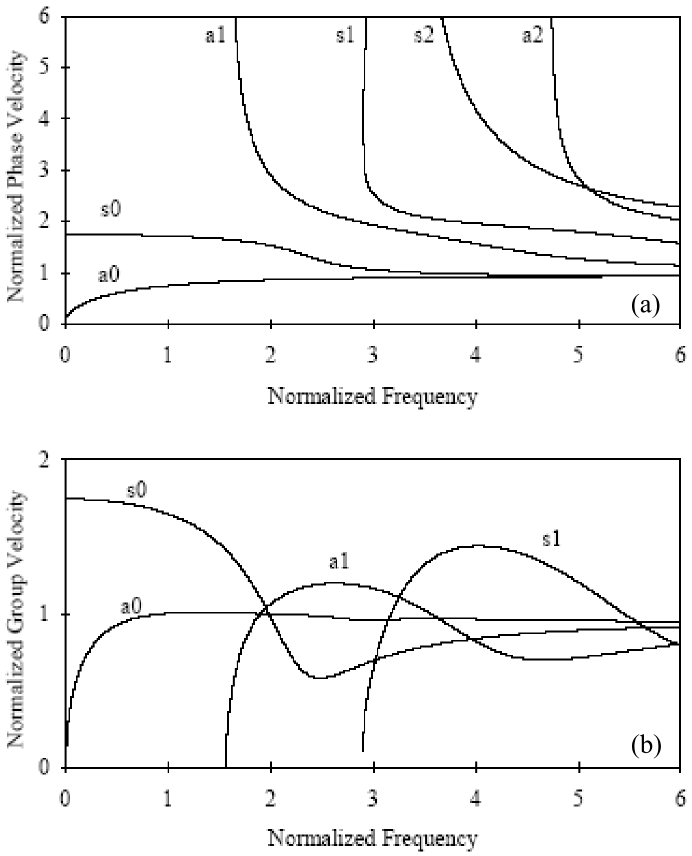

Figure 2.16. Normalized dispersion curves of L-wave modes in an aluminum plate. (a). phase velocity. (b). group velocity [69].

At high frequencies the symmetrical and anti-symmetrical Lamb waves come together and transfer to R-waves at the surfaces because the plate thickness becomes large with respect to the penetration depth of the R-wave. At this condition, the waves do not interact with the other surface and then L-waves will not be generated. By looking at Eq. 2.29, when the frequency is high enough we can assume $\tan(\beta d) \approx \tan(\alpha d) \approx 1$, which at the limit becomes a Rayleigh wave equation. On the other hand, when the frequency is low, the following approximation can be considered to be sufficient [69]:

$$\begin{cases} \tan(\alpha d) \approx \alpha h\left(1+\frac{1}{3}\alpha^2 d^2\right) \\ \tan(\beta d) \approx \beta h\left(1+\frac{1}{3}\beta^2 d^2\right) \end{cases} \tag{2.32}$$

To find the velocity for fundamental L-wave modes at low frequencies, Eq. 2.32 and Eq. 2.29 can be combined, leading to [69]:

$$\begin{cases} V_{ext} = \sqrt{\dfrac{E}{\left(1-\upsilon^2\right)}} \\ V_{flx} = \kappa d\sqrt{\dfrac{E}{3\rho\left(1-\upsilon^2\right)}} \end{cases} \tag{2.33}$$

Here, E is Young's modulus; V_{ext} is the symmetrical L-wave velocity when it is in fundamental mode. The L-wave phase velocity varies from this value to V_{flx} which is the global flexural mode of the plate and varies with the frequency (wave number) [69].

In order to find the particle displacement, the potential function can be written as follows:

$$\phi = A_s \cosh\left(\alpha_s z\right)e^{i\kappa_s x} + B_a \sinh\left(\alpha_a z\right)e^{i\kappa_a x} \tag{2.34}$$

$$\psi = \frac{2i\kappa_s\alpha_s \sinh\left(\alpha_s d\right)}{\left(\kappa_s^2+\beta_s^2\right)\sinh\left(\beta_s d\right)} A_s \sinh\left(\beta_s z\right)e^{i\kappa_s x} + \frac{2i\kappa_a\alpha_a \sinh\left(\alpha_a d\right)}{\left(\kappa_a^2+\beta_a^2\right)\sinh\left(\beta_a d\right)} B_a \sinh\left(\beta_a z\right)e^{i\kappa_a x} \tag{2.35}$$

Where $\alpha_{s,a} = \sqrt{\kappa_{s,a}^2 - \omega^2/V_p^2}$, and $\beta_{s,a} = \sqrt{\kappa_{s,a}^2 - \omega^2/V_s^2}$. By considering the potential functions as the sum of symmetrical and anti-symmetrical motions, the particle displacements can be written as [69]:

$$\begin{cases} u_s = A\kappa_s\left[\dfrac{\cosh\left(\alpha_s z\right)}{\sinh\left(\alpha_s d\right)} - \dfrac{2\alpha_s\beta_s}{\kappa_s^2+\beta_s^2}\cdot\dfrac{\cosh\left(\beta_s z\right)}{\sinh\left(\beta_s d\right)}\right]e^{i\left(\kappa_s x-\omega t-\frac{\pi}{2}\right)} \\ w_s = -A\alpha_s\left[\dfrac{\sinh\left(\alpha_s z\right)}{\sinh\left(\alpha_s d\right)} - \dfrac{2\kappa_s^2}{\kappa_s^2+\beta_s^2}\cdot\dfrac{\sinh\left(\beta_s z\right)}{\sinh\left(\beta_s d\right)}\right]e^{i\left(\kappa_s x-\omega t\right)} \\ u_a = B\kappa_a\left[\dfrac{\cosh\left(\alpha_a z\right)}{\sinh\left(\alpha_a d\right)} - \dfrac{2\alpha_a\beta_a}{\kappa_a^2+\beta_a^2}\cdot\dfrac{\cosh\left(\beta_a z\right)}{\sinh\left(\beta_a d\right)}\right]e^{i\left(\kappa_a x-\omega t-\frac{\pi}{2}\right)} \\ w_a = -B\alpha_a\left[\dfrac{\sinh\left(\alpha_a z\right)}{\sinh\left(\alpha_a d\right)} - \dfrac{2\kappa_a^2}{\kappa_a^2+\beta_a^2}\cdot\dfrac{\sinh\left(\beta_a z\right)}{\sinh\left(\beta_a d\right)}\right]e^{i\left(\kappa_a x-\omega t\right)} \end{cases} \tag{2.36}$$

Where A and B are arbitrary constants. There is a phase difference of $\pi/2$ in Eq. 2.36 in both symmetrical and anti-symmetrical L-wave modes between the horizontal and vertical displacements. Figure 2.17 presents particle displacements in L-wave modes of a plate with $\nu = 0.34, d/\lambda_R = 1, (\kappa_t d \approx 6)$ [69]. By increasing the thickness of plate, the properties of the wave's s_0 and a_0 change; they become more and more like one another until the condition of the R-wave is recovered [69].

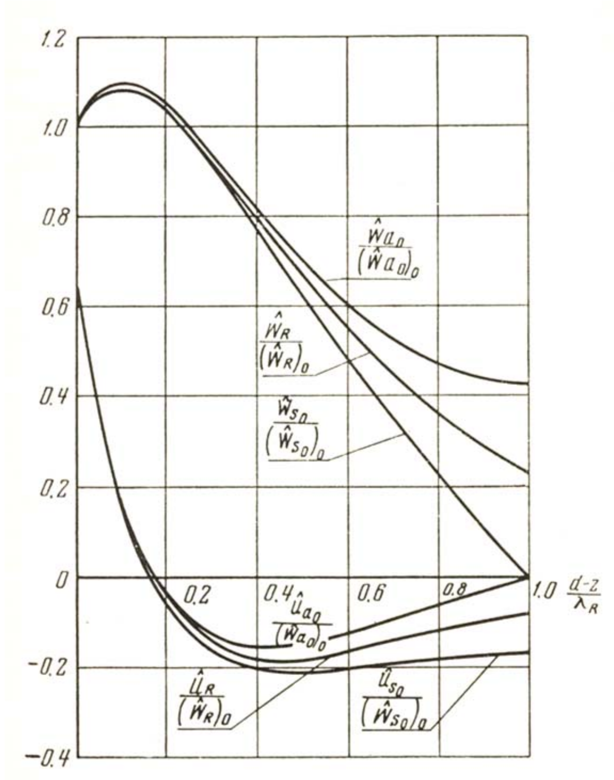

Figure2.17. Particle displacements for L-waves [69].

2.3.3. Wave propagation in circular cross-section bodies

Three modes of wave propagation in a circular cross section bodies are: longitudinal waves, torsional waves, and flexural waves. By assuming rotational symmetry of the rod with regard to the x axis, longitudinal elastic waves in structural rod specimen can be simplified. Because of the symmetry in all components (displacement, and stress) they will be independent from the angle.

Therefore in the case of longitudinal waves, the u_θ displacement components and $\gamma_{x\theta}$ and $\gamma_{r\theta}$ as deformation components must be equal to zero. It means that using Helmholtz decomposition the potential vector H has only one nonzero component H_θ [75, 76]. So, the displacement vector in rod can be presented as:

$$u_x = \frac{\partial \phi}{\partial x} + \frac{1}{r}\frac{(rH_\theta)}{\partial r}, \qquad u_r = \frac{\partial \phi}{\partial r} - \frac{\partial H_\theta}{\partial x} \tag{2.37}$$

Where, u_x and u_r are displacements in x and r directions, ϕ is the scalar potential, and vector potential $H = (H_x, H_r, H_\theta)$. Figure 2.18 shows a schematic of rod with Cartesian system (x, y, z) and cylindrical systems of coordinates (x, r, θ) and displacement vectors for a simple rod.

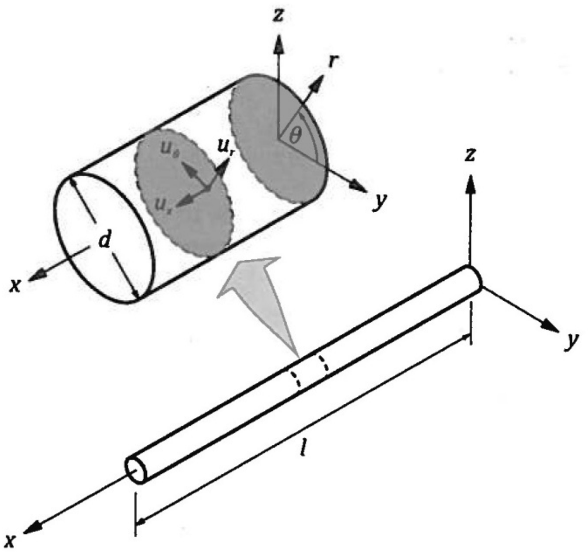

Figure 2.18. Structural rod elements [77].

By using harmonic wave propagation along the x axis in the rod, solution of wave equation can be achieved in a general complex form:

$$\phi = \hat{\phi}(r) e^{i(kx - wt)}, \qquad \psi = \hat{\psi}(r) e^{i(kx - wt)} \tag{2.38}$$

Where $\hat{\phi}$ and $\hat{\psi}$ are unknown functions. Bessel differential equations for functions $\hat{\phi}(r)$ and $\hat{\psi}(r)$ can be found through the substitution of Eq. 2.38 into the motion Equations.

$$\frac{d^2\hat{\phi}}{dr^2}+\frac{1}{r}\frac{d\hat{\phi}}{dr}+\alpha^2\hat{\phi}=0, \qquad \frac{d^2\hat{\psi}}{dr^2}+\frac{1}{r}\frac{d\hat{\psi}}{dr}+\beta^2\hat{\psi}=0 \tag{2.39}$$

Where:

$$\alpha^2=\frac{\omega^2}{{C_L}^2}-k^2, \beta^2=\frac{\omega^2}{{C_S}^2}-k^2$$

The solutions in the form of Bessel functions ($\hat{\phi}=AJ_0(\alpha r), \hat{\psi}=BJ_0(\beta r)$) in the general form of solutions (Eq. 2.38) will give the following equations:

$$\phi=AJ_0(\alpha r)e^{i(kx-wt)}, \qquad \psi=BJ_0(\beta r)e^{i(kx-wt)} \tag{2.40}$$

Where A and B are some constants. J_0 is the first order of Bessel function.

Longitudinal wave propagation in a rod requires defining the external boundary conditions of rod surface, which will accompany in the equation of motion:

$$\sigma_{rr}(x,r)=\tau_{xr}(x,r)=0, \quad dla \quad 0\le x\le l, \quad r=a=\frac{d}{2}$$

Where d is the rod diameter and l is length.

The Pochhammer frequency equation for longitudinal modes of wave propagation in rods can be derived by substituting Eq. 2.40 into the stress strain condition of Hooke's law. The Pochhammer equation has a nontrivial solution only if its determinant vanishes. This equation is related to the wavenumber *k* and the angular frequency ω [77].

$$\frac{2\alpha}{a}(\beta^2+k^2)J_1(\alpha a)J_1(\beta a)-(\beta^2-k^2)J_0(\alpha a)J_1(\beta a)-4k^2\alpha\beta J_1(\alpha a)J_0(Ba)=0 \tag{2.41}$$

Torsional and Flexural waves are consequence of vanishing displacements in different directions of wave propagation and on the circumferential angle θ and in the displacement vector respectively.

Chapter 3

Scanning device prototype

3.1. Introduction

Some devices work based on the magnetic memory of ferromagnetic materials: Contact method devices, and Non-contact method devices. Maximum penetration depth for contact method is 2 millimeter and welding test is their main application. Non-contact method with application of underground pipeline inspection has penetration depth of 1 meter to 7 meter. Clearly, the purpose of inspection for these two groups of devices is different. Contact devices are for exposed objects such as above-ground pipelines and other exposed metal structures. The maximum distance between the sensors and the object in this group of devices should not exceed one centimeter, a limitation imposed because of the sensitivity of sensors as well as the artificial magnetic fields around the object.

Non-contact devices are mostly useful for covered objects in regions where there are no other concentrations of ferromagnetic materials that could be generating artificial magnetic fields or distorting the earth's natural field. For example, in built-up areas with several buried infrastructure objects made of ferromagnesian materials, the deconvolution of the measured passive field is challenging, perhaps impossible, without a great deal of additional data. Ideally, only the object of interest is responsible for the deviations in the earth's local magnetic field. Again, in this situation there is a limitation of distance between the device and specimen; based on field measurements experience, this distance is if the range of ten to fifteen times the width (diameter) of the object. For example, a 15 mm steel reinforcing bar can be covered from 5 to 10 cm under the surface of the concrete and still provide a detectable magnetic field and analyzable signal.

A suitable device for reinforcement concrete inspection is designed for the typical embedment distance from the free surface. The minimum concrete cover to protect reinforcement is usually three inches (7.62 cm) for exposed casts [78]. This places reinforcing steel bars well within the limits delineated above, but because of the very weak magnetic field around the reinforcement and complex structure of reinforcements, passive magnetic methods have not yet been used for this purpose, and it appears that this study is the first in this area.

3.2. Procedure of making inspection device

The designed device has five main sections:

1. Main electronic board
2. Sensors
3. Positioning system
4. Data storage system
5. Power supply

Based on the required resolution for reinforced concrete inspection, magnetic sensors were selected. The intention was to collect magnetic field data in three axes (X, Y, and Z), therefore three identical sensors were selected. Each of these three sensors had different sensitivity to the magnetic field, and also their covering ranges of magnetic field were different. Prototype version.1 was designed based on the examination of three different sensors and finding the best one for desired application. The best sensor type which was suitable for desired application was selected to design a main board and sync other part of prototype to them. A rotary encoder was selected to use for record the location of each data point through the scanning process. A memory card board was selected to save all magnetic field data and location data into the memory card. 9 volt battery was used to supply electrical power for system. Details of boards and sensors are explained below.

3.2.1. Main body of prototype

The main board was designed for following roles:

1- Receive magnetic field data from magnetic sensors
2- Receive location data from rotary encoder sensor
3- Decode received voltage data to the text file
4- Send decoded data to the memory card for saving

Figure 4.1 shows a simple scheme of developed prototype version.2 which contains main board, sensors, wheels, storage board and power supply section. One wheel is attached to the rotary encoder in order to measure the length of scanning. Rotary encoder is synced to two magnetic sensors which provide specific location for each data point. Main board (Arduino due) gathers all data in voltage and changes it to text file line by line. Then main board transfers text lines to the memory card board and saves data in a memory card. Main board saves 10 sets of data per second from two magnetic sensors and one rotary encoder. It has an ability to save up to 25 data per second as well. Prototype version.1 contained one magnetic sensor with no positioning system. In version.1 data was transferred directly to PC with RS-232 cable.

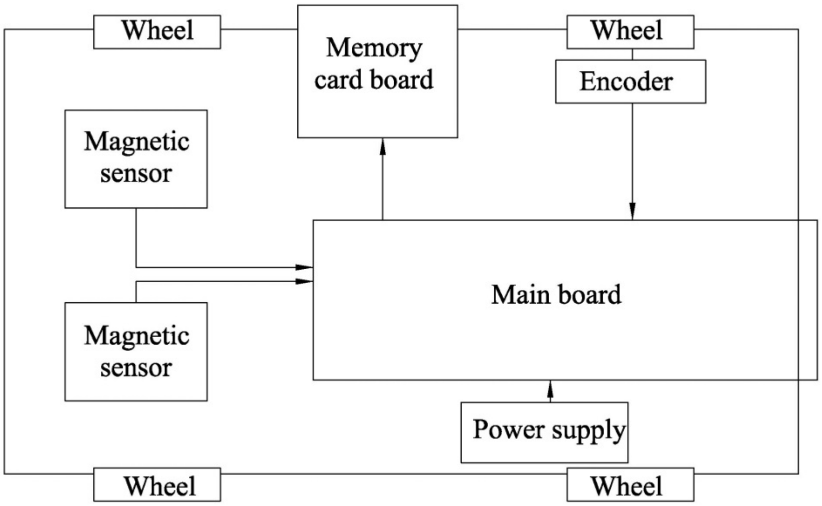

Figure 3.1. Simple scheme of developed prototype version 2.

3.2.2. Magnetic sensors

Magneto-inductive (MI) sensors were selected to use in the prototype version 2. These sensors contain very small coils 0.24 in (approximately 6 mm) in diameter. Because it is necessary to record magnetic data around the object in three directions, sensors are placed on three orthogonal axes: X, Y, and Z. Resolution and sensitivity of sensors can be changed, based on the typical thickness of concrete. Figure 4.2 shows a simple scheme of sensors and the sensors' board. MS1, MS2, and MS3 are small coils placed in directions X, Y, and Z, respectively. These sensors were connected directly to the main board (Figure 3.1).

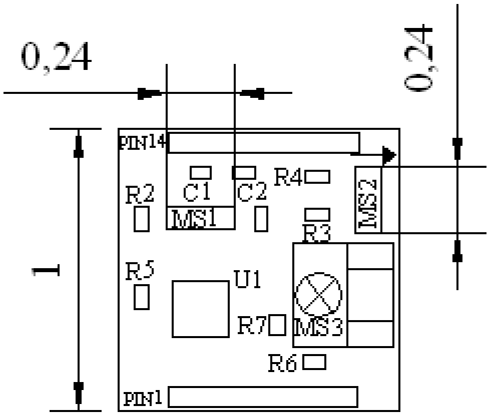

Figure 3.2. Simple scheme of the sensors' board; MS1, 2 and 3 are small coils placed in X, Y and Z directions, respectively.

3.2.4. Rotary encoder

Positioning system of prototype version.2 is modular incremental encoder type AMT10 [80]. The accuracy of this type of encoder is 0.25. Resolution of this encoder is from 48 PPR to 2048 PPR. It means that it can read 48 points to 2048 points per rotation. Working voltage is from 4.6 V to 6 V. This encoder is attached to one wheel. Selected resolution for developed prototype is 1024 PPR which means its minimum resolution is 0.13 mm based on wheels diameter. While attached wheel rotate, the encoder send a pulse to the main board.

3.2.4. Data recording procedure

The prototype contains a memory card board which is connected to main board. Main board will transfer voltage data from sensors to the text file and send it to memory card board. The text file will be saved as a text file in a memory card. The capacity of memory card is enough to save data for more than 10 hours of scanning. So, it will be enough for at least one day test.

3.3. Version.2 of PMI Prototype

Figure 4.3 shows the final design of prototype version.2 of Passive Magnetic Inspection (PMI) device. The body of device is prepared by 3D printing device. This device is able to scan reinforced concrete structures in the field. The procedure of scanning is very simple. There is a key on the top of the device which makes it on. Then the device should be moved on the concrete surface along the reinforcement direction. When scanning finished, the switch should be off. After bringing out the memory card from the memory board at bottom-right side of the device, data can be transfer from the memory card to the pc.

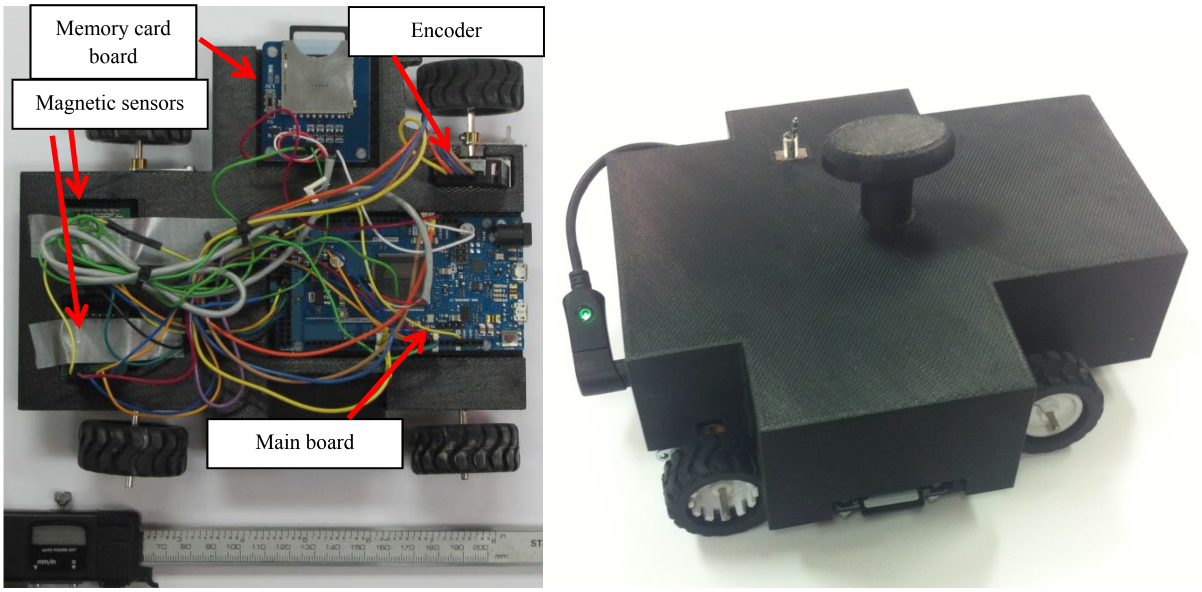

Figure 3.3. Prototype V.2. (a). Inside view. (b). Outside view.

3.4. Conclusion

The second version of prototype was designed and made with four main improvements from the first version. These changes are:

1- New main board with higher processing capability.
2- Two parallel magnetic sensors.
3- Positioning sensor.
4- Memory card board.

This version of device is ready for field test. However, it needs following improvements which will be implemented for next version. Some of improvements can be following items:

- More robust wheels system.
- Wireless transfer system.
- A system for showing scanned data and analysis on time.

Chapter 4

Detecting defects in steel reinforcement using the passive magnetic inspection method

4.1. Introduction

Reinforced concrete (RC) is used in the construction of most civil infrastructure (e.g. buildings, bridges, platforms, roadbeds, concrete pipelines and tunnel lining) [1]. The durability and longevity of RC depend on external environmental conditions such as exposure to corrosive fluids, solutions of road salt, stray electrical currents, and service temperature.

Some deterioration in reinforcement is the result of electrochemical and chemical processes, predominantly the effects of chloride and carbonation reactions. The penetration of chloride ions into concrete and the development of a carbonation depth greater than the concrete cover are key processes in the deterioration of RC structures [81]. Although there is a specified service life of RC structures based on standards [82], deterioration may cause steel reactions, cracking, and premature loss of structural integrity [3]. Steel deterioration is almost certainly the primary reason for reduction of lifespan and service level for RC structures [4].

Position, location, distribution, and deterioration percentage of reinforcement steel are necessary variables to assess RC structure deterioration over time. This information can then be used to define obligatory repair work or replacement schedules. Also, rapid non-destructive testing (NDT) for identification of deterioration sites in bars is desirable, as it is expensive and time consuming to use destructive methods on structural elements to quantify deterioration state. Common NDT methods such as acoustic probing, electrical and electrochemical methods have limitations related to variation in moisture and salinity conditions over time as well as the non-homogeneous properties of concrete. Sometimes these limitations make assessment of the reinforcement condition impossible [83, 84].

Steel reinforcement in RC structures is a ferromagnetic material. Recently, magnetic flux leakage (MFL) methods have been used to detect deterioration of reinforcement. In this method, an induction of a magnetic field is necessary to magnetize the reinforcement [85-89]. Applying such a magnetic field categorizes the MFL method in the "active, non-destructive" testing group. Superconducting quantum interference device (SQUID) is used to detect magnetic flux density changes because of corrosion around the reinforced concrete from electrochemical reactions. Electrochemical corrosion reactions produce an electrical current inside the bar. This current generates a magnetic flux density, which is the basis of using SQUID sensor methods [90, 91]. Using giant magneto-resistive (GMR) sensors is another approach to detect bar deterioration in reinforced concrete [92]. Although both methods are successful in detecting deterioration of reinforcement bars, the existence of electrical currents as the result of corrosion process is an issue, and applying currents through the specimen is necessary for detection of deterioration [90-92].

The earth's magnetic field magnetizes the steel reinforcing bar during its manufacturing process. This natural magnetic condition modifies the natural magnetic field around the steel member through a process called self-magnetic flux leakage (SMFL), which is the basis of the PMI method [93-95]. The strain and stress applied during reinforcement formation under the influence of the earth's magnetic field, give a specific and unique initial magnetic signature to steel reinforcement. The alignment of electron dipoles in magnetic domains and the irreversible oriented magnetization of these domains form the micro-structural explanation for the self-magnetic properties of all ferromagnetic materials [97]. The final permanent magnetic field of each reinforcement is different based on their magnetic properties and also their stress-strain history [97].

The PMI method has been used to detect possible locations of defects in industrial structures [94, 95, and 98] where the surface of the steel is exposed. Few studies have been done to evaluate the type of defects, their size, or the extent of deterioration in RC structures [98], or other steel structures, where the steel is embedded beneath a layer of concrete or soil.

This study first presents numerical simulations of magnetic flux density signals followed by experimental tests results for the use of PMI on RC specimens to find defect locations as a new application of the passive magnetic inspection method. For the experimental tests of this study, magneto-inductive (MI) sensors were used [79]. The main difference of the current study from previous ones [90-92] is the measurement of magnetic flux density of reinforcement bars without any electrochemical reaction or electrical current in the specimen. The numerical and experimental case presented is a proof-of-concept study to demonstrate that the PMI approach has the potential for practical application as a NDT to assess the condition of steel reinforcement covered by concrete.

The use of a PMI method for assessing the corrosion state of reinforcing bars in concrete is now presented and explained. Defect-related anomalies are hidden in the background magnetic field [99]. It was necessary to develop a signal processing methodology to subtract background magnetic field trends from raw data and extract signal anomalies related to defects in the experimental materials. Numerical simulation based on the magnetic stray field energy equations and cross-correlation of numerical simulation data to experimental test data enhances the interpretation of the test results, so they can be compared to the numerical simulation results; Figure 4.1 shows the methodology employed.

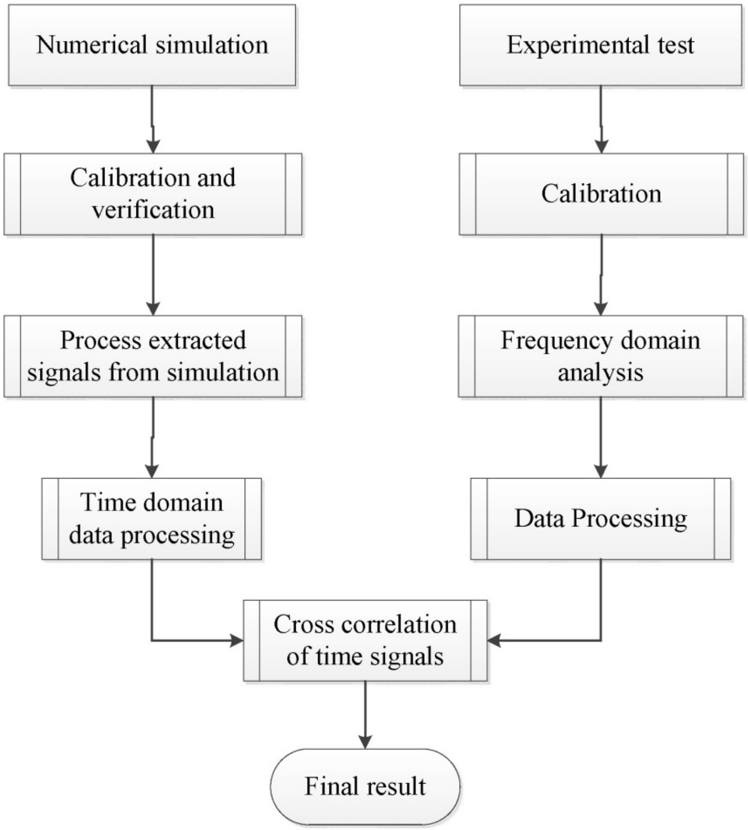

Figure 4.1. Methodology flow chart.

4.2. Theoretical background

Induced magnetization is related to the fabric of crystals in ferromagnetic materials and the earth's magnetic field direction when the crystals were magnetized during cooling and because of deformation. This magnetization process defines the anisotropic self-magnetization field energy for a ferromagnetic material in service [96]. The dependence of the self-magnetized energy on the direction of magnetization, which arises from aligned electron dipoles in the iron crystallite, leads to the distortion (perturbation) of the ambient magnetic field around a ferromagnetic material such as cold-deformed reinforcing steel. Both crystal anisotropy (microstructure) and induced magnetization anisotropy affect the ambient magnetic field. The basic crystal structure is the source of intrinsic crystal anisotropy, whereas oriented lattice defects or partial atomic ordering are examples of deviation of electron dipoles from the ideal state, leading to a general orientation of the electron dipoles, and leads to what is referred to as induced anisotropy [97].

There are two types of magnetic fields: stray and external [100-102]. Magnetic flux density of ferromagnetic material is related to these magnetic fields (Eq.4.1).

$$divB = div\left(\mu_0 H + J\right) = 0 \tag{4.1}$$

Where, B is the magnetic flux density, μ_0 is the vacuum magnetic permeability, H is the external magnetic field, and J is magnetic polarization.

The stray magnetic field and the stray magnetic field energy are required for the numerical simulation of the PMI method. The stray magnetic field is a consequence of the magnetic body itself, whereas the external magnetic field is the result of the earth's field, modified by local strongly magnetic bodies. Maxwell's equation is needed for the computation of the gradient of the stray field Hd and they are summarized from the derivations presented by Hubert and Schäfer [97].

$$divH_d = -div\left(J/\mu_0\right) \tag{4.2}$$

Here, H_d is the stray magnetic field, which can also be expressed as a magnetic charge that is always balanced by opposing energy and can be written as:

$$E_\mathrm{d} = \frac{1}{2}\mu_0 \int\limits_{\text{all space}} H_\mathrm{d}^2 \mathrm{d}V = -\frac{1}{2} \int\limits_{\text{sample}} H_\mathrm{d} \cdot J \mathrm{d}V \tag{4.3}$$

Here, E_d is the stray magnetic field energy, and V is the volume of the ferromagnetic material. Potential theory gives a general solution for the stray field problem. Magnetization (M) has a relation to volume charge density (λ_V) and the surface charge density ($\sigma_\mathrm{S} = M.n$). This special relationship happens when the second medium is non-magnetic. Figure 4.2 presents typical conditions of surface charge such that:

$$M\left(r\right) = J\left(r\right)/J_s \tag{4.4}$$

$$\lambda_\mathrm{V} = -\mathrm{div}M \tag{4.5}$$

where r is the position vector, n is the normal outward vector to the separation plane, and J_s is magnetization saturation. An interface charge develops when there are two materials with two different M values (M1, M2) and it is of magnitude: $\sigma_S = (M_1 - M_2) \cdot n$.

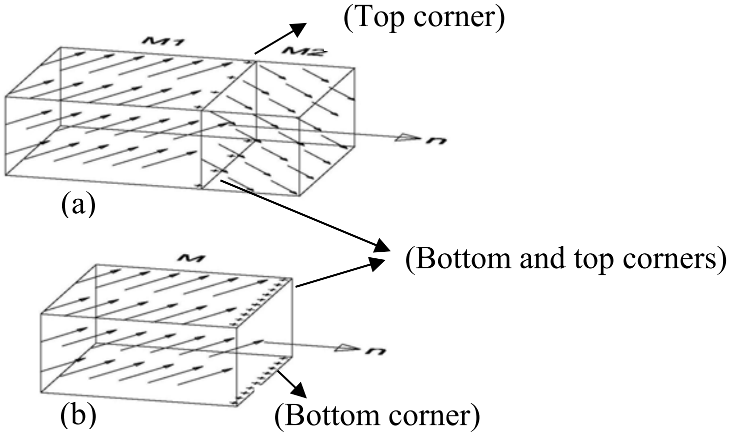

Figure 4.2. Schematic view of two different cases of surface magnetic charge (plus signs at edge of material shows the surface charge). (a). Two materials with different *M* values (*M1*, and *M2*). (b). One material with *M* value. (After Hubert & Schäfer, 1998).

To calculate the potential of the stray field energy (Φd (r)) using Eqs. 4.3, 4.4 and 4.5 at a position r, integration over the volume is required [103]:

$$\Phi_d(r) = \frac{J_s}{4\pi\mu_0}\left[\int \frac{\lambda_V(r')}{|r-r'|}\mathrm{d}V' + \int \frac{\sigma_S(r')}{|r-r'|}\mathrm{d}S'\right] \tag{4.6}$$

Where, r′ is derivative of position vector r.

By using Eq.4.6, the stray field can be computed by applying the following equation:

$$H_d(r) = -grad\Phi_d(r) \tag{4.7}$$

The stray field energy can also be derived from the following equation:

$$E_d = J_s\left[\int \lambda_V(r)\Phi_d(r)\mathrm{d}V + \int \sigma_S(r)\Phi_d(r)\mathrm{d}S\right] \tag{4.8}$$

Here, the stray field energy is integrated over the volume and the surface charge density is integrated over the surface.

Any increase in stray field energy at the top and bottom corners of the specimen shown in Figure 4.2 is important for defect detection. The configuration of smaller domains, which presumably charged the domain walls magnetically by denser aligned dipoles, is the reason for an increase in stray field energy [104]. To numerically simulate the effects of bar defects on the magnetic flux density, the gradient of the stray field energy is the most suitable way to detect the presence of domain changes, a method which is used in this study.

4.3. Numerical model

A steel rod (diameter: 1.6 cm) with three small holes (defects) in different positions and orientations is modelled (Figure 4.3). To better understand the magnetic flux density arising from a small hole in a steel bar, a numerical simulation is conducted using COMSOL Multiphysics V.4.4, which is based on finite element method (FEM) [105]. The relative magnetic permeability (ratio of magnetic permeability of specimen to the magnetic permeability of free space) of the type of low carbon steel used (ASTM 1020) is from 50 to 100 [106, 107], so the relative magnetic permeability in this study is chosen to be 75. Table 4.1 presents information about the three cylindrical holes' geometry in the steel reinforcement.

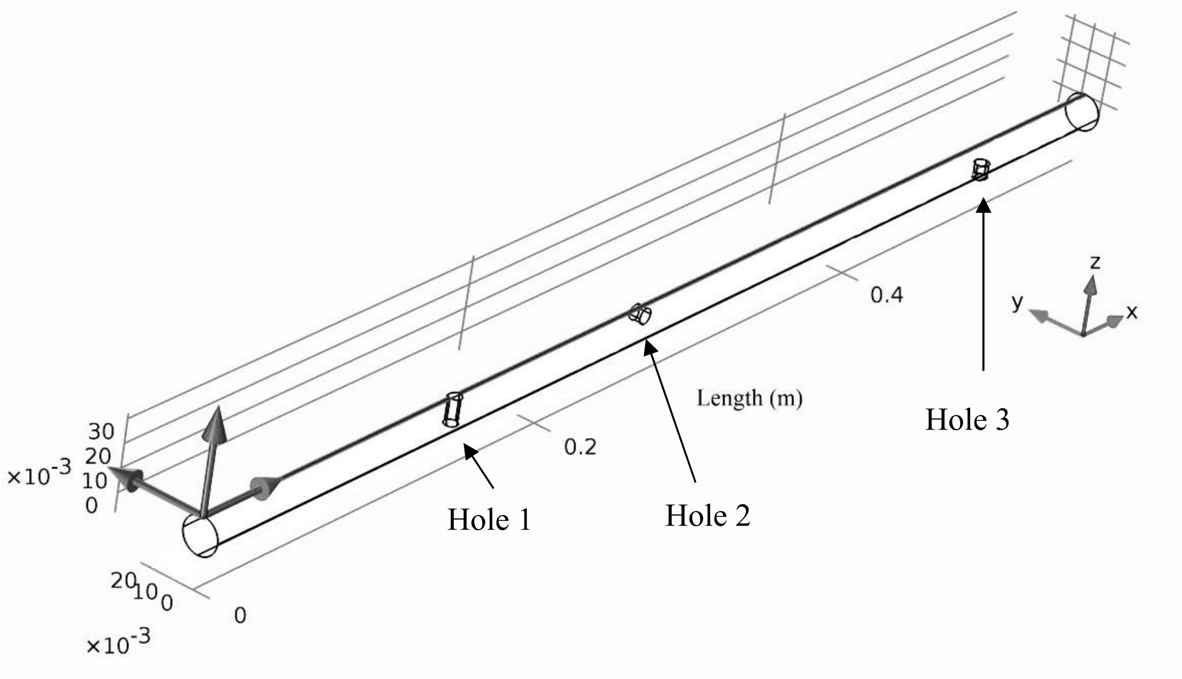

Figure 4.3. Three small holes in sound steel reinforcement (bar).

Table 4.1. Geometry of the three holes in a sound steel reinforcement bar.

Holes	Diameter (cm)	Depth (cm)	ϕ_{Hole}/ϕ_{bar}	X-Location on bar (m)	Position
H1	0.58	1.24	0.3625	0.14	Top
H2	0.68	0.57	0.4250	0.27	Left side
H3	0.66	0.67	0.4125	0.49	Bottom

Equation 4.1 was used to model the entire magnetic flux density in the x direction (Bx) around the reinforcement, and equation 4.8 was used to obtain stray field energy from the sharp edge effect of the hole. A free tetrahedral mesh discretization method was used for both bar and holes [105]. Maximum and minimum element sizes for the model of the bar were 0.00058 mm and 0.000113 mm, respectively (Table 4.2). Also, the maximum element size for the holes was 0.00029 mm and the minimum element size was 0.000029 mm. Element size gradually changes from maximum far from holes to minimum close to holes. Inside the holes, the minimum element size starts at the hole's edge and reached its maximum at the center of the hole. That is, the minimum element size is at the hole's edge, and the maximum element size is between two holes.

Figure 4.4 presents the 3D model of the magnetic flux density changes around the three holes because of the stray field effect. Figure 4.4(a) is a top view of the 3D model that shows the first hole at the top of the reinforcement bar. In Figures 4.5(b) and 4.5(c), the side and bottom holes are visible.

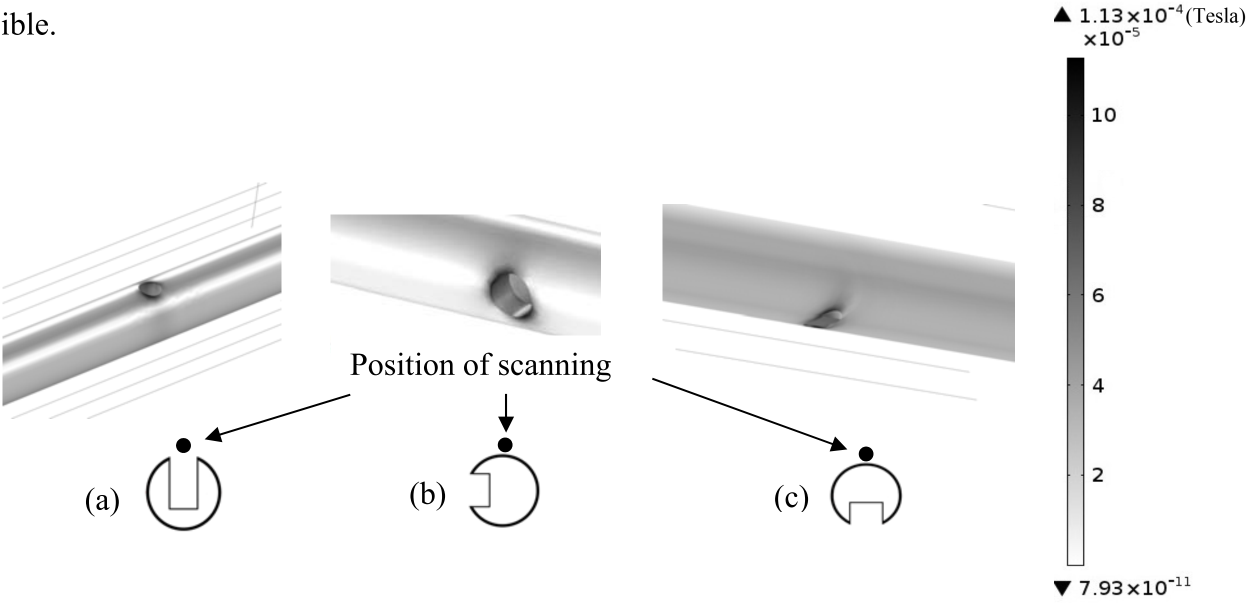

Figure 4.4. 3D magnetic flux density model around three holes in a steel bar because of the stray field energy. (a). Hole at top of the bar (H1). (b). Hole at left side of the bar (H2). (c). Hole at bottom of the bar (H3).

A two-step process was used for model calibration and verification; the first part of the data was reproduced by adjusting the independent parameters (calibration), then the model was run and results compared with the second part of the data from the experimental test results (verification) [104]. Also, parametric analysis was done to evaluate different parameters' effects on magnetic flux density.

4.4. Parametric analysis

To calibrate and verify the numerical simulations, the following independent parameters were selected: hole diameter, hole depth, and position of scanning line around the bar. For these simulations, the bar diameter was 1.6 cm, the same as in the experiments, and a constant 5 cm distance from the simulated sensor site to the top of the bar was maintained in order to represent the presence of a 5 cm thick non-magnetic concrete cover. Only the maximum magnitude of the x-component of magnetic flux density at the sensor site was used for the parametric studies and comparisons to the x-component of the magnetic flux density from experimental tests. To study hole diameter and depth effects on the magnetic flux density numerically, these parameters were changed in increments of 10% of their original size. For example, to study the effect of diameter, the simulations started from 10% percent of 0.58 cm, 10% of 0.68 cm and 10% of 0.66 cm for Holes 1, 2 and 3 respectively.

Figure 4.5 shows Hole-1 model with diameter equal to 1/10 of the original diameter, along with the mesh discretization used in the numerical simulation.

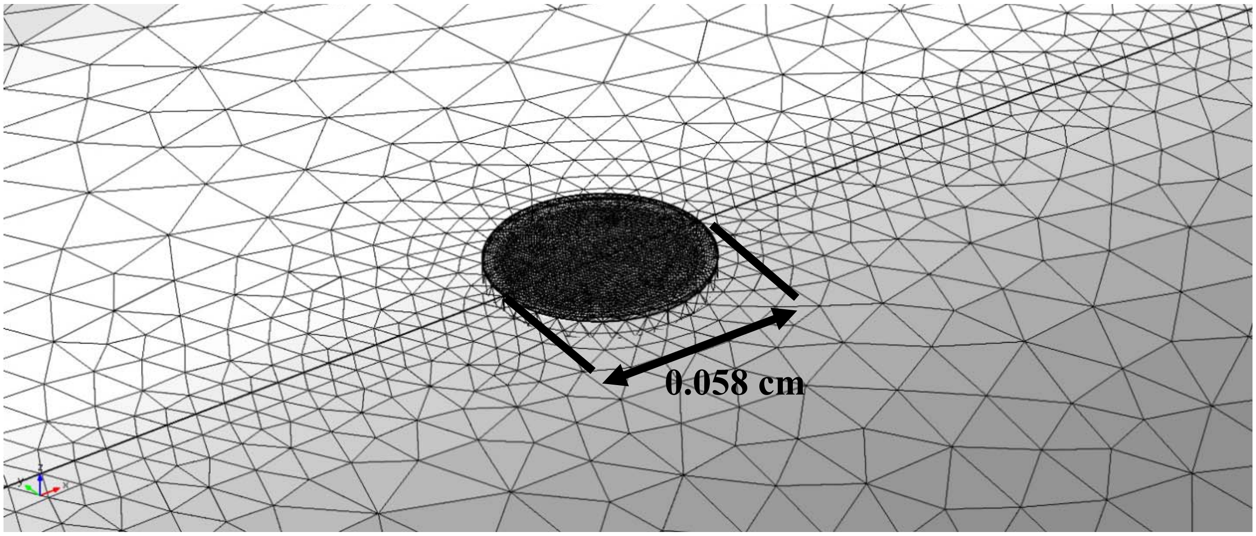

Figure 4.5. Element size changes around Hole-1 with ratio of 0.1 of its original diameter.

Table 4.2 presents mesh convergence analysis results. This was done to select proper mesh element size for numerical simulation, based on the minimum diameter of the hole in the parametric analyses (0.1 of the diameter of Hole-1). The minimum mesh element size of bar is at the edge of holes (Figure 4.5). The maximum magnetic flux density presented in Table 4.2 is from a numerical simulation above hole-1 with a ratio of 0.1 of its original diameter.

Table 4.2. Mesh element size analysis result.

No.	Max. mesh element size (mm)	Min. mesh element size (mm)	Number of degrees of freedom	Max. magnetic flux density (T)	Solution time (min)
1	0.00168	0.001213	1528395	1.30E-04	5.30E+01
2	0.00158	0.001113	1626482	1.30E-04	5.40E+01
3	0.00148	0.001013	1764000	1.30E-04	6.20E+01
4	0.00138	0.000913	1951915	1.31E-04	6.70E+01
5	0.00128	0.000813	2209100	1.33E-04	8.00E+01
6	0.00118	0.000713	2556759	1.42E-04	9.40E+01
7	0.00108	0.000613	3043013	1.46E-04	1.12E+02
8	0.00098	0.000513	3738213	1.48E-04	1.40E+02
9	0.00088	0.000413	4799231	1.48E-04	1.88E+02
10	0.00078	0.000313	6461920	1.49E-04	2.76E+02
11	0.00068	0.000213	9297889	1.49E-04	4.27E+02
12	0.00058	0.000113	14432535	1.50E-04	2.85E+03

Figure 4.6 (a) presents a mesh convergence plot to show the variation of magnetic flux density as a function of the size of the mesh element. As it is clear, when minimum mesh element size of bar reaches to below 0.004 cm, the maximum magnetic flux density value shows less variation for lower mesh element sizes. Figure 4.6 (b) shows the simulation process time due to mesh sizes. When mesh size decrease, the simulation takes longer and it means that there is a limitation in time and also in computer processor. Based on this mesh convergence analysis (Table 4.2, and Figure 4.6), maximum and minimum element sizes for the bar were chosen to be 0.00058 mm and 0.000113 mm, respectively.

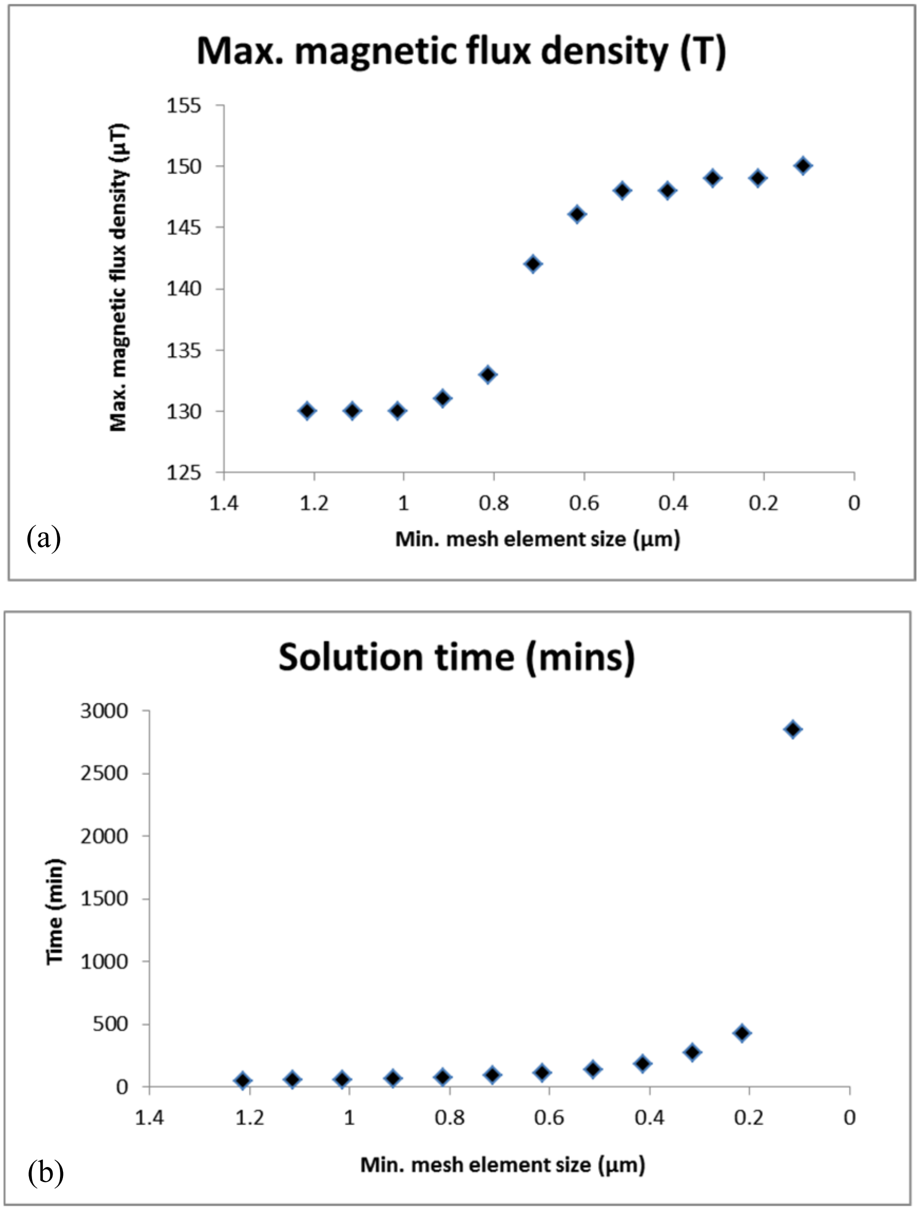

Figure 4.6. Mesh convergence plots, (a). Magnetic field changes due to mesh size (b). Simulation process time due to mesh size.

After data collection, the next simulation was run with 20% of the initial hole diameters and so on up to their original size in the experiments. The magnetic flux density variations as the results of diameter changes are shown in Figure 4.7. The magnetic flux density values for all parametric analyses including diameter, depth and angle of scanning changes for three holes shown in the figures were normalized to the maximum magnetic flux density value measured for hole 1 (1.51

E-04 Tesla). This maximum value in the magnetic flux density was obtained for a diameter of 10% of the original size (ratio = 0.10).

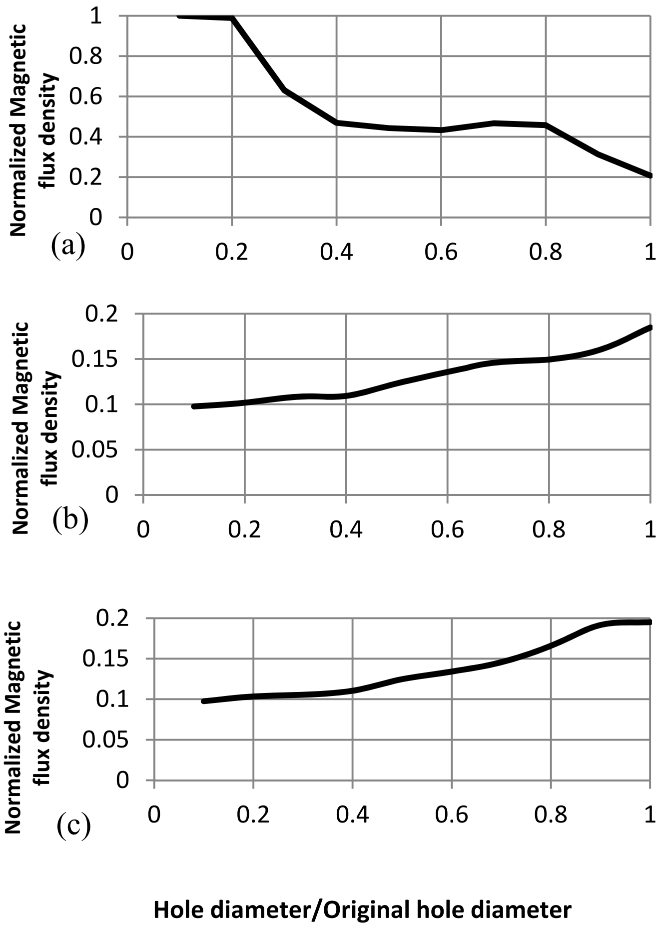

Figure 4.7. Effect of changes in hole diameter on magnetic flux density. (a). Hole-1 (H1). (b). Hole-2 (H2). (c). Hole-3 (H3).

The magnetic flux density around the bar normally decreased with increase in diameter for Hole-1 (H1) (top hole) (Figure 4.7(a)), but for the Hole-2 and Hole-3 (H2 and H3) the magnetic flux density increased with diameter (Figures 4.7(b) and 4.7(c)). For H1, when the diameter ratio is 0.1 (10 times less than original diameter of H1 in the experiments), the two sharp edges are very close to each other, facilitating the accumulation of magnetic stray field energy. For diameter ratios between 0.4 and 0.8, the magnetic flux density remained stable, but with a further increase in diameter, these accumulations decreased and consequently the maximum magnetic flux density decreased. The opposite behavior was observed for H2 and H3. Even though the absolute magnetic flux density response for these two holes was far weaker than the absolute value for H1, the normalized magnetic flux density increased as the hole diameter increased. The reason is that the distance from the side and bottom of the bar (positions of H2 and H3) to the top (scanning line) has more effect than the hole size (increased sharp edge proximity to the sensor location). For H2 and H3, until simulated diameters reached 40% of the original diameter, the magnetic flux density response was barely larger than the background level of the magnetic flux density.

To study the effect of hole depth, a similar procedure was followed. The first simulation was run with 10% of the experimental hole depth; Figure 4.8 shows the results. Figure 4.8(a) shows changes of normalized magnetic flux density at the top of H1 as a function of the changes in its depth. The trend generally is constant in amplitude with a slight slope from 10% of original depth to the original depth. This slight decrease happened because of increase in distance between the two sharp edges of the hole which gradually reduced the sharp edge effect on the magnetic flux density around the hole, but because the distance between sharp edges with respect to the scanning position did not change significantly (25%), the magnetic flux density changes are smaller than the changes induced by the hole diameter. The normalization value used for all plates is the maximum value obtained for the diameter parametric analysis (Figure 4.7(a)).

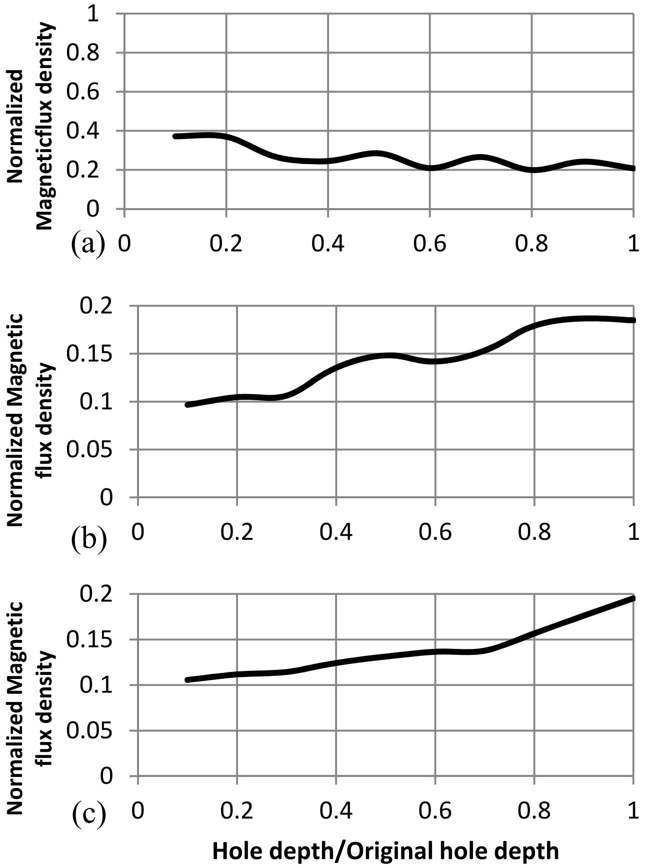

Figure 4.8. Effect of hole depth changes on magnetic flux density. (a). H1. (b). H2. (c). H3.

Increasing the depth of H2 and H3 caused an increase in the amplitude of the magnetic flux density. The bottom sharp edges of these holes became closer to the scanning line as depth increased; then, their effects on the magnetic flux density around the bar became perceptible, although the absolute effects on the magnetic flux density are far smaller than observed values for H1. The effect of the orientation of the edges of the hole with respect to the sensor location is studied next.

Figure 4.9 shows the scanning line locations in 10º rotation increments with respect to the three holes in the bar, shown in the z - y plane view. Each dot around the bar is a 10º rotational increment of scanning positions. The simulated scanning positions are actually 5 cm above the black dot positions to represent the concrete cover on top of the 1.6 cm diameter bar, as in the laboratory tests.

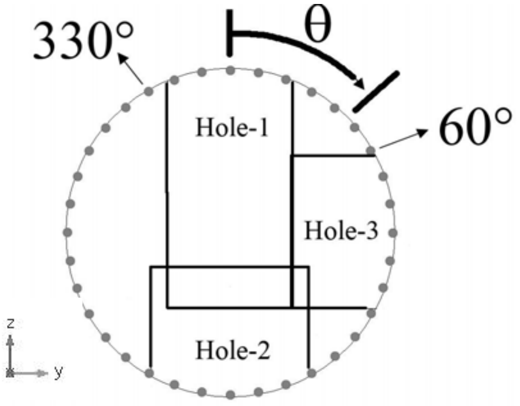

Figure 4.9. Numerical scanning locations (dots) at different angles (θ) with respect to bar geometry with three holes in the z-y plane.

Results for changing the scanning angle are presented in Figure 4.10. As expected, for H1 (Figure 4.10(a)) the maximum values are symmetrically distributed in the sector between 330° and 30°. Similar results are found for the other two holes and their angular orientations with respect to the scanning angle and holes edges. There are slight asymmetries in Figure 4.10 graphs, related to scanning positions and FEM meshing limitations and asymmetries. The high magnetic flux density peaks for the scanning positions are closer to a sharp edge (stray field energy) while for lower values the scanning positions are farther from a sharp edge.

Figure 4.11 shows the normalized amplitude of magnetic flux density around the bar with the three holes when the hole depths are equal to the bar diameter. In this simulation, holes fully penetrate the bar, and thus 180° rotational symmetry is expected. The main change in magnetic flux density anomalies happened because of the full penetration, in contrast to the simulation presented in Figure 4.10. Peak values of responses are almost the same as peak values in Figure 4.10. The main difference between graphs in Figure 4.10 and Figure 4.11 happened because of the initial increase in distance of the sharp edges at the bottom of the holes.

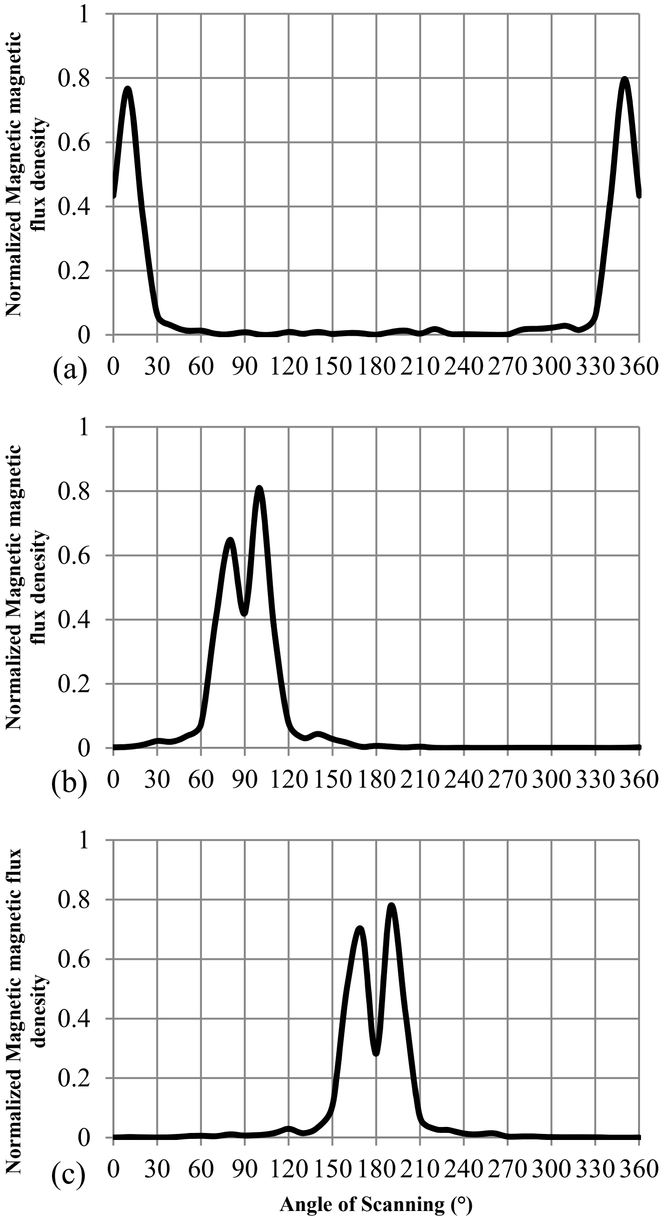

Figure 4.10. Normalized amplitude of magnetic flux density changes vs scanning angle. (a). H1. (b). H2. (c). H3.

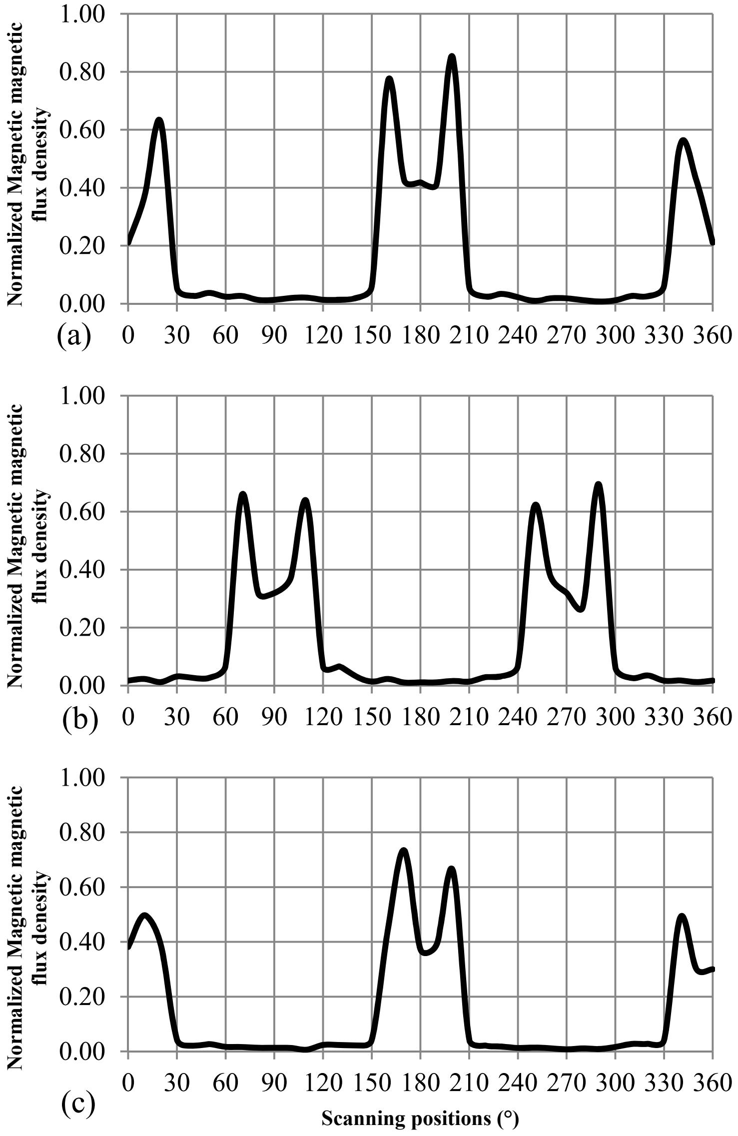

Figure 4.11. Normalized amplitude of magnetic flux density changes vs. scanning angle (Holes depths are equal to bar diameter, penetrating from one side to the other). (a). H1. (b). H2. (c). H3.

Numerical simulation permits extension and assessment of experimental results, and allows the calculation of various parameters effects (e.g. diameter, depth and orientation of blind holes). Trends noted in the results are comparable to the experimental test data (next section), to give insight into issues such as detectability and resolvability (multiple edges and their orientations, distances, and sharpness).

Figure 4.12 presents the magnetic flux density data derived from the 3D numerical model at a distance of 5 cm above the bar. There are two significant peaks at 0.14 m and 0.49 m, corresponding to the top and bottom holes. The middle peak at 0.27 m for the hole in the left side of the bar has a different pattern and magnetic flux density from the other two. These results show that valuable information about the orientation and shape of defects can be obtained by careful mapping of the magnetic flux density, calculating changes from a base model, and applying an inversion method.

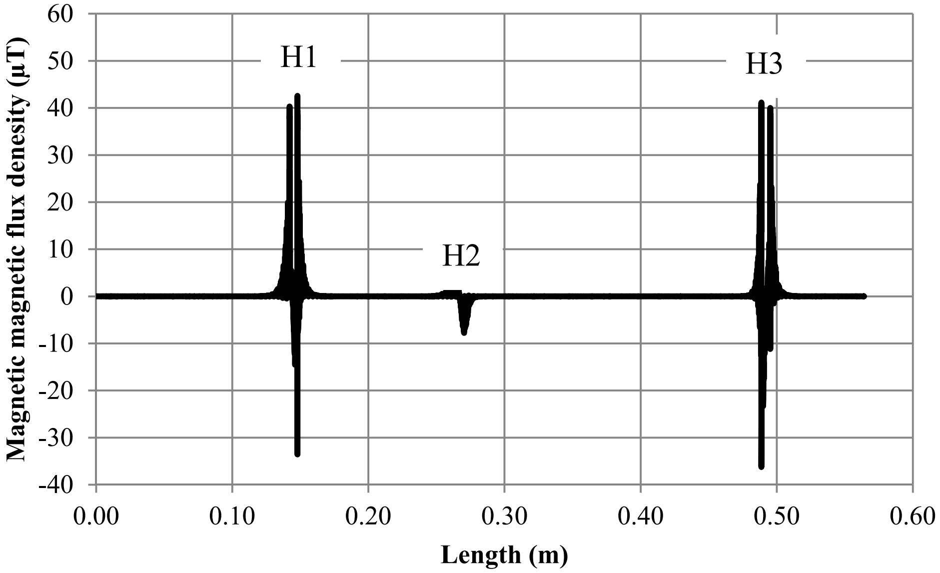

Figure 4.12. Magnetic flux density data from the numerical model.

Figure 4.13 shows an amplification of the three magnetic flux density responses to each of the three holes (H1, H2, and H3) indicated in Figure 4.4 to show the small scale fluctuations related to the discretization scale of the numerical model and the consequent changes in stray field energy. To suppress artefacts at numerical element borders in the modeling, a local regression using weighted linear least squares and a 2^{nd}-degree polynomial model is applied to the numerical results. It gives a good, point-wise approximation of the results with a low-order polynomial [108-110]. These results are presented in Figure 4.14, which are next compared with experimental data.

In order to evaluate the effect of smoothing, three different analyses were performed. The first uses the standard deviation (SD) of the raw and the smoothed data. The SD of smoothed data should be lower than the SD of raw data, and it is: 2.45 vs. 4.84. The variance ratio is the second approach; a higher value of this ratio expresses a lower noise fraction. To quantify this, the variance values of raw and smoothed data are calculated (14.77 and 6.00, respectively), giving a ratio of 2.46. The difference of integrals (DOI) is the third method used to show the accuracy of smoothed data, more accurate data having a value closer to zero; a value of 1.88 is obtained [111].

Based on these results, the smoothing process is considered successful in removing spatial numerical fluctuation effects on the data, without eliminating the effects of the holes on the magnetic flux density measurements. These numbers indicate that the smoothing of the numerical data used still leads to reliable estimates of the changes in the magnetic flux density. The smoothing does not significantly affect magnetic anomalies related to holes; hence, the numerical results are useful for comparison to real cases.

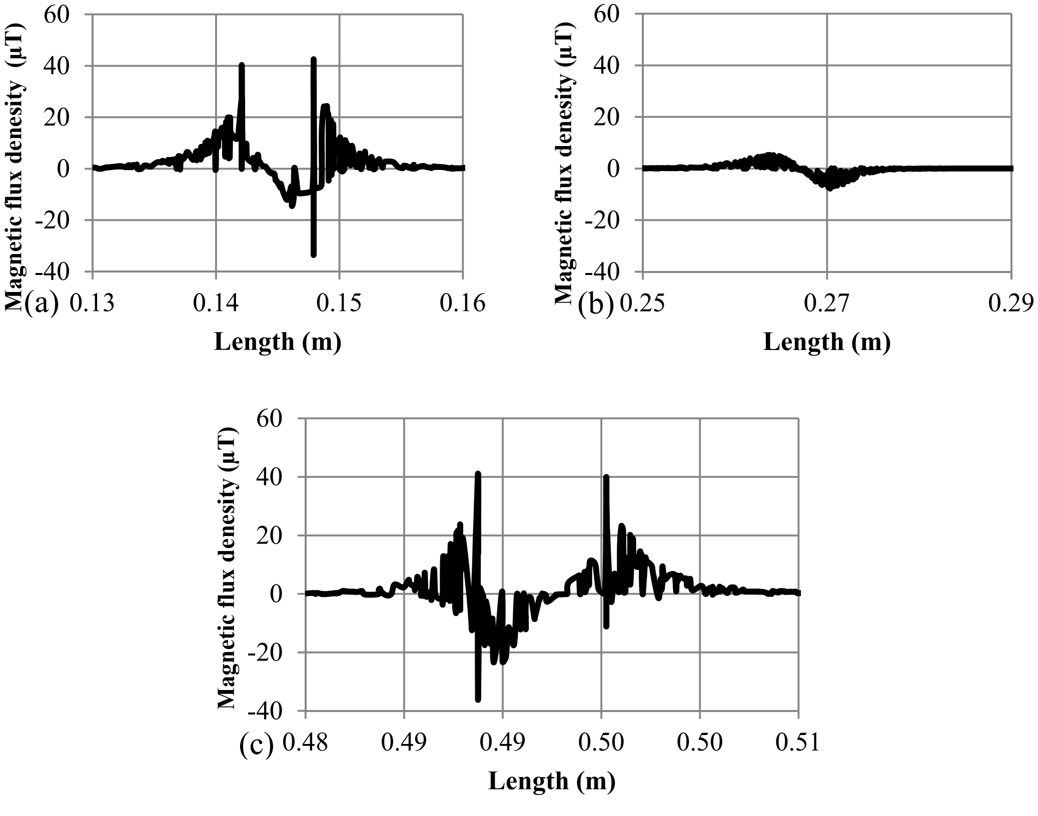

Figure 4.13. Fluctuation in the numerical data. (a). Top hole (H1). (b). Side hole (H2). (c). Bottom hole (H3).

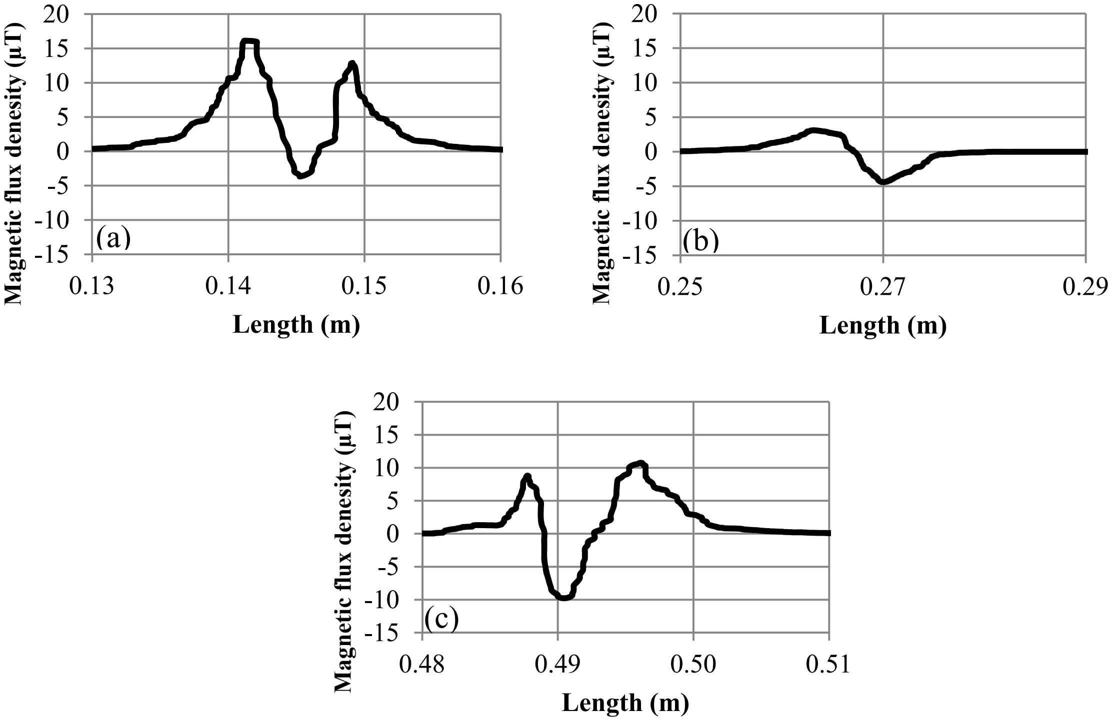

Figure 4.14. Smoothed numerical data. (a). Top hole (H1). (b). Side hole (H2). (c). Bottom hole (H3).

4.5. Experimental set-up and data processing

A concrete beam was made with the possibility of changing the reinforcement bar inside an internal longitudinal hole. As concrete is a non-magnetic material with a relative magnetic permeability of 1, it has no effect on magnetic flux density around the reinforcement bar [112]. In this study a typical concrete mixture was used based on ACI 211.1-91 [113]. Defects in the steel reinforcement (A572-G60, diameter 1.6 cm, Length 56.4 cm) are simulated by three holes (Figure 4.3).. Figure 4.15(a) shows the experimental set-up and Figure 4.15(b) shows the scanning machine prototype on the concrete specimen surface and reinforcement inside it.

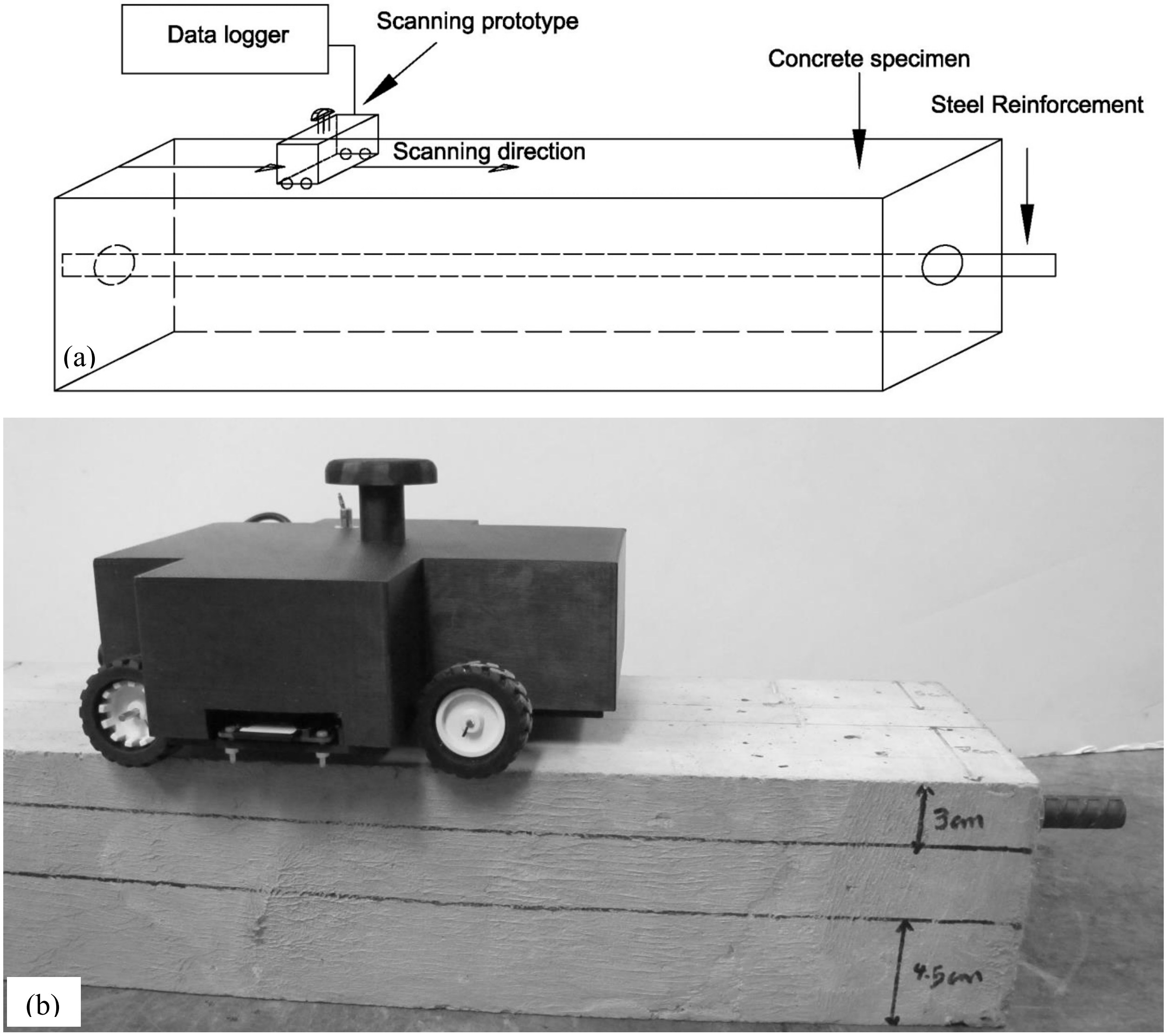

Figure 4.15. Experimental test (a). Scheme of test, (b). Scanning machine prototype and concrete specimen.

The magnetic flux density in the x direction (along the reinforcement direction) around the steel reinforcement with three holes underneath 5 cm of concrete is recorded using the same geometric configuration as in the numerical simulation. A prototype magnetometer using a Magneto-Inductive (MI) sensor [79] was developed to record the magnetic flux density around the reinforcement (Figure 4.15(b)). Recorded raw magnetic flux density data during the scanning process was transferred to the data logger directly.

The scanning method used was to move the prototype on the concrete surface in the same direction as the long axis of the reinforcement. While the scanner was moving, 10 data sets per second were transferred to the data logger. Before each test, the device precision accuracy was checked by recalibrating the device [114]. The experimental test is done at two different locations in the laboratory where the ambient magnetic flux densities are expected to be different. At each location, the magnetic flux density in the presence of the reinforcement steel within the concrete beam was measured 10 times and averaged. Figure 4.16 shows the experimental test procedure. The maximum standard deviations of experimental data for tests set at location 1 and location 2 are 14.6% and 21.4%, respectively. So, based on this, the data from test set 1 were selected for this study. Note that the relative magnetic permeability of concrete is equal to 1, thus it does not affect the magnetic flux density of the bar [115].

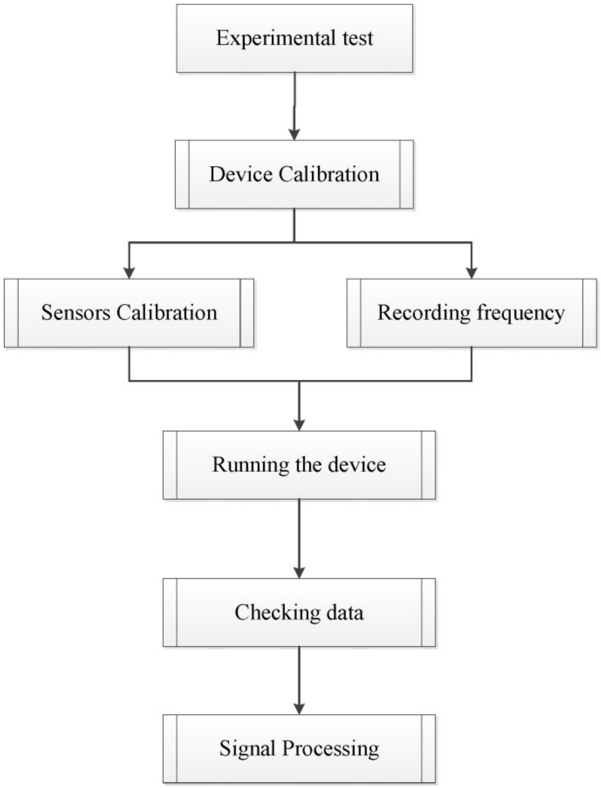

Figure 4.16. Experimental test procedure.

Figure 4.17 shows the raw magnetic flux density experimental data.

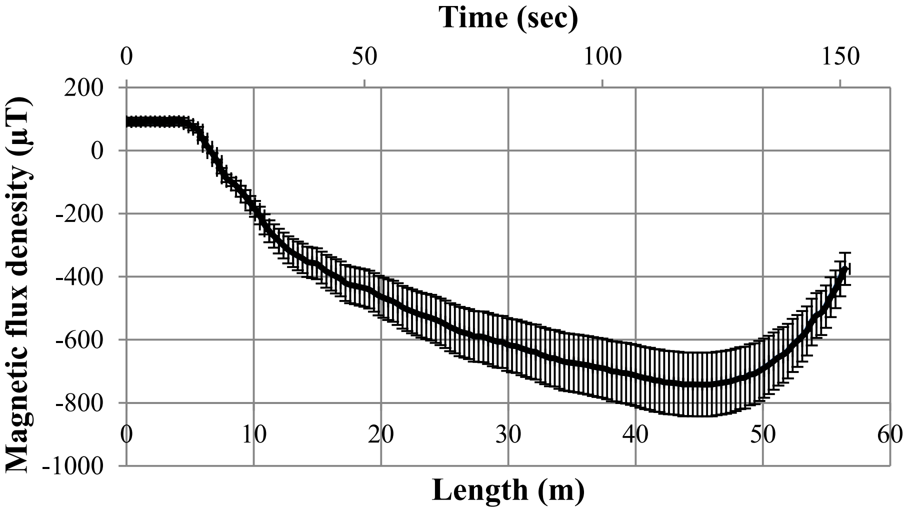

Figure 4.17. Raw magnetic flux density data above steel reinforcement from the experimental with ±14.6% SD.

The raw magnetic flux density data show different trends, and both high and low frequencies are found in the signal. Natural magnetic fields are spatially variable, giving a low-frequency trend in all such measurements. A high pass filter must therefore be applied to attenuate the low-frequency trend from the experimental raw data, so a frequency spectrum analysis (Figure 4.18) is carried out to define the appropriate filtering parameters. The Zero offset (DC level) correction is applied to data and afterward a Fast Fourier Transform (FFT) analysis is done by using a Hamming window to avoid fluctuation in the FFT result [116]. From this analysis, a frequency of 1.5 Hz was selected for the pass frequency parameter.

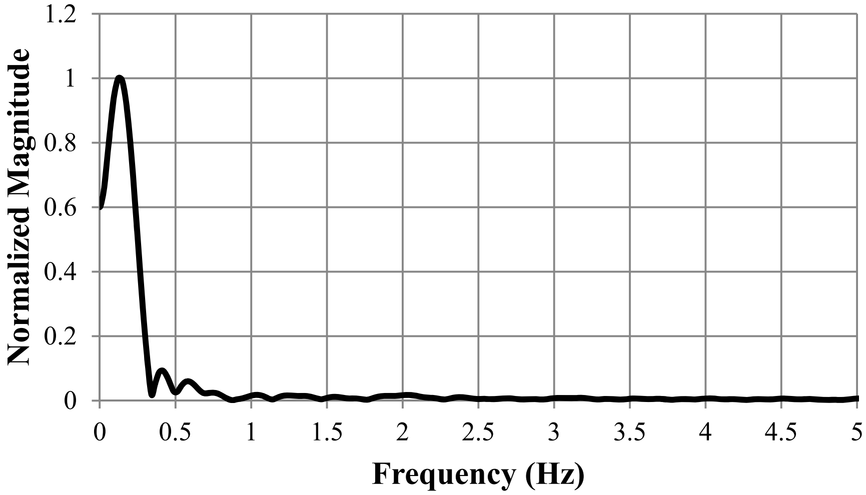

Figure 4.18. Frequency spectrum of magnetic data from the experimental test.

Once the low frequency response is removed from the experimental data, high-frequency data can be examined for anomalies which may be related to defects. To emphasize the point, this passive method will sample the magnetic effects related to the presence of a ferromagnetic substance in an ambient magnetic field, but the presence of an artificial magnetic field around the test specimen or the nature of the general magnetic field in the test area would have led to different trends in the magnetic flux density around the reinforcement steel. These trends can be of a low or high frequency nature, and the best way to remove these unwanted trends (noise) is to calibrate the inspection device before any test. The calibration process is to record the magnetic field at the test area in different three directions (x, y, and z), then subtract those values from the recorded test data [117]. Figure 4.19 shows the magnetic flux density data filtered in this manner, and it is now possible without further signal processing to identify two peaks at the positions of the top and bottom holes (0.14 m and 0.49 m).

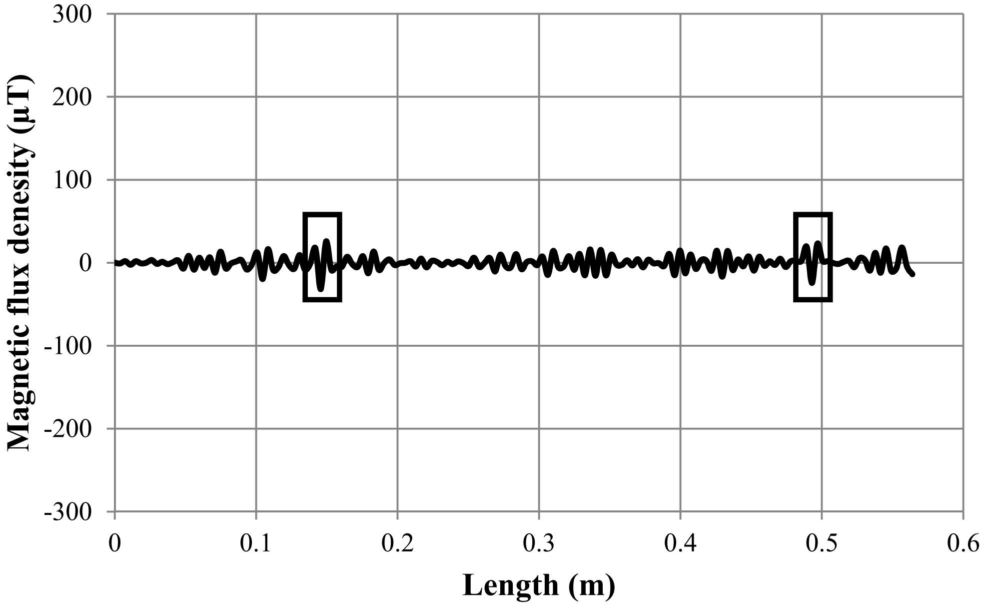

Figure 4.19. High pass filter (1.5 Hz) results from the experimental magnetic data. The two squares show two holes' locations at the top and bottom of the bar.

4.6. Comparisons of Results and Discussion

Filtered experimental data (Figure 4.19) have similar patterns at the right locations, compared to simulated results (Figure 4.15) for the top and bottom holes, at exactly the right positions. Figure 4.20 presents the simulated and experimental data together showing the spatial superposition of the two, with no adjustment in the horizontal position. There is a clear correspondence, but to have a better comparison, a scaling factor in amplitude is applied with a multiple of 0.1 between the two. The reason for the mismatch in amplitude is because of the difference between the real and the numerical model value assumed for magnetic properties of the reinforcement. In other words, the numerical model, although verified, was not specifically calibrated.

In this comparison, the middle hole (H2) in the side of bar shows a different response pattern and a much smaller amplitude than the top and bottom holes (Figure 4.13, and Figure 4.15(b)). The reason is most likely that the hole is more covered by metal, but it may also be that the edges of the steel were less sharp than the other holes in the direction of transit along the bar with the magnetometer device.

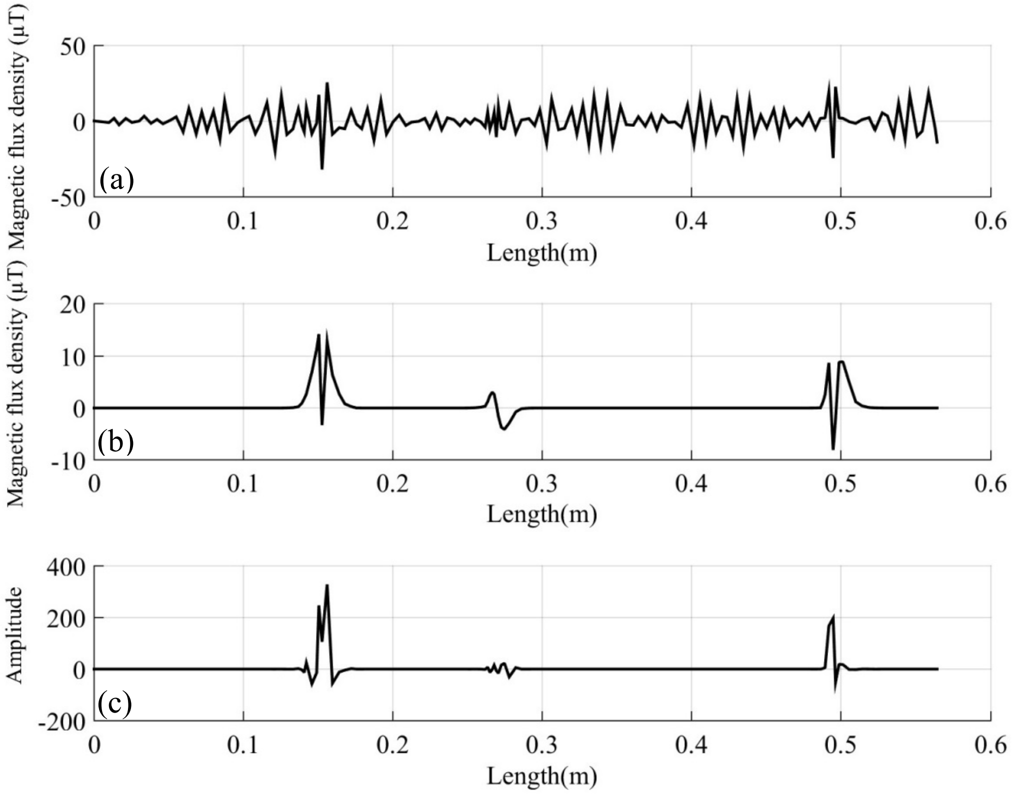

Figure 4.20. (a). Experimental test data, (b). simulation data, (c). Cross correlation result.

From Figures 20a and 20b, it seems clear that the experimental results after simple filtering have a reasonable match with the numerical data in the two large-response holes, the top and bottom holes in the bar. To further demonstrate this, a standard cross-correlation (product of two graphs) plot was extracted from these two signals with no spatial adjustment. Such results can be used as an auto-correlation method to estimate potential similarity between two signals or the similarity between them. In Figure 4.20(c) the two significant peaks simply mean that there are two regions with a high degree of correlation between the numerical and experimental data, confirming that the premises and procedures have led to reliable detectability of small anomalies with the passive magnetic measurement method.

4.7. Conclusions

The numerical simulation results from theory-based calculations present a reasonable match with the experimental data for small defects in reinforcement at 5 cm distance from the magnetometer. Similar to other passive NDT approaches, it is necessary to filter out non-related effects. The low frequency trend (result of magnetic flux density of bar) in experimental data is filtered out so that the high-frequency response of the holes can be extracted from the signal. Careful examination of the frequency spectrum of the experimental data is a good way to find the best cut-off frequency for the high pass filter for the experimental raw data. The following items are the main conclusion of this chapter:

1. Defect diameter, depth and location of small drilled holes (defects) with respect to the sensor are effective parameters, which control the magnetic flux density of a steel reinforcing bar.
2. The angle of scanning magnetic data with respect to a defect orientation has a large effect on the amplitude of recorded magnetic flux density, so recording magnetic data at different angles can be useful for inverse geometrical modeling of defects.
3. Edge effects are dominant among the parameters was assessed. Although the effects of changes in the depth of defects are also quite considerable.
4. The results with respect to the geometric characteristics of defects indicate that data inversion (replication) of actual defect geometry in practice is possible, but it is a complicated procedure that likely requires magnetic flux density measurements in a number of different directions at each sampling site.
5. Inverse modelling of defects based on absolute magnetic flux density values will be complicated if there are multiple defects affecting the response at a sampling site. Thus, resolvability of two closely spaced defects (for example) will be constrained; nevertheless, the anomalies simulated here should be, in practice, highly detectable.
6. Numerical simulation of altered magnetic flux density gives results that match well with experimental data. This match is apparent only after applying some simple signal processing techniques on both simulation and experimental data: numerical data were smoothed to reduce the FEM discretization effect; experimental data were filtered to remove low-frequency trends so as to reveal signal anomalies.
7. Two holes in different positions (top, and bottom) were readily detected from the magnetic flux density measurements in the bar axis direction. The reason may be the presence of two edges for each hole which were crossed by the inspection device during the experimental test.

8. As shown using auto-correlation analysis, there is a strong similarity of response between experimental and simulation data for the top and bottom holes.
9. The side hole presented a different and much lower amplitude pattern, compared to the top and bottom holes. This difference is probably because of the position (left side) of the middle hole such that the (linear) magnetometer sensor did not cross the magnetic flux density around this hole optimally. The noise and signal levels were similar, so the desired anomaly related to that hole could not be extracted. Numerical simulation confirms the low magnetic field impact of this hole configuration.

A better solution to detect all such holes is to simultaneously collect tri-axial (x-y-z) magnetometer data for co-processing.

This early-stage proof-of-concept analysis has been kept simple to demonstrate that steel bar deterioration (which radically alters the magnetic response) can be detected and analyzed with a passive magnetic approach, supplemented by standard signal filtering, and supported by theoretical calculations. However, shapes and sizes of three holes are different from real defects caused by corrosion in reinforcement concretes, but it seems that it is possible to apply this inspection method for a real corroded reinforced concrete. Because the method is purely passive (neither applied magnetic field nor electrical current in bar which applied artificially or caused by corrosion), and the fact that concrete is not a magnetic material, there is no effect from concrete condition on inspection results. This is the main advantage of PMI method.

Before the technique is applied in practice, parametric analysis is needed and testing in well-defined field conditions must be undertaken. Different filtering approaches will likely be needed in different conditions to extract anomalies because of deterioration or induced defects (cracks). These efforts are underway.

4.8. Principal Component Analysis

It is urgent to recognize RC structures, defects quantitatively by utilizing smart signal processing methods. Besides being tiring and time consuming, non-intelligent methods results are dependent on the human element of uncertainty. The applied mathematical relation between defects and magnetic fields is the reason to avoid these limitations. This study presents the application of Principal Component Analysis (PCA) to passive magnetic signal data, followed by the result of experimental tests using PMI on RC specimen, to locate defects. The simple case presented is a proof-of-concept study that demonstrates PCA method's ability to locate the deterioration of steel reinforcement covered by concrete.

4.8.1. PCA feature extraction for PMI method

The advantage of the PMI is the basis of this NDT method in self-magnetic potential of steel rebar, which categorize PMI as a passive NDT method. It means that there is no need to apply strong magnetic field before start the test. Self-magnetic potential occurs because of domain boundaries formation at accumulations of electron dipoles in an aligned direction. The alignment of dipoles is under the effect of earth's magnetic field as a natural magnetic source and mechanical force as an artificial factor. Any change in metal structure, affects the magnetic domain's size and distribution. Changes in a magnetic domain affect the electron dipole alignment and consequently change the magnetic response of ferromagnetic specimens [50, 94, 95, 23, 97, 121, 98, and 92].

The feature extraction technique applied in this study is Principal Component Analysis (PCA). Passive Magnetic Inspection (PMI) data is mainly carried out in the time domain. The first and main object of this non-destructive testing is locating any deteriorated areas quickly. Therefore, PCA analysis seems to be a sound approach [122].

PCA is a useful statistical solution for extracting principal components as a dominant feature. Field magnetic data around the reinforced concrete is suitable multivariate data in the time-domain for PCA analysis. Raw field magnetic data are selected from the experimental test as multivariate data. To achieve Eigensignals, Hn has been defined as a column vector with n variables. Because magnetic field data is collected in three different axes (x, y, and z), there will be an array matrix of *H*, with the size of 3 × n, as below:

$$H = [Hx, Hy, Hz] \tag{4.9}$$

where H_x, H_x and H_x are magnetic fields in x, y and z axes. The average signal ψ is defined by:

$$\psi = \frac{1}{3}\sum_{n=1}^{3} H_n \tag{4.10}$$

By subtracting the average signal from each signal column, difference signals that are subjected to principal component analysis are available, as follows:

$$\phi_{x,y,z} = H_{x,y,z} - \psi_{x,y,z}, \qquad \phi_n = H_n - \psi_n$$

(4.11)

Covariance matrix *C* should be calculated in order to find the orthogonal eigenvectors:

$$\mathrm{C} = \frac{1}{3}\sum_{\mathrm{n}=1}^{3} \phi_{\mathrm{n}} \times \phi_{\mathrm{n}}^{\mathrm{T}} = \frac{1}{3}\mathrm{A} \times \mathrm{A}^{\mathrm{T}} \tag{4.12}$$

where $\mathrm{A} = [\phi_x, \phi_y, \phi_z]$. If we consider v_i as the eigenvectors of $\mathrm{A} \times \mathrm{A}^{\mathrm{T}}$, then:

$$\mathrm{A} \times \mathrm{A}^{\mathrm{T}} v_i = u_i v_i, i = x, y, z \tag{4.13}$$

Therefore;

$$u_i = \mathrm{A} v_i \tag{4.14}$$

So, these u_i are referred to as Eigensignals. The principal components for any signal H are defined by:

$$w_i = u_i^T \left(H - \psi\right) \tag{4.15}$$

The value of w_i are the new features that might be correlated with the defects.

4.8.2. Experimental setup and test

Figure 4.21(a) shows the reinforced concrete specimen used for this study. It has three small holes (defects) in different positions and orientations (Figure 4.21(b)). This rebar type is A572-G60, based on ASTM standards, and its relative magnetic permeability is around 75 [123, 124]. Table 4.3 presents information about the three holes' geometry.

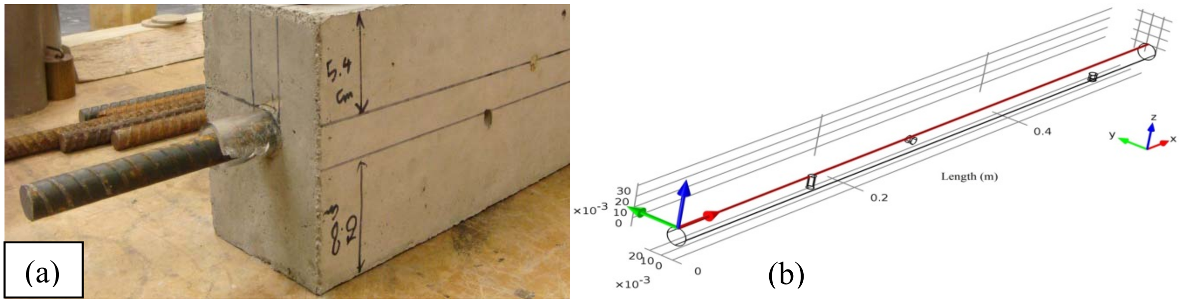

Figure 4.21. (a). Concrete beam specimen. (b). Three small holes in sound steel reinforcement (rebar).

Table 4.3. Geometry information for the three holes in the steel reinforcement

Holes	**Radius (cm)**	**Depth (cm)**	**Hole location on rebar (m)**	**Position**
H1	0.29	1.24	0.14	Top
H2	0.34	0.57	0.27	left side
H3	0.33	0.67	0.49	Bottom

Figure 4.22 shows raw magnetic field data from the top of the reinforced concrete (with 5.4 cm thickness), for the reinforcement (steel rebar) with three different holes in three different

locations. These raw magnetic fields data are in x, y, and z directions. These data are from an experimental test, and make it clear that locating the three holes is impossible (Table 4.3).

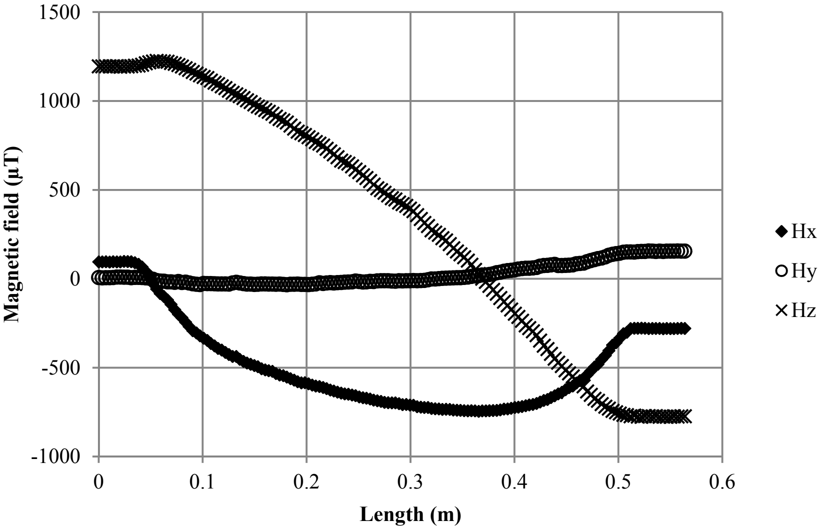

Figure 4.22. Raw magnetic field data from the surface of the drilled reinforced concrete beam.

As mentioned in Eq. 4.9, these data are input as column vectors. The same experimental test results from the sound steel reinforcement were used as threshold data (Figure 4.23).

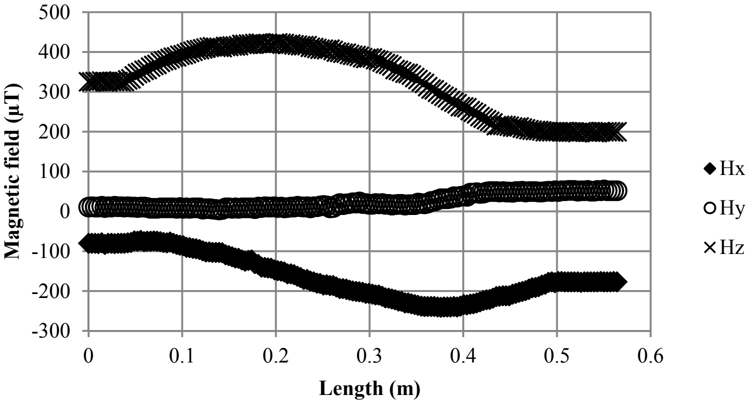

Figure 4.23. Raw magnetic field data from the surface of sound reinforced concrete beam.

4.8.3. Results

Based on the equations mentioned in Section 4.8.1 (Eq. 4.14, and Eq. 4.15), and by applying them on the experimental test data, a set of Eigensignals were derived. The first Eigensignals, shown in Figure 4.24, is the PCA analysis results for the sound steel reinforcement. These results were used as a threshold [123]. The threshold data is necessary to distinguish between the sound and deteriorated reinforcement.

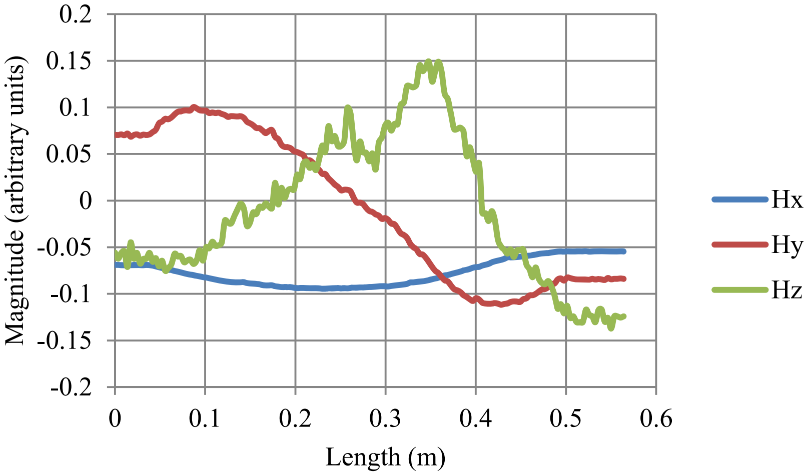

Figure 4.24. Eigensignals of sound steel reinforcement.

Figure 4.25 shows the Eigensignals derived from the drilled steel reinforcement. Again, the results from the PCA analysis from the sound and drilled reinforcements fail to show significant changes. Some changes occur in the pattern of magnetic field changes in the x and y directions. The important change is in the result of the magnetic field in z direction.

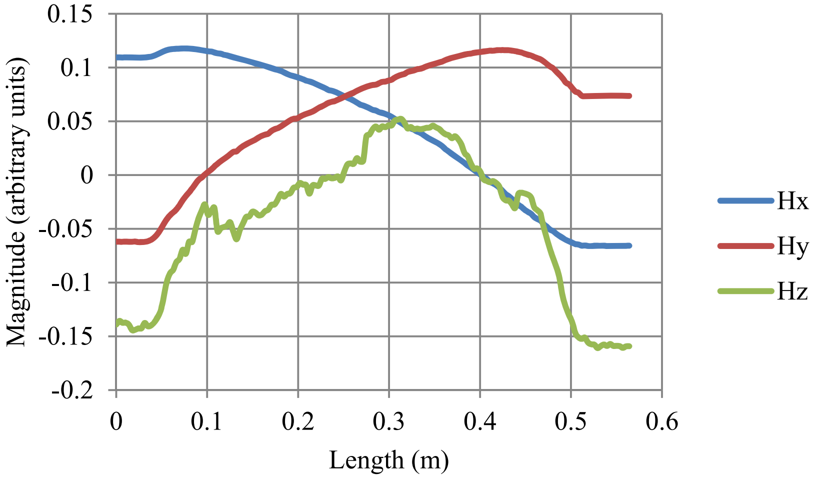

Figure 4.25. Eigensignals of drilled steel reinforcement.

Figure 4.26 shows the results of subtracting the drilled bar Eigensignals from the sound bar Eigensignals. The graphs from the x, and y axes do not present meaningful results, but magnetic data from the z axis show changes from negative to negative values on the hole's locations (Table 4.3). In field magnetic analysis the area it called a zero line [124], shown in red (dashed line) in the figure 4.26.

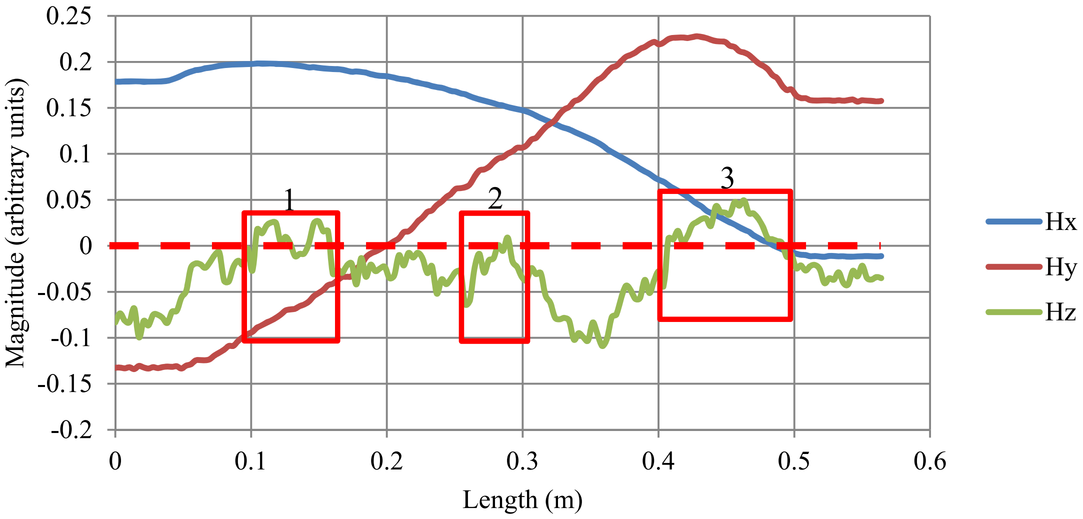

Figure 4.26. Subtraction of Eigensignal from threshold Eigensignal. Red line shows the zero line. Three red boxes show the locations of holes.

Red box no.1 in Figure 4.26 shows the top hole on the rebar. In this location the Eigensignal of the Z axis data crosses the zero line and, exactly at the start of the hole, it dips to below the zero line, stays below zero until the end of hole, returns to above it after and then drops below zero again. The second hole's story is different, because it is at the right side of the rebar. In this case (red box no.2), the Eigensignal climbed above the zero line and then return below. For the hole at the bottom of the rebar (hole-3), the Eigensignal shows a different pattern, but it still passes above the zero line before the hole and return after it. The anomaly width for this hole is wider than its diameter, perhaps because this hole's signal is a little bit wider than the other two. Because the Eigensignal graph shows different patterns for the three holes (top, right side, and bottom), this method may also be suitable for detecting the clock position of defects in reinforcement.

4.8.4. Conclusion

A PCA based feature extraction method has been used in a new PMI non-destructive testing method investing reinforced concrete. The method is shown to be applicable in detecting the location of holes in three different positions in a rebar, making this a successful case study. For each defect's position, the Eigensignals shows different patterns. These patterns are candidates for a future study on clock position detection of defect. Current study demonstrates a relatively fast investigation of PMI test data to find whether and where any problems exist in reinforcement. The answers to these two questions are important when investigating the severity of such problems and in deciding to repair or replacement reinforced concrete structures.

Chapter 5

De-bonding assessment of reinforced mortar using ultrasonic experiments test and numerical simulations

5.1. Introduction

One of the most used construction materials in civil structures (buildings, bridges, platforms), and also underground structures (e.g., roadbeds, concrete pipelines, and tunnels), is reinforced concrete (RC) [1]. Commonly, service times of reinforced concrete are designed to be more than 100 years, even in harsh environmental conditions [57]. External conditions such as exposure to corrosive industrial fluids, solutions of road salt, and service temperature, are known to reduce the durability and longevity of RC structures. Defects (corrosion and cracks) in steel reinforcement result from these conditions, and decrease the strength of RC structures, thus increasing their failure risk.

Recently there has been much work to improve the quality of the concrete matrix [58], or introducing different reinforcement protection approaches [59, 60, and 61]. Although these attempts increase the service time of RC structures, deterioration processes affecting the reinforcement never cease. Hence, condition assessment of RC structures remains vital to assess their serviceability and their level of safety over time. The standard ultrasonic approach as a Non Destructive Testing (NDT) method has been used for more than sixty years in industrial applications. Applying a 0.2-30 MHz range of the excitation wave, measuring arrival time, and calculating probable discontinuity occurrence are the main elements of conventional ultrasonic methods [125].

Guided waves (Rayleigh and Lamb waves) have been used progressively more than standard ultrasonic methods to estimate thickness changes of specimens in the last few decades [125]. The main advantage of guided waves is their confinement to the thickness of the plate or cylindrical medium, which gives the advantage of extracting more information about the state of the medium. This additional information can be the thickness of the plate, or the presence and nature of internal defects such as voids, cracks, and corrosion [77]. Guided waves, being less dispersive, can propagate through long distances, usually resulting in greater sensitivity or greater assessment lengths than most ordinary NDT methods. Furthermore, they are applicable for the assessment of multilayered structures, and in principal can serve as an appropriate method for non-invasive RC structures inspection [126].

The most common ultrasonic method based on guided waves is multichannel analysis of surface waves (MASW), used widely for various structures [73, 127]. This method has been used to evaluate concrete structure integrity, including defect detection [70, 128, 129, 130], or corrosion monitoring of reinforcement [57, 131]. Attenuation in time and frequency domains is a parameter which can be extracted from the MASW test; peak-to-peak amplitude changes are a strong energy loss indicator in the time domain, and attenuation in the frequency domain can be calculated by the spectra area method [132]. The dispersive characteristics of waves can be used as well to compare a sound specimen to deteriorated ones, and inversion of dispersion curves can be done in order to determine wave velocity and probable deterioration locations and size [133].

Piezoelectric transducers with different ranges of frequency are an important part of guided wave experimental tests, but details of the material properties of the transducer are usually not provided by the manufacturer. The main part of each piezoelectric transducer is the central piezoelectric crystal that reacts mechanically to an input electrical impulse, or can generate a current that is related to an applied mechanical force [142]. Although the principle is the same, based on their applications they have different crystal materials and dimensions [142]. After some years of using a transducer its response performance may be somewhat changed; thus, a clear understanding of the evolution of signals from a transducer is important, and because to have a proper numerical simulation the piezoelectric crystal should be simulated properly, careful calibration and re-calibration of the piezoelectric crystal is the best way to understand the actual input signal.

In practice it is difficult to determine the frequency and energy content of a transducer-transmitted wave throughout the specimen. The actual displacement response of piezoelectric transducers to excitation is a parameter that is needed to properly test and then evaluate experimental results. More information about the transmitted wave (input signal) through the specimen helps to improve the quality of results, and by knowing precisely the frequency, displacement and energy content of the input signal, detection of deterioration becomes more feasible [133].

Piezoelectricity behavior - first noted by the Curie brothers in the late 19th century [167] - involves transforming an electrical pulse to a mechanical pulse and vice versa through the use of transducers made of electro constrictive materials such as pure and highly crystalline oriented quartz crystals. Characterization of the transmitter and receiver behavior is necessary to quantify their effects on experimental results, and transducer calibration is an established method of characterization of the input signal [168]. The electrical properties of the transducers and the associated cabling are other important aspects which may affect transducer behavior. However, piezoelectric transducers involve complex aspects of rapidly changing electromagnetic fields, mechanical properties, and strain wave emissions, which presents certain challenges to mathematical simulation [169].

In this chapter, by using a laser vibrometer, the actual displacement of a transducer is measured at a nano-meter scale. Numerical simulation of the transducer behavior is carried out using a discrete finite element method [105] to compare modeled outputs to real displacements of the transducer as a means of verifying the validity of the simulation. Understanding and quantifying the real input signal is an aid to the more correct analysis of experimental data as the incorporation of a proper simulated input signal from the piezoelectric transducer allows more realistic and accurate numerical simulation of the whole specimen response.

Corrosion in reinforcement generates a narrow gap between the reinforcement and the concrete [57], a de-bonded condition where there are regions of minimal contact between the two components, although the gap can be very small (scale of microns). After calibration of the piezoelectric transducer, the guided wave method was used to test reinforced mortar cylinders in perfectly bonded and de-bonded conditions. The perfectly bonded and de-bonded conditions of the reinforced mortar cylinder were then numerically simulated for comparison with the experimental results and to evaluate the viability of de-bonding assessment using the guided wave acoustic assessment method.

5.2. Theoretical background

The steel-matrix bonding condition within a reinforced mortar cylinder was assessed in this study using intermediate frequency strain waves. Compressional waves (P-wave) and shear waves (S-wave) are strain body-wave propagation types within an appropriately excited infinite length perfect elastic cylinder [77]. In a homogeneous infinite medium without flaws, the P- and S-wave velocities are constant, but in a steel bar, reflection of waves from the boundaries allows propagation energy to remain within the bar. Therefore these waves behave as surface waves which have propagation velocities related to their frequency content, and dispersion curves show this behavior clearly [134]. Complex reflections from the boundaries and the dispersive behavior of surface waves because the surface of the bar is in contact with materials of different elastic properties generates different modes of wave propagation. The main advantage of using dispersion curves that are produced from testing bars is their predictable mode shapes and frequencies which can be calculated by the equations of wave propagation [135].

In a rebar with a consistent cross-section, there are longitudinal, flexural and torsional propagation modes for strain waves [77]. By attaching a transducer to one end of bar/rebar, as in this study, longitudinal waves can be generated [136]. Pochhammer (1876) was the first to transform the equations of motion in three-dimensional solid circular rods into cylindrical coordinates, and derived a frequency equation after applying the free surface boundary condition [137]. Similar work was done independently by Chree in 1889 [138]. The Pochhammer-Chree equation has the following form [77]:

$$\frac{2\alpha}{a}\left(\beta^2+k^2\right)J_1\left(\alpha a\right)J_1\left(\beta a\right)-\left(\beta^2-k^2\right)J_0\left(\alpha a\right)J_1\left(\beta a\right)-4k^2\alpha\beta J_1\left(\alpha a\right)J_0\left(Ba\right)=0 \tag{5.1}$$

$$\alpha^2 = (\omega^2/\mathrm{c_L}^2)-\mathrm{k}^2, \quad \beta^2 = (\omega^2/\mathrm{c_S}^2)-\mathrm{k}^2, \; C_L=\sqrt{\frac{\lambda+2\mu}{\rho}}, \quad C_S=\sqrt{\frac{\mu}{\rho}}$$

Here, k is wavenumber, ω is frequency, c_L is longitudinal P-wave velocity, c_S is transverse S-wave velocity, *a* is radius of the rebar, and J_0 and J_1 are the Bessel functions [139]. Prediction of mode shapes and frequencies in a sound solid circular rod became available with the application of Eq. 5.1.

While the longitudinal wave is propagating through the reinforcement, it is necessarily interacting with an interface between two different materials, the steel bar/rebar and the mortar, with different Young's modulus (E), density (ρ), and Poisson's ratio (υ). Reflection from the boundary of reinforcement or transmission into the mortar can happen. Wave transmission into the mortar media causes a loss of energy, called leakage (Figure 5.1) [140]. Elastic and damping properties of the mortar plus the bond quality between steel bar/rebar and mortar are the main parameters which affect energy leakage [141].

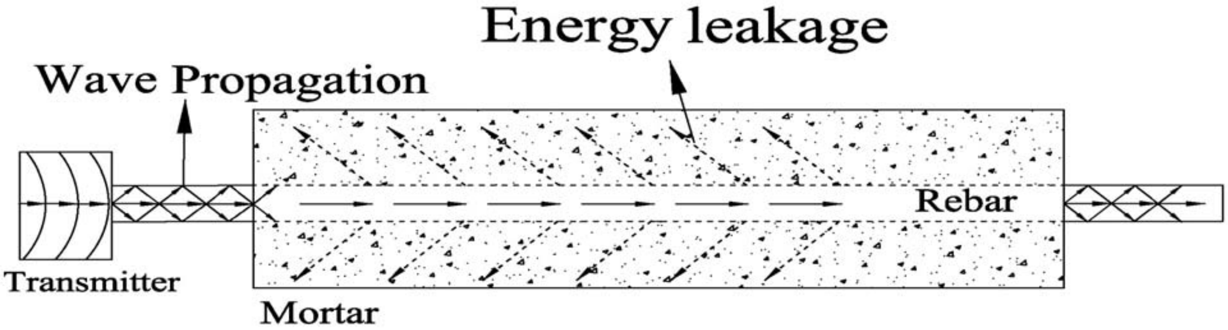

Figure 5.1. Leakage of longitudinal wave at reinforcement and mortar interface.

The acoustic impedance property – W – is used to quantify reflection and transmission of a longitudinal wave from the interface between two media [75]:

$$W = \rho c \approx \sqrt{\rho E} \tag{5.2}$$

$$R = \frac{W_2 - W_1}{W_1 + W_2} = \frac{\rho_2 c_2 - \rho_1 c_1}{\rho_1 c_1 + \rho_2 c_2} \tag{5.3}$$

$$T = \frac{2W_2}{W_1 + W_2} = \frac{2\rho_2 c_2}{\rho_1 c_1 + \rho_2 c_2} \tag{5.4}$$

Where c is the longitudinal wave velocity and ρ is density. R and T are reflection and transmission coefficients for the interface between the two materials. Large difference between acoustic impedance of two specimens led to complete reflection from their interface. No difference between acoustic impedance of two specimens causes a complete transmission of wave to another specimen if the interface is perfectly bonded. R will be less in the case of steel reinforcement perfectly bonded to the mortar, compared to the same reinforcement which is somewhat or totally de-bonded. Also, T (transmission coefficient) will be less for de-bonded reinforcement compared to perfectly bonded reinforcement. So, in the case of perfectly bonded reinforcement, more energy leakage will happen because of lowered reflection, and less energy can be captured at the other end of the reinforcement.

5.3. Experimental investigation

5.3.1. Experimental methodology

Figure 5.2 shows the work flow for this study. Tests and numerical simulations were carried out after two sets of calibrations. The first set of calibrations was done on the transducer. Face to Face calibration was done by using two similar transducers (Panametrics V102). The optimum force holding the transducers together was established by using a load cell. The optimum force was applied behind the transducer and, by using the laser vibrometer, the actual displacement was measured on the surface of the transducer. By using an X-ray device, the internal parts of the transducer (backing material, piezoelectric crystal, and matching layer) were delineated. Then, a numerical simulation was done using the discrete finite element method with the input voltage, electrical circuit and transducer parts defined based on the real experimental calibration of the transducer. Displacement from the numerical simulation was adjusted to correspond as closely as possible to the actual displacement from the laser test using trial and error. The closest numerical simulation result to the actual displacement of the transducer was used in the second step of numerical simulation.

Before casting rebars and bars in mortar, tests were done using the laser vibrometer to verify the optimum weight from the load cell, and also to compare experimental results with numerical simulation results and the theoretical solution for a cylinder. Numerical simulation of the transducer and free bar was performed and again was adjusted using the laser vibrometer experimental test results, in a manner similar to the transducer calibration described above. Dispersion curves of longitudinal wave propagation from numerical simulation of the free bar were extracted and compared with dispersion curves calculated from the theoretical method. The final numerical simulations were to define similar final specimens to verified simulations as a means of calibration.

Comparing results has confirmed the validity and value of the numerical simulations. The final section of this study involved analyzing guided wave propagation data from experimental tests of bonded and de-bonded reinforced mortar cylinders for bar and rebar reinforcements. Test results and numerical simulations were compared once the testing was completed. In summary, the peak to peak amplitudes of the de-bonded bar and the de-bonded rebar in experimental tests and the de-bonded bar numerical simulations were 4.68, 6.24, and 9.88 times more than the case of perfectly bonded samples.

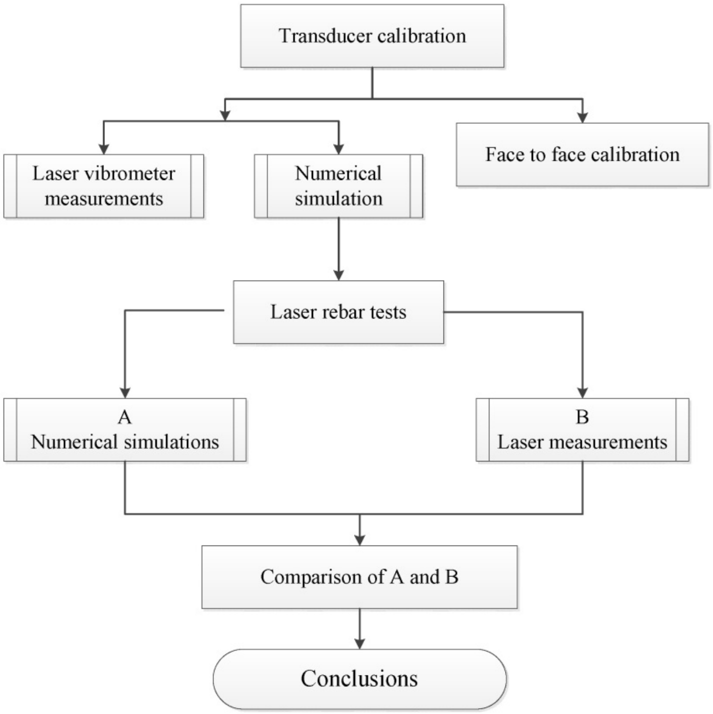

Figure 5.2. Procedure work flow.

5.3.2. Preparations

Two steel rebars type A572-G60 (E = 200 GPa; $\upsilon = 0.3$; $\rho = 7850$ kg/m^3) and two steel bars (low carbon grade 1020) (E = 210 GPa; $\upsilon = 0.29$; $\rho = 7870$ kg/m^3) were embedded in mortar (E = 5 GPa; $\upsilon = 0.16$; $\rho = 1770$ kg/m^3). Bars and rebars have a radius of 7.91 mm and a length of 1.168

m. The final mortar cylinder has a diameter of 16 cm and a length of 97 cm. One bar and one rebar were wrapped with 5 layers of plastic food wrap to make a 0.1 mm space before casting to achieve a de-bonded condition. Two reinforced mortar cylinders were cast with bar (sample 1) and rebar (sample 3) to have perfect bonding samples (Figure 5.4(a) and 4(c)), and two reinforced mortar were cast with plastic wrapped bar (sample 2) and plastic wrapped rebar (sample 4) (Figure 5.4(b) and 6.4(d)).

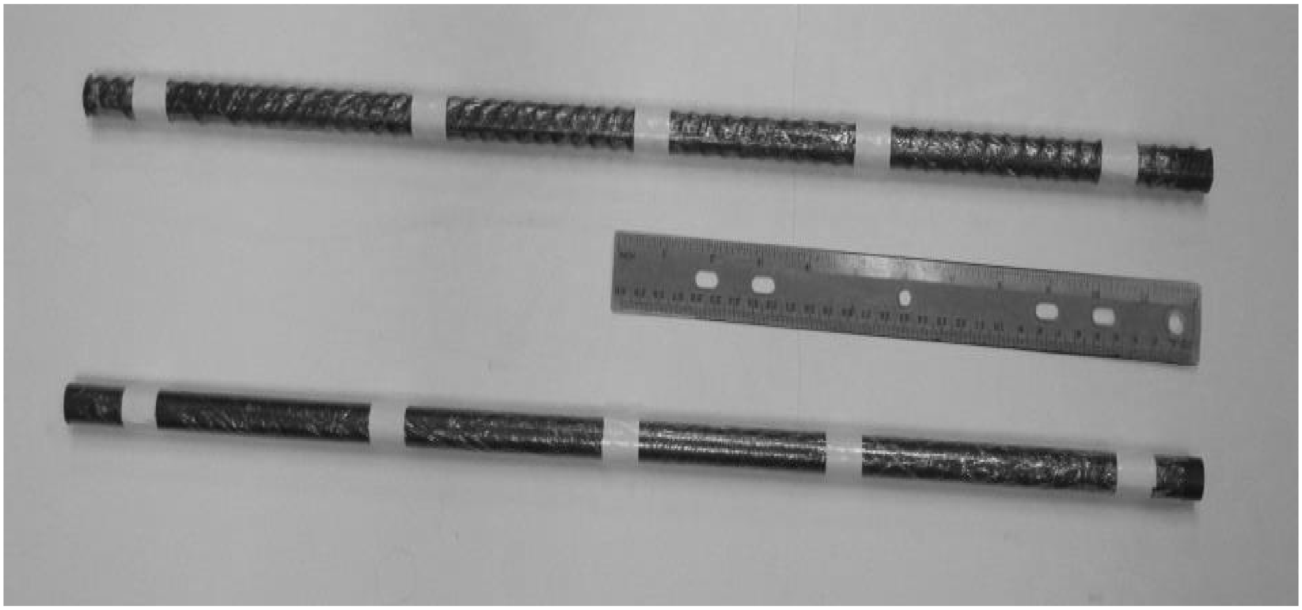

Figure 5.3. Wrapped bar (bottom) and rebar (top) with plastic wrap.

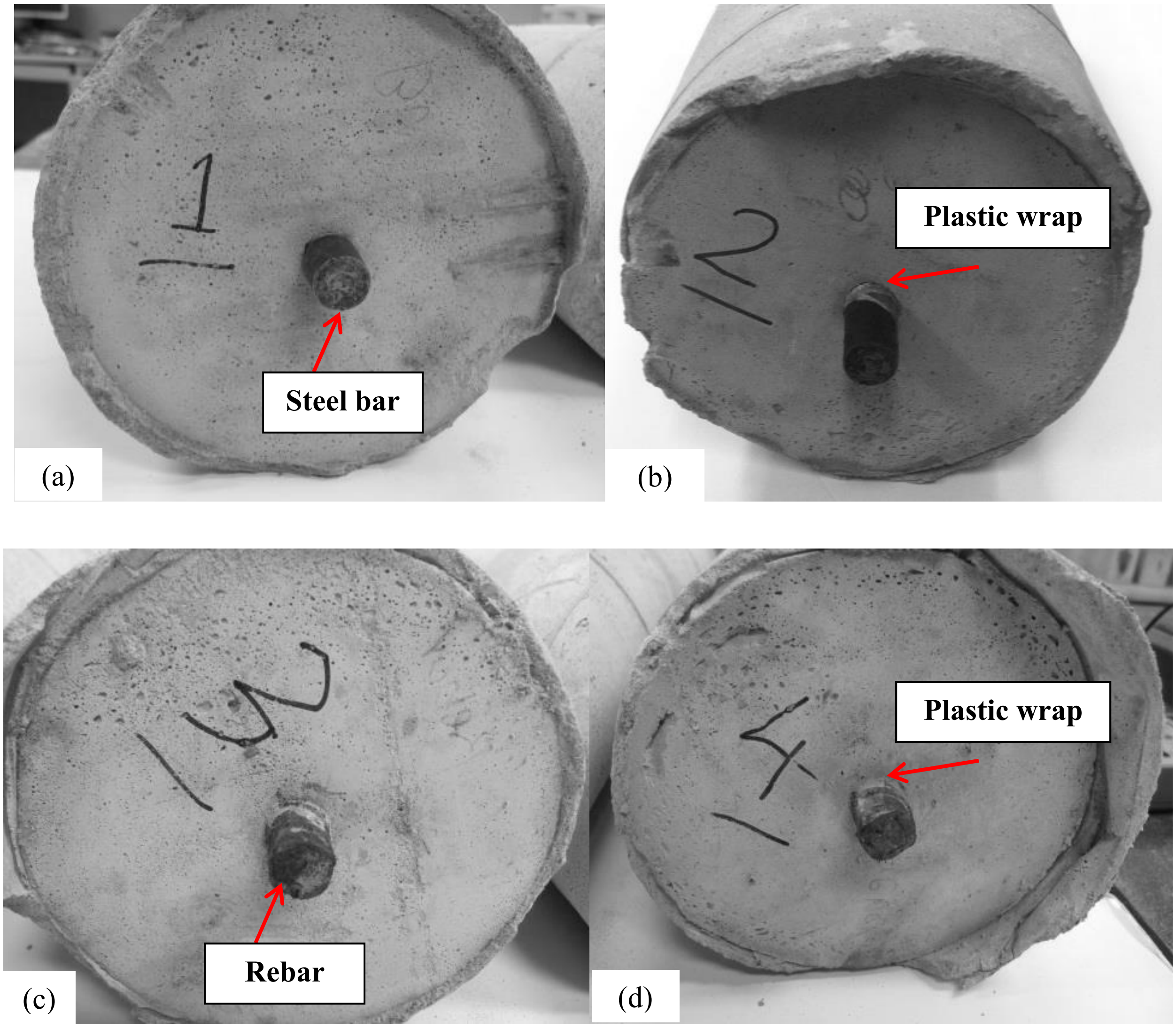

Figure 5.4. Reinforced mortar cylinders. (a). Perfectly bonded bar. (b). de-bonded bar with plastic wrap. (c). Perfectly bonded rebar. (d). de-bonded rebar with plastic wrap.

5.3.3. Experimental setup

In this study a 1 MHz piezoelectric transducer (Panametrics V102, 1-inch diameter) was selected as a transmitter to generate mechanical waves in the specimen. The excitation pulse was generated by a pulse generator (Panametric Pulser Receiver Model 5052PR). A constant pressure was applied to the back of the transducer using a load cell (Model 20210-100, 445N). Having a constant load is critical to avoid weak coupling and to transmit constant energy from the transmitter to the specimen. The load cell output was monitored with the digital multi-meter to measure the pressure applied on the transducers. For each test, a sample was equipped at one end by the transducer on the frame equipped with the load cell. Vacuum grease was used as an ultrasonic couplant between the transducer and the specimen. A constant pressure of approximately 100 kPa was maintained in all tests to improve the repeatability of the results. A laser vibrometer (Polytec Inc.) was used to capture signals at the end of rebar/bar. Figure 5.5 presents the experimental setup which was used for the reinforced mortar cylinder specimens. The same setup was prepared for calibration of piezoelectric transducers and reinforcements before casting to mortar cylinders.

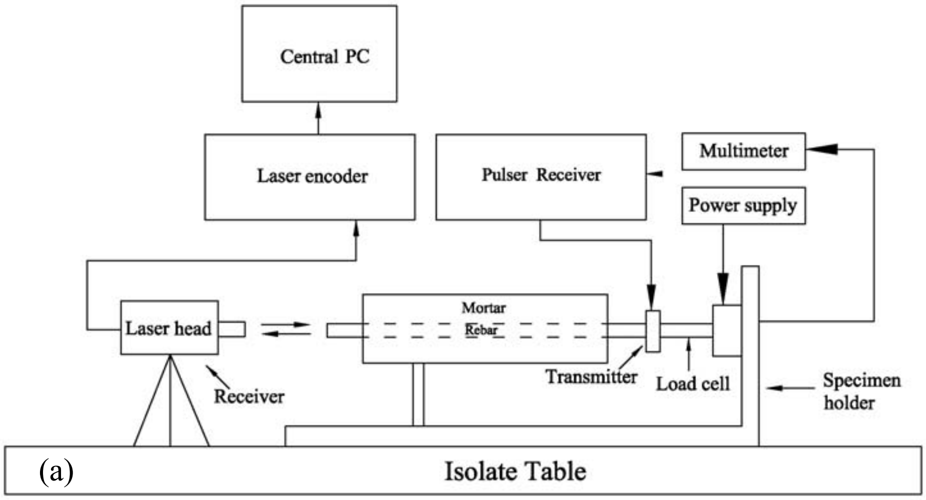

Figure 5.5. Schematic drawing of experimental setup.

5.3.4. Transducer calibration

In order to calibrate the transducer response and model it numerically, an X-ray image was captured from the transducer. An X-ray computed tomography device (Phoenix Nanomex, 2D X-ray inspection - 3D computed tomography) was used to take an X-ray image (Figure 5.6(a)). By using the X-ray image, a transducer schematic was drawn (Figure 5.6(b)). Correct dimensions of the transducer parts play a key role for the numerical model; however, these were not supplied by the transducer supply company (Figure 5.6(b)).

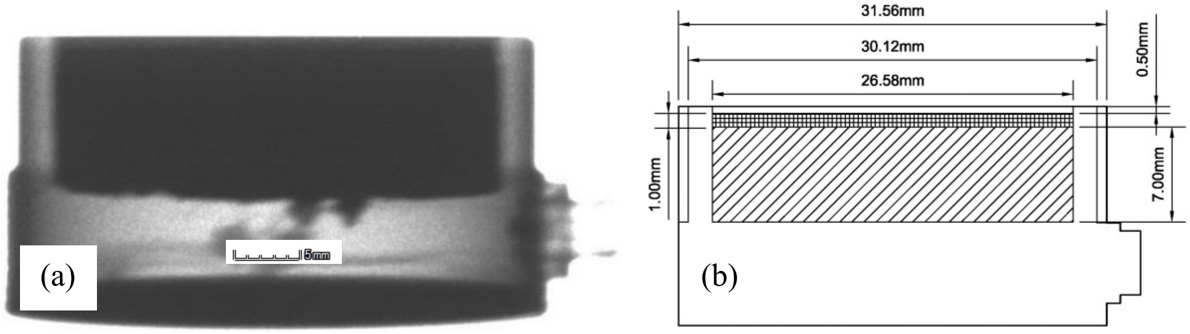

Figure 5.6. Piezoelectric transducer used in the tests (a). X-ray image. (b). Schematic picture with dimensions.

Real dimensions of the piezoelectric transducer are needed to form a more realistic numerical model (this simulation will be explained in the numerical simulation section of this study). The actual displacement at the top of the transducer was measured using a laser vibrometer head (Polytec OFV-534). The laser head covered an area of 400 mm^2 of the transducer's surface by scanning 441 points; the spacing between each point was 1.00 mm. The scanning area was covered by using a motion controller (PI micos-SMC corvus eco). The transducer was placed on a moving stage to move point by point under the control of the automatic motion controller.

Figure 5.7(a) shows a displacement time signal of the piezoelectric transducer calibration test with the laser vibrometer at the center point of the transducer. Figure 5.7(b) shows the minimum displacement of the whole transducer surface area. Each signal is a result of averaging 3000 readings to decrease the noise effect. While the increment of scanning was 1.00 mm, the gridding increment was 0.1 mm as shown in Figure 5.7(b).

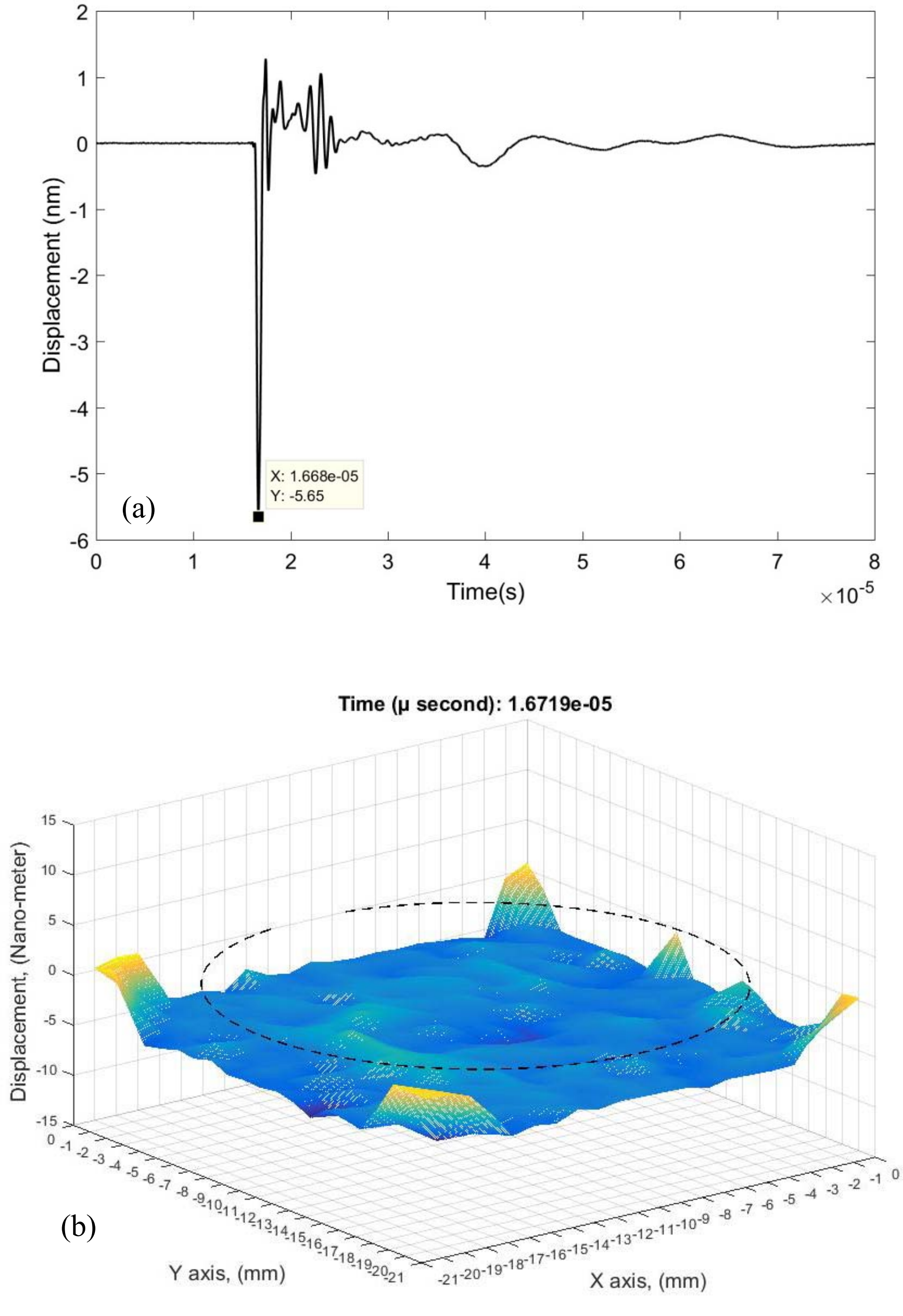

Figure 5.7. Piezoelectric transducer calibration test results from the laser vibrometer. (a). Single time signal from the center of the transducer surface. (b). Surface displacement of matching layer surface at the minimum point.

Voltage, displacement, and velocity time signals (121 signals for each) from the center of the transducer (121 mm^2) were measured using a laser vibrometer. Figure 5.8 presents the average displacement time signal as a center curve. The two curves above and below the center curve represent average plus and minus one standard deviation respectively.

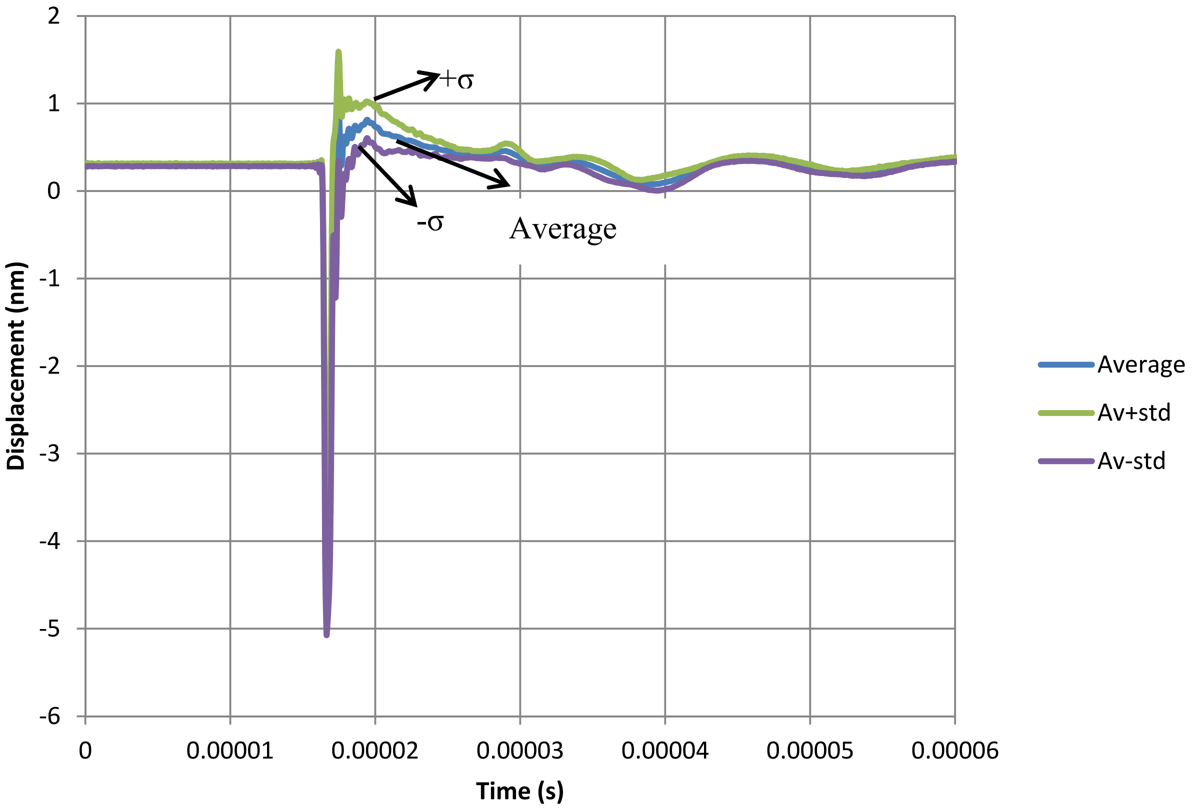

Figure 5.8. Displacement time signals from the laser vibrometer (Average of 121 points from the center).

In order to evaluate the calibration test results from the laser vibrometer, the average value of time signals from the laser test was compared to the output signal from the receiver resulting from the face-to-face test. Two transducers (Panametrics V102, 1 inch diameter) were contacted through their faces by using vacuum grease and a constant weight of 36 kN applied with the load cell at the back of the transmitter. Based on the face-to-face calibration test with the load cell (Figures 5.9(a) and 5.9(b)), the voltage peak-to-peak value was constant after a 25 kN load.

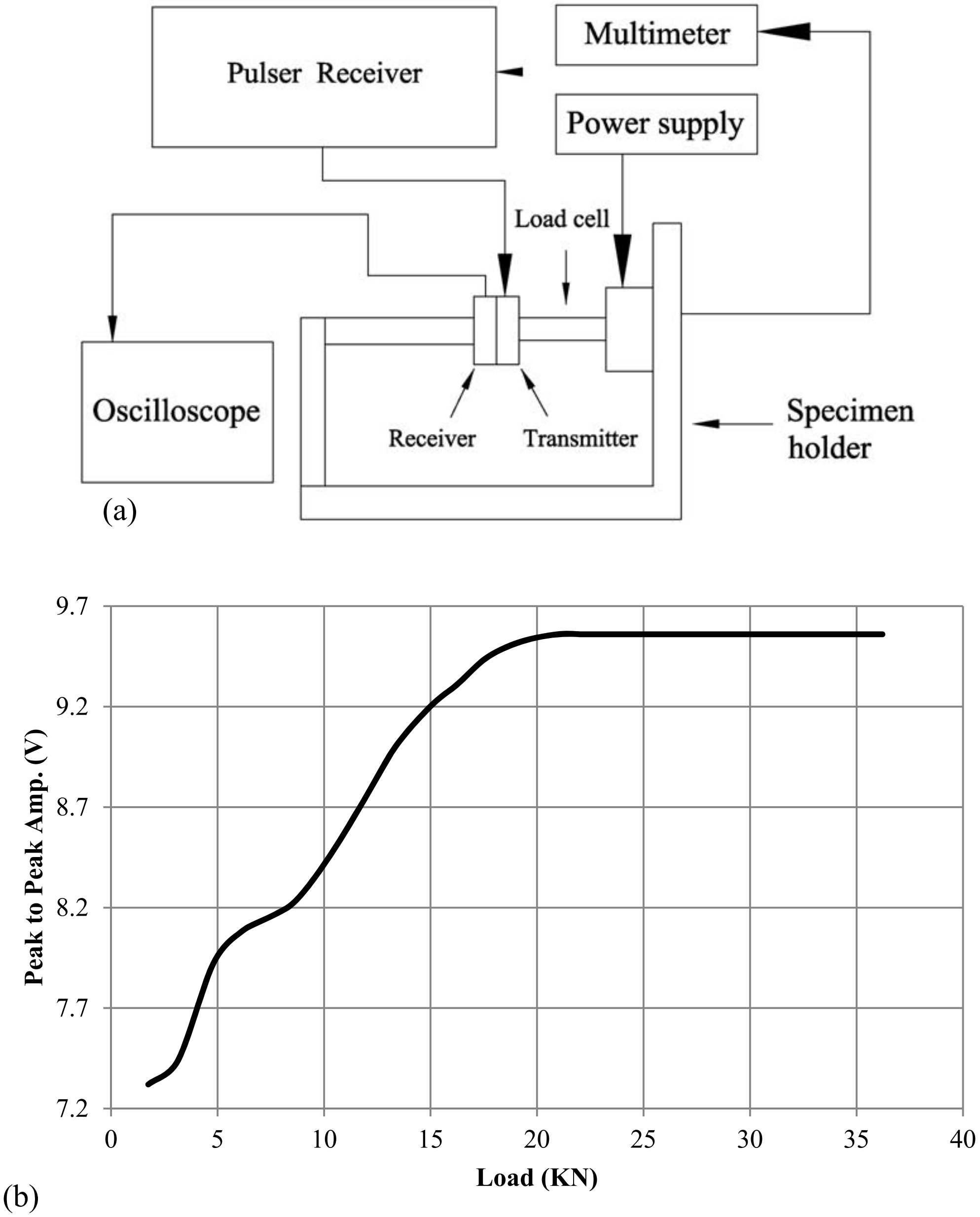

Figure 5.9. (a). Face-to-face calibration Schematic. (b). Load cell calibration result.

In order to properly calibrate the experimental test result from the receiver, three averaged time signals from the laser test (displacement and velocity) were compared to the face-to-face test results (voltage). To have a reasonable comparison, zero offset was done for all time signals as well as normalization to their maximum values. Figures 5.10(a) and 5.10(b) present averaged time signals from the laser test for displacement and velocity respectively, and Figure 5.10(c) shows the voltage time signal result from the face-to-face test.

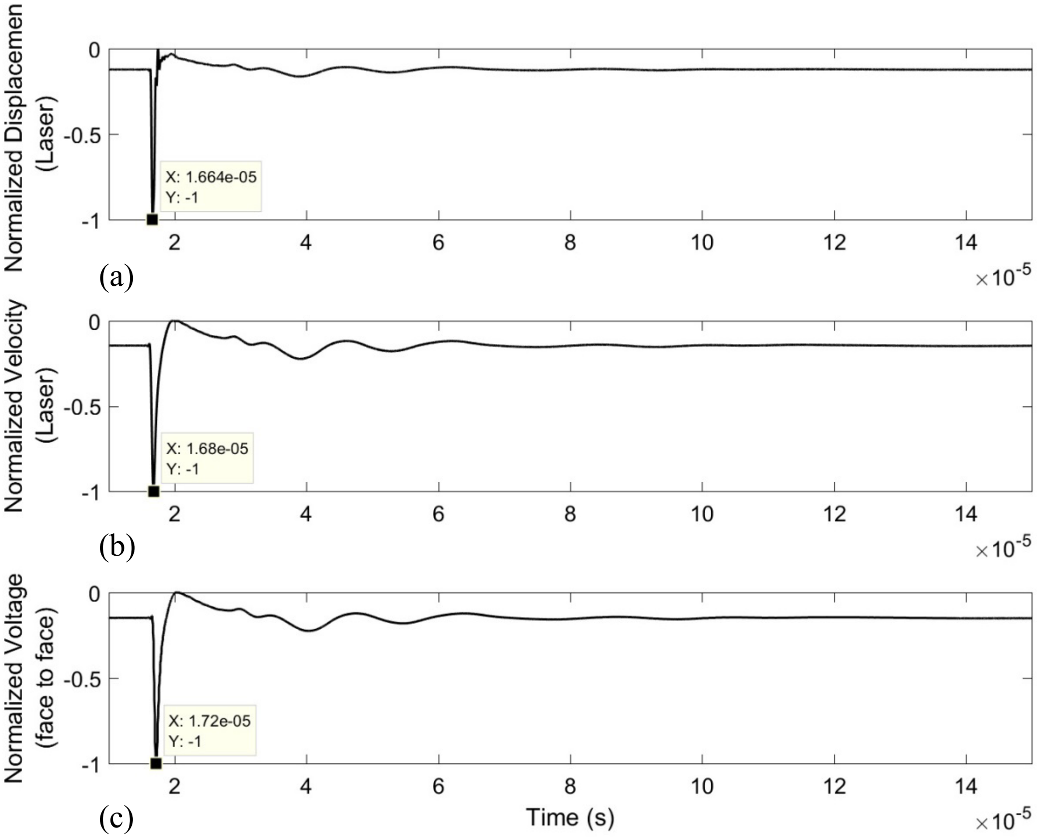

Figure 5.10. Time signals. (a). Normalized average displacement from laser vibrometer. (b). Normalized average velocity from laser vibrometer. (c). Normalized average voltage from face-to-face test.

A comparison of displacement and velocity signals (Figures 5.10(a) and 5.10(b)) from the laser test shows that there is only a small difference. Also, the voltage signal from the face-to-face test (Figure 5.10(c)) shows a slight difference from displacement and velocity signals. Minimum peak for displacement, velocity, and voltage signals occurred at 1.66×10^{-5} second, 1.68×10^{-5} second, and 1.67×10^{-5} second respectively. In the case of the face-to-face test, the generated pulse from the transmitter should travel from the wearing plate of the transmitter and then pass through the space between the transmitter and the receiver, again traveling from the wearing plate of the receiver and finally reaching the piezo crystal of the receiver. The piezo crystal transforms the receiving mechanical pulse to a voltage. Instead, with the laser vibrometer, the actual displacement pulse is captured by the laser light. This may be the main reason for the difference between the transducer signal and the laser vibrometer.

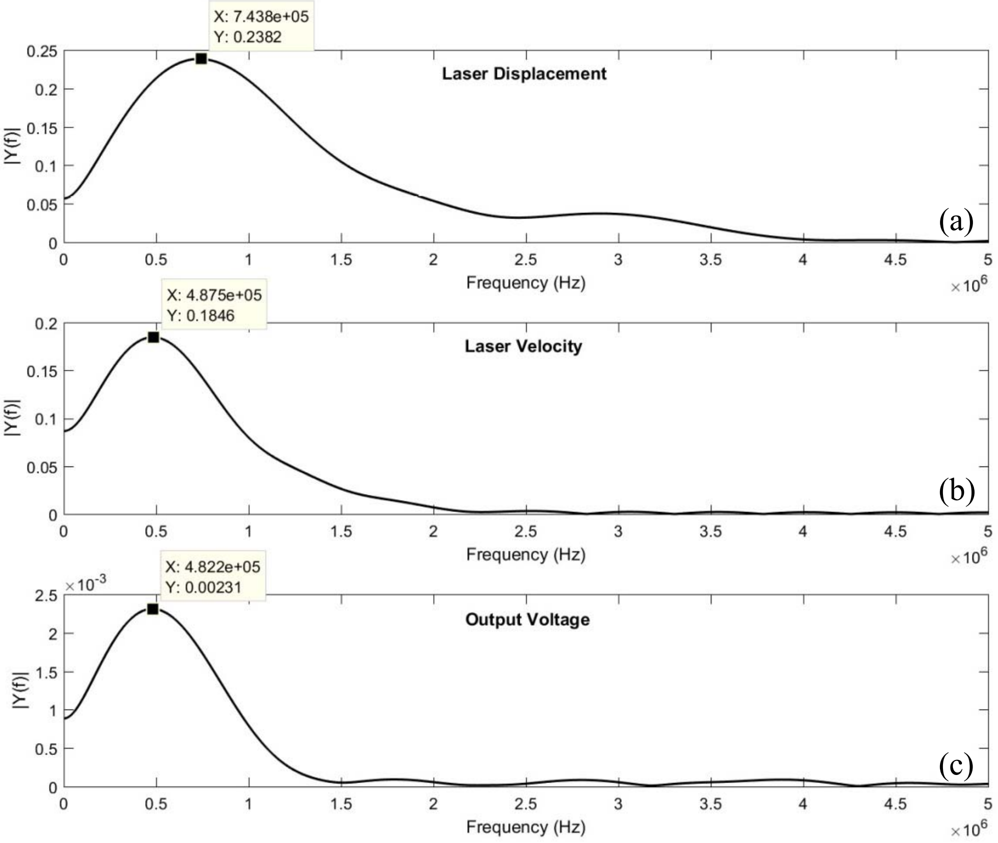

Figure 5.11. Frequency analysis of: (a). Displacement. (b). Velocity (from laser vibrometer test). (c). Voltage from face-to-face test.

Frequency analyses of time signals (Figure 5.10) are presented in Figure 5.11. As shown in Figure 5.11(a), the closest frequency to the transducer frequency is obtained from a Fourier transform of the displacement time signal (almost 743 kHz). The main frequency deduced peaks from the velocity signal and voltage signal are almost 493 kHz and 671 kHz, respectively.

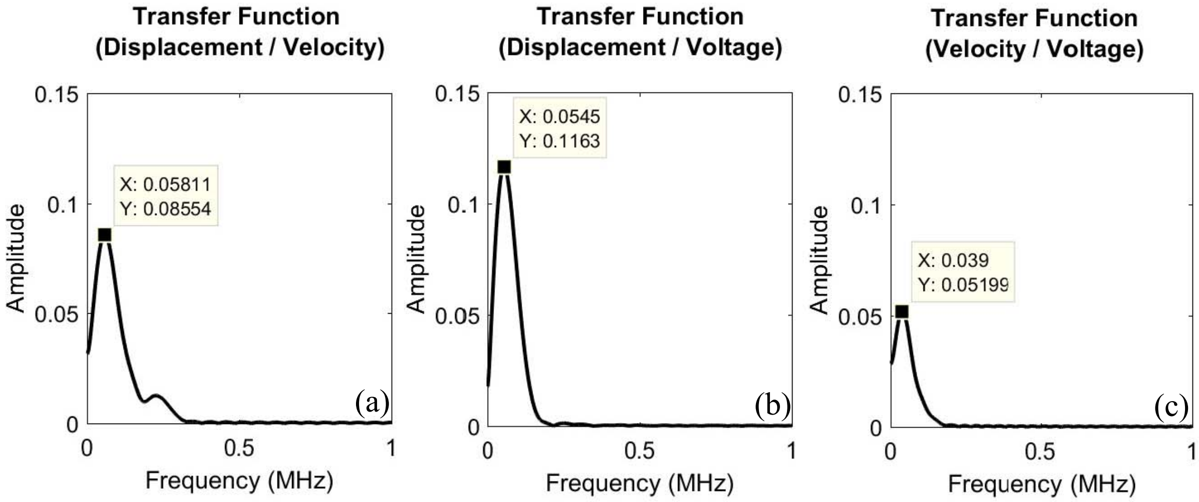

Figure 5.12. Transfer functions of Fourier transform. (a). Displacement over Velocity. (b). Displacement over Voltage. (c). Velocity over Voltage.

Figure 5.12 shows the transfer functions of the Fourier transform of displacement over velocity, displacement over voltage, and velocity over voltage. Although transfer function results do not show a good match between these three types of time signals (displacement, velocity, and voltage), the transfer function of the Fourier transform of the displacement time signal over voltage shows a higher peak value (0.1163 magnitude).

The piezoelectric transducers (PZT) did not have a calibrated response. The actual displacement of the piezoelectric transducer was measured for the first time and compared to the velocity and voltage time signals. The PZT response includes the transfer function of the transmitter (H_T) plus coupling (H_C) plus receiver (H_R), whereas the captured displacement time signal from the laser vibrometer is only the transfer function of the transmitter (H_T).

5.4. Numerical Simulation

A discrete finite element method was used to simulate the piezoelectric transducer [105]. Three physics interfaces were used in this simulation: Solid Mechanics, Electrostatics, and Electrical Circuit. Electrostatics and Electrical Circuit interfaces were used to generate the same input voltage to the transducer, and the Solid Mechanics interface was used to transfer the mechanical load from the piezo crystal to the matching layer and finally the reinforcement.

5.4.1. Transducer simulation

Analyzing the piezoelectric transducer was the first step of simulation. Table 5.1 and Table 5.2 present the information about the piezoelectric transducer which was used in the simulation. The geometry of the transducer was defined based on an X-ray image (Figure 5.6(a)).

Table 5.1. Piezoelectric transducer information.

	Thickness (mm)	Diameter (mm)	Type of Material	Density* (kg/m^3)	Young's Modulus* (Pa)	Poisson's ratio*
Piezoelectric crystal	1.2	14.29	PZT-5A	7750	7.4×10^{10}	0.35
Matching layer	0.6	14.29	Aluminum	2700	70×10^{9}	0.33
Backing Material	7	14.29	P-silicon	2320	160×10^{9}	0.22

*. Ref: [105]

Table 5.2. Piezoelectric and elastic matrix parameters.

Elastic constant* (GPa)	C_{11}=120, C_{12}=75, C_{13}=75, C_{33}=111, C_{44}=21, C_{66}=23
Piezoelectric constant* (C/m^2)	e_{31}=-5.35, e_{33}=15.78, e_{15}=12.29
Relative permittivity**	$\epsilon_{11}^S/\epsilon_0$=919.1, $\epsilon_{22}^S/\epsilon_0$=919.1, $\epsilon_{33}^S/\epsilon_0$=926.6

* Values obtained by trial and error for best curve fitting.

** $\epsilon_0 = 8.85\times10^{-12}F.m^{-1}$

To apply the same voltage source which was used in the experimental test, a pulse source type (a type of source voltage used in finite element software) was used in the numerical simulation through Electrostatic and Electrical Circuit interfaces. Different electrical circuits for the resistor and capacitor were used to simulate the input voltage as an experimental test. Figure 5.13(a) shows simulated electrical circuit to get input voltage similar to the experimental test. Figure 5.13(b) shows the input voltage source for the numerical simulation and the experiment respectively.

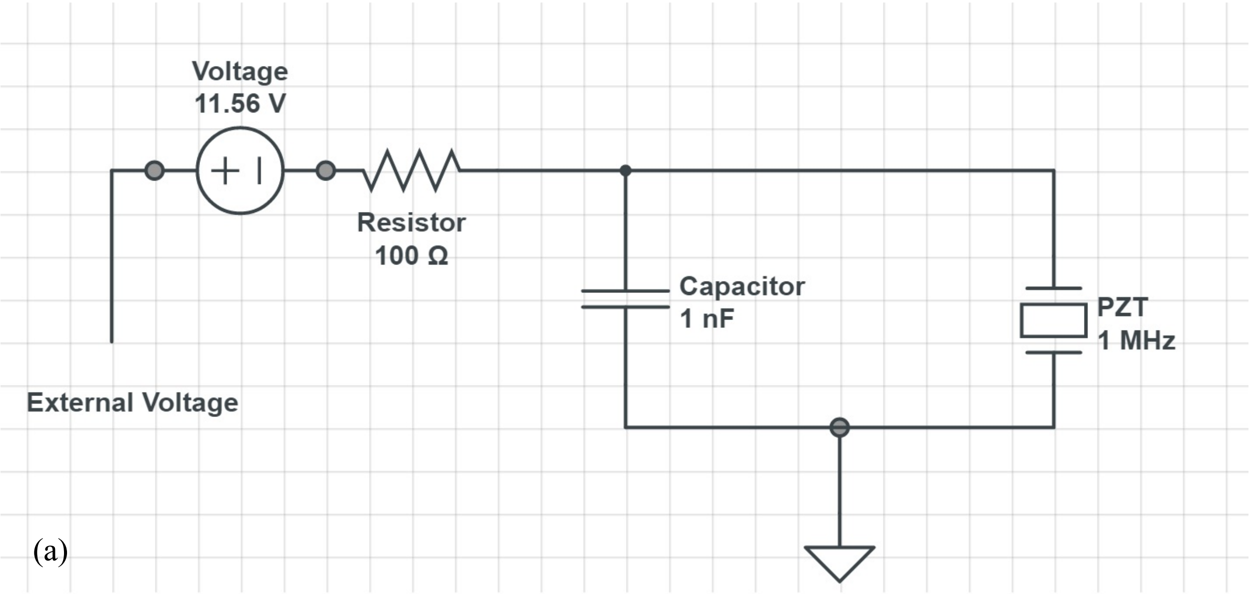

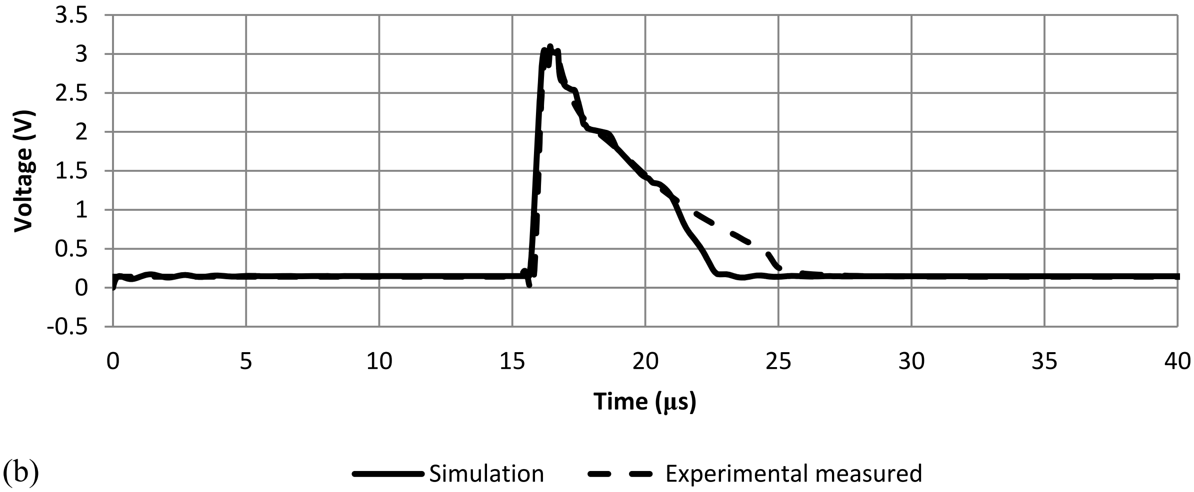

Figure 5.13. (a). Defined electrical circuit to get input voltage. (b). Simulation and experimental input voltages for transmitter.

In order to obtain a similar dynamic response of the piezoelectric transducer in the numerical simulation compared to the experimental test on the transducer, damping properties of the three elements in the piezoelectric transducer should be applied correctly [143]. Selected Rayleigh damping parameters for the piezoelectric transducer elements are presented in Table 5.3.

Table 5.3. Rayleigh damping properties of the piezoelectric transducer [144, 145, and 146].

Material	Mass damping α_{dM} (1/s)	Stiffness damping β_{dK} (s)
Piezo crystal	209440	1.1×10^{-8}
Matching layer	0	10.0×10^{-8}
Backing material	0	1.5×10^{-5}

Figure 5.14 shows the minimum displacement of the whole transducer surface area. For this simulation different mesh element sizes were used for each section of the piezoelectric transducer. Mesh element size was 0.03 mm for the matching layer, 0.04 mm for the piezo crystal, and 0.75 mm for the backing material. The mesh element size for backing material did not have an effect on the transducer dynamic response. Backing material simply absorbs part of the generated wave from the piezo crystal and does not let the wave reflect back to the piezo crystal and after that to the matching layer.

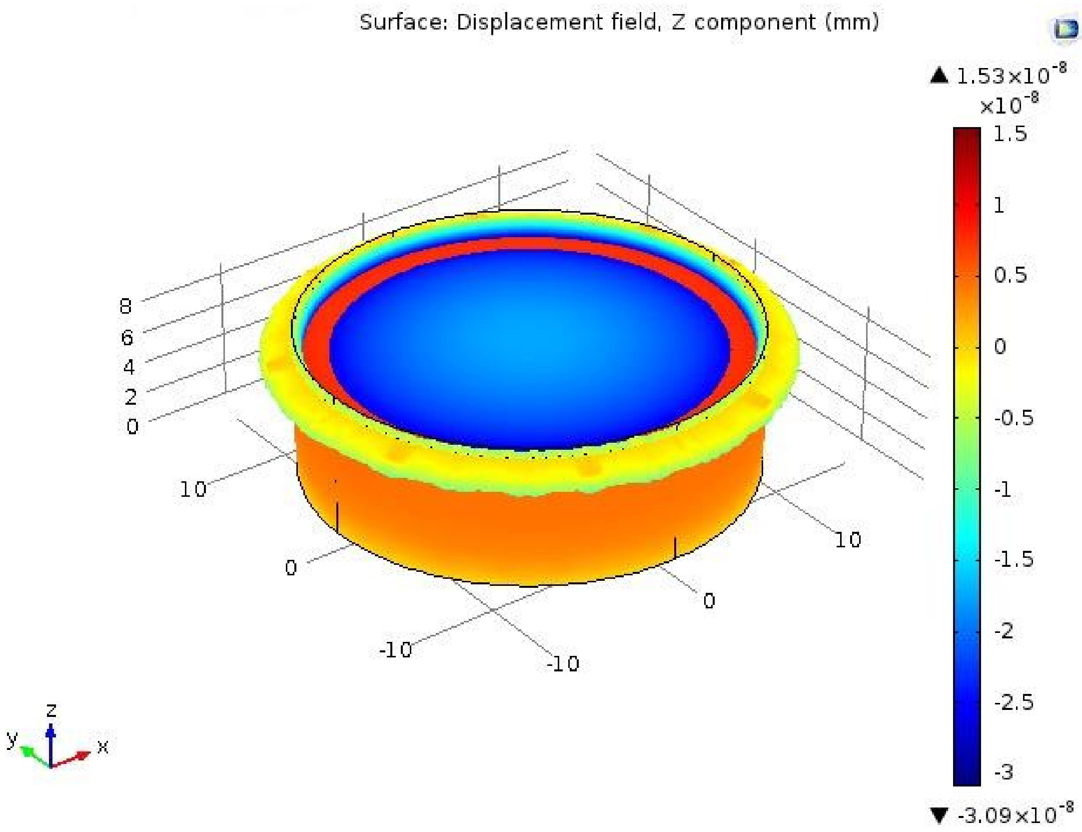

Figure 5.14. Numerical simulation of transducer. Displacement of matching layer surface at the minimum point (time 15.8750 ×10^{-5} s) (Radial displacement scale is different than geometry scale).

Figure 5.15 shows the averaged (121 points) normalized time signal of the transducer calibration experiment with the laser vibrometer (with normalization factor of 0.69) and normalized time signal of the transducer numerical simulation (with normalization factor of 0.71). The transducer simulation result shows a good correlation with the calibration test with the laser vibrometer for the first peak. There is a low frequency wave after the first peak in the experimental test. This could be the result of the presence of the polymer foam upon which the transducer was settled during the experimental test.

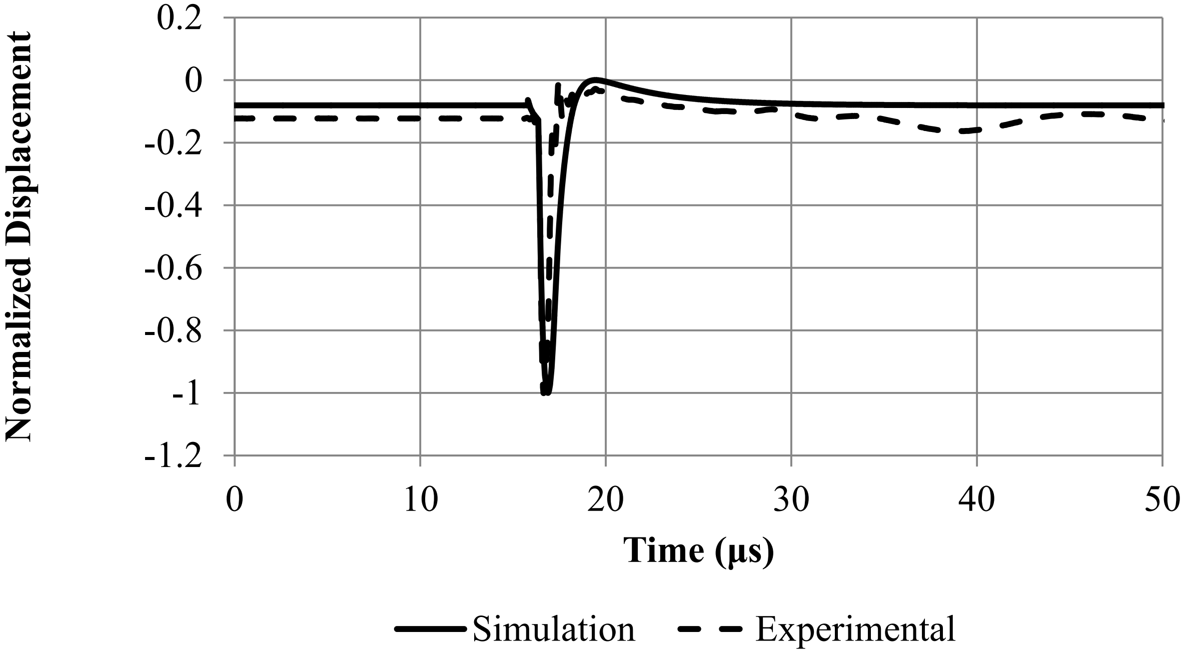

Figure 5.15. Piezoelectric simulation and experimental results.

5.4.2. Reinforced mortar simulation

The finite element method was used for numerical simulation of elastic wave propagation [150]. Mesh element sizes were chosen to be greater than 20 nodes per wavelength to represent wave propagation accurately [147].

$$l_e = \frac{\lambda_{\min}}{20} \tag{6.5}$$

Where l_e is the minimum element mesh size and $\lambda_{\min}$ is the shortest wavelength. Sampling frequency was selected based on experimental test values with the laser Vibrometer which were 25.6 MHz. Total time in this simulation was also similar to the experimental test (T = 0.00128 s).

Free boundary conditions were applied to all edges while the specimen was fixed to avoid free body motion. The bonding between mortar and bar was assumed to be a perfect contact for the "perfectly bonded" test specimen. For de-bonded samples, 0.1 mm spacing was applied to the model with air as the material in this space. The excitation was applied by the piezoelectric transducer which was previously studied and simulated (Section 6.4). Displacement signals in the Z direction were extracted at the end of the bar, as with the experimental test.

Figures 5.16(a) and 5.16(b) show wave propagation simulation results in perfectly bonded and de-bonded specimens respectively. Generated waves from the transducer propagate first through the small section of the free bar and then reach the anchorage location in the mortar block. From here, part of the wave leaks to the mortar and part of the wave is propagated through the remaining part of the bar. It is clear from the third snapshot of the simulation which waves are propagating in the mortar and which in the bar. The arrival wave at the end of the bar is shown in the next picture. It is clear that the wave energy is not as strong as when it was first generated at the other end.

(a.1)

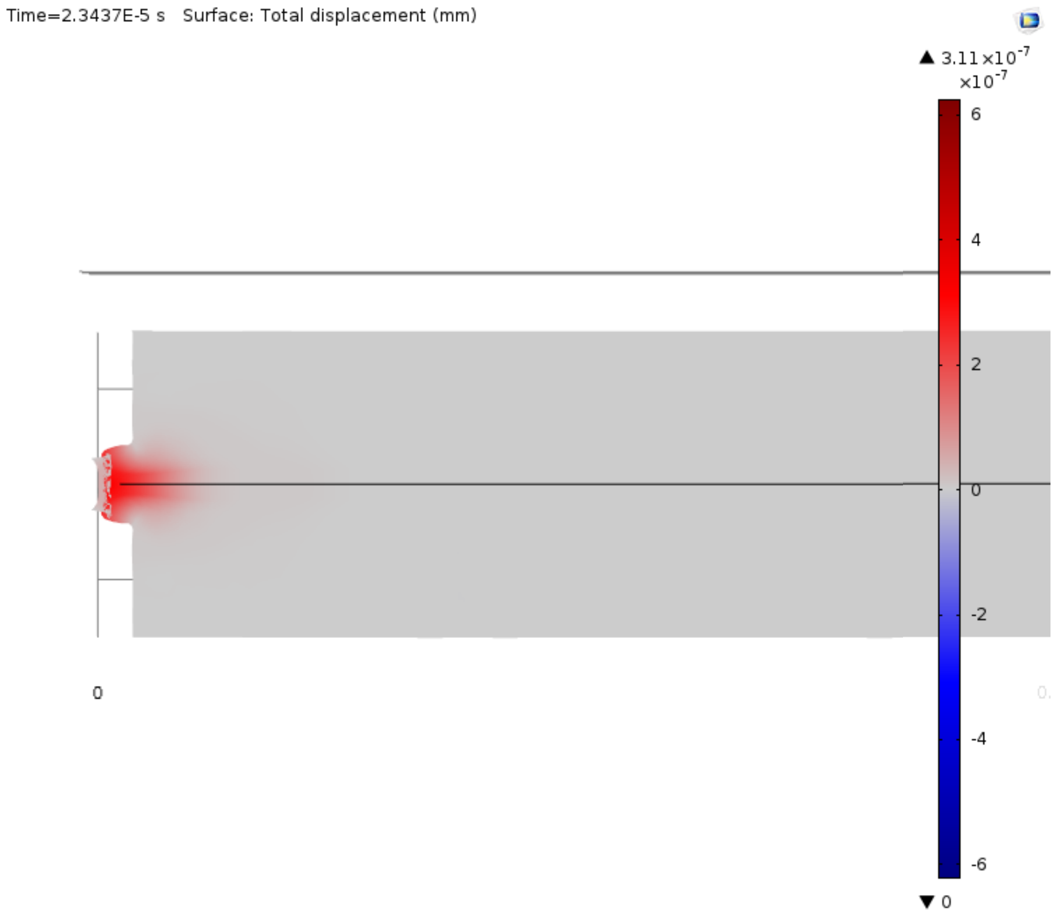

(a.2)

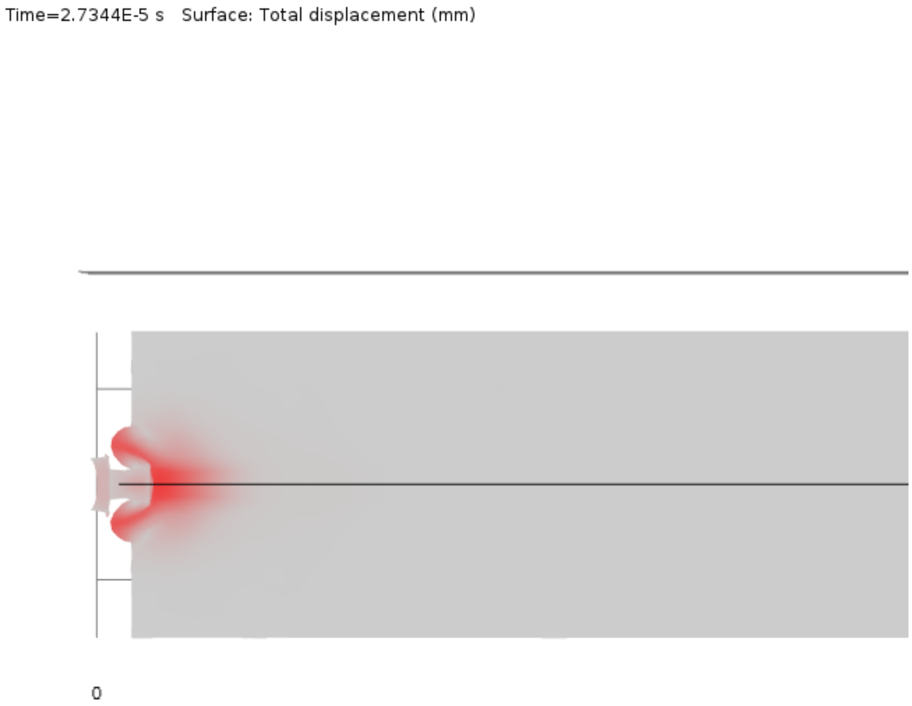
Time=2.7344E-5 s Surface: Total displacement (mm)
0

(a.3)

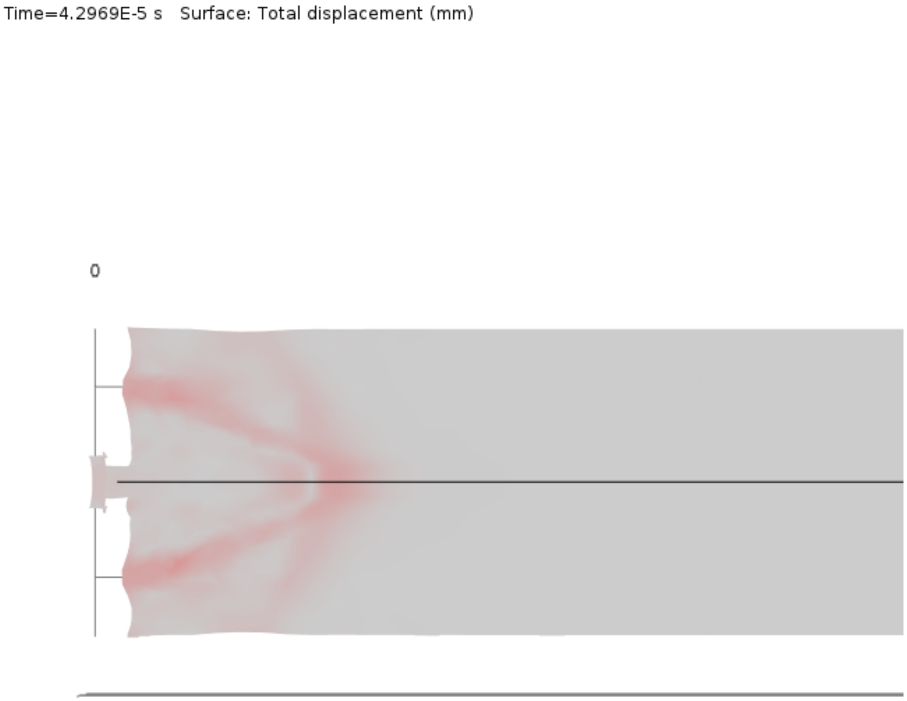
Time=4.2969E-5 s Surface: Total displacement (mm)
0

(a.4)

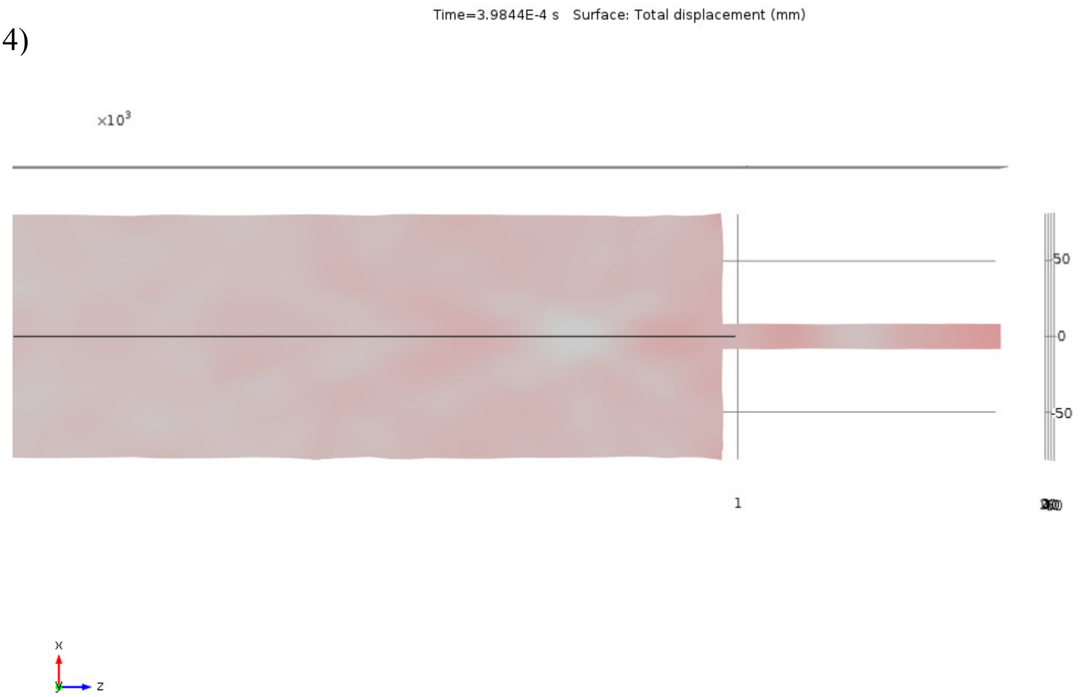
Time=3.9844E-4 s Surface: Total displacement (mm)
×10^3
50
0
-50
1
x
y
z

(b.1)

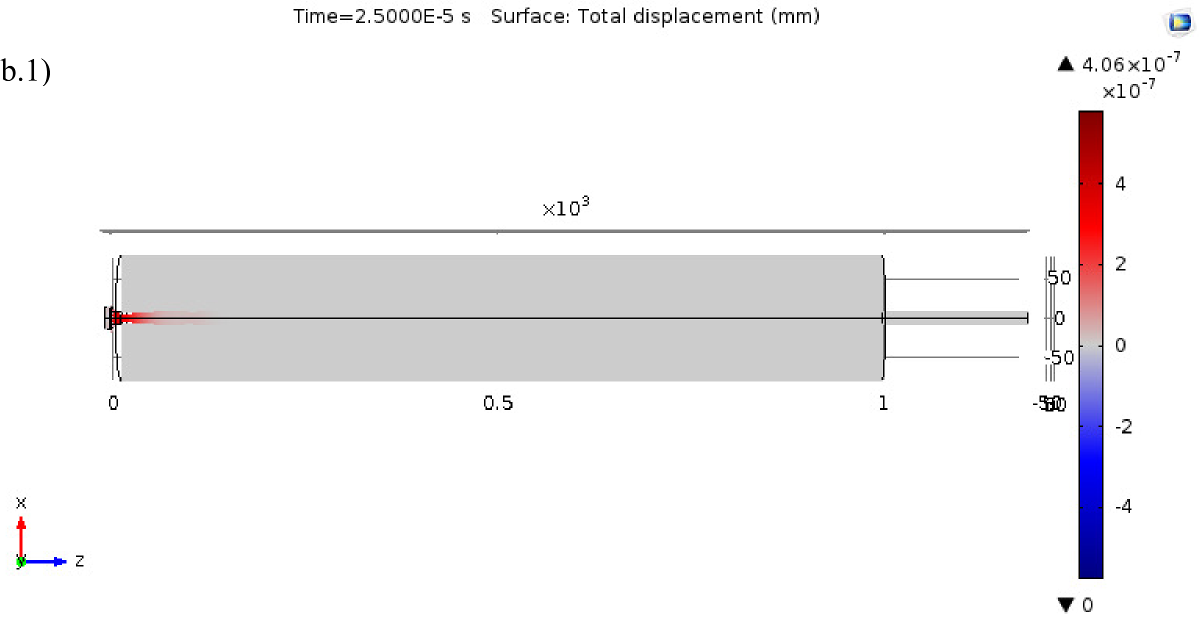
Time=2.5000E-5 s Surface: Total displacement (mm)
▲ 4.06×10^{-7}
×10^{-7}
4
2
0
-2
-4
▼ 0
×10^3
50
0
-50
0
0.5
1
x
y
z

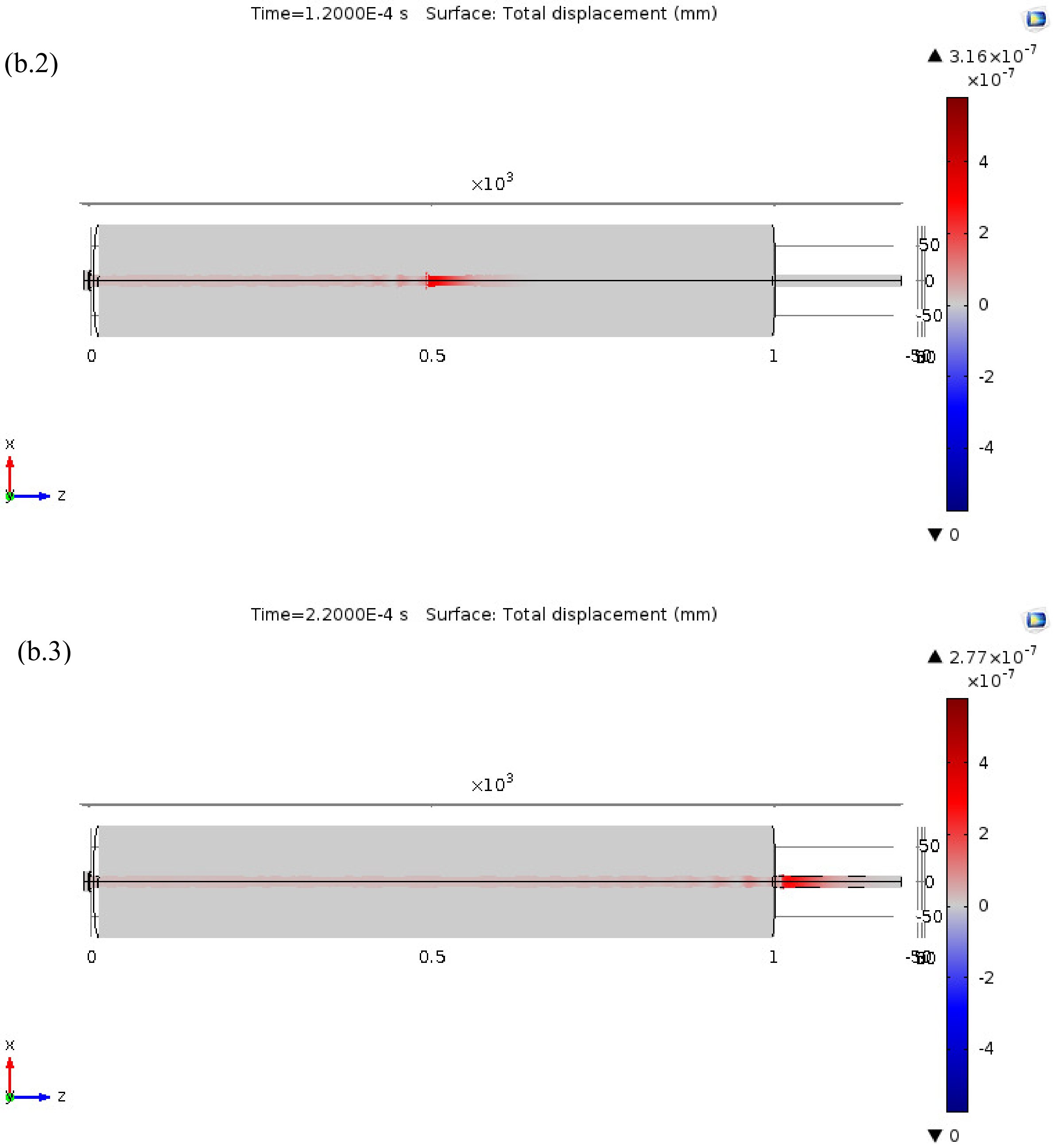

Figure 5.16. Simulation result of wave propagation through the reinforced mortar cylinder. (a). Perfectly bonded sample. (b). De-bonded sample.

Figure 5.16(b).1 shows a generated wave from the piezoelectric transducer for the de-bonded mortar cylinder. The generated wave propagates through the bar without leakage to the mortar. There is no clear sign of wave refraction to the mortar in Figure 5.16(b).2. Figure 5.16(b).3 shows the first arrival at the end of the bar. The wave has amplitude more than five times larger than the arrival wave at the end of the bar in the perfectly bonded sample, showing the large leakage effect. Wave reflection arrived at the source location at 0.465 ms. Arrival times correspond to a compressional wave velocity of bar ($V_p \approx 5480$ m/s).

The difference between the perfectly bonded and the de-bonded bar is because of the leaked energy from the bar to the mortar in a perfectly bonded sample; however, in a de-bonded sample, the energy remains in the bar, as was expected (Figures 5.16(a) and 5.16(b)).

To verify the numerical simulation of wave propagation though the bar, the dispersion curve of surface waves from the numerical simulation was compared with the dispersion curve obtained from the theoretical model. Displacements from the side of the bar in the Y direction were extracted, and a F-K plot was calculated from the time signals, then dispersion curves were extracted from the F-K plot. Also, the theoretical dispersion curves were calculated using Eq. 5.1. Figure 5.17 presents dispersion curves from the theoretical model and the numerical simulation.

Dispersion curves from the numerical simulation have a good correlation with the theoretical model. The difference between the dispersion curves from the numerical simulation and the theoretical model may be the result of simplifications in both methods.

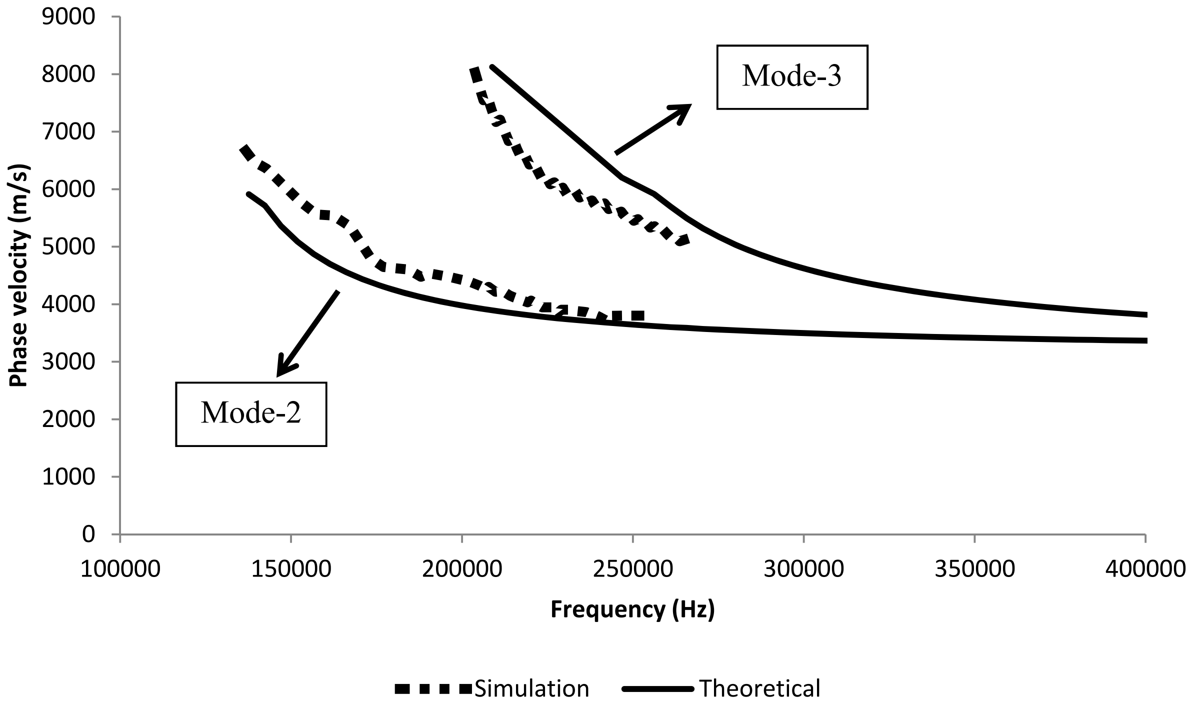

Figure 5.17. Dispersion curves from the numerical simulation and the theoretical model (Eq.5.1).

5.5. Experimental results

Experimental results for four reinforced mortar samples are presented here. Two mortar cylinders were embedded with steel bars in which one was perfectly bonded and one was de-bonded (Figures 5.4(a) and 5.4(b)). Also, two mortar cylinders were embedded with rebars in which one was perfectly bonded and one was de-bonded (Figures 5.4(c) and 5.4(d)). Figure 5.18 shows four snapshots of the three-dimensional movement of time signals at the end of the bar in sample 1 (perfectly bonded). Four differently shaped modes of wave propagation are presented in this figure. First, the compressional wave reaches the end of the bar (Figure 6.18(a)), and after that there is arrival of a longitudinal mode of surface wave (Figure 5.18(b)). Finally, flexural mode of wave propagation starts which is also associated with compression wave (Figure 5.18(c)) followed by a complete flexural mode at the end (Figure 5.18(d)). In this case the compressional wave and longitudinal mode of surface wave are the main types of wave propagation in a perfectly bonded bar.

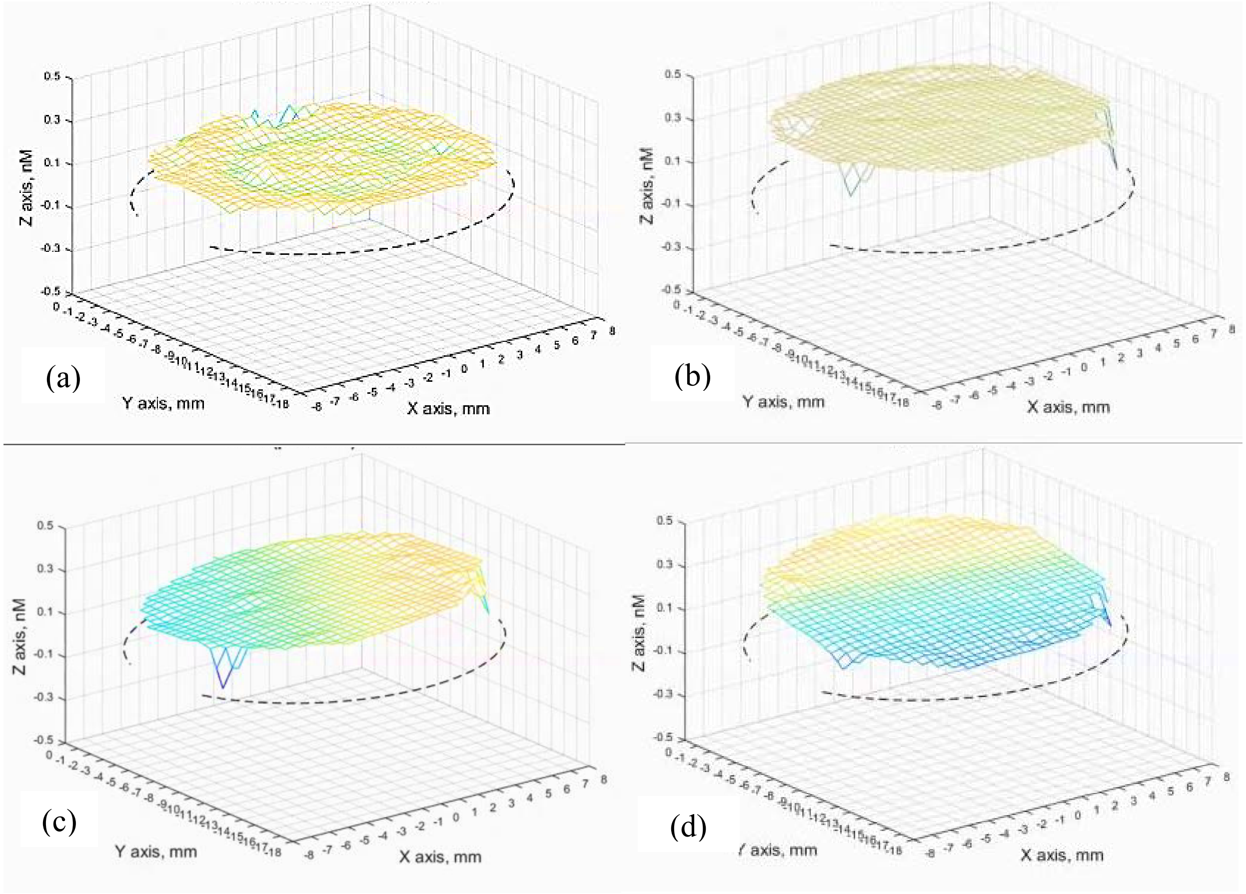

Figure 5.18. Mode shapes of wave propagation at the end of bar for sample 1. (a). Compressional wave. (b). Longitudinal wave. (c). Flexural mode. (d). Flexural mode.

Figure 5.19 shows four snapshots of three-dimensional movements of time signals on the surface of the de-bonded bar embedded in mortar cylinder (sample 2). As can be seen in Figure 5.19(a), the first arrival wave is a compressional wave which has higher amplitude than in sample 1. The longitudinal mode of the surface wave is associated with the first arrival wave. This can be seen clearly in Figure 5.19(b) when the compressional wave goes below zero. Figure 5.19(c) shows the flexural mode of the surface wave which can be a type of anti-symmetric mode of the Lamb wave. This mode of wave propagation is apparent in Figure 5.19(d).

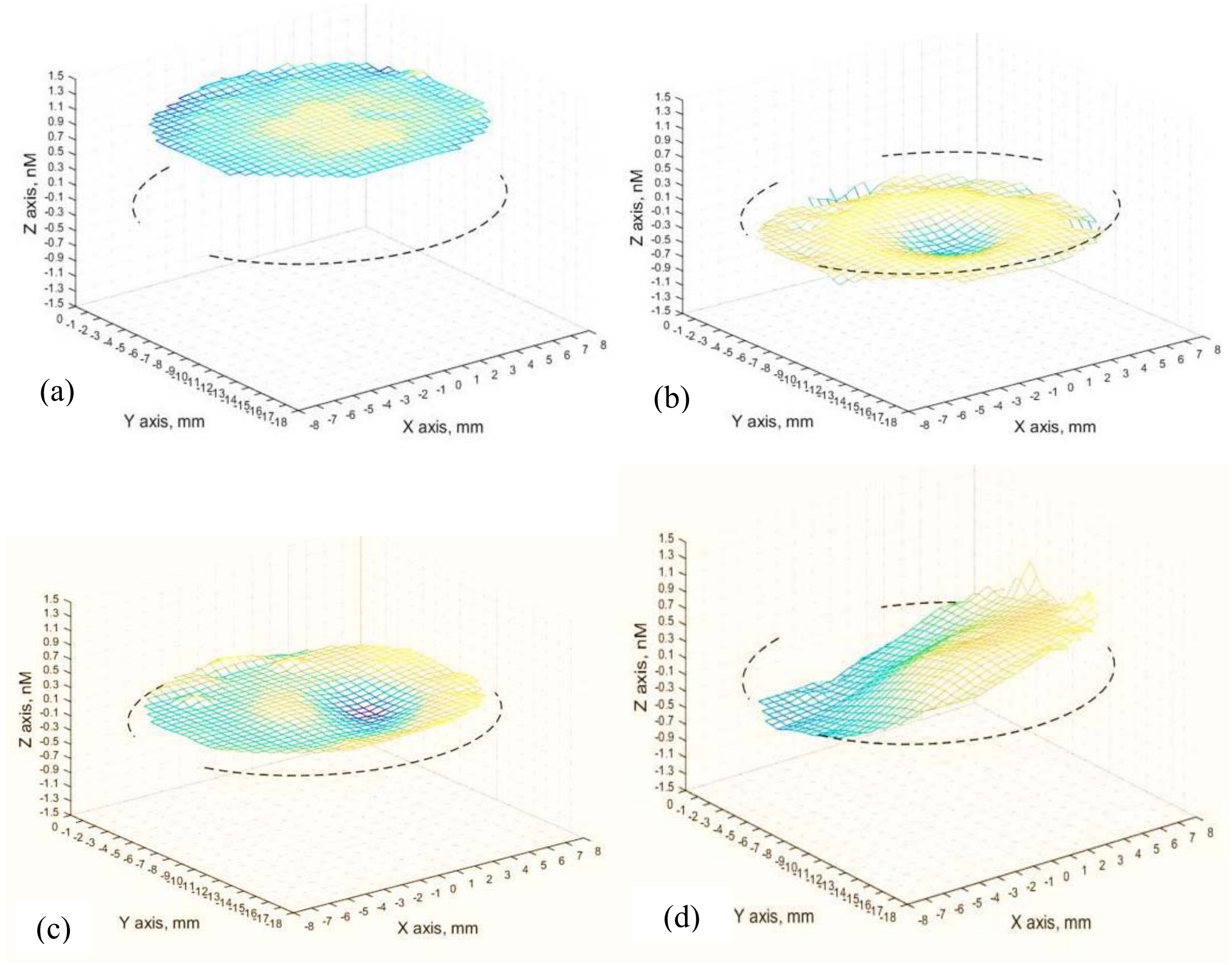

Figure 5.19. Mode shapes of wave propagation at the end of the bar for sample 2. (a). Compressional wave. (b). Longitudinal mode. (c). Flexural mode. (d). Flexural mode.

Figure 5.20 shows four snapshots of time signals from the surface of the perfectly bonded rebar (sample 3). Maximum and minimum amplitude of wave propagation in this test is almost the same as sample 1, and less than sample 2. Two different modes of wave propagation can be seen in these figures. Compressional wave is the first arrival wave which reaches the end of the rebar (Figure 5.20(a)). Following the compressional wave, the flexural mode of the surface wave arrives but it is associated with the first mode (Figures 5.20(b) and 5.20(c)). At the end, only the flexural mode is propagating through the rebar (Figure 5.20(d)).

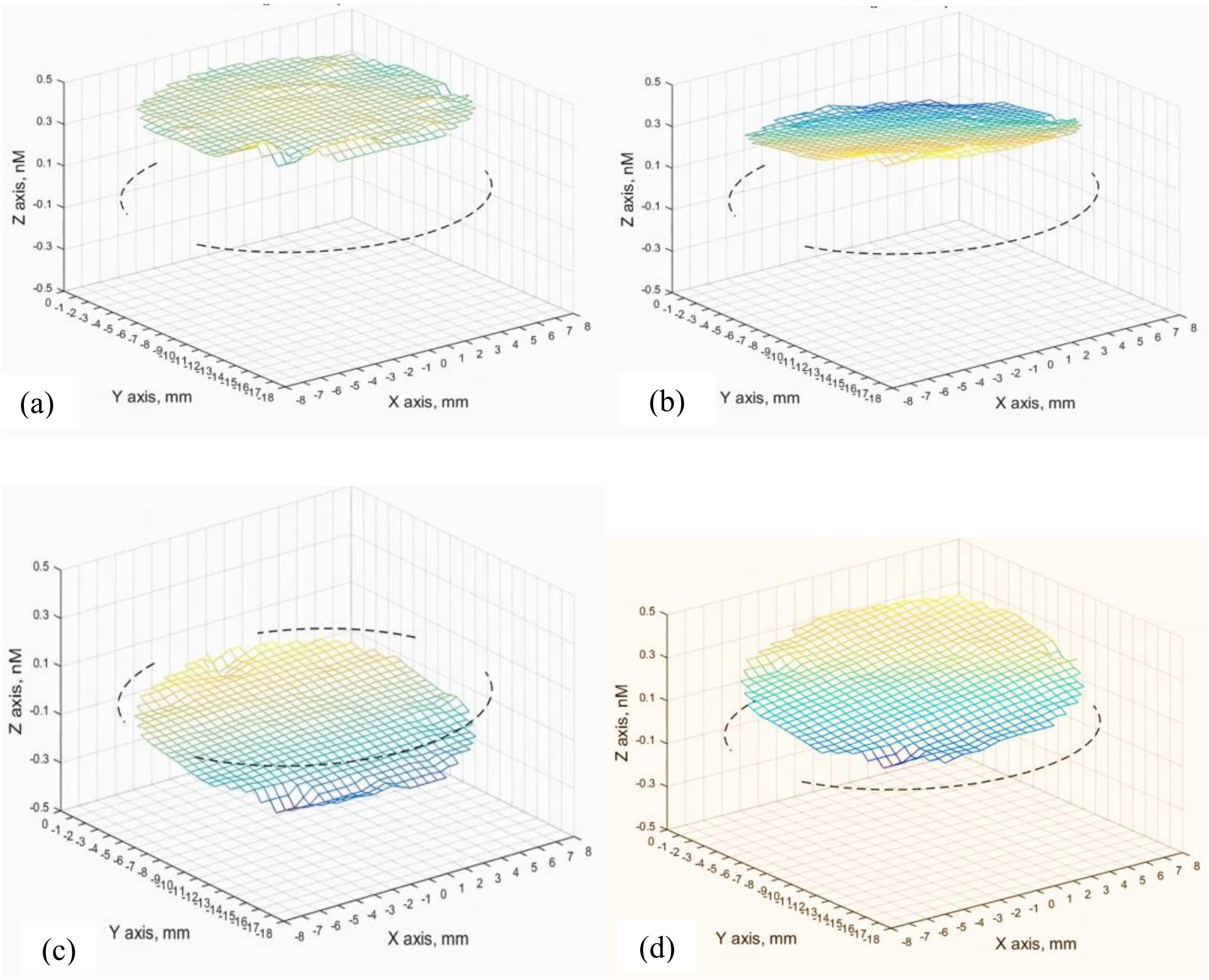

Figure 5.20. Mode shapes of wave propagation at the end of the rebar for sample 4. (a). Compressional wave. (b). Flexural mode. (c). Flexural mode. (d). Flexural mode.

Figure 5.21 shows snapshots of time signals from the end of the de-bonded rebar embedded in the mortar cylinder (sample 4). Amplitude of wave propagation modes are five times more than sample 4. The first arrival wave is the compressional wave (Figure 5.21(a)). The longitudinal mode of the surface wave appears afterwards (Figure 5.21(b)). The flexural mode of the surface wave is another type of wave propagation which appears, as seen in Figure 5.21(c). Another flexural mode of surface wave appears at the end (Figure 5.21(d)).

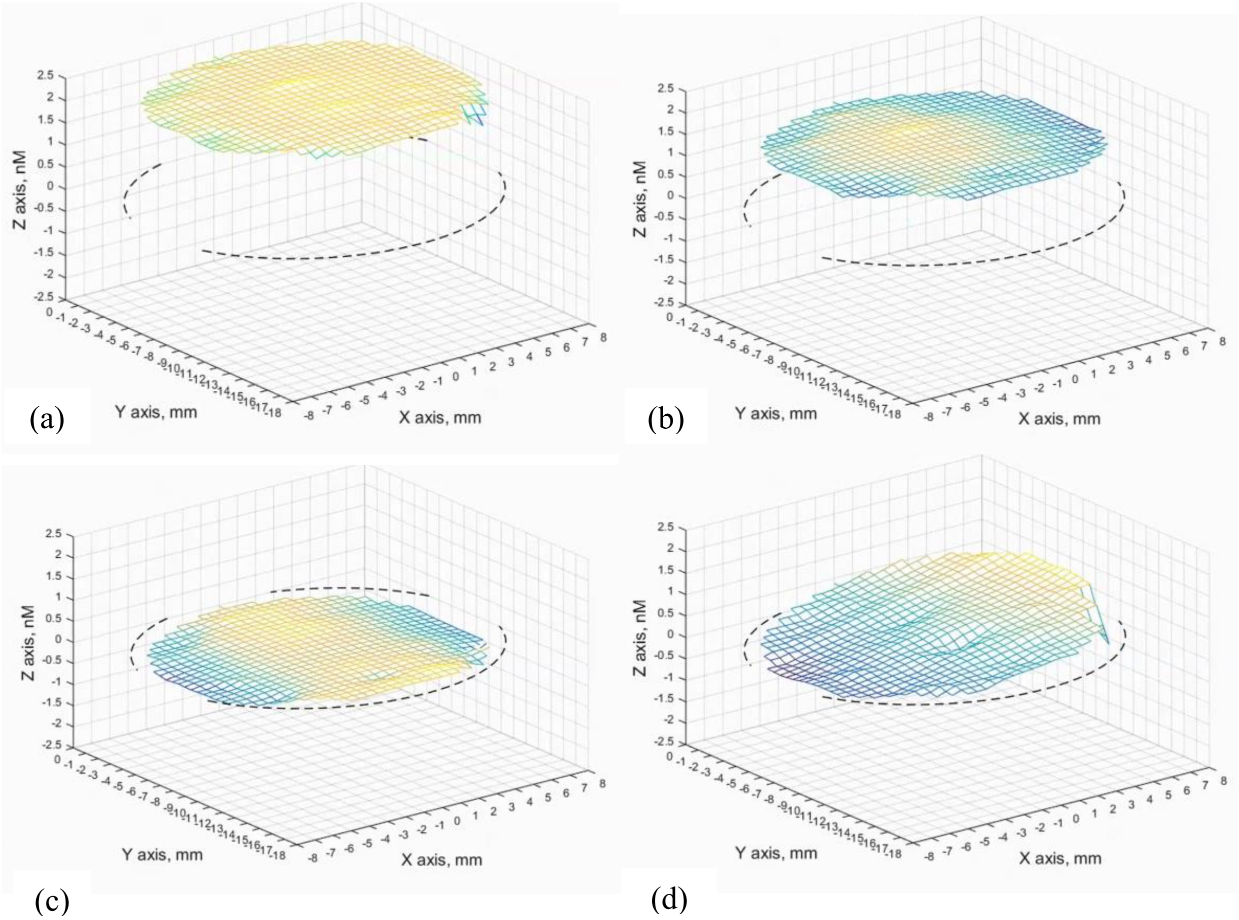

Figure 5.21. Mode shapes of wave propagation at the end of the rebar for sample 4. (a). Compressional wave. (b). Longitudinal mode. (c). Flexural mode. (d). Flexural mode.

5.5.1. Comparison of numerical and experimental results

Figure 5.22 shows the center point time signals of the experimental test for sample 1 and the numerical simulation result for sample 1. Numerical simulation shows a good correlation with the experimental test for this sample; the first arrival waves show much lower amplitude in numerical simulation compared to the experimental test time signal, but the peaks follow the same trend. The second arrivals from both time signals match well almost up to the end of the recording time.

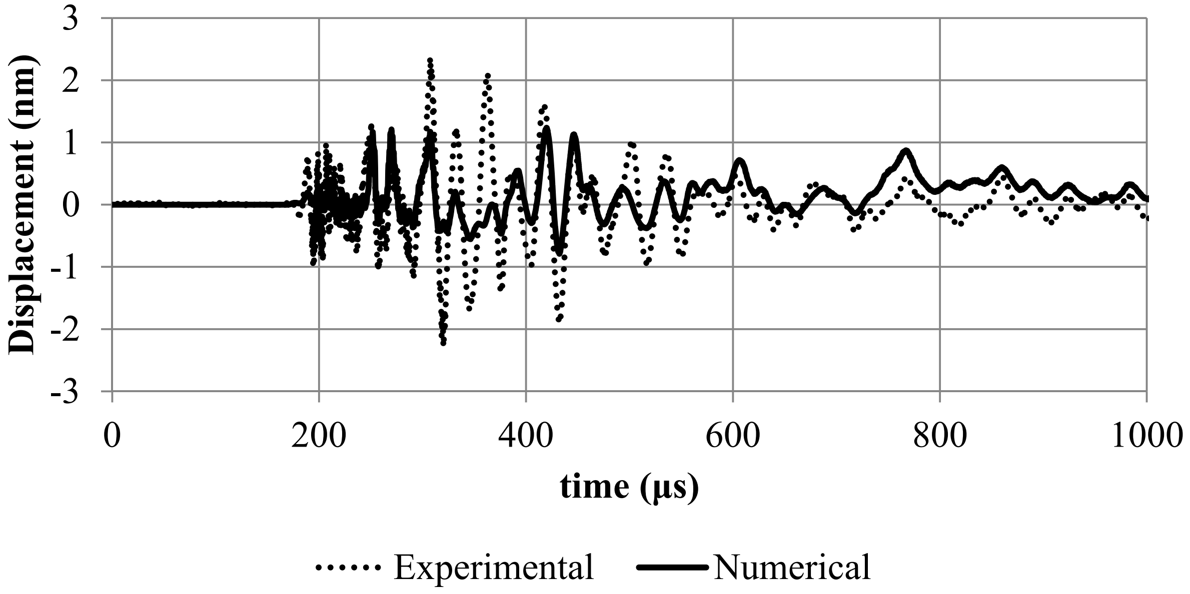

Figure 5.22. Experimental test result with the laser vibrometer and numerical simulation of sample 1 (perfectly bonded bar).

The experimental time signal of sample 2 and numerical simulation of de-bonded bar are presented in Figure 5.23. It is evident that the first peak from the simulation has a very good correlation with the experimental test. Also, the second reflection at 0.433 milliseconds matches very well. After the first arrival, the displacement signals in the simulation attenuate more than the signal from the experimental test. This may be because of the difference between the damping ratio of the actual bar and the simulated bar.

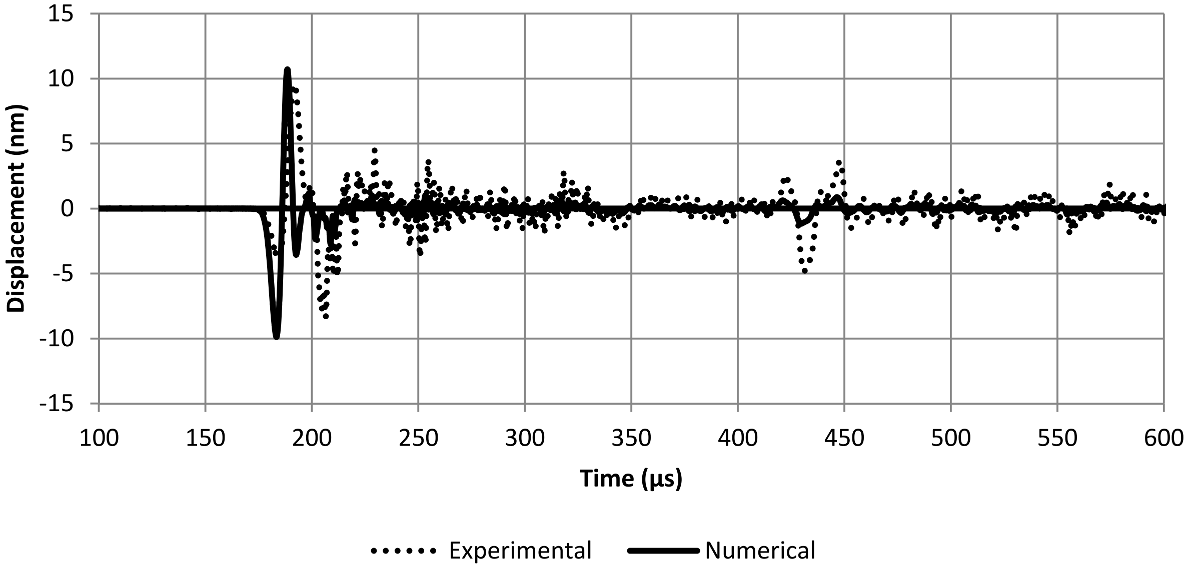

Figure 5.23. Experimental test result of the Laser vibrometer and the numerical simulation of sample 2 (de-bonded bar).

Although much effort was put toward modeling specimen response as close as possible to real response, the materials in the numerical simulations are completely homogenous materials, but the real ones are heterogeneous to some degree. The coupling between the transducer and the specimen was assumed to be completely perfect, but in reality it is very difficult to obtain close-to-perfect coupling. Contact condition between the bar and mortar is another important difference between the simulation and the real test. The isolation condition of the experimental test also has an effect on the test results. All of these factors contribute toward the differences between the numerical simulation results and the experimental test results as revealed in Figures 5.22 and 5.23.

5.5.2. De-bonding identification

Experimental test results with the laser vibrometer are shown in Figure 5.24. Experimental and numerical simulation tests clearly show that amplitude of time signals is almost five to six times more in de-bonded samples than perfectly bonded samples. Also, the energy dissipated in both the perfectly bonded bar and the rebar specimens after 0.001 second, but in de-bonded samples, there was still displacement occurring after 0.001 second. Table 5.4 presents results of the ratio of first peak-to-peak time signals of the de-bonded samples to the "perfectly bonded" samples. For all specimens, it is evident that peak-to-peak amplitudes are far higher for de-bonded samples compared to "perfectly bonded" samples.

Table 5.4. Ratio of peak-to-peak amplitudes of de-bonded samples time signals and perfectly bonded sample.

Specimen	Maximum Peak to peak amplitude (nm)	Amplitude (de-bonded/bonded)
sample 1	3.66	4.90
sample 2 (de-bonded bar)	17.94	
sample 3	0.72	6.34
sample 4 (de-bonded rebar)	4.57	
Simulation sample 1	4.06	5.07
Simulation sample 2	20.59	

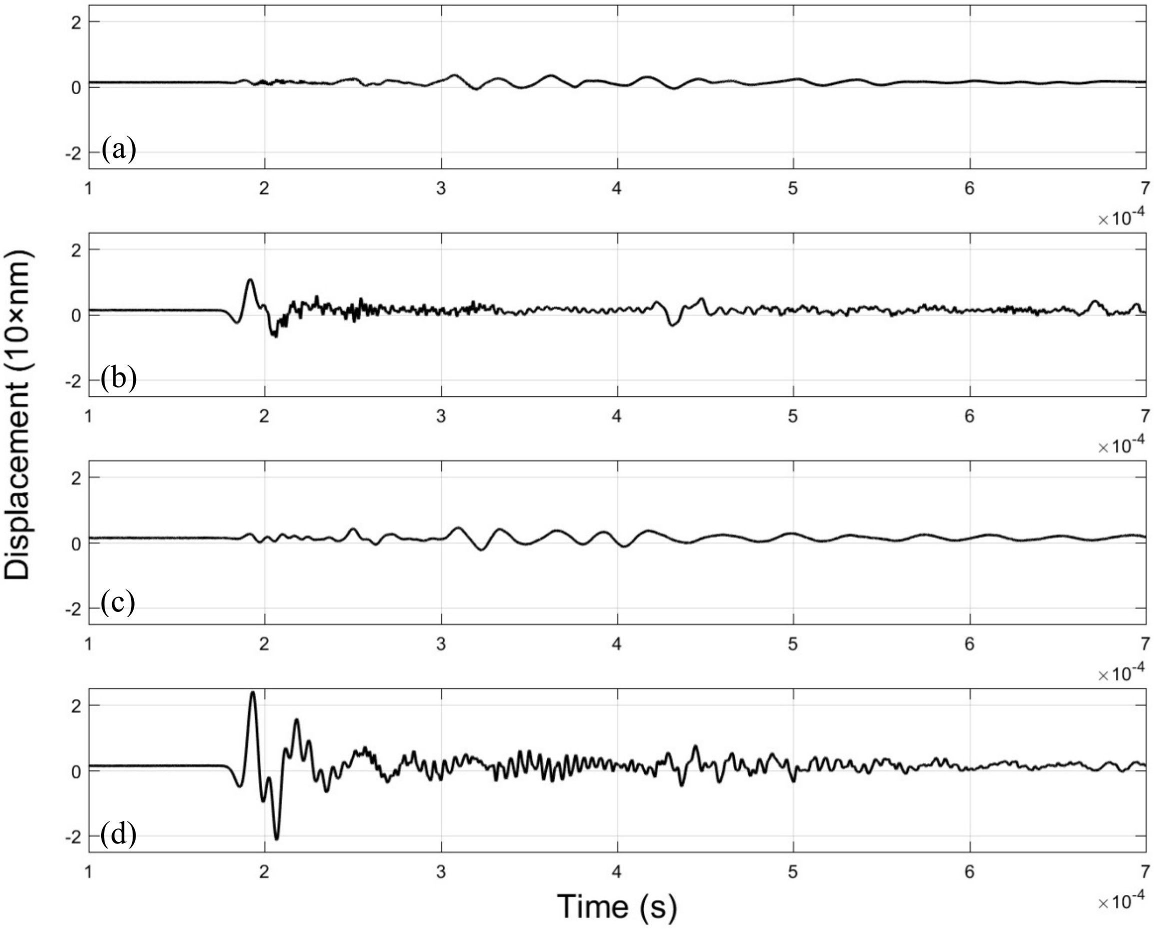

Figure 5.24. Experimental test results from the center point at the end of the bar and rebar. (a). Perfectly bonded bar. (b). De-bonded bar. (c). Perfectly bonded rebar. (d). De-bonded rebar.

Figure 5.25 shows the numerical simulation results for the perfectly bonded bar (Figure 5.25(a)) and the de-bonded bar (25(b)). Peak-to-peak amplitude of wave propagation is larger for the de-bonded specimen, which means that there is less leakage of energy through the mortar. Also, after 0.001 second, the energy is almost dissipated for the perfectly bonded simulated sample, but for the de-bonded simulated sample, there is higher peak-to-peak amplitude of displacement signal.

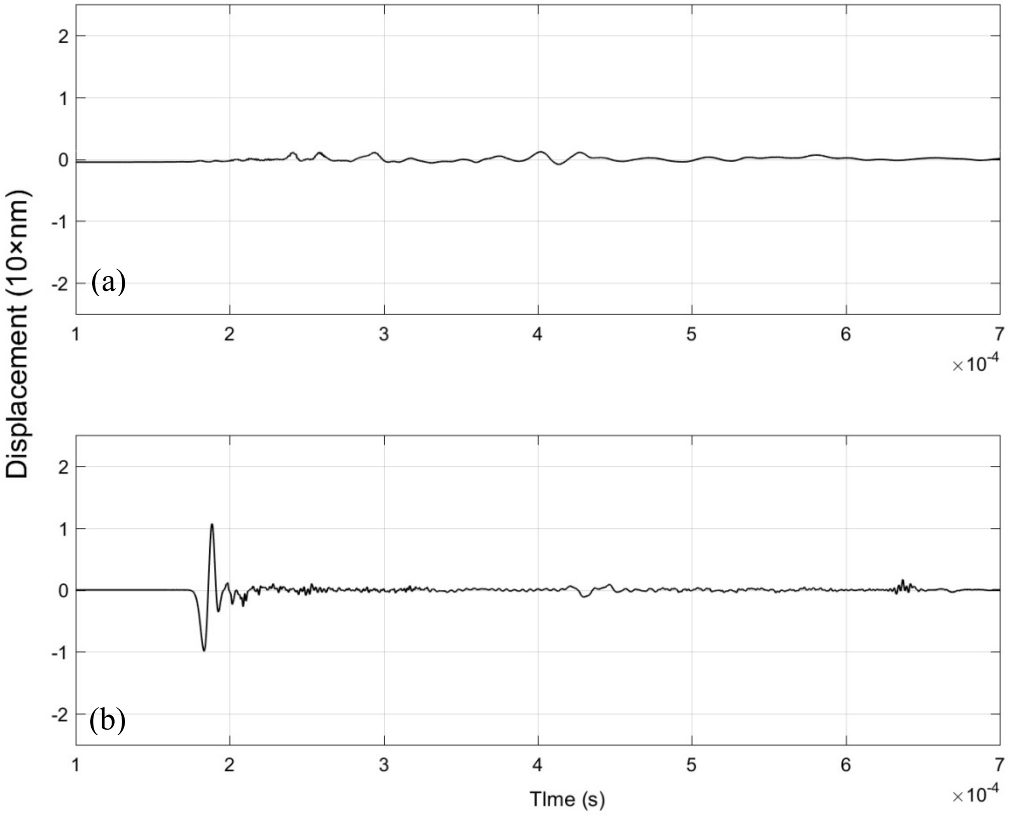

Figure 5.25. Numerical simulation results from the center point at the end of the bar. (a). Perfectly bonded bar. (b). De-bonded bar.

Figures 5.26(a) and 5.26(b) present the frequency response of the experimental test for the perfectly bonded bar and the de-bonded bar specimens respectively. The frequency range of the perfectly bonded bar is 19% of the frequency range of the de-bonded bar, and the magnitude of the perfectly bonded bar is 37% of the magnitude of the de-bonded bar. As shown in Figures 5.26(c) and 5.26(d), the frequency range of the perfectly bonded bar is 8.6% of the de-bonded rebar and the magnitude of the perfectly bonded rebar is 14% of the de-bonded rebar. The frequency analyses of numerical simulations are shown in Figures 5.26.e and 5.26.f. The magnitude of frequency is 48% less for the perfectly bonded bar than the de-bonded bar. Also, the frequency range of the perfectly bonded bar is 8.8% less than the de-bonded bar. When there is a perfect bonding between reinforcement and mortar, more energy leaks to the mortar. In addition, waves with a higher frequency range dissipate sooner and will not reach to the end of the bar/rebar. When there is imperfect bonding between the bar/rebar and mortar, waves with higher frequency range travel through the reinforcement without less leaking and reach the end of the reinforcement bar.

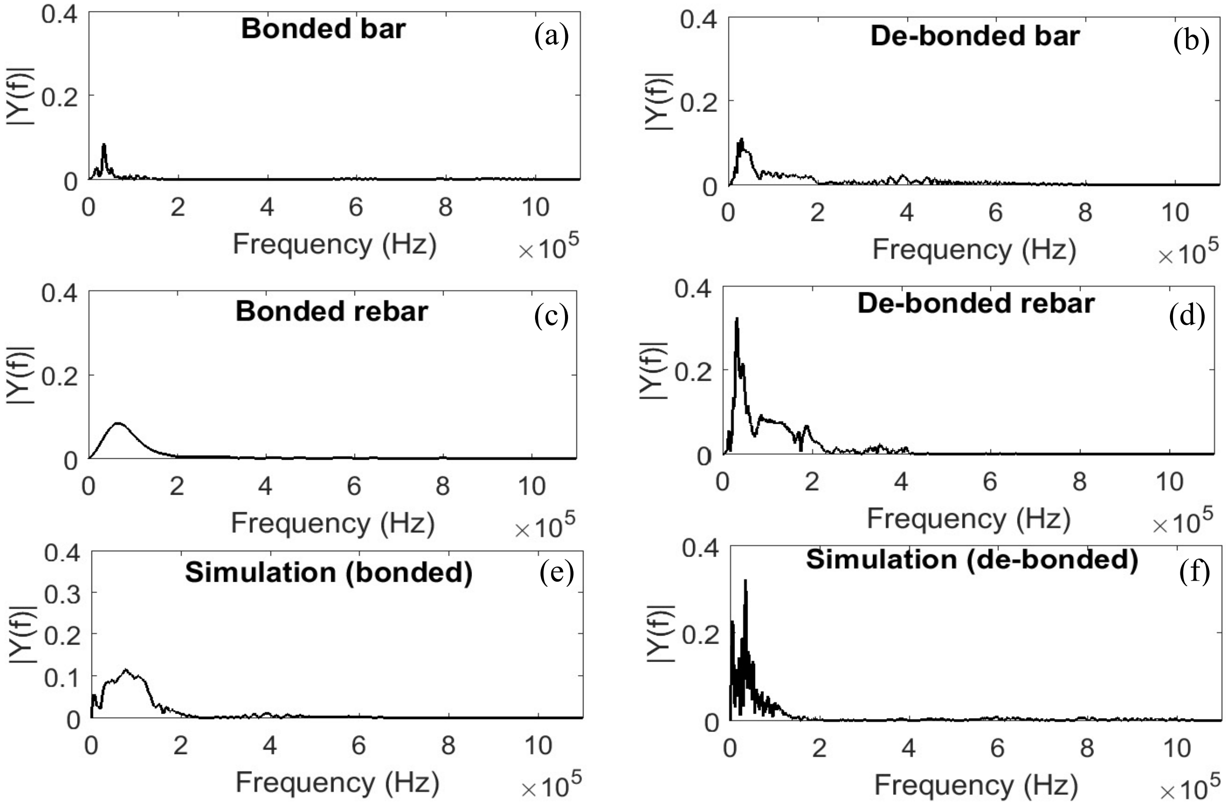

Figure 5.26. Frequency response of the experimental test and the numerical simulation. (a). Perfectly bonded bar. (b). De-bonded bar. (c). Perfectly bonded rebar. (d). De-bonded rebar. e. Simulation result of perfectly bonded bar. f. Simulation result of de-bonded bar.

5.6. Conclusions

In this study, a piezoelectric transducer was simulated numerically using the discrete finite element method. For this simulation, an X-ray image was used to obtain the actual geometry of the same piezoelectric transducer that was used in the experimental test. The electrical circuit of the piezoelectric transducer was also modeled in order to simulate input voltage more similar to that of the experimental test. Through the modeled electrical circuit, the same input voltage of the calibration test on the transducer as with the laser vibrometer was used in the numerical simulation. By using the laser vibrometer, experimental tests were conducted on the piezoelectric transducer for calibration. Transducer numerical simulation results were compared to experimental test results on the transducer with the laser vibrometer.

The main contributions of this study are as follows:

- A new model of 1 MHz piezoelectric transducer was simulated using its actual geometry and actual input voltage. This simulation was compared with real displacement measurements using a laser vibrometer.
- Actual displacement of the piezoelectric transducer was measured for the first time and compared to the velocity and voltage time signals. The piezoelectric transducers (PZT) do not have a calibrated response provided by the manufacturer.
- The PZT response includes the transfer function of the transmitter (H_T) plus coupling (H_C) plus receiver (H_R), whereas the captured displacement time signal from laser vibrometer involves only a transfer function related to the transmitter (H_T).

De-bonding of reinforcement from the mortar was experimentally tested through the laser vibrometer on four specimens and two numerical simulations. The main conclusions of this study from the experimental tests and numerical simulations are as follows:

- Peak-to-peak amplitude ratios were 4.90, 6.34, and 5.07 times more for de-bonded bar, de-bonded rebar, and simulated de-bonded bar respectively.
- Frequency response range of the perfectly bonded bar was 19% of the de-bonded bar.
- Frequency response range of the perfectly bonded rebar was 8.5% of the de-bonded rebar.
- Frequency response range of the simulated perfectly bonded bar was 8.7% of the de-bonded simulated bar.
- Frequency magnitudes of the de-bonded bar were 2.67 times more than the perfectly bonded bar.
- Frequency magnitudes of the de-bonded bar were 7.20 times more than the perfectly bonded bar.

- Frequency magnitudes of the simulated de-bonded bar were 2.06 times more than the simulated perfectly bonded bar.

Results from the tests and numerical simulations confirmed that when there is “perfect bonding” between reinforcement and mortar, wave energy leaks easily into the mortar and higher frequency waves dissipate before arriving at the end of the reinforcement. In contrast waves travel mostly through the reinforcement for de-bonded samples.

“Perfect bonding” of reinforcement with mortar is a desired condition in practice. Any kind of defects on the reinforcement (corrosion, crack) or within the concrete (crack) makes reinforcement somewhat more de-bonded from the mortar/concrete. This study indicates that the acoustic wave propagation method can reveal de-bonding of reinforcement, and it is most likely to be useful on a year-to-year basis to evaluate progressive de-bonding from corrosion.

Chapter 6

General Metal Loss, and Local Corrosion Detection with the Passive Magnetic Inspection Method and Wavelet Analysis

6.1. Introduction

In Chapter 3, a rebar with three holes was tested by using a device based on the Passive Magnetic Inspection method. Numerical simulation was compared with experimental data to prove the concept of the method, and also to increase the reliability of the results. In Chapter 4, a Principal Component Analysis method (PCA) was applied to data from the same specimen. Results show that PCA method has an ability to extract features from Passive Magnetic raw data.

In this chapter, experimental test results of six rebars are presented. Each rebar has a different percentage of metal loss. Rebars were placed sequentially into the same concrete specimen to have the same distance from the rebar and the same intervening material. The experimental test is to distinguish among the corroded rebars using recorded passive magnetic data obtained with the scanning device prototype.

6.2. Experimental test specimens preparation

6.2.1. Concrete specimen

A concrete specimen holder was cast in such a way to provide flexibility in changing corroded rebars and in using a different thickness of concrete. At the approximate middle of the casting mold (Figure 6.1) an acrylic tube with diameter slightly bigger than the rebars' diameter (15 mm) was placed to allow easy changing out of different rebars. The tube was not exactly at the center of casting mold to allow for different thicknesses of concrete. As shown in Figure 6.2, this gave thickness ranges along the tube axis on the four sides of the specimen holder as 2.3-4.0 cm, 5.2-4.7 cm, 5.4-5.6 cm, and 6.8-7.0 cm.

Figure 6.1. Acrylic tube inside the casting mold.

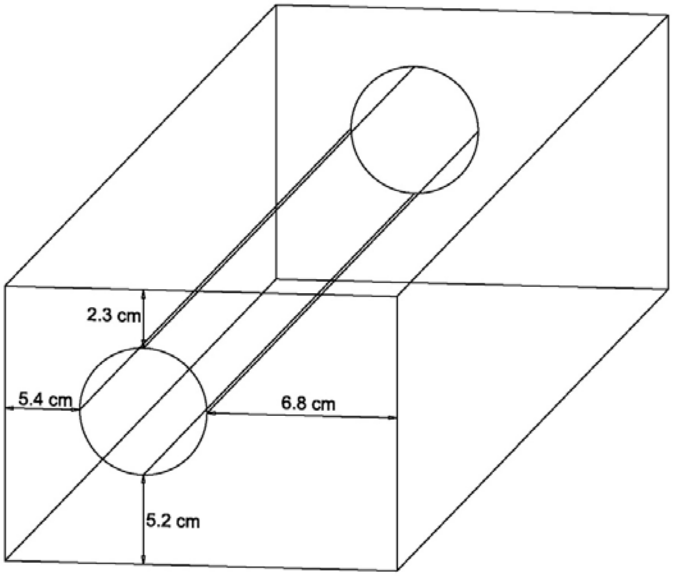

Figure 6.2. Schematic picture of the concrete specimen.

Figure 6.3 shows the final picture of the concrete specimen, acrylic tube, and different thicknesses from the concrete surface to the acrylic tube. By scanning along each flat surface of concrete, different overburden thicknesses can be achieved. In this study a typical concrete mixture was used based on ACI 211.1-91 [113]

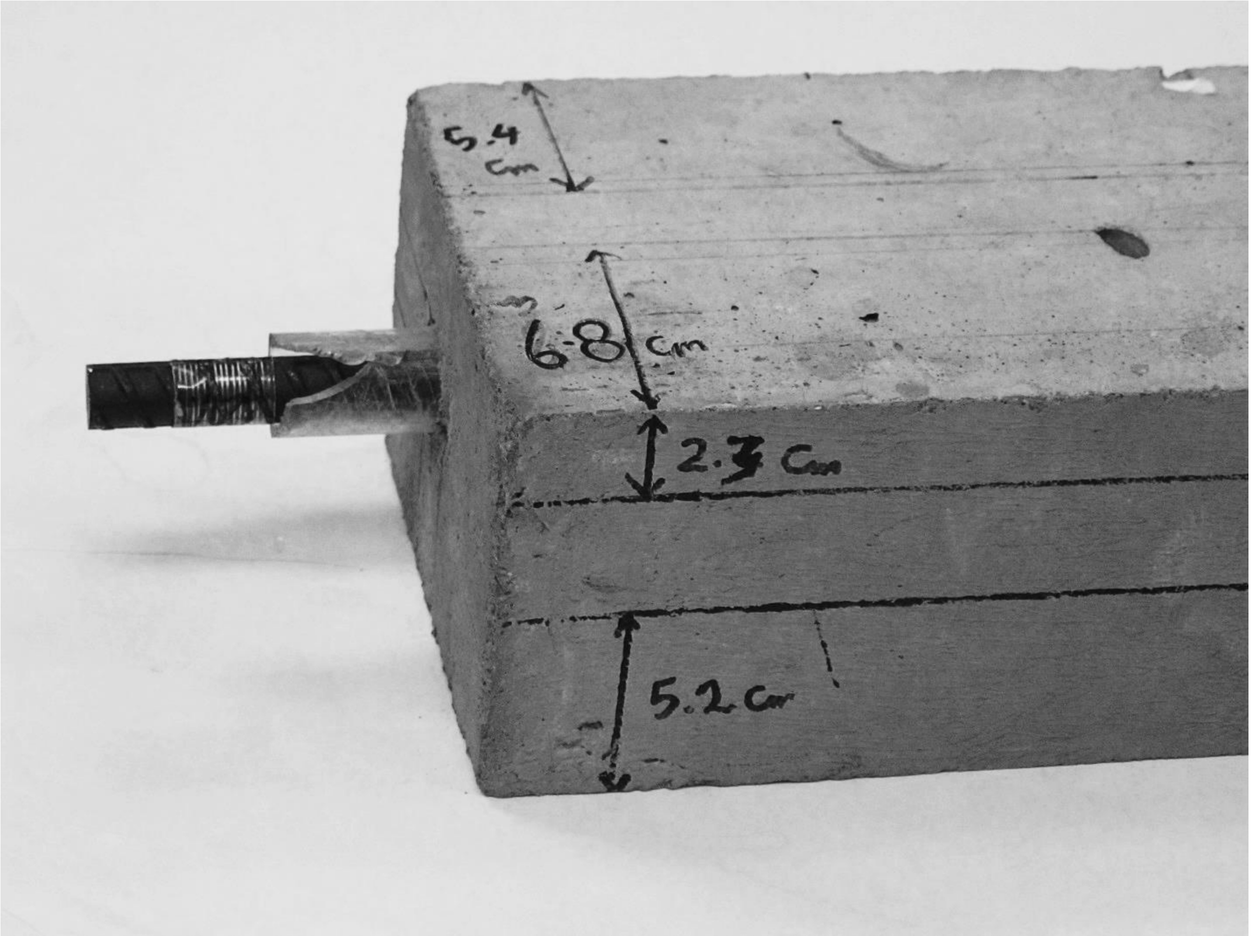

Figure 6.3. Cured concrete specimen with acrylic tube in the center and a rebar inside the tube.

6.2.2. Rebars

Six rebars with different corroded rebars were used. Rebars were Grade 400 steel according to CSA Standard CSA-G30.18 [148]. Rebar No. 6 was completely sound. Table 6.1 presents metal losses percentage for each rebar, and Figure 6.4 shows rebars used in this experimental test.

Table 6.1. Percentage of metal loss for studied bars [148].

Rebar No.	Metal Loss (%)
1	4.73
2	7.02
3	9.07
4	12.2
5	14.3
6	0

Figure 6.4. Seven bars with different percentages of metal loss.

6.3. Experimental test procedure

As concrete is a non-magnetic material with relative magnetic permeability of almost 1, it will not have an effect on the magnetic flux density around the reinforcement bar [112]. Because of different parameters to study such as rebars metal losses and different overburden thicknesses, experimental tests were done in 30 unique conditions. Each unique condition was tested 20 times, and Table 6.2 presents all the unique conditions of the experimental test procedure.

Table 6.2. Variation of tests with different sensor to rebar (SR) distance.

Bar No.	Metal loss (%)	Sensor to rebar distance (cm)				
1	4.73	6.5-7	8-8.5	8.5-9	10-10.5	10.5-11
2	7.02	6.5-7	8-8.5	8.5-9	10-10.5	10.5-11
3	9.07	6.5-7	8-8.5	8.5-9	10-10.5	10.5-11
4	12.2	6.5-7	8-8.5	8.5-9	10-10.5	10.5-11
5	14.3	6.5-7	8-8.5	8.5-9	10-10.5	10.5-11
6	0	6.5-7	8-8.5	8.5-9	10-10.5	10.5-11

All data were saved as a text file in the memory card of prototype device. Figure 6.5(a) shows the experimental set-up and Figure 6.5(b) shows the scanning machine prototype on the concrete specimen surface with the rebar in place.

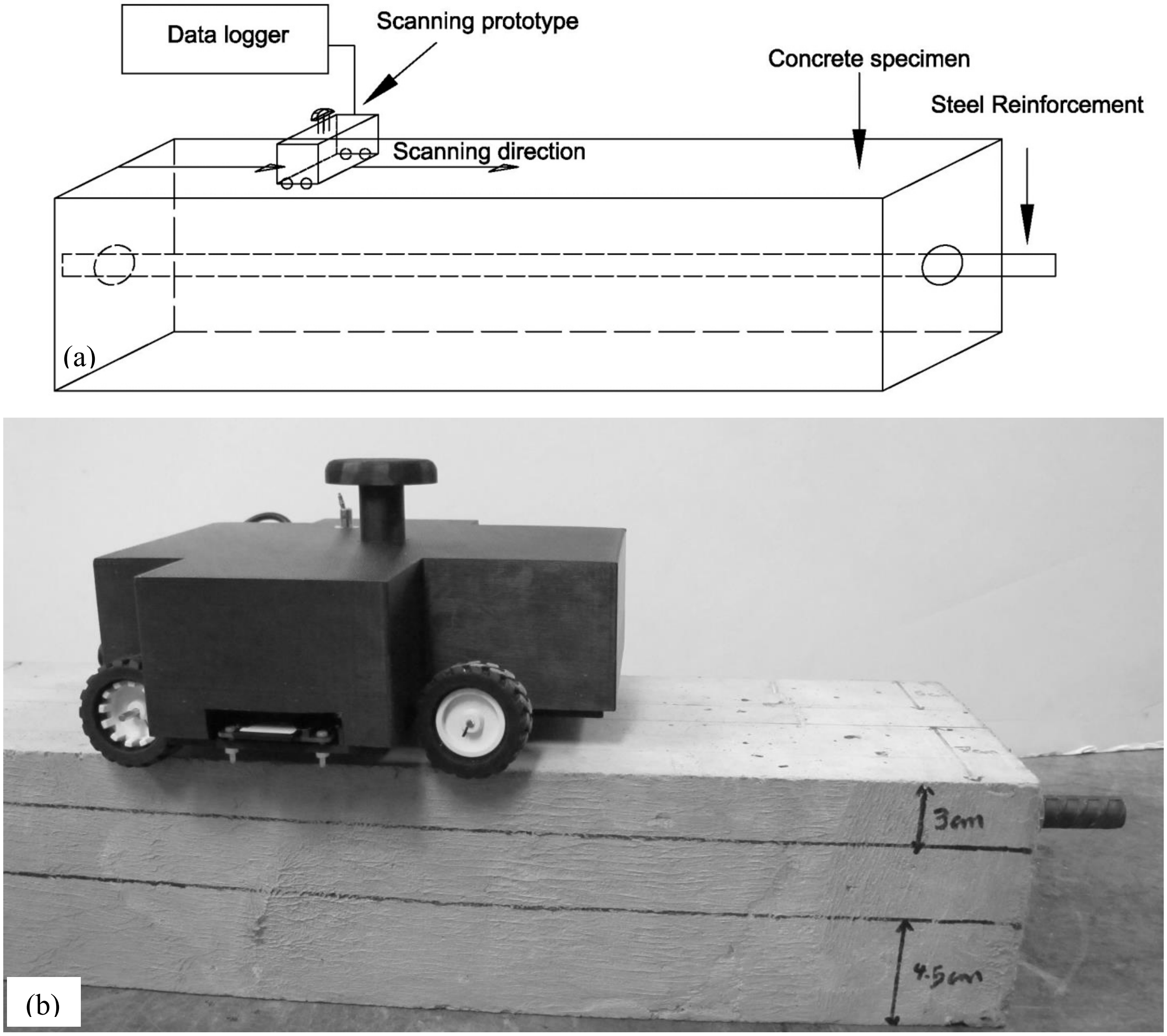

Figure 6.5. Experimental test (a). Scheme of test, (b). Scanning machine prototype and concrete specimen.

6.4. Data analysis

Based on domain theory [24, 25, 28, 29, 31, 33, 34, and 35] and stress state in relation to the magnetic value of ferromagnetic materials [16, 21, 22, 36, and 39], sudden changes of magnetic values can occur because of domain displacement due to stress state changes. Also, another main reason for change in domain structure is the generation of a defect (corrosion, crack, and pitting) in the crystalline structure [97]. Therefore, a first quick analysis technique to determine any structural changes of rebars such as corrosion, cracking or pitting may be achieved by exploring the first derivative of raw magnetic data recorded on the concrete surface above the reinforcement bar.

Based on first derivative analysis, it is possible to distinguish corroded bars from healthy bars for different levels of corrosion and thicknesses. Figures 6.6(a) and 6.6(b) show first derivative curves of magnetic data in x, y, and z directions on bars with 4.73% metal loss and 0% metal loss. The spacing between the magnetic sensors and the top surface of reinforcement in this test was 6.5 to 7 cm. The maximum magnetic intensity for the steel reinforcement bar with 0.0% metal loss is approximately 100 A/m, but for the rebar with 4.7% metal loss, it is close to 300 A/m. By increasing the concrete thickness the magnetic intensity was reduced for both rebars. Figure 6.7 shows the first derivative of magnetic data for 10.5 to 11.0 cm thickness. Again, in these figures the difference between a corroded bar (Figure 4.7(a), 4.7% metal loss) and a non-corroded bar is clear. The maximum magnetic intensity for a sound rebar is 88 A/m, but for a corroded rebar it is 145 A/m.

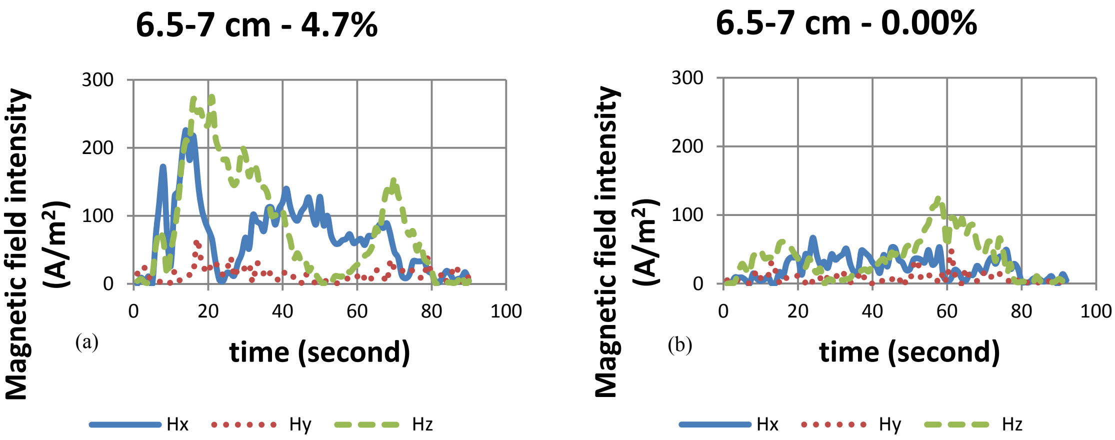

Figure 6.6. First derivative of magnetic data from bars at X, Y and Z directions. The concrete thickness is 6.5-7.0 cm. (a). Bar with 4.7% metal loss. (b). Bar with 0.0% metal loss.

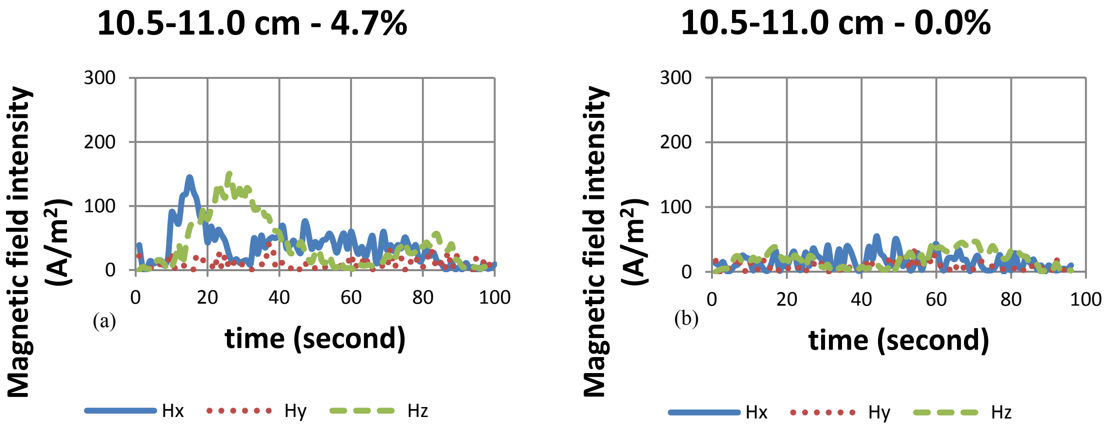

Figure 6.7. First derivative of magnetic data from bars at X, Y and Z directions. The concrete thickness is 10.5-11.0 cm. (a). Bar with 4.7% metal loss. (b). Bar with 0.0% metal loss.

The same analysis method was applied to all rebars and concrete thicknesses, and all the figures are available in Appendix I. Table 6.3 presents the analysis results for different conditions; The data show that there is a big difference in magnetic intensity between corroded bars and un-corroded bars in all testing modes.

Table 6.3. Magnetic intensity for different sensor to rebar distances.

Sensor to rebar distance (cm)	Metal loss %	Maximum Magnetic Intensity (A/m)
7	0	127
8	0	76
9	0	52
10	0	51
11	0	50
7	4.73	275
8	4.73	240
9	4.73	235
10	4.73	189
11	4.73	150
7	7.02	293
8	7.02	244
9	7.02	185
10	7.02	149

11	7.02	131
7	9.07	300
8	9.07	276
9	9.07	196
10	9.07	162
11	9.07	156
7	12.2	267
8	12.2	196
9	12.2	159
10	12.2	112
11	12.2	101
7	14.3	225
8	14.3	124
9	14.3	124
10	14.3	102
11	14.3	91

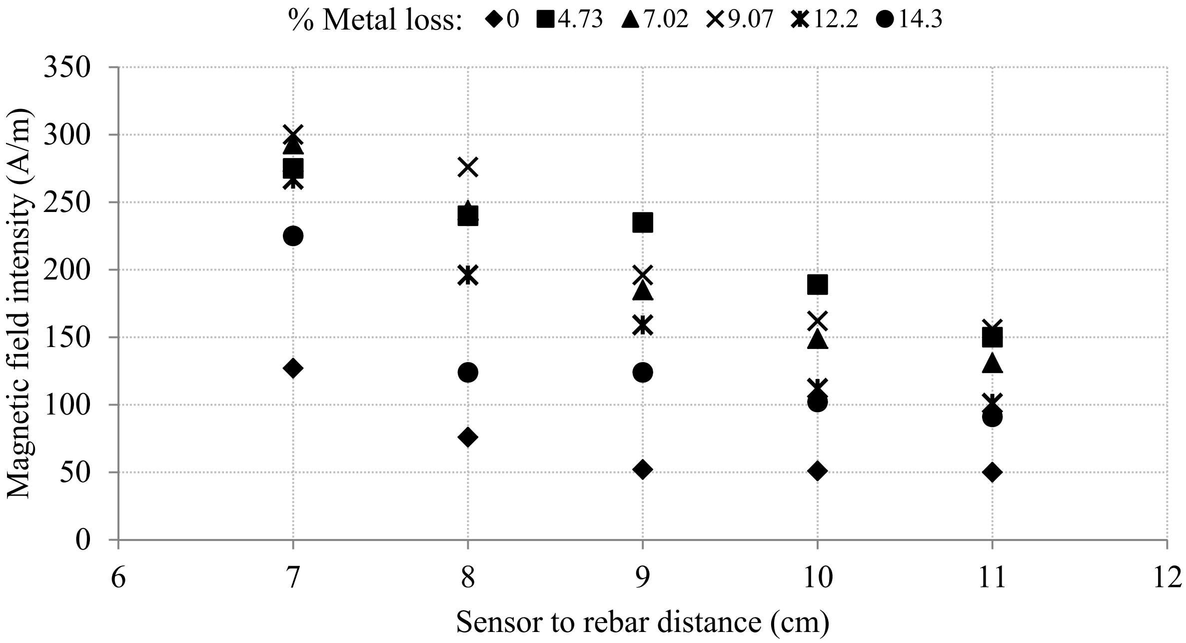

Figure 6.8. Changes in magnetic field intensity due to spacing changes between sensors and rebar.

It is reasonable to expect that by increasing the spacing between the sensor and rebar the recorded magnetic field would decrease gradually. However, the magnetic field intensity is higher for corroded rebars, and it is because of the additional stray field energy from corroded edges in the steel. Figure 6.8 is a plot of the results in Table 6.3. Spacing here means distance between the sensor to the surface of the concrete plus the thickness of concrete to the top of the rebar.

6.4.1. Wavelet analysis

Wavelet transform is a mathematical process which divides continuous time signals into different frequency components in time. The wavelet analysis of a signal allows the study of each frequency component with a resolution matched to its scale [171]. Let *x(t)* a signal with finite energy the definition of the continuous wavelet of *x(t)* is given by equation 6.1 [173]:

$$W_x(u,s)=\int_{-\infty}^{+\infty} x(t)\frac{1}{\sqrt{s}}\psi^*\left(\frac{t-u}{s}\right)dt \qquad (6.1)$$

In equation 6.1, the function ψ is the wavelet, u represents the translation time factor, s represents the scale or dilation factor, (*) represents the complex conjugate operation. The function ψ must satisfy some strict mathematical properties. As for the Fourier transform it is possible to reconstruct the signal *x(t)* from its wavelet transform, if this wavelet functions are orthogonal:

$$x(t)=\frac{1}{K_\psi}\int_0^{+\infty}\int_{-\infty}^{+\infty} W_x(u,s)\frac{1}{\sqrt{s}}\psi\left(\frac{t-u}{s}\right)du\frac{ds}{s^2} \qquad (6.2)$$

where K_ψ is a constant value. The implementation on a computer of the continuous wavelet transform needs the discretization of the u and s values. This discretization process leads to the discrete wavelet transform. The discrete wavelet transform decomposes the signal into mutually orthogonal set of wavelets. This is a main property of the discrete wavelet transform and the main difference from the continuous wavelet transform. The continuous wavelet transform is based on the utilization of the wavelet [170, 171]:

$$\psi_{u,s}(t)=\frac{1}{\sqrt{s}}\psi\left(\frac{t-u}{s}\right) \qquad (6.3)$$

In discrete wavelet transform, the function *ψ(t)* is shifted (*u* factor) and is dilated (*s* factor) by factors expressed as a power of two.

$$\psi_{j,k}(t)=\frac{1}{\sqrt{2^j}}\psi\left(\frac{t-k2^j}{2^j}\right) \tag{6.4}$$

The wavelet coefficient of the decomposition of signal *x(t)* are the computed by:

$$C^{x}_{j,k}=\int_{-\infty}^{+\infty}x(t)\psi^{*}_{j,k}(t)dt \tag{6.5}$$

The main difference between Fourier Transform and wavelet transform is that Fourier transform allows the localization of phenomenon in the frequency domain and the wavelet transform allows the localization of the phenomenon in the frequency domain but also in the time domain. Another advantage of the wavelet transform over the traditional Fourier transform is its ability to analyze the physical consequence (result) of probable signal anomalies. The development of wavelets happened independently in different fields of science and engineering (mathematics, physics, geophysics, electrical engineering) new applications of wavelet analysis for image analysis, earthquake predictions, radar data analysis, and non-destructive testing methods are the result of interchanges among different disciplines [149].

Classical Fourier transform analysis has some limitations for signal processing such as localizing time and frequency simultaneously, the irreversibility of spectral analysis in stationary signals, and limitations in analyzing signals that are inherently not composed of the superposition of periodic signals. Wavelet analysis was developed as a means of providing an analysis approach to overcome these limitations. With the wavelet transform, it is possible to localize different frequencies in the time scale [150]. Figure 6.9 presents the difference between Fourier and wavelet transforms. Signals in figures 6.9(a) and 6.9(b) have the same frequency content, but there is a clear difference in appearance, despite very similar Fourier transforms. The continuous Morlet (Appendix III.a) wavelet spectra (bottom) show the clear existence of each frequency contents in its specified time domain [151].

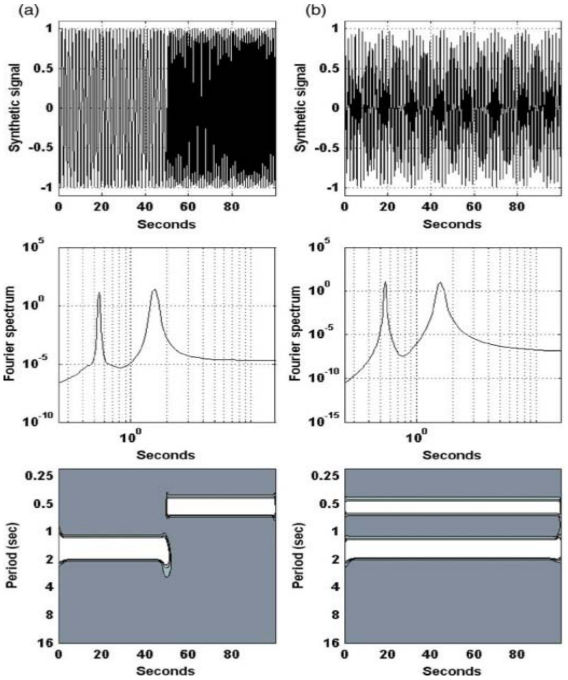

Figure 6.9. Fourier and continuous wavelet transform on synthetic signals [172].

Wavelet energy

The wavelet energy concept was defined in the context of studies of atmospheric turbulence [152], and then applied to the analysis of diurnal and nocturnal turbulence [153]. Wavelet variance study and its applications are continuing fields of study [154, 155, 156, and 157]. If the Fourier transform *F(x(t))* of the time signal *x(t)* exits it is possible to calculate distribution of energy across frequencies *ω* using a power spectrum density as follows:

$$P_{XX}(\omega) = \left|F\left(x(t)\right)\right|^2 \tag{6.6}$$

By using the wavelet transform the conservation of energy between the time domain and the time-frequency domain described by the Parceval theorem we will have [151]:

$$\int_{-\infty}^{+\infty} |x(t)|^2 \, dt = \frac{1}{K_\psi} \int_0^{+\infty} \int_{-\infty}^{+\infty} |W_x(u,s)|^2 \, du \frac{ds}{s^2} \tag{6.7}$$

So, the total energy of signal can be presented in the wavelet domain and wavelet spectrum [158]:

$$P_{w}^{x}\left(u,s\right)=W_{X}\left(u,s\right)W_{X}^{*}\left(u,s\right)=\left|W_{X}\left(u,s\right)\right|^{2} \tag{6.8}$$

where P_x^W *(u, s)* is the wavelet spectrum also named scalogram. An orthogonal multiresolution approach can also be used to define the concept of wavelet energy [159]. As demonstrated in Chapters 3 and 4, defect-related signals have different frequency content. This different frequency content has different energy contents at specific locations. All these characteristics make wavelet energy analysis a suitable signal processing method for this study.

Wavelet energy analysis

Figure 6.10 shows wavelet energy analysis results of the X-direction magnetic field measured above the rebars. Morlet wavelet was used for wavelet energy calculations based on equation 6.4 [160]. Using wavelet energy analysis for different corroded rebars shows an increase in wavelet energy with increasing general metal loss. Figure 6.11 shows wavelet energy analysis results of the Z-direction magnetic field data scanned along the rebar length. A similar pattern is observed, but as the metal loss percentage of rebars increased, the maximum value of wavelet energy increased.

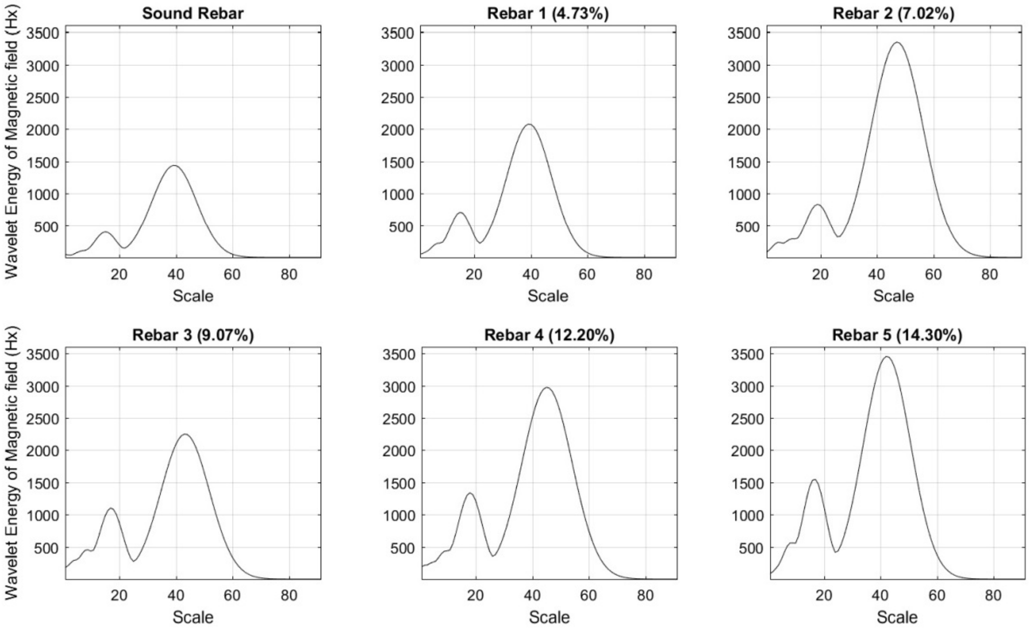

Figure 6.10. Wavelet energy result of magnetic field in X direction for different corroded rebars.

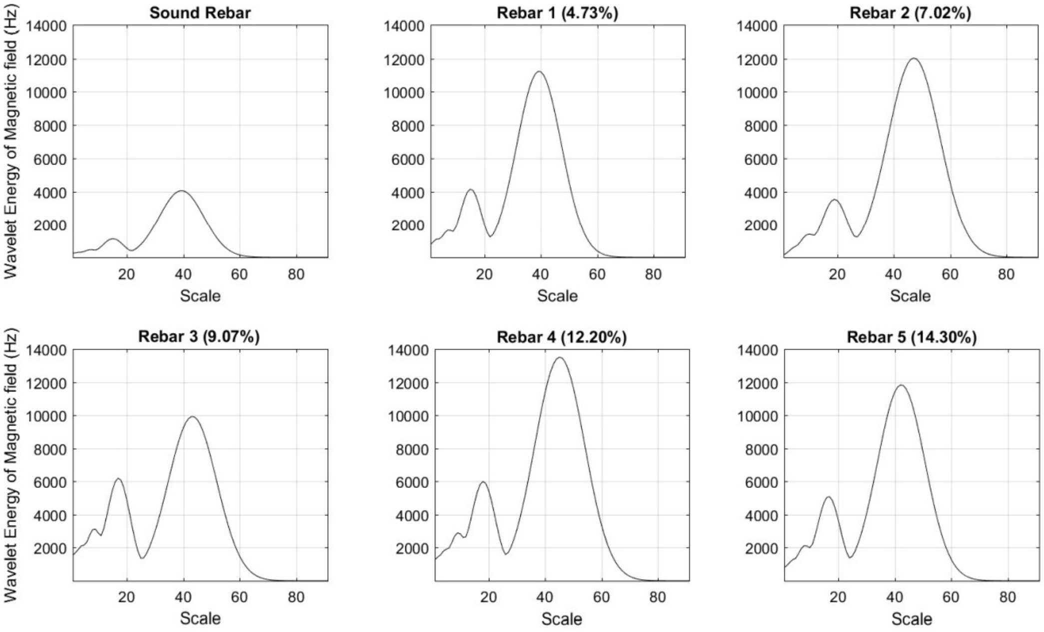

Figure 6.11. Wavelet energy result of magnetic field in Z direction for different corroded rebars.

Based on these maximum values result of wavelet energy analysis and linear regression method, two linear equations (Eq. 6.5, and Eq. 6.6) were extracted (Figure 6.12). Although the coefficient of determinations are 0.67 and 0.62 for X and Z graphs respectively, but these two equations can be used as a good indicator for general metal loss prediction.

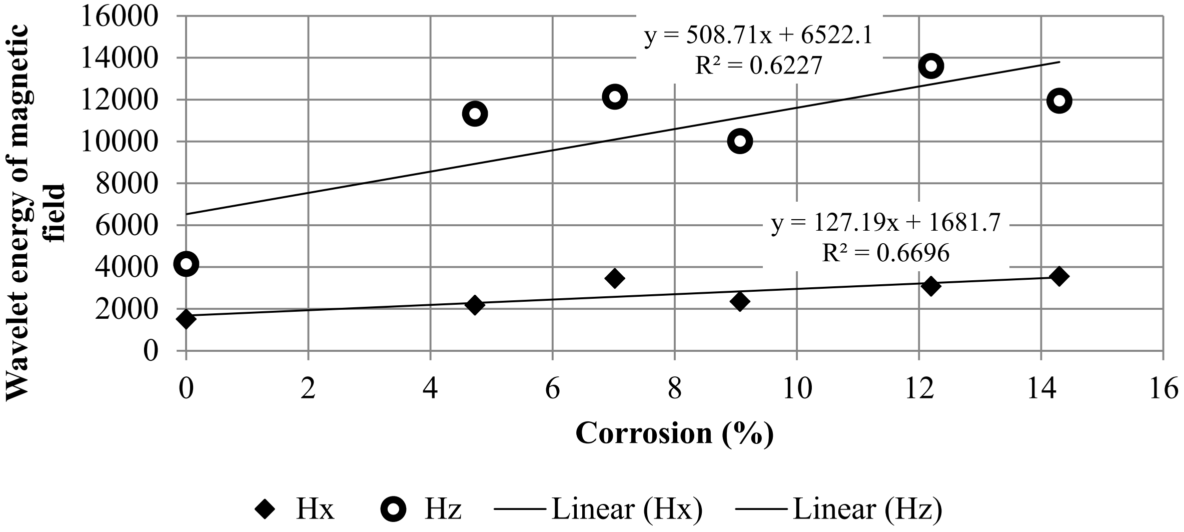

Figure 6.12. Linear regression from maximum wavelet energy values respect to metal loss presented in table 6.4.

$$E_{wx} = 127.19\,Cr + 1681.7 \tag{6.5}$$

$$E_{wz} = 508.71Cr + 6522.1 \tag{6.6}$$

Here, E_{wx} and E_{wz} are maximum wavelet energy values in the X and Z directions, and Cr is metal loss percentage of rebars.

6.5. Locally corroded rebars

In this section three stainless streel rebar sections with local corrosion were selected. This local corrosion developed on rebars by making artificial cracks in reinforced concrete specimens at specific locations and applying chloride ingress to speed up the chemical reactions [161]. Table 6.4 presents information on the rebar sections, and Figure 6.13 shows these corroded rebars.

Table 6.4. Locally corroded rebars information.

Sample	Steel type	Corrosion types	Rebar Length (cm)	Location of corrosion (cm)
C1	MMFX	General corrosion	36	20.5 to 24
C2	2101	Spot corrosion	36	6 to 10, 15.5, 18
C3	MMFX	General corrosion	36	22.5 to 24.5

Figure 6.13. Locally corroded rebars (C1, C2, and C3). Red circles show corroded sections.

6.5.1. Experimental results

Rebars were scanned with the PMI device, version 2 (Figure 6. 5), moving the prototype on the concrete surface in the same direction of the rebar. Before each test, the device precision accuracy is checked by calibrating the device [114]. While the scanner was moving, 10 data points per second were recorded into the memory card. The experimental test is done at two different locations in the laboratory where the ambient magnetic flux density are expected to be different. At each location, the magnetic flux density in the presence of the reinforcement steel within the concrete beam was measured 10 times and averaged [162, 163]. Figure 6.14 shows ten experimental test results of sample C1 after the high pass filter process (Chapter 3, section 5). A clear peak appeared between 16.5 cm to 20.4 cm. Figure 6.15 presents the mean value of all 10 experimental tests of sample C1, and two more lines representing the mean value plus and minus standard deviation. The maximum standard deviation of this experimental data set was 0.8 percent (Figure 6.16). Note that the relative magnetic permeability of concrete is equal to 1, thus it does not affect the magnetic flux density of the bar [115].

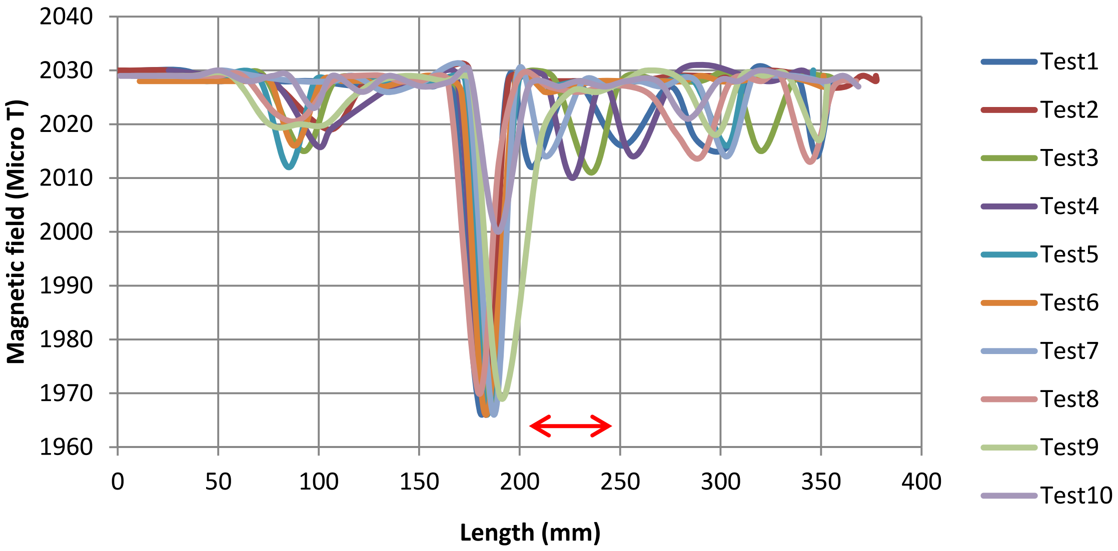

Figure 6.14. Ten PMI test results on rebar C1 (red arrow shows corrosion area).

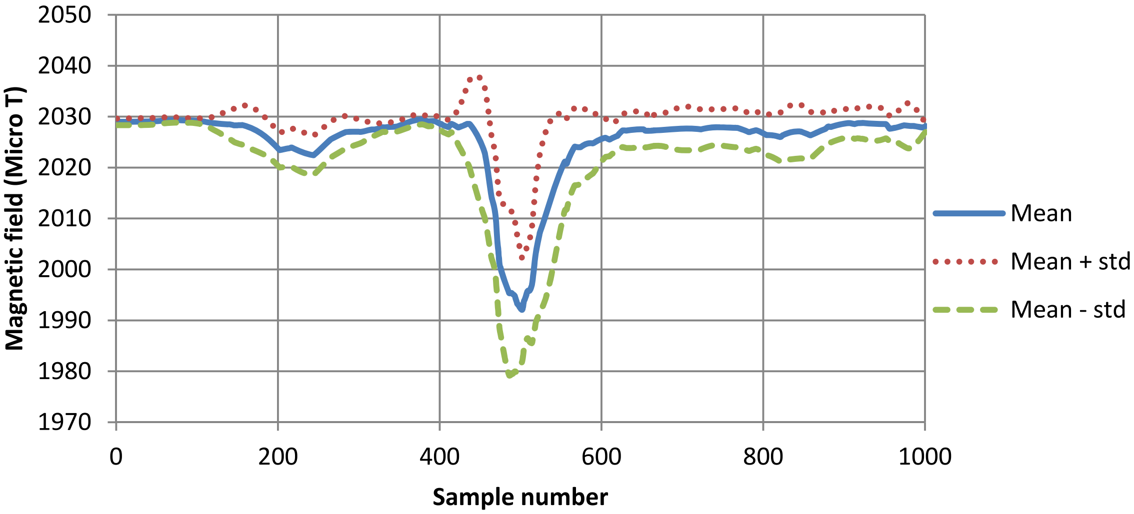

Figure 6.15. Mean value, mean value plus standard deviation, and mean value minus standard deviation of PMI experimental test on rebar C1.

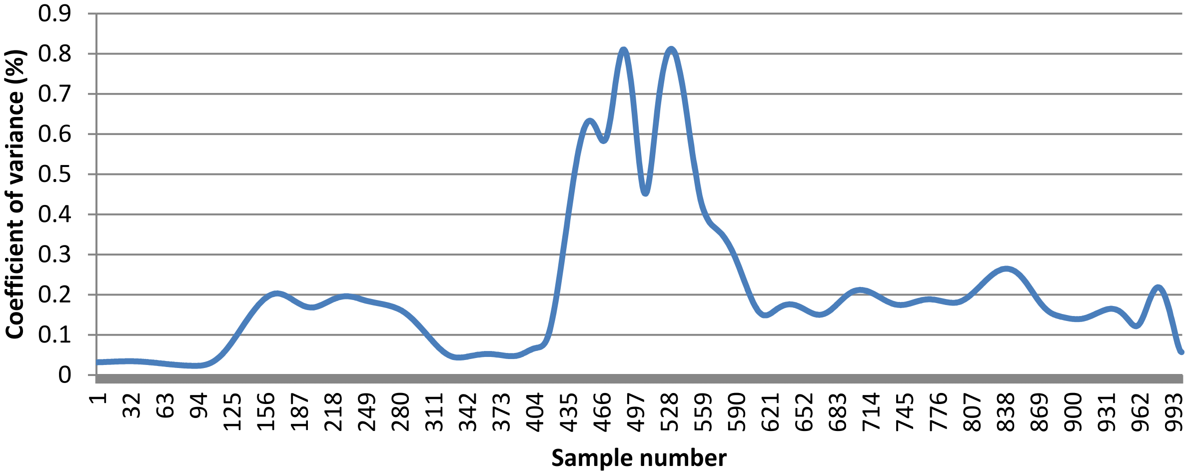

Figure 6.16. Coefficient of variance for sample C1.

Figure 6.17 shows the eleven experimental test results from sample C2 after the high pass filter process is applied (Chapter 3, Section 5). There are a number of peaks appearing between 5 cm and 18 cm scan length. As shown in Figure 6.13, there are three spot corrosion areas between 6 cm to 18 cm. Figure 6.18 presents the mean value of all eleven experimental scans of sample C2, and two more graphs representing mean value plus and minus standard deviation. The maximum standard deviation of this experimental test was slightly more than 1 percent, which is considered acceptable for anomaly detection (Figure 6.19).

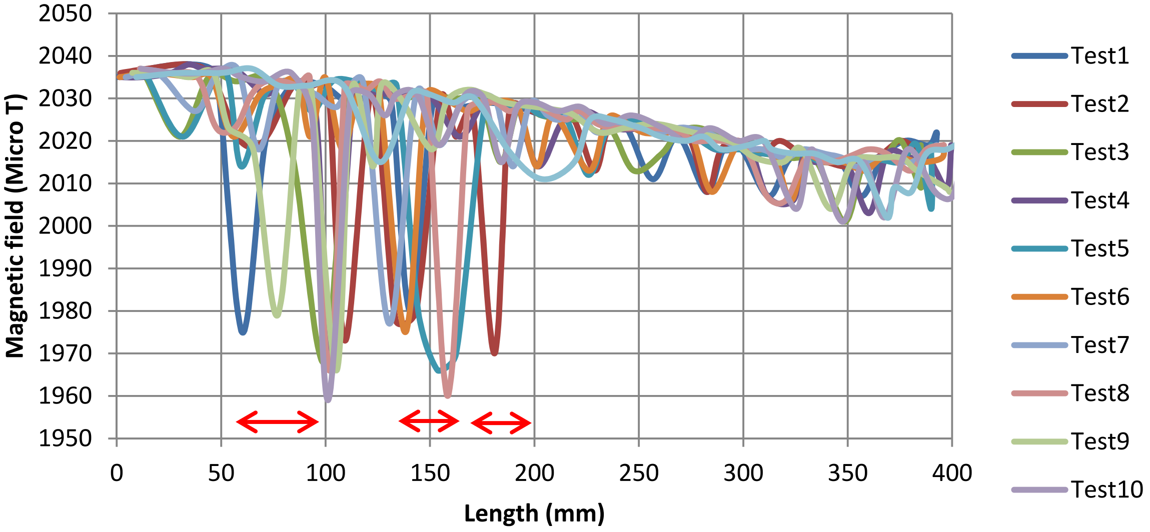

Figure 6.17. PMI ten test results on rebar C2 (red arrows show corrosion areas).

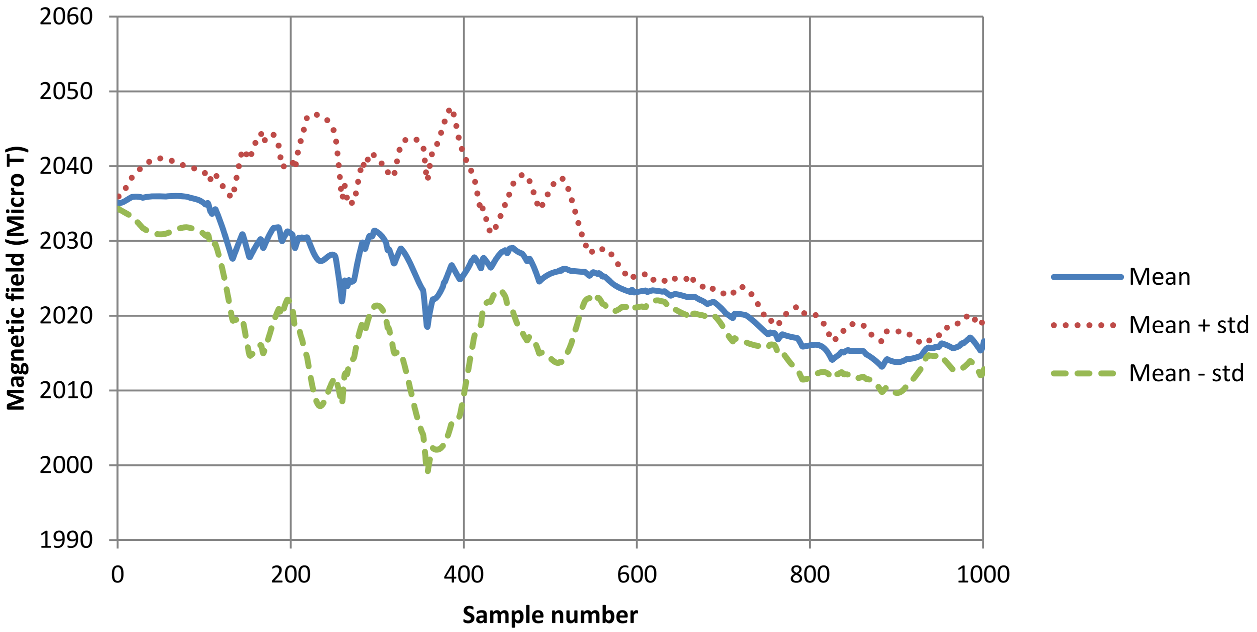

Figure 6.18. Mean value, mean value plus standard deviation, and mean value minus standard deviation of PMI experimental test on rebar C2.

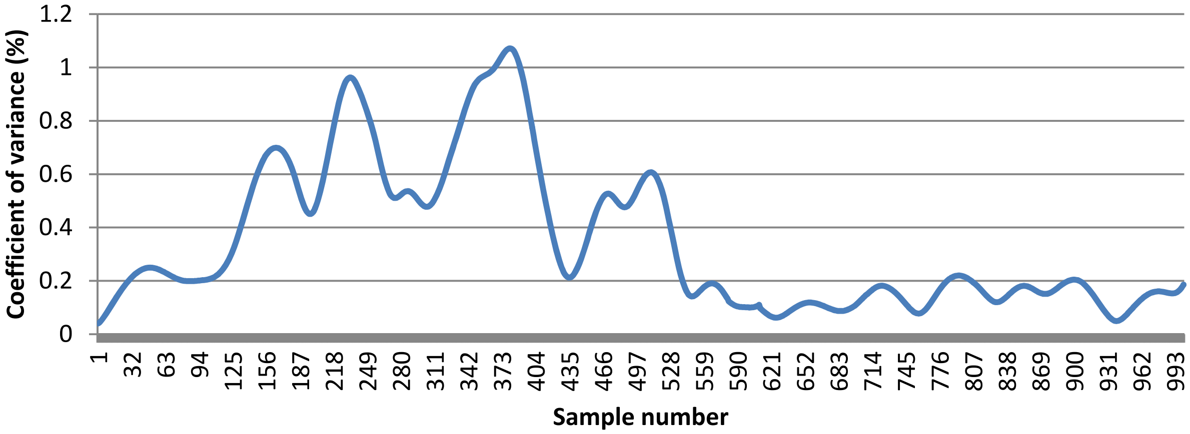

Figure 6.19. Coefficient of variance for sample C2.

Figure 6.20 shows ten experimental test results from sample C3 after the high pass filtering process (Chapter 3, section 5). There are some anomalies between 22 and 28 cm. It seems that there is less discrimination of peak locations relative to the actual location of the corrosion. Figure 6.21 presents mean values of all eleven experimental tests on sample C3, and two more graphs representing mean value plus and minus one standard deviation. The maximum standard deviation of this experimental test was slightly more than 0.5 percent (Figure 6.22).

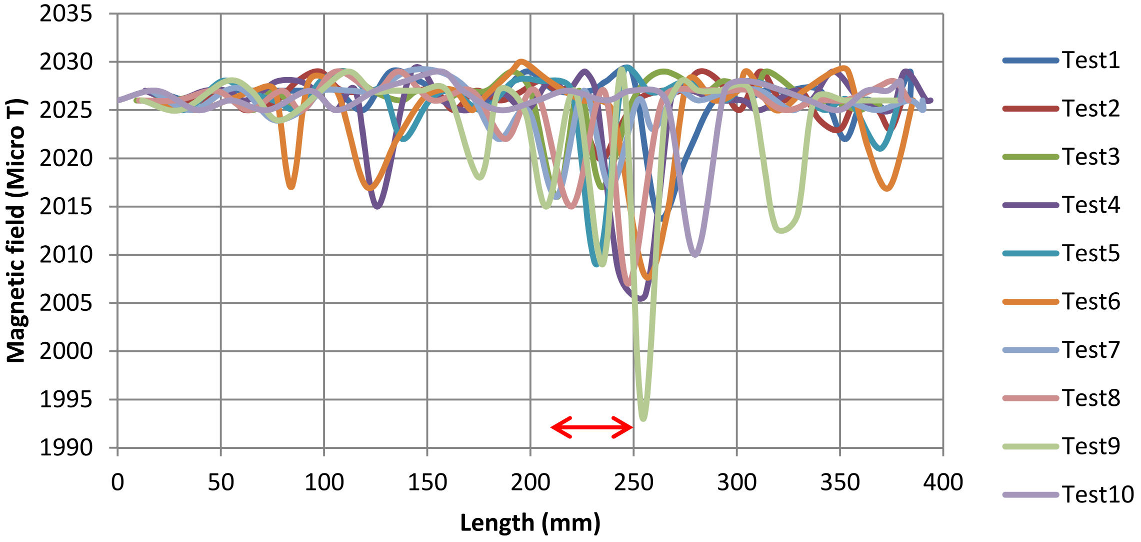

Figure 6.20. PMI ten test results on rebar C3 (red arrow shows corrosion area).

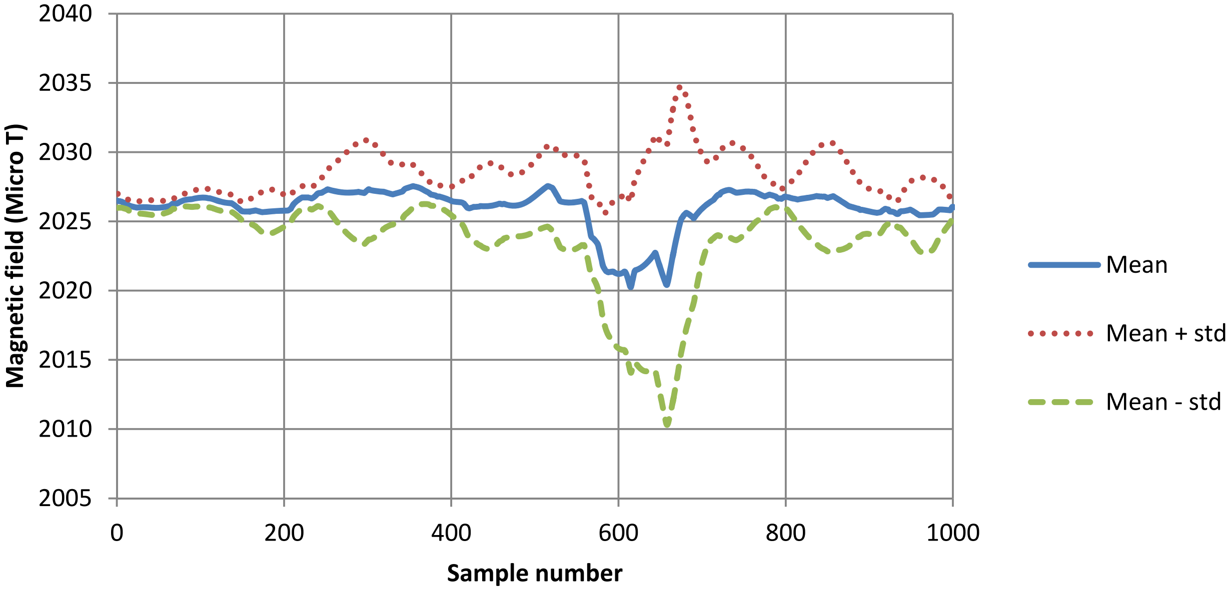

Figure 6.21. Mean value, mean value plus standard deviation, and mean value minus standard deviation of PMI experimental test on rebar C3.

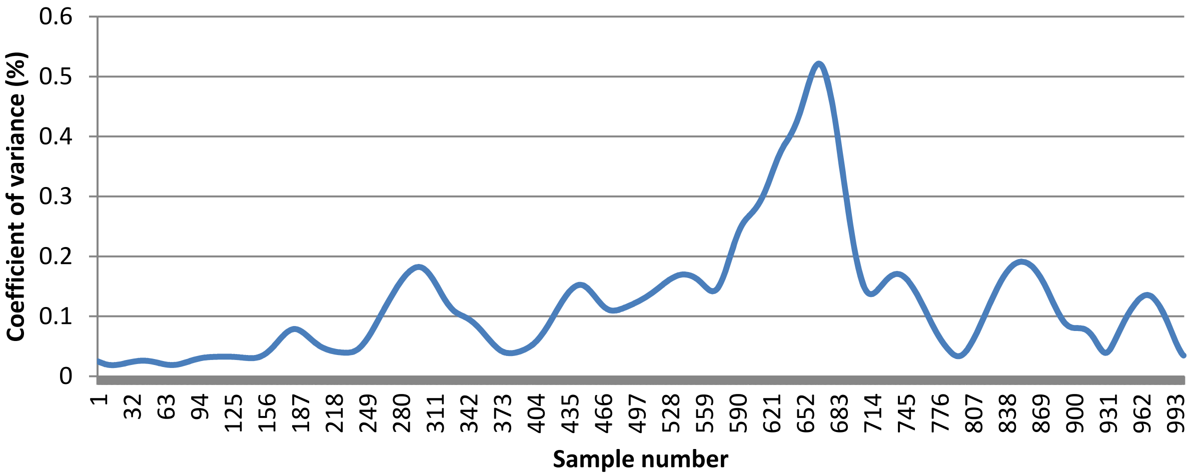

Figure 6.22. Coefficient of variance for sample C3.

6.5.2. Continuous wavelet analysis

Continuous wavelet transform (CWT) has a computational efficiency that provides an opportunity to extract features from non-stationary signals. It has the ability to separate the frequency component of signals [164]. Energy distribution in the time domain can be represented by a scalogram. This is the squared value of the wavelet transform, based on Parseval's theorem. The intensity of the signal can be represented in an image with different shades of color [165]. The Haar wavelet (Appendix III.b) was used as the mother wavelet for this study, selected because of the nature of the signals to be studied, and because of initial successful results for damage extraction using the Haar wavelet [166].

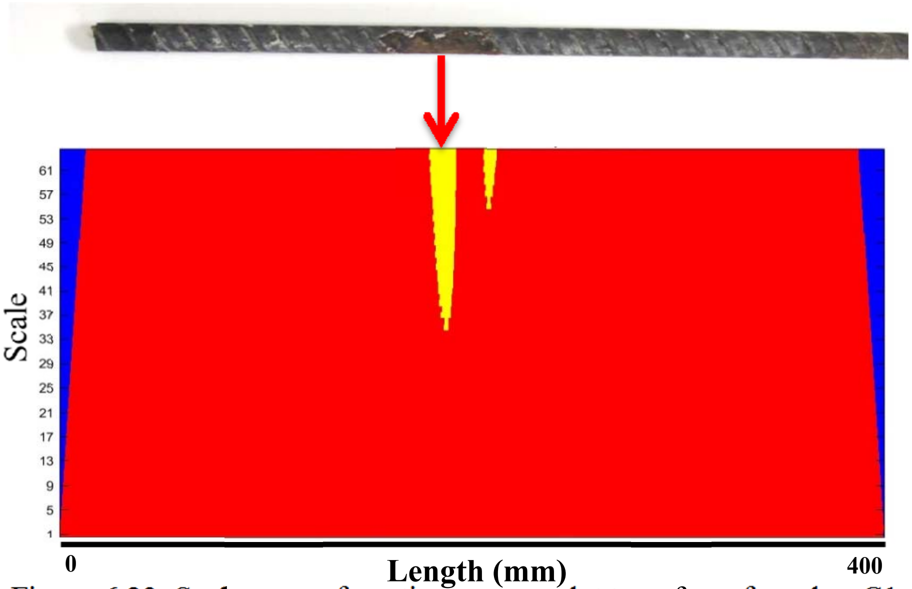

Figure 6.23. Scalogram of continuous wavelet transform for rebar C1.

Figure 6.23 presents a scalogram of a continuous wavelet transform from experimental tests on Sample C1. The two yellow colored sections in the middle of graph present different energy magnitudes related to the corrosion regions in rebar Sample C1. The two sections probably present two edges of the corroded region, and the sharp response confirms the importance of sharp edge effects on the magnetic stray energy field (Chapter 3, Section 2).

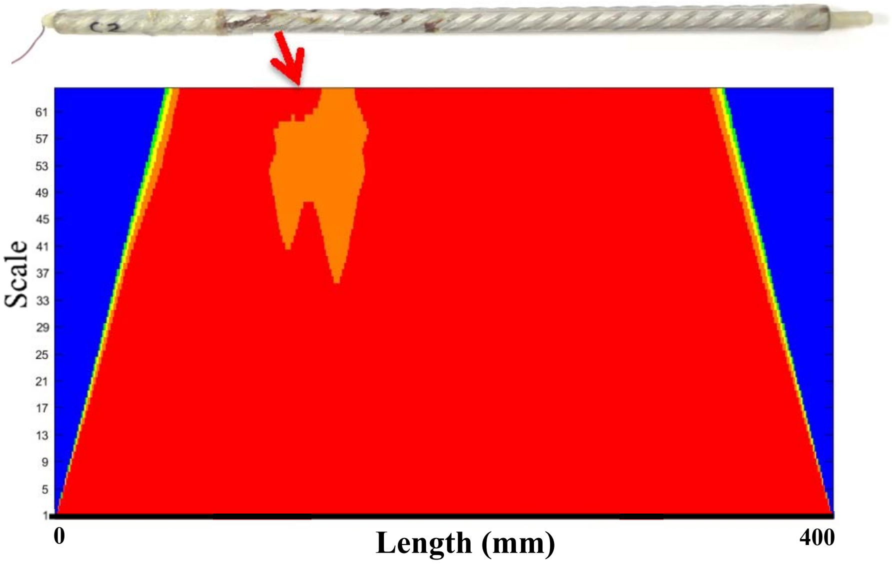

Figure 6.24. Scalogram of continuous wavelet transform for rebar C2.

Figure 6.24 presents a scalogram of a continuous wavelet transform of experimental test data collected on Sample C2. The orange colored section is different than the corrosion response of

Sample C1 because of the different nature of the corrosion. In bar C1 there were only two fairly large corroded regions, in C2 many smaller spot corrosions over the central part of the bar. The location of the orange area matches with the location of the spot corrosions on Sample C2, but although they were appeared separate on the bar, the scalogram analysis did not differentiate them. This may simply be the effect of the distance from the rebar to the magnetic sensors, or it may be because of a low sampling rate from the scanning device. Perhaps other sampling methods (several axial magnetometers) or analysis methods could be developed to differentiate them, but this is a subject for more research.

Figure 6.25 presents the scalogram of a continuous wavelet transform of the experimental data from Sample C3. The pink color section is a similar pattern as Sample C1. There is a difference between number of pink section (one) in Sample C3 and yellow sections (two) in Sample C1 because of the differences in length of the corroded region in these two samples. Also, the location of the pink area matches with the location of the corroded area on Sample C3.

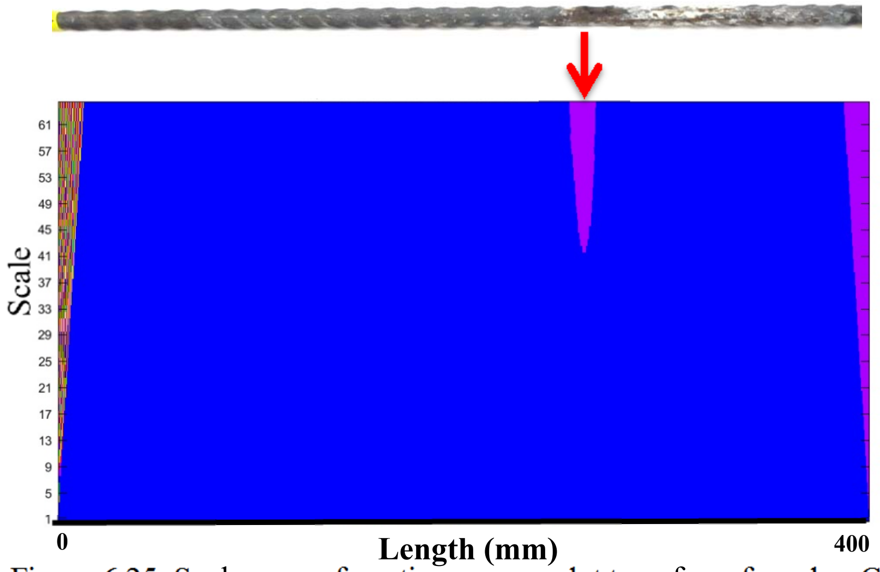

Figure 6.25. Scalogram of continuous wavelet transform for rebar C3.

6.6. Conclusion

In this chapter two set of experimental tests with the scanning passive magnetometer device were presented. The first set of experimental tests was done on rebars with different percentages of general corrosion (metal loss), and the second set was done on several locally corroded rebars.

The main signal processing method used to generate the results in this chapter was wavelet transform analysis to calculate the wavelet energy of the magnetic field around the rebars. For the first set of experiments, a Morlet wavelet was used as the mother wavelet, whereas for the second set a Harr wavelet was selected.

The following conclusions from these proof-of-concept tests are:

1. The passive magnetic field signal from a corroded rebar has more distortion of energy than that from a sound rebar. It can be detected by wavelet energy analysis. It demonstrates the proof of the concept that analysing the distortions in the natural magnetic field caused by corroded rebar (compared to the intact rebar) is a viable means of non-destructive and remote detection of corrosion under concrete cover.
2. There is a relation between the wavelet energy of the magnetic field signals and the percentage of metal loss because of general corrosion.
3. In order to determine more accurate relationships between wavelet energy and metal loss, more experimental tests are necessary, and this study is to be taken as a proof-of-concept pointing the direction for improvements in scanner design and test data analysis. Additional tests on different types of rebar of different diameters, with different nature of corrosion are necessary, and preferably this could be done in the field, analyzed, and then excavated for independent confirmation.
4. A continuous wavelet transform can be used to extract data about local corrosion regions from the passive magnetic field signal around the rebar. A color-differentiated scalogram is a good visual indicator of the presence of spot corrosion by showing different color ranges for corroded regions.
5. The location of corrosion spots can be extracted from scalogram analysis.
6. It appears that the scalogram characteristics may be useful to detect the type of corrosion in rebars, but as stated above, there remains experimental work to be done to refine a method that is quick, consistent and discriminatory.

Chapter 7

Conclusion and Recommendations

Taking advantage of the residual magnetic properties of ferromagnetic materials for non-destructive testing is the basic applied thrust of this thesis – the Passive Magnetic Inspection method (PMI). PMI was used for application to defect (corrosion, cracks) detection in steel bars in reinforced concrete structures. Defects (corrosion, cracks) in rebar change the direction of electron dipoles in magnetic domains of crystalline structures, which causes changes in the magnetic domains. These changes in magnetic domains result in anomalies in the natural magnetic field around the steel rebar, and these anomalies can be identified and analyzed.

Based on this premise, a scanning device was developed to scan the magnetic field around an embedded rebar from the concrete surface. The first version of the device was based on one sensor and a board to collect and transfer data to a PC. The second version of the device had an array of sensors to cover a larger area during scanning. A locating sensor was added to record the location of each point and a memory card reader board was added to record data during the scanning time. Numerical tools (filtering, modelling…) were developed to analyze the magnetometer scan data to identify anomalies arising from corrosion.

Besides using the magnetometer device to scan corroded rebar, an ultrasonic method was used for de-bonding detection of rebar in reinforced concrete, due to corrosion. In this study, a laser vibrometer was used to detect de-bonding. The actual displacement of a 1 MHz transducer was measured and modelled numerically by using the laser vibrometer at a scale of Nano-meters. Using this calibration of a transducer, 0.1 mm of de-bonding was detected using experimental tests, and the results were verified with numerical simulation.

In summary, the novel contributions are:

- an unique prototype was developed for defect (corrosion/crack) detection of reinforced concrete structures.
- a procedure of signal processing methods was defined for processing raw magnetic data.

- based on wavelet energy analysis, two equations were derive for general metal loss estimation.
- a unique method was used to calibrate a piezoelectric transducer.
- reinforcement de-bonding was detected using an ultrasonic method and laser vibrometer.
- local corrosion was detected using a continuous wavelet transform and data from the developed device.

7.1. Conclusions

The following items comprise summaries of results associated with the various chapters of this thesis.

7.1.1. Scanning device prototype

The last version of prototype with four main improvements worked well in the lab. The main improvements which applied to device are:

- New main board with higher processing capability
- Two parallel magnetic sensors
- Positioning sensor
- Memory card board

7.1.2. Defect detection in steel reinforcement

The numerical simulation results from theory-based calculations present a reasonable match with the experimental data for small defects in steel reinforcement bars located at 5 cm distance from the magnetometer. Similar to other passive NDT approaches, it is necessary to filter out non-related effects. The low frequency trend (the result of magnetic flux density of the bar) in experimental data is filtered out so that the high-frequency response from the defects can be extracted from the signal. Careful examination of the frequency spectrum of the experimental data provides a way to find the best cut-off frequency for the high pass filter for the experimental raw data. The following items are the main conclusion of this section:

- Defect diameter, depth and location of small drilled holes (defects) with respect to the sensor are parameters, which control the magnetic flux density of the bar.
- The angle of scanning magnetic data with respect to a defect orientation has a large effect on the amplitude of recorded magnetic flux density; therefore recording magnetic data at different angles can be useful for inverse geometrical modelling of defects.
- Edge effects are dominant among the parameters assessed, although the effects of changing the defect depth are also quite considerable.
- The results with respect to the geometric characteristics of defects indicate that data inversion “replication” of actual defect geometry in practice is possible, but it is a complicated procedure that likely requires magnetic flux density measurements in a number of different directions at each sampling site.
- Inverse modelling of defects based on absolute magnetic flux density values will be complicated if there is more than one defect affecting the response at a sampling site. Thus, resolvability of two closely spaced defects (for example) will be constrained.
- Nevertheless, the anomalies simulated in the laboratory work, although small, should be, in practice, highly detectable.
- Numerical simulation of altered magnetic flux density gives results that match well with experimental data. This match is apparent only after applying some simple signal processing techniques on both simulation and experimental data: numerical data were smoothed to reduce the FEM discretization effect; experimental data were filtered to remove low-frequency trends so as to reveal signal anomalies.
- Two holes in different positions (top, and bottom) were readily detected from the magnetic flux density measurements in the bar axis direction. The reason may be the presence of two edges for each hole which were crossed by the inspection device during the experimental test.
- As shown using auto-correlation analysis, there is a strong similarity of response between experimental and simulation data for the top and bottom holes.

- The side hole presented a different and much lower amplitude pattern, compared to the top and bottom holes. This difference is probably because of the position (left side) of the middle hole such that the (linear) magnetometer sensor did not cross the magnetic flux density around this hole optimally. The noise and signal levels were similar, so the desired anomaly related to that hole could not be extracted. Numerical simulation confirms the low magnetic magnitude effect of this hole configuration.

7.1.3. Principal component analysis

A PCA-based feature extraction method is shown to be applicable in detecting the location of holes in three different positions in a rebar. Also, Eigensignal analysis shows different patterns for each hole.

This study demonstrates a relatively fast investigation of PMI test data to find whether and where any corrosion or crack problems exist in reinforcement. The answers to these two questions are important when investigating the severity of such problems and affect decisions on whether and when to repair or replace reinforced concrete structures.

7.1.4. De-bonding assessment

In this study, a piezoelectric transducer was simulated numerically through the discrete finite element method. De-bonding of reinforcement from the mortar was experimentally tested through the laser vibrometer on four specimens and with two numerical simulations. The main conclusions from the experimental tests and numerical simulations of de-bonding are:

- Peak-to-peak amplitudes were higher for de-bonded specimens.
- Peak-to-peak amplitude was higher for de-bonded sample in numerical simulations.
- Frequency response ranges were wider for de-bonded specimens.
- Frequency response range was wider for de-bonded sample in numerical simulations.
- Frequency magnitudes were wider for de-bonded specimens.
- Frequency magnitude was wider for de-bonded sample in numerical simulations.

Results from the experimental tests and numerical simulations confirmed that when there is a perfect bonding between reinforcement and mortar, wave energy leaks through the mortar, and higher frequency waves dissipate before arriving at the end of the reinforcement bar, whereas for de-bonded samples, waves travel mostly through the reinforcement bar (less attenuation).

Perfect bonding of reinforcement is a desired condition for which any kind of defect on the reinforcement (corrosion, cracks) or in the concrete (crack) leads to reinforcement de-bonding from the mortar/concrete. In this study, it is shown that this method can be used to quantify de-bonding of reinforcement.

7.1.5. Metal loss and corrosion detection using wavelet analysis

Two sets of experimental tests were carried out with the magnetometer device. The first set of experimental tests was done on rebar with different percentages of general corrosion (metal loss), and the second set of experimental tests were done on locally corroded rebars. The main signal processing method used in these sets of tests was wavelet transform analysis to calculate wavelet energy of the magnetic field around the tested rebars. For the first set of experimental tests, a Morlet wavelet was used as a mother wavelet, whereas for the second set of experimental tests, a Harr wavelet was selected. Main conclusions for this study are:

1. The magnetic field signal of a corroded rebar has more chaos (noise) than that from a sound rebar, and this can be detected and quantified by wavelet energy analysis.
2. There is a relation between wavelet energy of magnetic field signals and percentage of metal loss, but more testing is necessary to refine this relationship in practice.
3. A continuous wavelet transform can be used to extract local corrosion data from the magnetic field signal around the locally corroded rebar.
4. The scalogram is a good indicator of corrosion by showing different color ranges for corroded areas.
5. The location of corrosion can be extracted from scalogram analysis, and it may be capable of detecting types of corrosion in rebars.

7.2. Contributions

The main scientific contributions of this project are:

- A new prototype for corrosion/crack detection of reinforced concrete structures was developed.
- A signal processing methodology for analyzing passive magnetic data from experimental tests.
- Ultrasonic transducer is characterized using a laser vibrometer.

7.3. Future work

Recommendations for possible future work in these areas are now formulated. These recommendations are categorized into three main sections: i) device development, ii) experimental tests, and iii) simulation and numerical modelling.

7.3.1. Device development

The second generation corrosion-detector magnetometer device is ready for field testing. However, it needs improvements which will be implemented for the next generation. Some improvements are:

- more robust wheels system to allow trouble free and quick transit.
- wireless transfer system.
- adding a system to show scanned data.
- real time analysis system to find corrosion/crack on site.

7.3.2. Experimental tests

The following experimental tests are suggestions regarding a more comprehensive experimental program that would help develop a better understanding of corrosion detection and quantification:

- ultrasonic test on corroded reinforced concrete using the laser vibrometer.
- passive magnetic test on corroded reinforced concrete using the magnetometer-based system but taking tri-axial field data during the scans.
- passive magnetic field corrosion detection at real sites to address environmental impacts and standardization practices.

7.3.3. Simulation and numerical modelling

Numerical simulation in this study was performed on simple bar. Rebar has a corrugated surface which helps it to achieve better bonding. This corrugation also makes change on the magnetic field around rebar compare to simple bar. Because of this it is difficult to carry out numerical simulations of more realistic bar shapes because of all the edges and corners that are introduced during the discretization. These issues are reasons for the following recommendations:

- Surface scanning of generally corroded rebars with laser scanning, and using scanned results as an input geometry for numerical simulations.
- Surface scanning of more locally corroded or cracked rebars with laser scanning, and using scanned results as an input geometry for numerical simulations.
- Numerical simulation of ultrasonic test on scanned rebars (general corrosion, and local corrosion).
- Examination of more issues related to discretization, smoothness of the surface, and so on, working toward better inversion of results so that in the field, practical value can be provided in a quick time frame to guide engineering decisions.

Bibliography

[1] Bohni, H. (2005) Corrosion in reinforced concrete structures (First Ed.). England and USA: Woodhead Publishing Limited and CRC Press LLC.

[2] Khan., A., and Teja., T.S. (2010). An Experimental Study On Prevention Of Reinforcement Corrosion In Concrete Structures, Ijrras 5 (2), November.

[3] Abdulrahman, A. S. Ismail, M., Hussain, M.S. (2011). Corrosion inhibitors for steel reinforcement in concrete a review, Scientific Research and Essays Vol. 6(20), pp. 4152-4162, 19 September.

[4] Ahmad, S. (2003). Reinforcement corrosion in concrete structures, its monitoring and service life prediction-a review, Cement & Concrete Composites 25, 459–471.

[5] Uhlig HH. (1949). The Cost of Corrosion in the United States. Chemical and Engineering News, 27: 2764.

[6] Transportation report, (1991), Special report 235, Highway Deicing comparing salt and calcium magnesium acetate, transportation research board, National Academi of Science, Washington, DC.

[7] Koch, G. H, Brongers, M. P. H., Thompson, N. G., Virmani, Y. P., and Payer, J. H. (2001) Corrosion Costs and Preventive Strategies in the United States. FHWA-RD-01-156. Springfield, VA, National Technical Information Service.

[8] G2MT labs report, (2013). Cost of corrosion annually in the US over $1 trillion, NACE corrosion costs study.

[9] BDM Federal, Inc. (1998). Corrosion Detection Technologies, Sector Study, Final report.

[10] Arndt, R., Jalinoos , F. (2009). NDE for corrosion detection in reinforced concrete structures – a benchmark approach., NDTCE'09, Non-Destructive Testing in Civil Engineering Nantes, France, June 30th – July 3rd.

[11] Broomfield, J. P. (2007) Corrosion of Steel in Concrete: Understanding, Investigation and Repair, E&FN Spon, London, Great Britain, 277p.

[12] Naumann, J., Haardt, P. (2003). NDT Methods for the inspection of highway structures, Proc. of the Int. Symp. NDT-CE, Sept., Berlin, Germany.

[13] Song, H.W., Saraswathy,V. (2007), Corrosion Monitoring of Reinforced Concrete structures – A Review, Int. J. Electrochem. Sci., 2, 1- 28.

[14] Clarke, E.T. (1989). Cobalt-60 Radiography of Concrete, Materials Evaluation, Vol.47, Jan., pp.1200-1204.

[15] Ujike,I., Okazaki,O., Yamate, M., and Matsue, H. (2011). A study on non-destructive measurement using Prompt Gamma-ray Analysis of chloride profile in concrete, Computational Vision and Medical Image Processing, Sep., 405-412.

[16] Ciolko, A. T., Tabatabai., H. (1999). Nondestructive Methods for Condition Evaluation of Pre-stressing Steel Strands in Concrete Bridges, NCHRP Web Document 23 (Project 10-53) Contractor's Final Report: Phase I-Technology Review.

[17] Grosse, C.U., Ohtsu, M. (2008). Acoustic Emission Testing, 406 p. 270 illus., Hardcover, ISBN: 978-3-540-69895-1.

[18] Blitz, J. (1997). Electrical and Magnetic Methods of Non-Destructive Testing, Chapman and Hall edition, ISBN: 0412791501.

[19] ASM Handbooks Online, Volume 17, Nondestructive Evaluation and Quality Control Magnetic Particle Inspection.

[20] Kundu, T. (2012). Ultrasonic and Electromagnetic NDE for Structure and Material Characterization, ISBN: 978-1-4398-3663-7.

[21] Gontarz, S., Radkowski, S., Jinsheng D. (2009). Use of passive magnetic method for stress assessment, Reliability, Maintainability and Safety. ICRMS. 8th International Conference on, vol., no., pp.966-971, 20-24 July 2009, doi: 10.1109/ICRMS.2009.5269977.

[22] Gontarz, S., Radkowski, S. (2012). Impact of Various Factors on Relationships between Stress and Eigen Magnetic Field in a Steel Specimen, Magnetics, IEEE Transactions on, vol.48, no.3, pp.1143-1154.

[23] Vlasov V.T., Dubov A.A. (2004). Physical bases of the metal magnetic memory method. ZAO "TISSO", Moscow, p 424.

[24] Kittel, C., Galt, J.K. (1956). Ferromagnetic Domain Theory, In: Frederick Seitz and David Turnbull, Editor(s), Solid State Physics, Academic Press, Volume 3, Pages 437-564.

[25] Bozorth, R.M. (1949). Ferromagnetic domains, Physica, Volume 15, Issues 1–2, April, Pages 207-219, ISSN 0031-8914, 10.1016/0031-8914(49)90045-2.

[26] Irodov, I.E. (1991). Basic laws of electromagnetism, Manual, Vyschaya Shkola, publishing house, Moscow.

[27] Bitter, F. (1931). On inhomogeneity's in the magnetization of ferromagnetic materials Phys. Rev. 38 1903–1905.

[28] Fowler, A., Fryer, Jr. and E. M. (1952). MAGNETIC DOMAINS ON SILICON IRON BY THE LONGITUDINAL KERR EFFECT, PhysRev.86.426.

[29] Saito, K., Park, H.S., Shindo, D., Yoshizawa, Y. (2006). Magnetic domain structure in Fe78.8−xCoxCu0.6Nb2.6Si9B9 nanocrystalline alloys studied by Lorentz microscopy, Journal of Magnetism and Magnetic Materials, Volume 305, Issue 2, October, Pages 304-309, 2006.01.015.

[30] Semat, H., Katz, R. (1958). Magnetic Properties of Matter, Robert Katz Publications, Chapter 33, paper 185.

[31] Kim, J., Lee, H., Lee, Y., Ryu, K., Shin, S., Akinaga, H. (2006). Effect of magnetic field on the magnetic domain structure of MnAs film on GaAs (001), Magnetics Conference, INTERMAG 2006. IEEE International, vol., no., pp.179, 8-12 May.

[32] Miron, I. M., Gaudin, G. S. (2010). Current-driven spin torque induced by the Rashba effect in a ferromagnetic metal layer, Nature Materials, vol. 9, no. 3, pp. 230–234.

[33] Liu, Z. Y., Li, N., Zhang, F., Xu, B., He, J. L., Yu, D. L., Tian, Y. J., Yu, G. H. (2008). Effect of magnetic field on domain-wall structures in two antiferromagnetically coupled Co/Pt multilayers, Appl. Phys. Lett. 93, 032502.

[34] Pyatako, A.P., Meshkov, G.A., Nikolaev, A.V., Nikolaeva, E.P., Logginov, A.S. (2008). Electric Field Induced Transformation of Magnetic Domain Structure in Magnetoelectric Iron Garnet Films, eprint arXiv: 0806.0811.

[35] Piao, H.G., Lee, H., Yoon, J., Kim, D.H., You, C.Y., Kim, T.W. (2010). Ratchet Effect of Domain Wall Motion by GHz AC Magnetic Field in Asymmetric Sawtooth-Shaped Ferromagnetic Nanowires, Magnetics, IEEE Transactions on, vol.46, no.6, pp.1844, 1847.

[36] Atherton, D.L., Ton, V. (1990). The effects of stress on a ferromagnet on a minor hysteresis loop," Magnetics, IEEE Transactions on, vol.26, no.3, pp.1153, 1156.

[37] Jiles, D.C., Atherton, D.L. (1986). Theory of ferromagnetic hysteresis, Journal of Magnetism and Magnetic Materials, Volume 61, Issues 1–2, September, Pages 48-60, ISSN 0304-8853, 10.1016/0304-8853(86)90066-1.

[38] Atherton, D.L., Rao, T.S., de Sa, V., Schonbachler, M. (1988). Thermodynamic correlation tests between magnetostrictive and magnetomechanical effects in 2% Mn pipeline steel, Magnetics, IEEE Transactions, vol.24, no.5, pp.2177,2180, Sep, doi: 10.1109/20.3425.

[39] Atherton, D.L., Rao, T.S., Schonbachler, M. (1988). Effect of applied stress on the reversible and irreversible differential permeabilities in 2% Mn pipeline steel," Magnetics, IEEE Transactions on, vol.24, no.3, pp.2033, 2037, May, doi: 10.1109/20.3397.

[40] Jiles, D. C., Atherton, D. L. (1984). Theory of the magnetization process in ferromagnets and its application to the magnetomechanical effect, J. Phys. D, Appl. Phys., vol. 17, pp. 1265-1281.

[41] Lloyd, M.G. (1910). Magnetic Hysteresis, the journal of the Franklin institute, vol. CLXX July, no. I.

[42] Vonsovskiy S.V. (1974). Magnetism. NEW YORK, HALSTED PRESS, a division of JON WILEY & SONS, INC.

[43] Billings, S., Pasion, L., Oldenburg, D., Foley, J. (2004). The influence of magnetic viscosity on electromagnetic sensors, Proceedings of EUDEM-SCOT2, International Conference on Requirements and Technologies for the Detection, Removal and Neutralization of Landmines and UXO.

[44] Coey, J.M.D. (2009). Magnetism and Magnetic Materials, Cambridge University Press.

[45] Jiles, D. (1998). Introduction to Magnetism and Magnetic Materials, Nelson Thornes, Cheltenham, UK.

[46] Morrish, A. H. (2001). The Physical Principles of Magnetism, Wiley-IEEE Press, New York/Piscataway, NJ.

[47] Bozorth, R. M. (1994). Ferromagnetism, Wiley-IEEE Press, New York/Piscataway, NJ.

[48] Keffer, F. (1967). The Magnetic Properties of Materials, Scientific American, Vol. 217, No. 3, September, pp. 222–234.

[49] Terunobu, M., Hanmin, J. (2012). The Physics of Ferromagnetism, Series: Springer Series in Materials Science, Vol. 158, XVI, 482 p. 261 illus., 52 illus.

[50] Wilson, J., Tian, G.Y., Barrans, S. (2007) Residual Magnetic Field Sensing for Stress Measurement and Defect Detection, Sensors and Actuators A: Physical 135/2, 381-387.

[51] Jiles, D. C. (1995). Theory of the magnetomechanical effect, J. Phys. D: Appl. Phys., 28, 1537 1546.

[52] Bulte, D.P., Langman, R.A. (2002). Origins of the magnetomechanical effect, Journal of Magnetism and Magnetic Materials, Volume 251, Issue 2, October, Pages 229-243, ISSN 0304-8853, 10.1016/S0304-8853(02)00588-7.

[53] Chen, Y., Kriegermeier-Sutton, B. K., Snyder, J. E., Dennis, K. W., McCallum, R. W., Jiles, D. C. (2001). Magnetomechanical effects under torsional strain in iron, cobalt and nickel, J. Magn. Magn. Mater., 236-131 138.

[54] Zheng, J., Cao, S., Wang, H. (2008). Modeling of magnetomechanical effect behaviors in a giant magnetostrictive device under compressive stress, Sensors and Actuators A: Physical, Volume 143, Issue 2, 16 May, Pages 204-214, ISSN 0924-4247.

[55] Mamsurova, L.G., Pigalskiy, K.S., Sakun, V.P., Scherbakova, L.G. (1992). Hysteresis of the dynamical magnetic permeability of a YBa2Cu3O7−δ single crystal, Physica C: Superconductivity, Volume 200, Issues 1–2, 15 September, Pages 175-182.

[56] Chess, P.M., Broomfield, J.P. (2013). Cathodic Protection of Steel in Concrete and Masonry (Second ed.). CRC Press.

[57] Ervin, B.L., Reis, H. (2008). Longitudinal guided waves for monitoring corrosion in reinforced mortar. Measurement Science & Technology, 19(1), 1–19.

[58] Wootton, I.A., Spainhour, L.K., Yazdani N. (2003). Corrosion of steel reinforcement in carbon fiber-reinforced polymer wrapped concrete cylinders J. Compos. Constr. 7 339–47

[59] Bennett, J., Schue, T.J., Clear, K.C., Lankard, D.L., Hartt, W.H., Swiat, W.J. (1993). Electrochemical chloride removal and protection of concrete bridge components: laboratory studies Strategic Highway Research Program Report (SHRP-S-657)
[60] Sanjurjo, A., Hettiarachchi, S., Lau, K., Wood, B., Cox, P. (1993). Development of metallic coatings for corrosion protection of steel rebars Strategic Highway Research Program Report (SHRP-I-622).
[61] Broomfield, J.P., Tinnear, J.S. (1992). Cathodic protection of reinforced concrete bridge components Strategic Highway Research Program Report (SHRP-92-618)
[61] Santoni, G.B., Lingyu, Y., Buli, X., Giurgiutiu, V. (2007). Lamb wave-mode tuning of piezoelectric wafer active sensors for structural health monitoring."TRANSACTIONS-AMERICAN SOCIETY OF MECHANICAL ENGINEERS JOURNAL OF VIBRATION AND ACOUSTICS 129, no. 6: 752.
[62] Sakharov, V.E., Kuznetsov, S.A., Zaitsev, B.D., Kuznetsova, I.E., Joshi, S.G. (2003). Liquid level sensor using ultrasonic Lamb waves, Ultrasonics, Volume 41, Issue 4, June, Pages 319-322, ISSN 0041-624X.
[63] Wasley, R.J. (1973). Stress wave propagation in solids. New York: Marcel Dekker Inc.
[64] Bolt, B. A. (1978). Earthquakes: A primer. San Francisco: W.H. Freeman and Co.
[65] Xia, J., Miller, R.D., Park, C.B. (2000). Advantage of calculating shear-wave velocity from surface waves with higher modes. Expanded Abstracts of Technical Program with Biographies, SEG, 70th Annual Meeting, Calgary, Canada, p. 1295–8. 1295 8 2000.
[66] Rayleigh, L. (1885). On waves propagated along the plane surface of an elastic solid: Proc. Lond. Math. Soc., 17, 4.
[67] Babuska, V., and Cara, M. (1991). Seismic anisotropy in the Earth: Kluwer Academic Publishers, Boston.
[68] Garland, G. D. (1979). Introduction to geophysics: Mantle, Core and Crust (2nd edition): W. B. Saunders Company, Philadelphia.
[69] Victorov, I.A. (1967). Rayleigh and Lamb waves. New York: Plenum Press.
[70] Yang, Y., Cascante, G., and Polak, M.A. (2009). Depth detection of surface-breaking cracks in concrete plates using fundamental Lamb modes. NDT&E International, 42(6), 501 - 512.
[71] Lai, C.G., Wilmanski, K. (2005). Surface waves in geomechanics: Direct and inverse modeling for soils and rocks. CISM Courses and Lectures No. 481, International Center for Mechanical Sciences.
[72] Blitz, J., Simpson, G. (1996). Ultrasonic Methods of Non-destructive Testing. Chapman & Hall: New York, NY.
[73] Su, Z., Ye, L., Lu, Y. (2006). Guided Lamb waves for identification of damage in composite structures: A review, Journal of Sound and Vibration, Volume 295, Issues 3–5, 22 August, Pages 753-780.
[74] Graff, K. (1991). Wave motion in elastic solids, Dover Publications Inc, New York, NY.
[75] Rose, J.L. (1999). Ultrasonic Waves in Solid Media, Cambridge University Press, Cambridge.

[76] Achenbach, J.D. (1973). Wave Propagation in Elastic Solids, North-Holland Publishing Company, Amesterdam.
[77] Ostachowicz, W., Kudela, P., Krawczuk, M., Żak, A. (2012). Guided Waves in Structures for SHM The Time – domain Spectral Element Method, ISBN–13: 978–0–470–97983–9 – John Wiley & Sons, (monograph).

[78] ACI standard building code requirements for reinforced concrete (ACI 318-77) American Concrete Institute. Committee 318, Detroit, Mich.: American Concrete Institute 1978, c1977.

[79] Jagiella, M., Fericean, S., Droxler, R., Dorneich, A. (2004). New magneto-inductive sensing principle and its implementation in sensors for industrial applications. Proceedings of IEEE , 2, 1020-1024.

[80] http://www.cui.com/product/components/encoders/incremental/modular/amt10-series

[81] Zhou, Y., Gencturk, B., Willam, K., Attar, A. (2014). Carbonation-Induced and Chloride-Induced Corrosion in Reinforced Concrete Structures. Journal of Materials in Civil Engineering, 0(0), 04014245. doi:10.1061/(ASCE)MT.1943-5534.0001209.

[82] Saraswathy, V., Song, H.W. (2007). Improving the durability of concrete by using inhibitors. Building and Environment, 42(1), 464-472.

[83] Mancio, M., Zhang, J., Monteiro, P. (2004). Nondestructive surface measurement of corrosion of reinforcing steel in concrete. Canadian Civil Engineer, 21(2), 12-14-18.

[84] Qian, S. Y. (2001). Assessment of corrosion of reinforcement in concrete. Canadian Civil Engineer, 18(2), 20-21.

[85] Fernandes, B., Titus, M., Karl Nims, D., Ghorbanpoor, A., and Devabhaktuni, V. (2012). "Field Test of Magnetic Methods for Corrosion Detection in Prestressing Strands in Adjacent Box-Beam Bridges. 'J. Bridge Eng. 17, Special Issue: Nondestructive Evaluation and Testing for Bridge Inspection and Evaluation, 984-988.

[86] Fernandes B., Wade, J.D., Nims, D.K., Devabhaktuni, V.K. (2012). A New Magnetic Sensor Concept for Nondestructive Evaluation of Deteriorated Prestressing Strand, Research in Nondestructive Evaluation, 23:1, 46-68, DOI: 10.1080/09349847.2011.626144.

[87] Gaydecki, P., Fernandes, B., Quek, S., Benitez, D., Miller, G., & Zaid, M. (2007). Inductive and magnetic field inspection systems for bar visualization and corrosion estimation in reinforced and pre-stressed concrete, Nondestructive Testing and Evaluation, 22:4, 255-298, DOI: 10.1080/10589750701362616.

[88] Krause, H.J., Wolf, W., Glaas, W., Zimmermann, E., Faley, M.I., Sawade, G., Mattheus, R., Neudert, G., Gampe, U., Krieger, J. (2002). SQUID array for magnetic inspection of prestressed concrete bridges, Physica C: Superconductivity, Volume 368, Issues 1–4, 1 March 2002, Pages 91-95, ISSN 0921-4534.

[89] Makar, J., Desnoyers, R. (2001). Magnetic field techniques for the inspection of steel under concrete cover, NDT & E International, Volume 34, Issue 7, Pages 445-456, ISSN 0963-8695.

[90] Bellingham, J.G., MacVicar, M.L. A., Nisenoff, M. Searson, P.C. (1986). Detection of magnetic fields generated by electrochemical corrosion. J. Electrochem. Soc. 133, 1753 – 1754.

[91] Bellingham, J.G., MacVicar, M.L. A., Nisenoff, M. (1987). SQUID technology applied to the study of electrochemical corrosion. IEEE Trans. Magn. 23, 477-479.

[92] Gallo, G.E. (2010). Investigation of Magnetic Sensing System for in-place Corrosion Characterization in Metals, PhD thesis, University of Illinois at Urbana-Champaign, IL, 153pp.

[93] Wilson, J.W., Tian, G.Y., Barrans, S. (2007). Residual magnetic field sensing for stress measurement. Sensors & Actuators: A. Physical, 135(2), 381-387.

[94] Doubov, A.A. (2000). The express-technique of welded joints examination with use of metal magnetic memory. NDT and E International, 33(6), 351-362.

[95] Doubov, A.A. (1998). Screening of weld quality using the metal magnetic memory. Weld World, 41, 196-199.

[96] Vlasov V.T., Doubov A.A. (2004). Physical bases of the metal magnetic memory method. Moscow: Tisso Co., 389 p.

[97] Hubert, A., & Schäfer, R. (1998). Magnetic Domains: The Analysis of Magnetic Microstructures, Springer, Berlin, New York.
[98] Wang, Z.D., Yao, K., Deng, B., & Ding, K.Q. (2010). Quantitative study of metal magnetic memory signal versus local stress concentration. NDT & E International, 43(6), 513-518.
[99] Sezgin, M. (2011). Simultaneous buried object detection and imaging technique utilizing fuzzy weighted background calculation and target energy moments on ground penetrating radar data EURASIP J. Adv. Signal Process 1–12.
[100] Döring, W. (1966). Mikromagnetismus. In S. Flügge (Ed.), Handbuch der physic, Springer, Berlin, Heidelberg, New York, Vol. 18/2 ed., pp. 341-437.
[101] Brown, W.F. (1962). Magnetostatic Principles in Ferromagnetism. Amsterdam: North-holland Pub. Co.
[102] Aharoni, A. (2000). Introduction to the Theory of Ferromagnetism. Oxford: Oxford University Press.
[103] Kronmüller, H. (1987). Theory of nucleation fields in inhomogeneous ferromagnets. Phys. Status Solidi B, 144, 385-396.
[104] Schneider, C.M., de Haas, O., Muschiol, U., Cramer, N., Oelsner, A., Klais, M., Schmidt, O., Fecher, G.H., Jark, W., Schönhense, G. (2001). Photoemission microscopy from magnetically coupled thin-film systems, Journal of Magnetism and Magnetic Materials, Volume 233, Issues 1–2, Pages 14-20.
[105] COMSOL Multiphysics®. 2014. Version 4.4. COMSOL, Inc., Burlington, MA, USA.
[106] Rose, J.H., Uzal, E., Moulder, J.C. (1995). Magnetic permeability and eddy current measurements. In Review of Progress in Quantitative NDE, 14, 315-322.
[107] Ribichini, R. (2011). Modelling of electromagnetic acoustic transducers. PhD Dissertation, Department of Mechanical Engineering, Imperial College London.
[108] Katkovnik, V.Y. (1979). Linear and nonlinear methods of nonparametric regression analysis. Avtomatika (Soviet Automatic Control), 5, 35-46.
[109] Fan, J., & Gijbels, I. (1999). Local polynomial modelling and its applications. Biometrics, 55(4), 1321-1321.
[110] Loader, C. (1999). Local regression and likelihood. New York: Springer.
[111] Ranjan, A., Jetley, P. (2014). Evaluation of signal smoothing algorithms for stability of a quadrotor MAV. Autonomous Robot Systems and Competitions (ICARSC), IEEE International Conference on, 309-314.
[112] Laurens, S., Balayssac, J.P., Rhazi, J., Klysz, G., Arliguie, G. (2005). Nondestructive evaluation of concrete moisture by GPR: experimental study and direct modeling. In Materials and Structures, pages 827–832, November.
[113] ACI 211.1-91 (2009). Standard Practice for Selecting Proportions for Normal, Heavyweight and Mass Concrete, American Concrete Institute, Farmington Mills, Michigan, USA.
[114] Kim, S., Surek, J., Baker-Jarvis, J. (2011). Electromagnetic metrology on concrete and corrosion. Journal of Research of the National Institute of Standards and Technology, 116, 655–669.
[115] Stoica, P., Moses, R.L. (1997). Introduction to spectral analysis (Vol.1). Upper Saddle River: Prentice hall.
[116] Ripka, P., Zikmund, A. (2013). Testing and Calibration of Magnetic Sensors. Sensor Letters. vol. 11, no. 1, p. 44-49. ISSN 1546-198X.
[117] Lewis, J. P. (1995). Fast template matching. Vision Interface, 95, 120-124.

[118] Oliver, J., Linero, D.L., Huespe, A.E., Manzoli, O.L. (2008). Two-dimensional modeling of material failure in reinforced concrete by means of a continuum strong discontinuity approach, Computer Methods in Applied Mechanics and Engineering, vol. 197, no. 5, pp. 332-348.
[119] Abdulrahman, A.S., Ismail, M., Hussain, M.S. (2011). Corrosion inhibitors for steel reinforcement in concrete: A review. Scientific Research and Essays, 6(20), 4152-4162.
[120] Ahmad, S. (2003). Reinforcement corrosion in concrete structures, its monitoring and service life prediction—a review. Cement and Concrete Composites, 25(4-5), 459-471.
[121] Hironaka, K., Uedaira, S. (1990). Soft magnetic properties of Co-Fe-P and Co-Fe-Sn-P amorphous films formed by electroplating, Magnetics, IEEE Transactions on, vol. 26, no. 5, pp. 2421-2424.
[122] Ying, T., Meng, P., FeiLu, C. (2011). Feature extraction based on the principal component analysis for pulsed magnetic flux leakage testing, Mechatronic Science, Electric Engineering and Computer (MEC), International Conference on, pp. 2564.
[123] Chen, T., Tian, G.Y., Sophian, A., Que, P.W. (2008). Feature extraction and selection for defect classification of pulsed eddy current NDT, NDT & E International, vol. 41, no. 6, pp. 467-476.
[124] Murthy, I.V.R., Rao, D.B. (1978). The zero-line method of interpreting total field magnetic anomalies of spherical ore-bodies, Pure and Applied Geophysics, vol. 116, no. 6, pp. 1191-1199.
[125] Ultrasonic Testing Of Materials At Level 2, IAEA, Vienna, 1988, IAEA-TECDOC-462.
[126] Hay, T.R., Rose, J.L. (2004). Interfacing guided wave ultrasound with wireless technology Proc. SPIE 5391 314–20.
[127] Ihn, J.B., Chang, F.K. (2008). Pitch-catch active sensing methods in structural health monitoring for aircraft structures. Struct Health Monit; 7(1): 5–19.
[128] Lu, Y., Li, J.C., Ye, L. (2013). Guided waves for damage detection in rebar-reinforced concrete beams. Constr Build Mater; 47(1): 370–378.
[129] Na, W.B., Kundu, T., Ehsani, M.R. (2003). Lamb waves for detecting delamination between steel bars and concrete. Comput-Aided Civ Inf; 18(1): 58–64.
[130] Wang, Y., Zhu, X., Hao, H. (2009). Guided wave propagation and spectral element method for debonding damage assessment in RC structures. J Sound Vib; 324(3): 751–772.
[131] Sharma, S., Mukherjee, A. (2010). Longitudinal guided waves for monitoring chloride corrosion in reinforcing bars in concrete. Struct Health Monit; 9(6): 555–567.
[132] Wu, Y., Cascante, G., West, J.S., Pandey, M.D. (2015). Ultrasonic Testing of a Grouted Steel Tank for Debonding Conditions. Journal of Environmental & Engineering Geophysics,20 (1): 31.
[133] Ryden, N., Park, C.B. (2004). Surface waves in inversely dispersive media: Near Surface Geophysics, 2(4) 187–197.
[134] Pavlakovic, B.N., Cawley, P. (2000). DISPERSE User's Manual Version 2.0.1.1. London, UK: Imperial College: University of London.
[135] Lowe M J S, (1995). Matrix techniques for modeling ultrasonic waves in multilayered media. IEEE Trans Ultrason Ferroelectr Freq Control; 42 (4): 525–42.
[136] Na, W.B., Kundu, T., Ehsani, M.R. (2002). Ultrasonic guided waves for steel bar concrete interface testing. Mater Eval; 60(4):437–44.
[137] Pochhammer, L. (1876). Uber die Fortpflanzungsgeschwindigkeiten kleiner Schwingungen in unbe-grenzten isotropen Kreiszylinder (On the propagation velocities of small vibrations in an infinite isotropic cylinder), Zeitschrift f¨ur Reine und Angewandte Mathematik 81 324–336. (in German)

[138] Chree, C. (1889). The equation of an isotropic elastic solid in polar and cylindrical coordinates, their solution and applications, Transactions of the Cambridge Philosophical Society 14, 250–369.

[139] Abramowitz, M., Stegun, I.A. (1965). Handbook of mathematical functions: With formulas, graphs, and mathematical tables, Dover Publications.

[140] Pavlakovic, B.N. (1998). Leaky guided ultrasonic waves in NDT. PhD Thesis. London (UK): Imperial College of Science Technology and Medicine.

[141] Ervin, B.L., Kuchma, D.A., Bernhard, J.T., Reis, H. (2009). Monitoring corrosion of rebar embedded in mortar using high frequency guided ultrasonic waves. ASCE J Eng Mech; 135(1): 9–19.

[142] Gautschi, G. (2002). Piezoelectric sensorics: Force, strain, pressure, acceleration and acoustic emission sensors, materials and amplifiers, Springer, Berlin.

[143] Nader, G., Silva, E.C.N., Adamowski, J.C. (2003). Determination of Piezoelectric Transducers Damping by Using Experimental and Finite Element Simulations", 10th SPIE (Annual International Symposium On Smart Structures And Materials), San Diego, California, USA.

[144] Filoux, E., Calle, S., Lou-Moeller, R., Lethiecq, M., Levassort, F. (2010). 3-D numerical modeling for axisymmetrical piezoelectric structures: Application to high-frequency ultrasonic transducers. IEEE Trans. Ultrason. Ferroelectr. Freq. Control , vol. 57 , pp.1188 -1199.

[145] San Miguel Medina, J.E., Buiochi, F., Adamowski, J.C. (2006). Numerical modeling of a circular piezoelectric ultrasonic transducer radiating in water. ABCM Symposium Series in Mechatronics - Vol. 2, pp. 458–464.

[146] Nader, G.. Silva, E.C.N., Adamowski, J.C. (2004). Effective Damping Value of Piezoelectric Transducer Determined by Experimental Techniques and Numerical Analysis. ABCM Symposium Series in Mechatronics - Vol. 1 - pp.271-279.

[147] Moser, F., Jacobs, L.J., Qu, J. (1999). Modelling elastic wave propagation in waveguides with the finite element method. – Nondestructive Testing and Evaluation International, vol.32, pp.225-234.

[148] Al-Hammoud, R., Soudki, K., Topper, T. H. (2011). Fatigue flexural behavior of corroded reinforced concrete beams repaired with CFRP sheets. Journal of composites for construction, 15, 42–51.

[149] Albora, A.M., Hisarli, Z.M., Ucan, O.N. (2004). Application of wavelet transform to magnetic data due to ruins of the Hittite, civilization in Turkey Pure and Applied Geophysics, 161 (2004), pp. 907–930.

[150] Blanco, S., Figliola, A., Quiroga, R.Q., Rosso, O.A., Serrano, E. (1998). Time–frequency analysis of electroencephalogram series. III. Wavelet packets and information cost function. Physical Review E 57 (1), 932–940.

[151] Labat, D. (2005). Recent advances in wavelet analyses: Part 1. A review of concepts.. Journal of Hydrology, Volume 314, Issues 1–4, 25 November 2005, Pages 275-288, ISSN 0022-1694.

[152] Hudgins, L.H., Friehe, C.A., Mayer, M.E. (1993). Wavelet transform and atmospheric turbulence, Phys. Rev. Lett., 71, 3279–3282.

[153] Brunet, Y., Collineau, S. (1995). Wavelet analysis of diurnal and nocturnal turbulence above a maize crop. In: Foufoula-Georgiou, E., Kumar, P. (Eds.), Wavelets in Geophysics. Academic Press, New York, pp. 129–150.

[154] Percival, D. (1995). On estimation of wavelet variance. Biometrika 82 (3), 619–631.

[155] Percival, D., Mofjeld, H.O. (1997). Analysis of subtidal coastal sea level fluctuations using wavelets. Journal of the American Statistical Association 92 (493), 868–880.

[156] Poggie, J., Smits, A.J. (1997). Wavelet analysis of wall-pressure fluctuations in a supersonic blunt-fin flow. AIAA Journal 35 (10), 1597–1604.

[157] Li, H., Nozaki, T. (1997). Application of wavelet cross-correlation analysis to a plane turbulent jet. JSME International Journal, Series B 40 (1), 58–66.

[158] Liu, P.C. (1995). Wavelet spectrum analysis and ocean wind waves. In: Foufoula-Georgiou, E. Kumar, P. (Eds), Wavelets in Geophysics. Academic Press, New York, pp. 151-166.

[159] Meneveau, C. (1991). Analysis of turbulence in the orthonormal wavelet representation. Journal of Fluid Mechanics 232, 469-520.

[160] Bafroui, H.H., Ohadi, A. (2014). Application of wavelet energy and Shannon entropy for feature extraction in gearbox fault detection under varying speed conditions, Neurocomputing, Volume 133, 10 June, Pages 437-445, ISSN 0925-2312.

[161] Van Niejenhuis1, C.B., Walbridge, S., Hansson, C. M. (2015). The performance of austenitic and duplex stainless steels in cracked concrete exposed to concentrated chloride brine, J Mater Sci (2016) 51:362–374. DOI 10.1007/s10853-015-9387-0.

[162] Tallavo, F., Pandey, M.D., Cascante, G. (2012). Probabilistic characterization of ultrasonic wave propagation in wood poles. Canadian Journal of Civil Engineering, 2012, 39:484-493, 10.1139/l2012-019.

[163] Breysse, D. (2012). Nondestructive evaluation of concrete strength: An historical review and a new perspective by combining NDT methods, Construction and Building Materials, Volume 33, August 2012, Pages 139-163, ISSN 0950-0618.

[164] Reda Taha, M.M., Noureldin, A., Lucero, J.L., Baca, T.J. (2006). Wavelet transform for structural health monitoring: a compendium of uses and features. Struct Health Monit 5(3):267–295. doi:10.1177/1475921706067741.

[165] Mallat, S. (1999). A wavelet tour of signal processing, 2nd edn. Academic Press, New York.

[166] Smith, C., Akujuobi, C.M., Hamory, P., Kloesel, K. (2007). An approach to vibration analysis using wavelets in an application of aircraft health monitoring, Mechanical Systems and Signal Processing, Volume 21, Issue 3, April, Pages 1255-1272, ISSN 0888-3270.

[167] T. L. Szabo and P. A. Lewin, "Piezoelectric materials for imaging", J Ultrasound Med., vol. 26, pp. 283-288.

[168] Schmerr, L.W., Lopez-Sanchez, A., Huang, R. (2006). Complete ultrasonic transducer characterization and its use for models and measurements, Ultrasonics, Volume 44, Supplement, 22 December, Pages e753-e757, ISSN 0041-624X.

[169] Elgazzar, M. (2011). A New Method to Improve the Simulation Of Piezoelectric Transducer Using PSPIGE And Genetic Algorithms, International Journal on Computer Science and Engineering, vol. 3, pp. 1689-1696..

[170] Daubechies, I. (1990). The wavelet transform, time-frequency localization and signal analysis. IEEE Transactions on Information Theory, 36(5):961-1005, Sep 1990.

[171] Daubechies, I. (1992). Ten Lectures on Wavelets. Society for Industrial and Applied Mathematics.

[172] Labat, D. (2005). Recent advances in wavelet analyses: Part 1. a review of concepts. Journal of Hydrology, 314(14):275 - 288.

[173] Mallat. S. (2008). A Wavelet Tour of Signal Processing, Third Edition: The Sparse Way. Academic Press, 3rd edition.

Apendix I:

Matlab code of numerical simulation (Chapter 3):

```
function out = model
%
% FinalDrilledrebarmodel.m
%
% Model exported on Mar 25 2016, 16:39 by COMSOL 4.4.0.248.


import com.comsol.model.*
import com.comsol.model.util.*

model = ModelUtil.create('Model');

model.modelPath('C:\JournalPapersForMyThesis\1\new journal Journal of
Nondestructive Evaluation\Review results 21-10-2015\element size analysis');

model.modelNode.create('mod1');

model.geom.create('geom1', 3);

model.mesh.create('mesh1', 'geom1');

model.physics.create('mfnc', 'MagnetostaticsNoCurrents', 'geom1');

model.geom('geom1').feature.create('cyl1', 'Cylinder');
model.geom('geom1').feature('cyl1').set('r', '0.008');
model.geom('geom1').feature('cyl1').set('h', '0.555');
model.geom('geom1').runAll;
model.geom('geom1').feature('cyl1').set('axistype', 'x');
model.geom('geom1').runAll;

model.name('1.mph');

model.geom('geom1').run;

model.param.set('gB', '5e-5[T]');
model.param.descr('gB', 'Geomagnetic');
model.param.descr('gB', 'Geomagnetic Field');

model.physics('mfnc').prop('BackgroundField').set('SolveFor', 1,
'ReducedField');
model.physics('mfnc').prop('BackgroundField').set('Hb', {'gB/mu0_const'
'gB/mu0_const' 'gB/mu0_const'});
model.physics('mfnc').feature('mfc1').set('mur_mat', 1, 'userdef');
model.physics('mfnc').feature.create('exfd1', 'ExternalMagneticFluxDensity',
2);
model.physics('mfnc').feature('exfd1').selection.all;
model.physics('mfnc').feature.create('ms1', 'MagneticShielding', 2);
model.physics('mfnc').feature('ms1').selection.all;
model.physics('mfnc').feature('ms1').set('mur_mat', 1, 'userdef');
```

```
model.physics('mfnc').feature('ms1').set('mur', {'75000' '0' '0' '0' '75000'
'0' '0' '0' '75000'});
model.physics('mfnc').feature('ms1').set('ds', 1, '0.008');

model.mesh('mesh1').feature.create('ftet1', 'FreeTet');
model.mesh('mesh1').feature('size').set('custom', 'off');
model.mesh('mesh1').feature('size').set('hauto', '3');
model.mesh('mesh1').run;

model.study.create('std1');
model.study('std1').feature.create('stat', 'Stationary');
model.study('std1').feature('stat').activate('mfnc', true);

model.sol.create('sol1');
model.sol('sol1').study('std1');
model.sol('sol1').feature.create('st1', 'StudyStep');
model.sol('sol1').feature('st1').set('study', 'std1');
model.sol('sol1').feature('st1').set('studystep', 'stat');
model.sol('sol1').feature.create('v1', 'Variables');
model.sol('sol1').feature('v1').set('control', 'stat');
model.sol('sol1').feature.create('s1', 'Stationary');
model.sol('sol1').feature('s1').feature.create('fc1', 'FullyCoupled');
model.sol('sol1').feature('s1').feature.create('i1', 'Iterative');
model.sol('sol1').feature('s1').feature('i1').set('linsolver', 'cg');
model.sol('sol1').feature('s1').feature('fc1').set('linsolver', 'i1');
model.sol('sol1').feature('s1').feature('i1').feature.create('mg1',
'Multigrid');
model.sol('sol1').feature('s1').feature('i1').feature('mg1').set('prefun',
'amg');
model.sol('sol1').feature('s1').feature.remove('fcDef');
model.sol('sol1').attach('std1');
model.sol('sol1').runAll;

model.result.create('pg1', 'PlotGroup3D');
model.result('pg1').run;
model.result('pg1').set('edges', 'off');
model.result('pg1').feature.create('slc1', 'Slice');
model.result('pg1').feature('slc1').set('expr', 'mfnc.normB');
model.result('pg1').feature('slc1').set('descr', 'Magnetic flux density
norm');
model.result('pg1').feature('slc1').set('quickplane', 'xy');
model.result('pg1').feature('slc1').set('quickzmethod', 'coord');
model.result('pg1').feature('slc1').set('quickz', '-15');
model.result('pg1').run;
model.result('pg1').feature('slc1').set('quickz', '0');
model.result('pg1').feature('slc1').set('quickzmethod', 'number');
model.result('pg1').run;
model.result('pg1').set('allowtableupdate', true);
model.result('pg1').set('renderdatacached', true);
model.result('pg1').feature('slc1').set('quickplane', 'yz');
model.result('pg1').run;
model.result('pg1').feature('slc1').set('quickxnumber', '20');
model.result('pg1').run;
model.result('pg1').run;
model.result('pg1').feature.create('vol1', 'Volume');
model.result('pg1').feature('vol1').set('expr', 'mfnc.normB');
```

```
model.result('pg1').feature('vol1').set('descr', 'Magnetic flux density
norm');
model.result('pg1').run;
model.result('pg1').run;
model.result('pg1').feature('slc1').active(false);
model.result('pg1').run;

model.physics('mfnc').prop('BackgroundField').set('Hb', {'1' '1'
'gB/mu0_const'});

model.sol('sol1').study('std1');
model.sol('sol1').feature.remove('s1');
model.sol('sol1').feature.remove('v1');
model.sol('sol1').feature.remove('st1');
model.sol('sol1').feature.create('st1', 'StudyStep');
model.sol('sol1').feature('st1').set('study', 'std1');
model.sol('sol1').feature('st1').set('studystep', 'stat');
model.sol('sol1').feature.create('v1', 'Variables');
model.sol('sol1').feature('v1').set('control', 'stat');
model.sol('sol1').feature.create('s1', 'Stationary');
model.sol('sol1').feature('s1').feature.create('fc1', 'FullyCoupled');
model.sol('sol1').feature('s1').feature.create('i1', 'Iterative');
model.sol('sol1').feature('s1').feature('i1').set('linsolver', 'cg');
model.sol('sol1').feature('s1').feature('fc1').set('linsolver', 'i1');
model.sol('sol1').feature('s1').feature('i1').feature.create('mg1',
'Multigrid');
model.sol('sol1').feature('s1').feature('i1').feature('mg1').set('prefun',
'amg');
model.sol('sol1').feature('s1').feature.remove('fcDef');
model.sol('sol1').attach('std1');
model.sol('sol1').runAll;

model.result('pg1').run;
model.result('pg1').run;
model.result('pg1').feature.remove('vol1');
model.result('pg1').run;
model.result('pg1').run;
model.result('pg1').feature.remove('slc1');
model.result('pg1').run;
model.result('pg1').feature.create('vol1', 'Volume');
model.result('pg1').feature('vol1').set('expr', 'mfnc.normB');
model.result('pg1').feature('vol1').set('descr', 'Magnetic flux density
norm');
model.result('pg1').run;

model.view('view1').set('scenelight', 'off');
model.view('view1').set('transparency', 'off');

model.physics('mfnc').prop('BackgroundField').set('Hb', {'1' '1' '1'});

model.mesh('mesh1').run;

model.sol('sol1').updateSolution;

model.result('pg1').run;
```

```
model.physics('mfnc').prop('BackgroundField').set('Hb', {'1' '1'
'gB/mu0_const'});

model.sol('sol1').updateSolution;

model.result('pg1').run;
model.result('pg1').run;

model.physics('mfnc').prop('BackgroundField').set('Hb', {'gB/mu0_const' '1'
'1'});

model.result('pg1').run;

model.sol('sol1').updateSolution;

model.result('pg1').run;
model.result('pg1').run;
model.result('pg1').feature('vol1').set('rangedataactive', 'off');
model.result('pg1').feature('vol1').set('rangecoloractive', 'on');
model.result('pg1').feature('vol1').set('rangedataactive', 'off');
model.result('pg1').feature('vol1').set('rangecolormin', '5E-5');
model.result('pg1').feature('vol1').set('rangecolormax', '8E-5');

model.physics('mfnc').prop('BackgroundField').set('Hb', {'gB/mu0_const'
'gB/mu0_const' 'gB/mu0_const'});

model.sol('sol1').updateSolution;

model.result('pg1').run;

model.material.create('mat1');
model.material.create('mat2');
model.material('mat2').name('A572 Grade 50 [solid]');
model.material('mat2').info.create('Composition');
model.material('mat2').info('Composition').body('bal. Fe, 1.35 Mn, 0.23 C
max, (0.005-0.05) Nb, (0.01-0.15) V, 0.015 N max, 0.04 P max, 0.05 S max, 0.4
Si max (wt%)');
model.material('mat2').set('family', 'iron');
model.material('mat2').propertyGroup('def').set('dL', '(dL(T[1/K])-
dL(Tempref[1/K]))/(1+dL(Tempref[1/K]))');
model.material('mat2').propertyGroup('def').set('CTE', 'CTE(T[1/K])[1/K]');
model.material('mat2').propertyGroup('def').set('thermalconductivity',
'k(T[1/K])[W/(m*K)]');
model.material('mat2').propertyGroup('def').set('thermalexpansioncoefficient'
, '(alpha(T[1/K])[1/K]+(Tempref-293[K])*if(abs(T-Tempref)>1e-
3,(alpha(T[1/K])[1/K]-alpha(Tempref[1/K])[1/K])/(T-
Tempref),d(alpha(T[1/K]),T)[1/K]))/(1+alpha(Tempref[1/K])[1/K]*(Tempref-
293[K]))');
model.material('mat2').propertyGroup('def').set('mu', 'mu(T[1/K])[Pa]');
model.material('mat2').propertyGroup('def').set('density',
'rho(T[1/K])[kg/m^3]');
model.material('mat2').propertyGroup('def').set('kappa',
'kappa(T[1/K])[Pa]');
model.material('mat2').propertyGroup('def').func.create('dL', 'Piecewise');
```

```
model.material('mat2').propertyGroup('def').func('dL').set('funcname', 'dL');
model.material('mat2').propertyGroup('def').func('dL').set('arg', 'T');
model.material('mat2').propertyGroup('def').func('dL').set('extrap',
'constant');
model.material('mat2').propertyGroup('def').func('dL').set('pieces', {'294.0'
'1065.0' '-0.002440417+5.044861E-6*T^1+1.2594E-8*T^2-4.727316E-12*T^3';
'1065.0' '1254.0' '-0.0145039+2.05632E-5*T^1'});
model.material('mat2').propertyGroup('def').func.create('CTE', 'Piecewise');
model.material('mat2').propertyGroup('def').func('CTE').set('funcname',
'CTE');
model.material('mat2').propertyGroup('def').func('CTE').set('arg', 'T');
model.material('mat2').propertyGroup('def').func('CTE').set('extrap',
'constant');
model.material('mat2').propertyGroup('def').func('CTE').set('pieces',
{'294.0' '1065.0' '5.044861E-6+2.5188E-8*T^1-1.418195E-11*T^2'});
model.material('mat2').propertyGroup('def').func.create('k', 'Piecewise');
model.material('mat2').propertyGroup('def').func('k').set('funcname', 'k');
model.material('mat2').propertyGroup('def').func('k').set('arg', 'T');
model.material('mat2').propertyGroup('def').func('k').set('extrap',
'constant');
model.material('mat2').propertyGroup('def').func('k').set('pieces', {'294.0'
'500.0' '234.5899-1.989374*T^1+0.007548095*T^2-1.209641E-5*T^3+6.968605E-
9*T^4'; '500.0' '774.0' '40.19827+0.08548251*T^1-1.715148E-4*T^2+8.281573E-
8*T^3'});
model.material('mat2').propertyGroup('def').func.create('alpha',
'Piecewise');
model.material('mat2').propertyGroup('def').func('alpha').set('funcname',
'alpha');
model.material('mat2').propertyGroup('def').func('alpha').set('arg', 'T');
model.material('mat2').propertyGroup('def').func('alpha').set('extrap',
'constant');
model.material('mat2').propertyGroup('def').func('alpha').set('pieces',
{'294.0' '1065.0' '4.702292E-6+2.930806E-8*T^1-2.805246E-11*T^2+9.790445E-
15*T^3'; '1065.0' '1254.0' '-1.044381E-6+1.019586E-8*T^1'});
model.material('mat2').propertyGroup('def').func.create('mu', 'Piecewise');
model.material('mat2').propertyGroup('def').func('mu').set('funcname', 'mu');
model.material('mat2').propertyGroup('def').func('mu').set('arg', 'T');
model.material('mat2').propertyGroup('def').func('mu').set('extrap',
'constant');
model.material('mat2').propertyGroup('def').func('mu').set('pieces', {'4.0'
'274.0' '8.626526E10+1636497.0*T^1-108981.6*T^2+291.1261*T^3-0.3377859*T^4';
'274.0' '1050.0' '8.301552E10+9184755.0*T^1-38834.5*T^2'; '1050.0' '1500.0'
'7.694034E10-2.580357E7*T^1'});
model.material('mat2').propertyGroup('def').func.create('rho', 'Piecewise');
model.material('mat2').propertyGroup('def').func('rho').set('funcname',
'rho');
model.material('mat2').propertyGroup('def').func('rho').set('arg', 'T');
model.material('mat2').propertyGroup('def').func('rho').set('extrap',
'constant');
model.material('mat2').propertyGroup('def').func('rho').set('pieces',
{'294.0' '1065.0' '7919.309-0.124948*T^1-2.88651E-4*T^2+1.131694E-7*T^3';
'1065.0' '1254.0' '8184.48-0.4654125*T^1'});
model.material('mat2').propertyGroup('def').func.create('kappa',
'Piecewise');
model.material('mat2').propertyGroup('def').func('kappa').set('funcname',
'kappa');
model.material('mat2').propertyGroup('def').func('kappa').set('arg', 'T');
```

```
model.material('mat2').propertyGroup('def').func('kappa').set('extrap',
'constant');
model.material('mat2').propertyGroup('def').func('kappa').set('pieces',
{'4.0' '100.0' '1.800573E11-3478717.0*T^1+151512.1*T^2-
5485.327*T^3+28.28329*T^4'; '100.0' '274.0' '1.818111E11-
4.023792E7*T^1+84204.68*T^2-94.09453*T^3'; '274.0' '1500.0' '1.842649E11-
2.509462E7*T^1-28588.37*T^2'});
model.material('mat2').propertyGroup('def').addInput('temperature');
model.material('mat2').propertyGroup('def').addInput('strainreferencetemperat
ure');
model.material('mat2').propertyGroup.create('Enu', 'Young''s modulus and
Poisson''s ratio');
model.material('mat2').propertyGroup('Enu').set('youngsmodulus',
'E(T[1/K])[Pa]');
model.material('mat2').propertyGroup('Enu').set('poissonsratio',
'nu(T[1/K])');
model.material('mat2').propertyGroup('Enu').func.create('E', 'Piecewise');
model.material('mat2').propertyGroup('Enu').func('E').set('funcname', 'E');
model.material('mat2').propertyGroup('Enu').func('E').set('arg', 'T');
model.material('mat2').propertyGroup('Enu').func('E').set('extrap',
'constant');
model.material('mat2').propertyGroup('Enu').func('E').set('pieces', {'4.0'
'274.0' '2.217366E11+5020008.0*T^1-305140.4*T^2+926.6601*T^3-1.145454*T^4';
'274.0' '1050.0' '2.109875E11+4.572844E7*T^1-106319.6*T^2'; '1050.0' '1500.0'
'2.024261E11-6.77381E7*T^1'});
model.material('mat2').propertyGroup('Enu').func.create('nu', 'Piecewise');
model.material('mat2').propertyGroup('Enu').func('nu').set('funcname', 'nu');
model.material('mat2').propertyGroup('Enu').func('nu').set('arg', 'T');
model.material('mat2').propertyGroup('Enu').func('nu').set('extrap',
'constant');
model.material('mat2').propertyGroup('Enu').func('nu').set('pieces', {'4.0'
'120.0' '0.2850355-1.662951E-6*T^1'; '120.0' '274.0' '0.2848011-7.147353E-
6*T^1+6.558945E-8*T^2'; '274.0' '1054.0' '0.2712267+7.030261E-5*T^1-
4.856929E-8*T^2+1.246582E-11*T^3'; '1054.0' '1500.0' '0.3165268-1.242823E-
6*T^1+1.661461E-9*T^2'});
model.material('mat2').propertyGroup('Enu').addInput('temperature');
model.material('mat2').set('family', 'iron');
model.material('mat2').selection.all;

model.physics('mfnc').feature('ms1').set('mur_mat', 1, 'from_mat');

model.sol('sol1').updateSolution;

model.result('pg1').run;
model.result('pg1').feature.create('vol2', 'Volume');
model.result('pg1').run;
model.result('pg1').feature('vol1').active(false);
model.result('pg1').run;
model.result('pg1').run;
model.result('pg1').feature('vol2').set('expr', 'mfnc.normB');
model.result('pg1').feature('vol2').set('descr', 'Magnetic flux density
norm');
model.result('pg1').run;

model.name('1.mph');
```

```
model.result('pg1').run;

model.geom('geom1').run('cyl1');
model.geom('geom1').feature.create('cyl2', 'Cylinder');
model.geom('geom1').feature('cyl2').set('r', '0.00291');
model.geom('geom1').feature('cyl2').set('h', '0.01241');
model.geom('geom1').feature('cyl2').setIndex('pos', '0.17', 0);
model.geom('geom1').feature('cyl1').set('h', '0.564');
model.geom('geom1').feature('cyl2').setIndex('pos', '0.145', 0);
model.geom('geom1').runAll;
model.geom('geom1').feature('cyl2').setIndex('pos', '-0.008', 1);
model.geom('geom1').runAll;
model.geom('geom1').feature('cyl2').set('axistype', 'x');
model.geom('geom1').runAll;
model.geom('geom1').feature('cyl2').set('axistype', 'y');
model.geom('geom1').runAll;
model.geom('geom1').feature('cyl2').set('axistype', 'z');
model.geom('geom1').runAll;
model.geom('geom1').feature('cyl2').setIndex('pos', '0', 1);
model.geom('geom1').runAll;
model.geom('geom1').feature('cyl2').setIndex('pos', '-0.008', 2);
model.geom('geom1').runAll;

model.view('view1').set('renderwireframe', true);
model.view('view1').set('transparency', 'on');
model.view('view1').set('renderwireframe', false);

model.geom('geom1').feature('cyl2').setIndex('pos', '0.008', 2);
model.geom('geom1').runAll;
model.geom('geom1').feature('cyl2').setIndex('pos', '-0.00359', 2);
model.geom('geom1').runAll;
model.geom('geom1').feature('cyl2').setIndex('pos', '-0.00358', 2);
model.geom('geom1').runAll;
model.geom('geom1').feature('cyl2').setIndex('pos', '-0.00350', 2);
model.geom('geom1').runAll;
model.geom('geom1').feature('cyl2').setIndex('pos', '-0.003', 2);
model.geom('geom1').runAll;
model.geom('geom1').feature('cyl2').setIndex('pos', '-0.0036', 2);
model.geom('geom1').runAll;
model.geom('geom1').feature('cyl2').setIndex('pos', '-0.0037', 2);
model.geom('geom1').runAll;
model.geom('geom1').feature('cyl2').setIndex('pos', '-0.004', 2);
model.geom('geom1').runAll;
model.geom('geom1').feature('cyl2').setIndex('pos', '-0.0045', 2);
model.geom('geom1').runAll;
model.geom('geom1').feature('cyl2').setIndex('pos', '-0.0044', 2);
model.geom('geom1').runAll;
model.geom('geom1').run('cyl2');
model.geom('geom1').feature.create('cyl3', 'Cylinder');
model.geom('geom1').feature('cyl3').setIndex('pos', '0.268', 0);
model.geom('geom1').feature('cyl3').set('r', '0.003395');
model.geom('geom1').feature('cyl3').set('h', '0.00569');
model.geom('geom1').feature('cyl3').set('axistype', 'y');
model.geom('geom1').runAll;
model.geom('geom1').feature('cyl3').setIndex('pos', '0.008', 2);
model.geom('geom1').runAll;
```

```
model.geom('geom1').feature('cyl3').setIndex('pos', '0.000', 2);
model.geom('geom1').runAll;
model.geom('geom1').feature('cyl3').setIndex('pos', '0.00231', 1);
model.geom('geom1').runAll;
model.geom('geom1').feature('cyl3').setIndex('pos', '0.1', 2);
model.geom('geom1').runAll;
model.geom('geom1').feature('cyl3').setIndex('pos', '0.0', 2);
model.geom('geom1').runAll;
model.geom('geom1').feature('cyl2').setIndex('pos', '-0.00445', 2);
model.geom('geom1').runAll;
model.geom('geom1').feature('cyl2').setIndex('pos', '-0.00359', 2);
model.geom('geom1').runAll;
model.geom('geom1').feature('cyl2').setIndex('pos', '-0.00358', 2);
model.geom('geom1').runAll;
model.geom('geom1').feature('cyl2').setIndex('pos', '-0.00355', 2);
model.geom('geom1').runAll;
model.geom('geom1').feature('cyl2').setIndex('pos', '-0.00350', 2);
model.geom('geom1').runAll;
model.geom('geom1').feature('cyl2').setIndex('pos', '-0.0036', 2);
model.geom('geom1').runAll;
model.geom('geom1').feature('cyl2').setIndex('pos', '-0.0038', 2);
model.geom('geom1').runAll;
model.geom('geom1').feature('cyl2').setIndex('pos', '-0.0039', 2);
model.geom('geom1').runAll;
model.geom('geom1').run('cyl3');
model.geom('geom1').feature.create('cyl4', 'Cylinder');
model.geom('geom1').feature('cyl4').set('r', '0.003255');
model.geom('geom1').feature('cyl4').set('h', '0.00636');
model.geom('geom1').feature('cyl4').setIndex('pos', '0.492', 0);
model.geom('geom1').runAll;
model.geom('geom1').feature('cyl4').setIndex('pos', '-0.008', 2);
model.geom('geom1').runAll;
model.geom('geom1').feature('cyl4').setIndex('pos', '-0.007', 2);
model.geom('geom1').runAll;
model.geom('geom1').feature('cyl4').setIndex('pos', '-0.0075', 2);
model.geom('geom1').runAll;
model.geom('geom1').feature('cyl4').setIndex('pos', '-0.0074', 2);
model.geom('geom1').runAll;
model.geom('geom1').feature('cyl4').setIndex('pos', '-0.0073', 2);
model.geom('geom1').runAll;
model.geom('geom1').feature('cyl4').setIndex('pos', '-0.00732', 2);
model.geom('geom1').runAll;
model.geom('geom1').feature('cyl2').setIndex('pos', '-0.00395', 2);
model.geom('geom1').runAll;
model.geom('geom1').feature('cyl2').setIndex('pos', '-0.00396', 2);
model.geom('geom1').runAll;
model.geom('geom1').feature('cyl2').setIndex('pos', '-0.003965', 2);
model.geom('geom1').runAll;
model.geom('geom1').run;

model.material('mat2').selection.set([1 2 3 4 5 6 7 8 9]);
model.material('mat2').selection.all;
model.material.remove('mat1');
model.material('mat2').selection.set([1]);

model.geom('geom1').feature('cyl4').setIndex('pos', '-0.0073', 2);
```

```
model.geom('geom1').runAll;
model.geom('geom1').feature('cyl4').setIndex('pos', '-0.007', 2);
model.geom('geom1').runAll;
model.geom('geom1').feature('cyl4').setIndex('pos', '-0.00732', 2);
model.geom('geom1').runAll;
model.geom('geom1').feature('cyl4').setIndex('pos', '-0.00735', 2);
model.geom('geom1').runAll;
model.geom('geom1').run;
model.geom('geom1').feature('cyl4').setIndex('pos', '-0.0074', 2);
model.geom('geom1').runAll;
model.geom('geom1').run;

model.mesh('mesh1').run;
model.mesh('mesh1').feature('size').set('hauto', '4');
model.mesh('mesh1').run;
model.mesh('mesh1').feature('size').set('hauto', '5');
model.mesh('mesh1').run;
model.mesh('mesh1').feature('size').set('hauto', '2');
model.mesh('mesh1').run;
model.mesh('mesh1').feature('size').set('hauto', '6');
model.mesh('mesh1').run;
model.mesh('mesh1').feature('size').set('custom', 'off');
model.mesh('mesh1').feature('size').set('hauto', '3');
model.mesh('mesh1').feature('size').set('custom', 'on');
model.mesh('mesh1').run;
model.mesh('mesh1').run;
model.mesh('mesh1').run;
model.mesh('mesh1').feature('size').set('custom', 'off');
model.mesh('mesh1').feature('size').set('hauto', '4');
model.mesh('mesh1').run;
model.mesh('mesh1').feature.remove('ftet1');
model.mesh('mesh1').feature.create('swe1', 'Sweep');
model.mesh('mesh1').current('swe1');
model.mesh('mesh1').feature.remove('swe1');
model.mesh('mesh1').clearMesh;
model.mesh('mesh1').feature.create('bl1', 'BndLayer');
model.mesh('mesh1').feature('bl1').feature.create('blp', 'BndLayerProp');
model.mesh('mesh1').feature('bl1').feature('blp').selection.all;
model.mesh('mesh1').feature('bl1').feature('blp').selection.set([1 2 3 4 5
45]);
model.mesh('mesh1').run;

model.physics('mfnc').feature('ms1').selection.set([1 2 3 4 5 45]);
model.physics('mfnc').feature('ms1').set('materialType', 1, 'solid');

model.sol('sol1').study('std1');
model.sol('sol1').feature.remove('s1');
model.sol('sol1').feature.remove('v1');
model.sol('sol1').feature.remove('st1');
model.sol('sol1').feature.create('st1', 'StudyStep');
model.sol('sol1').feature('st1').set('study', 'std1');
model.sol('sol1').feature('st1').set('studystep', 'stat');
model.sol('sol1').feature.create('v1', 'Variables');
model.sol('sol1').feature('v1').set('control', 'stat');
model.sol('sol1').feature.create('s1', 'Stationary');
model.sol('sol1').feature('s1').feature.create('fc1', 'FullyCoupled');
```

```
model.sol('sol1').feature('s1').feature.create('i1', 'Iterative');
model.sol('sol1').feature('s1').feature('i1').set('linsolver', 'cg');
model.sol('sol1').feature('s1').feature('fc1').set('linsolver', 'i1');
model.sol('sol1').feature('s1').feature('i1').feature.create('mg1',
'Multigrid');
model.sol('sol1').feature('s1').feature('i1').feature('mg1').set('prefun',
'amg');
model.sol('sol1').feature('s1').feature.remove('fcDef');
model.sol('sol1').attach('std1');

model.result('pg1').run;
model.result('pg1').run;
model.result('pg1').run;

model.physics('mfnc').feature('ms1').set('mur_mat', 1, 'userdef');

model.sol('sol1').study('std1');
model.sol('sol1').feature.remove('s1');
model.sol('sol1').feature.remove('v1');
model.sol('sol1').feature.remove('st1');
model.sol('sol1').feature.create('st1', 'StudyStep');
model.sol('sol1').feature('st1').set('study', 'std1');
model.sol('sol1').feature('st1').set('studystep', 'stat');
model.sol('sol1').feature.create('v1', 'Variables');
model.sol('sol1').feature('v1').set('control', 'stat');
model.sol('sol1').feature.create('s1', 'Stationary');
model.sol('sol1').feature('s1').feature.create('fc1', 'FullyCoupled');
model.sol('sol1').feature('s1').feature.create('i1', 'Iterative');
model.sol('sol1').feature('s1').feature('i1').set('linsolver', 'cg');
model.sol('sol1').feature('s1').feature('fc1').set('linsolver', 'i1');
model.sol('sol1').feature('s1').feature('i1').feature.create('mg1',
'Multigrid');
model.sol('sol1').feature('s1').feature('i1').feature('mg1').set('prefun',
'amg');
model.sol('sol1').feature('s1').feature.remove('fcDef');
model.sol('sol1').attach('std1');
model.sol('sol1').runAll;

model.result('pg1').run;
model.result('pg1').run;
model.result('pg1').run;
model.result('pg1').run;
model.result('pg1').feature('vol2').active(false);
model.result('pg1').run;
model.result('pg1').run;
model.result('pg1').feature('vol1').active(true);
model.result('pg1').run;

model.mesh('mesh1').clearMesh;
model.mesh('mesh1').feature.remove('bl1');
model.mesh('mesh1').feature.create('ftet1', 'FreeTet');
model.mesh('mesh1').feature('ftet1').selection.geom('geom1', 3);
model.mesh('mesh1').feature('ftet1').selection.all;
model.mesh('mesh1').run;

model.sol('sol1').updateSolution;
```

```
model.result('pg1').run;

model.view('view1').set('transparency', 'off');

model.result('pg1').set('allowtableupdate', true);
model.result('pg1').set('renderdatacached', true);

model.view('view1').set('renderwireframe', true);
model.view('view1').set('transparency', 'on');

model.geom('geom1').feature('cyl2').setIndex('pos', '-0.00399', 2);
model.geom('geom1').runAll;
model.geom('geom1').feature('cyl2').setIndex('pos', '-0.004', 2);
model.geom('geom1').runAll;
model.geom('geom1').feature('cyl2').setIndex('pos', '-0.005', 2);
model.geom('geom1').runAll;
model.geom('geom1').feature('cyl2').setIndex('pos', '-0.004', 2);
model.geom('geom1').runAll;
model.geom('geom1').feature('cyl2').setIndex('pos', '-0.003', 2);
model.geom('geom1').runAll;
model.geom('geom1').feature('cyl2').setIndex('pos', '-0.0035', 2);
model.geom('geom1').runAll;
model.geom('geom1').feature('cyl3').setIndex('pos', '0.0025', 1);
model.geom('geom1').runAll;
model.geom('geom1').feature('cyl3').setIndex('pos', '0.0027', 1);
model.geom('geom1').runAll;
model.geom('geom1').feature('cyl4').setIndex('pos', '-0.0085', 2);
model.geom('geom1').runAll;
model.geom('geom1').feature('cyl4').setIndex('pos', '-0.0080', 2);
model.geom('geom1').runAll;
model.geom('geom1').feature('cyl4').setIndex('pos', '-0.0075', 2);
model.geom('geom1').runAll;
model.geom('geom1').feature('cyl4').setIndex('pos', '-0.0078', 2);
model.geom('geom1').runAll;
model.geom('geom1').run;

model.mesh('mesh1').feature('ftet1').selection.set([1 2 3 4 5]);
model.mesh('mesh1').feature('ftet1').selection.all;
model.mesh('mesh1').feature('ftet1').selection.set([1]);
model.mesh('mesh1').feature('size').set('hauto', '3');
model.mesh('mesh1').run;

model.physics('mfnc').feature('ms1').selection.all;
model.physics('mfnc').feature('ms1').selection.set([1 2 3 4 5 44]);
model.physics('mfnc').feature('ms1').set('ds', 1, '0.016');

model.sol('sol1').study('std1');
model.sol('sol1').feature.remove('s1');
model.sol('sol1').feature.remove('v1');
model.sol('sol1').feature.remove('st1');
model.sol('sol1').feature.create('st1', 'StudyStep');
model.sol('sol1').feature('st1').set('study', 'std1');
model.sol('sol1').feature('st1').set('studystep', 'stat');
model.sol('sol1').feature.create('v1', 'Variables');
```

```
model.sol('sol1').feature('v1').set('control', 'stat');
model.sol('sol1').feature.create('s1', 'Stationary');
model.sol('sol1').feature('s1').feature.create('fc1', 'FullyCoupled');
model.sol('sol1').feature('s1').feature.create('i1', 'Iterative');
model.sol('sol1').feature('s1').feature('i1').set('linsolver', 'cg');
model.sol('sol1').feature('s1').feature('fc1').set('linsolver', 'i1');
model.sol('sol1').feature('s1').feature('i1').feature.create('mg1',
'Multigrid');
model.sol('sol1').feature('s1').feature('i1').feature('mg1').set('prefun',
'amg');
model.sol('sol1').feature('s1').feature.remove('fcDef');
model.sol('sol1').attach('std1');
model.sol('sol1').runAll;

model.result('pg1').run;
model.result('pg1').set('allowtableupdate', true);
model.result('pg1').set('renderdatacached', true);
model.result('pg1').run;
model.result('pg1').feature('vol1').active(false);
model.result('pg1').run;
model.result('pg1').run;
model.result('pg1').feature('vol2').active(true);
model.result('pg1').run;

model.view('view1').set('transparency', 'off');

model.name('Drilled rebar models.mph');

model.result('pg1').run;
model.result.dataset.create('cln1', 'CutLine3D');
model.result.dataset('cln1').set('method', 'twopoint');
model.result.dataset('cln1').run;
model.result.dataset('dset1').set('frametype', 'spatial');
model.result.dataset('dset1').run;

model.view.remove('view2');

model.result.dataset('dset1').run;

model.view.remove('view2');

model.result('pg1').run;
model.result.dataset('dset1').run;

model.view.remove('view2');

model.result.dataset.create('cpl1', 'CutPlane');
model.result.dataset('cpl1').set('quickplane', 'xz');
model.result.dataset('cpl1').run;
model.result.dataset('dset1').set('frametype', 'material');
model.result.dataset('dset1').run;

model.view.remove('view2');
```

```
model.result.export.create('data1', 'cpl1', 'Data');
model.result('pg1').run;
model.result.export('data1').set('expr', {'mfnc.normB'});
model.result.export('data1').set('descr', {'Magnetic flux density norm'});
model.result.export('data1').set('unit', {'T'});
model.result.export('data1').set('filename', 'C:\Documents and
Settings\Administrator\Desktop\training Comsol\Healthy and drilled rebar\new
data.txt');
model.result.export('data1').run;
model.result('pg1').run;
model.result('pg1').set('allowtableupdate', true);
model.result('pg1').set('renderdatacached', true);
model.result.table.create('evl3', 'Table');
model.result.table('evl3').comments('Interactive 3D values');
model.result.table('evl3').name('Evaluation 3D');
model.result.table('evl3').addRow([0.1467414607542168 0.0022867829728401845
0.006432588736491274 7.479777156928616E-5]);
model.result('pg1').run;
model.result.export.create('data2', 'cln1', 'Data');
model.result.export('data2').set('filename', 'new line data');
model.result('pg1').run;
model.result.export('data2').set('expr', {'mfnc.normB'});
model.result.export('data2').set('descr', {'Magnetic flux density norm'});
model.result.export('data2').set('unit', {'T'});
model.result.export('data2').run;
model.result.export('data2').set('filename', 'C:\Documents and
Settings\Administrator\Desktop\training Comsol\Healthy and drilled rebar\new
line data.txt');
model.result.export('data2').run;
model.result.dataset('cln1').setIndex('genpoints', '0.564', 1, 0);
model.result.dataset('cln1').setIndex('genpoints', '0.008', 0, 2);
model.result.dataset('cln1').setIndex('genpoints', '0.008', 1, 2);
model.result.export.create('data3', 'cln1', 'Data');
model.result.export('data3').set('expr', {'mfnc.normB'});
model.result.export('data3').set('descr', {'Magnetic flux density norm'});
model.result.export('data3').set('unit', {'T'});
model.result.export('data3').set('filename', 'C:\Documents and
Settings\Administrator\Desktop\training Comsol\Healthy and drilled rebar\new
line data-2.txt');
model.result.export('data3').run;
model.result.dataset('cln1').set('genparaactive', 'off');
model.result.export('data3').set('expr', {'mfnc.normB'});
model.result.export('data3').set('descr', {'Magnetic flux density norm'});
model.result.export('data3').set('unit', {'T'});
model.result.export('data3').set('filename', 'C:\Documents and
Settings\Administrator\Desktop\training Comsol\Healthy and drilled rebar\new
line data2.txt');
model.result.export('data3').run;
model.result.dataset('cln1').setIndex('genpoints', '0', 1, 2);
model.result.dataset('cln1').setIndex('genpoints', '00', 0, 2);
model.result.dataset('cln1').run;
model.result.export.create('data4', 'cln1', 'Data');
model.result.export('data4').set('expr', {'mfnc.normB'});
model.result.export('data4').set('descr', {'Magnetic flux density norm'});
model.result.export('data4').set('unit', {'T'});
```

```
model.result.export('data4').set('filename', 'C:\Documents and
Settings\Administrator\Desktop\training Comsol\Healthy and drilled rebar\new
line data2.txt');
model.result.export('data4').run;
model.result.export.remove('data3');
model.result.export.remove('data4');
model.result.dataset('cln1').setIndex('genpoints', '0.008', 0, 2);
model.result.dataset('cln1').setIndex('genpoints', '0.0', 1, 2);
model.result.dataset('cln1').setIndex('genpoints', '0.00', 1, 2);
model.result.dataset('cln1').setIndex('genpoints', '0.008', 1, 2);
model.result.dataset('cln1').run;
model.result.dataset('cln1').run;
model.result.export.create('data3', 'cln1', 'Data');
model.result.export('data3').set('expr', {'mfnc.normB'});
model.result.export('data3').set('descr', {'Magnetic flux density norm'});
model.result.export('data3').set('unit', {'T'});
model.result.export('data3').set('filename', 'C:\Documents and
Settings\Administrator\Desktop\training Comsol\Healthy and drilled rebar\new
line data2.txt');
model.result.export('data3').run;
model.result.export('data3').set('expr', {'mfnc.Hx'});
model.result.export('data3').set('descr', {'Magnetic field, x component'});
model.result.export('data3').set('unit', {'A/m'});
model.result.export('data3').run;
model.result.dataset('cln1').setIndex('genpoints', '0.0079', 0, 2);
model.result.dataset('cln1').setIndex('genpoints', '0.007', 1, 2);
model.result.dataset('cln1').setIndex('genpoints', '0.0079', 1, 2);
model.result.dataset('cln1').run;
model.result.export('data3').run;
model.result('pg1').run;
model.result.dataset.create('cpl2', 'CutPlane');
model.result.dataset('cpl2').set('quickplane', 'xz');
model.result.dataset('cpl2').set('genparaactive', 'off');
model.result.dataset('cpl2').run;
model.result.export.create('data4', 'cpl2', 'Data');
model.result.export('data4').set('expr', {'mfnc.Hx'});
model.result.export('data4').set('descr', {'Magnetic field, x component'});
model.result.export('data4').set('unit', {'A/m'});
model.result.export('data4').set('filename', 'C:\Documents and
Settings\Administrator\Desktop\training Comsol\Healthy and drilled rebar\new
line data4.txt');
model.result.export('data4').run;
model.result.dataset('cpl2').set('quickplane', 'xy');
model.result.dataset('cpl2').run;
model.result.dataset('cpl2').set('quickz', '0.008');
model.result.dataset('cpl2').run;
model.result.dataset('cpl2').set('quickz', '0.0079');
model.result.dataset('cpl2').run;
model.result.dataset('cpl2').set('quickz', '0.0070');
model.result.dataset('cpl2').run;
model.result.dataset('cpl2').set('quickz', '0.006');
model.result.dataset('cpl2').run;
model.result.dataset('cpl2').set('quickz', '0.00795');
model.result.dataset('cpl2').run;
model.result.export.create('data5', 'cpl2', 'Data');
model.result.export('data5').set('expr', {'mfnc.Hx'});
model.result.export('data5').set('descr', {'Magnetic field, x component'});
```

```
model.result.export('data5').set('unit', {'A/m'});
model.result.export('data5').set('filename', 'C:\Documents and
Settings\Administrator\Desktop\training Comsol\Healthy and drilled rebar\new
line data4.txt');
model.result.export('data5').run;

model.name('Drilled rebar models.mph');

model.result('pg1').run;
model.result('pg1').set('allowtableupdate', false);
model.result('pg1').set('title', 'Volume: Magnetic flux density norm (T)');
model.result('pg1').set('renderdatacached', false);
model.result('pg1').set('allowtableupdate', true);
model.result('pg1').set('renderdatacached', true);
model.result('pg1').feature('vol2').set('colortable', 'GrayScale');
model.result('pg1').feature('vol2').set('colortablerev', 'on');

model.name('Drilled rebar models.mph');

model.result('pg1').run;
model.result('pg1').run;
model.result.export.create('plot1', 'Plot');
model.result('pg1').feature('vol2').active(false);
model.result('pg1').set('window', 'graphics');
model.result('pg1').run;
model.result('pg1').set('window', 'graphics');
model.result('pg1').set('windowtitle', '');
model.result('pg1').feature('vol2').active(true);
model.result.export.remove('plot1');
model.result.create('pg2', 'PlotGroup1D');
model.result('pg2').run;
model.result('pg2').feature.create('lngr1', 'LineGraph');
model.result('pg2').feature('lngr1').set('data', 'cln1');
model.result('pg2').feature('lngr1').set('expr', 'mfnc.Bx');
model.result('pg2').feature('lngr1').set('descr', 'Magnetic flux density, x
component');
model.result('pg2').run;
model.result('pg1').run;
model.result('pg1').feature('vol2').set('colortable', 'Rainbow');
model.result('pg1').feature('vol2').set('colortablerev', 'on');

model.name('Final Drilled rebar model.mph');

model.result('pg1').run;
model.result('pg2').run;
model.result.export.remove('data2');
model.result.export.remove('data3');
model.result.export.remove('data4');
model.result.export.remove('data5');
model.result.export('data1').set('expr', {'mfnc.Bx'});
model.result.export('data1').set('descr', {'Magnetic flux density, x
component'});
model.result.export('data1').set('unit', {'T'});
model.result('pg2').run;
model.result.export('data1').set('expr', {'mfnc.Bx' 'mfnc.By'});
```

```
model.result.export('data1').set('descr', {'Magnetic flux density, x
component' 'Magnetic flux density, y component'});
model.result.export('data1').set('expr', {'mfnc.Bx' 'mfnc.By' 'mfnc.Bz'});
model.result.export('data1').set('descr', {'Magnetic flux density, x
component' 'Magnetic flux density, y component' 'Magnetic flux density, z
component'});
model.result.export('data1').set('expr', {'mfnc.Bx' 'mfnc.By' 'mfnc.Bz'
'mfnc.normB'});
model.result.export('data1').set('descr', {'Magnetic flux density, x
component' 'Magnetic flux density, y component' 'Magnetic flux density, z
component' 'Magnetic flux density norm'});

model.param.set('R', '0.008[m]');
model.param.descr('R', 'Radius of bar');
model.param.set('L', '0.564[m]');
model.param.descr('L', 'Length of bar');
model.param.set('rh1', '0.00291');
model.param.set('rh2', '0.003395');
model.param.set('rh3', '0.003255');
model.param.set('rh1', '0.00291[m]');
model.param.set('rh2', '0.003395[m]');
model.param.set('rh3', '0.003255[m]');
model.param.set('dh1', '0.01241[m]');
model.param.set('dh2', '0.00569[m]');
model.param.set('dh3', '0.00636');
model.param.descr('rh1', 'Radius of hole 1');
model.param.descr('rh2', 'Radius of hole 1');
model.param.descr('rh3', 'Radius of hole 1');
model.param.descr('rh2', 'Radius of hole 2');
model.param.descr('rh3', 'Radius of hole 3');
model.param.descr('dh1', 'Depth of hole 1');
model.param.descr('dh2', 'Depth of hole 1');
model.param.descr('dh3', 'Depth of hole 1');
model.param.descr('dh2', 'Depth of hole 2');
model.param.descr('dh3', 'Depth of hole 3');

model.geom('geom1').feature('cyl2').set('r', 'rh1');
model.geom('geom1').feature('cyl2').set('h', 'dh1');
model.geom('geom1').feature('cyl3').set('r', 'rh2');
model.geom('geom1').feature('cyl3').set('h', 'dh2');
model.geom('geom1').feature('cyl4').set('r', 'rh3');
model.geom('geom1').feature('cyl4').set('h', 'dh3');
model.geom('geom1').run('fin');
model.geom('geom1').feature('cyl1').set('r', 'R');
model.geom('geom1').feature('cyl1').set('h', 'L');
model.geom('geom1').run('fin');

model.label('Final Drilled rebar model.mph');

model.geom('geom1').feature('cyl2').set('r', 'rh1/10');
model.geom('geom1').feature('cyl3').set('r', 'rh2/10');
model.geom('geom1').feature('cyl4').set('r', 'rh3/10');
model.geom('geom1').runPre('fin');
model.geom('geom1').run;

model.mesh('mesh1').run;
```

```
model.mesh('mesh1').feature('size').set('hauto', '1');
model.mesh('mesh1').run;
model.mesh('mesh1').feature('size').set('custom', 'on');
model.mesh('mesh1').feature('size').set('hmax', '0.00031');
model.mesh('mesh1').feature('size').set('hmin', '2.26e-5');
model.mesh('mesh1').run('size');
model.mesh('mesh1').create('ftet2', 'FreeTet');
model.mesh('mesh1').feature('ftet2').create('size1', 'Size');
model.mesh('mesh1').feature('ftet1').create('size1', 'Size');
model.mesh('mesh1').feature('ftet2').selection.geom('geom1', 3);
model.mesh('mesh1').feature('ftet2').selection.set([1]);
model.mesh('mesh1').feature('ftet2').feature('size1').set('hauto', '2');
model.mesh('mesh1').feature('ftet1').selection.remaining;
model.mesh('mesh1').feature('ftet1').feature('size1').set('custom', 'on');
model.mesh('mesh1').feature('ftet1').feature('size1').set('hmaxactive',
'on');
model.mesh('mesh1').feature('ftet1').feature('size1').set('hminactive',
'on');
model.mesh('mesh1').feature('ftet1').feature('size1').set('hmax', '2.29e-5');
model.mesh('mesh1').feature('ftet1').feature('size1').set('hmin', '2.29');
model.mesh('mesh1').feature('ftet1').feature('size1').set('hmax', '2.29e-4');
model.mesh('mesh1').feature('ftet1').feature('size1').set('hmin', '2.29e-5');
model.mesh('mesh1').run;

model.geom('geom1').feature('cyl2').set('pos', {'0.145' '0' '-0.0034'});
model.geom('geom1').run('cyl2');
model.geom('geom1').feature('cyl2').set('pos', {'0.145' '0' '-0.0030'});
model.geom('geom1').run('cyl2');
model.geom('geom1').feature('cyl2').set('pos', {'0.145' '0' '-0.0037'});
model.geom('geom1').run('cyl2');
model.geom('geom1').feature('cyl2').set('pos', {'0.145' '0' '-0.0038'});
model.geom('geom1').run('cyl2');
model.geom('geom1').feature('cyl2').set('pos', {'0.145' '0' '-0.0045'});
model.geom('geom1').run('cyl2');
model.geom('geom1').feature('cyl2').set('pos', {'0.145' '0' '-0.0042'});
model.geom('geom1').run('cyl2');
model.geom('geom1').feature('cyl2').set('pos', {'0.145' '0' '-0.0043'});
model.geom('geom1').run('cyl2');
model.geom('geom1').run;
model.geom('geom1').feature('cyl2').set('pos', {'0.145' '0' '-0.0044'});
model.geom('geom1').run('cyl2');
model.geom('geom1').run;

model.mesh('mesh1').run;

model.sol('sol1').runAll;

model.result('pg1').run;
model.result('pg2').run;
model.result('pg2').run;
model.result('pg2').feature('lngr1').set('expr', 'mfnc.Hx');
model.result('pg2').feature('lngr1').set('descr', 'Magnetic field, x
component');
model.result('pg2').feature('lngr1').set('cutline', 'cln1');
model.result('pg2').feature('lngr1').set('linefirst', [0.28200000524520874
1.9499985501170158E-4 -0.00800000037997961]);
```

```
model.result('pg2').feature('lngr1').set('linesecond', [0.28200000524520874
1.9499985501170158E-4 0.008009999990463257]);
model.result('pg2').feature('lngr1').set('lineisinit', true);
model.result.dataset('cln1').set('method', 'twopoint');
model.result.dataset('cln1').set('genpoints', [0.281998 1.94999E-4 -0.008;
0.281998 1.94999E-4 0.00801]);
model.result('pg2').feature('lngr1').set('cutmode', 'off');
model.result('pg2').run;
model.result('pg2').feature('lngr1').set('expr', 'mfnc.Bx');
model.result('pg2').feature('lngr1').set('descr', 'Magnetic flux density, x
component');
model.result('pg2').run;
model.result('pg2').run;
model.result('pg2').run;
model.result('pg2').feature('lngr1').set('expr', 'mfnc.Bx');
model.result('pg2').feature('lngr1').set('descr', 'Magnetic flux density, x
component Magnetic field, x component');
model.result('pg2').feature('lngr1').set('expr', 'mfnc.Bx');
model.result('pg2').run;
model.result('pg2').feature('lngr1').set('expr', 'mfnc.Bx');
model.result('pg2').feature('lngr1').set('descr', 'Magnetic flux density, x
component');
model.result('pg2').feature('lngr1').set('expr', 'mfnc.Hx');
model.result('pg2').feature('lngr1').set('descr', 'Magnetic field, x
component');
model.result('pg2').run;
model.result('pg2').feature('lngr1').set('data', 'cln1');
model.result.dataset.remove('cpl1');
model.result.dataset.remove('cpl2');
model.result.dataset('cln1').run;
model.result.dataset('cln1').setIndex('genpoints', '0', 0, 0);
model.result.dataset('cln1').setIndex('genpoints', '0.56', 1, 0);
model.result.dataset('cln1').setIndex('genpoints', '0', 0, 1);
model.result.dataset('cln1').setIndex('genpoints', '0', 1, 1);
model.result.dataset('cln1').setIndex('genpoints', '0.79', 0, 2);
model.result.dataset('cln1').setIndex('genpoints', '0.79', 1, 2);
model.result.dataset('cln1').run;
model.result.dataset('cln1').run;
model.result.dataset('cln1').setIndex('genpoints', '0.079', 0, 2);
model.result.dataset('cln1').setIndex('genpoints', '0.079', 1, 2);
model.result.dataset('cln1').run;
model.result.dataset('cln1').setIndex('genpoints', '0.0079', 0, 2);
model.result.dataset('cln1').setIndex('genpoints', '0.0079', 1, 2);
model.result.dataset('cln1').run;
model.result('pg2').run;
model.result('pg2').feature('lngr1').set('expr', 'mfnc.Bx');
model.result('pg2').feature('lngr1').set('descr', 'Magnetic flux density, x
component');
model.result('pg2').run;
model.result.export.create('data1', 'Data');
model.result.export('data1').set('data', 'cln1');

model.mesh('mesh1').feature('ftet1').feature('size1').set('hmax', '1.45e-4');
model.mesh('mesh1').feature('ftet1').feature('size1').set('hmin', '1.45e-5');
model.mesh('mesh1').run;
model.mesh('mesh1').feature('ftet2').feature('size1').set('hauto', '1');
model.mesh('mesh1').run;
```

```
model.sol('sol1').runAll;

model.result('pg1').run;
model.result('pg2').run;
model.result('pg2').run;
model.result.export('data1').set('expr', {'mfnc.Bx'});
model.result.export('data1').set('descr', {'Magnetic flux density, x
component'});
model.result.export('data1').set('unit', {'T'});

model.mesh('mesh1').feature('ftet2').feature('size1').set('custom', 'on');
model.mesh('mesh1').feature('ftet2').feature('size1').set('hminactive',
'on');
model.mesh('mesh1').feature('ftet2').feature('size1').set('hmin', '1.13E-4');
model.mesh('mesh1').feature('ftet2').feature('size1').set('hmaxactive',
'on');
model.mesh('mesh1').run;
model.mesh('mesh1').feature('ftet2').feature('size1').set('hmax', '0.00113');
model.mesh('mesh1').run;
model.mesh('mesh1').feature('ftet2').feature('size1').set('hmax',
'0.000565');
model.mesh('mesh1').run;

model.sol('sol1').runAll;

model.result('pg1').run;
model.result('pg2').run;
model.result('pg2').run;

model.mesh('mesh1').feature('ftet2').feature('size1').set('hmax', '0.00029');
model.mesh('mesh1').feature('ftet2').feature('size1').set('hmin', '0.565e-
4');
model.mesh('mesh1').run;

model.label('Final Drilled rebar model.mph');

model.mesh('mesh1').feature('ftet1').feature('size1').set('hmax', '2.9e-4');
model.mesh('mesh1').feature('ftet1').feature('size1').set('hmin', '2.9e-5');
model.mesh('mesh1').feature('ftet2').feature('size1').set('hmax', '0.00058');
model.mesh('mesh1').feature('ftet2').feature('size1').set('hmin', '1.13e-4');
model.mesh('mesh1').run;

model.label('Final Drilled rebar model.mph');

out = model;
```

Appendix II:

Matlab code of wavelet energy analysis (Chapter 7):

```
%% General comments
clear;
%Wavelet definition
wname  = 'Morl';
par    = 6;
WAV    = {wname,par};

%% Wavelet for Hx
load('Rebar5.mat');
%sampling frequency
scales = 1:0.1:10;
dt = 1/10;
s1{1} = xb;
s1{2} = dt;
cwt_s1_lin = cwtft(s1,'scales',scales,'wavelet',WAV,'plot');
cwt_s1_pow = cwtft(s1,'plot');

% Compute the energy distribution over scales.
cfs = cwt_s1_lin.cfs;
energyX = sum(abs(cfs),2);
percentageX = 100*energyX/sum(energyX);

[maxenergy,maxenergyScaleIDX] = max(energyX+100);
figure;
plot(energyX,'k','Markersize',100);
hold on
plot(maxenergyScaleIDX,maxenergy,'.k','Markersize',20);
title ('Rebar 5 (14.30% general corrosion)');
xlabel('Indices of Scales');
ylabel('Wavelet Energy of Magnetic field (Hz)');
axis tight
grid
MaxEner = scales(maxenergyScaleIDX)
% Detect the scale of greatest energy.

[maxpercent,maxScaleIDX] = max(percentageX)
figure;
plot(percentageX,'.-r');
hold on
plot(maxScaleIDX,maxpercent,'.k','Markersize',20);
xlabel('Indices of Scales');
ylabel('Percentage of energy');
axis tight
grid
scaMaxEner = scales(maxScaleIDX)

%Step 2: Reconstruction of System Anomaly Signature in the Time Domain
cwt_anomalyX1 = cwt_s1_pow;
% Find the index of logarithmic scale detecting the anomaly.
[valMin,anomaly_index_scales] = min(abs(cwt_s1_pow.scales-scaMaxEner))
anomaly_cfs = cwt_s1_pow.cfs(anomaly_index_scales,:);
```

```
newCFS = zeros(size(cwt_s1_pow.cfs));
newCFS(anomaly_index_scales,:) = anomaly_cfs;
cwt_anomalyX1.cfs = newCFS;
% Reconstruction from the modified structure.
anomalyX1= icwtft(cwt_anomalyX1,'plot','signal',s1);
%ax = findobj(gcf,'type','axes','tag','');
%set(ax,'XLim',[250 500]);
%Step 3: A Second Reconstruction of System Anomaly Signature
% First step for building the new structure corresponding to the anomaly.
cwt_anomalyX2 = cwt_s1_lin;
% Choose a vector of scales centered on the most energetic scale.
dScale = 5;
anomaly_index_scales = (maxScaleIDX-dScale:maxScaleIDX+dScale);
anomaly_cfs = cwt_s1_lin.cfs(anomaly_index_scales,:);
newCFS = zeros(size(cwt_s1_lin.cfs));
newCFS(anomaly_index_scales,:) = anomaly_cfs;
cwt_anomalyX2.cfs = newCFS;
% Reconstruction from the modified structure.
anomalyX2 = icwtlin(cwt_anomalyX2,'plot');
```

Appendix III: Wavelet

a. Morlet wavelet (real part)

Equation: $\psi(x) = e^{-x^2/2}\cos(5x)$

Matlab code for graph:

```
lb = -4;
ub = 4;
n = 1000;
[psi,xval] = morlet(lb,ub,n);
plot(xval,psi)
title('Morlet Wavelet');
```

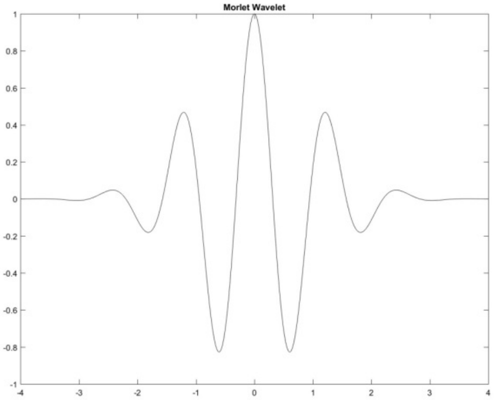

b. Haar wavelet

Equation: $$\psi(t) = \begin{cases} 1 & 0 \le t \le \frac{1}{2} \\ -1 & \frac{1}{2} \le t \le 1 \\ 0 & \text{otherwise} \end{cases}$$

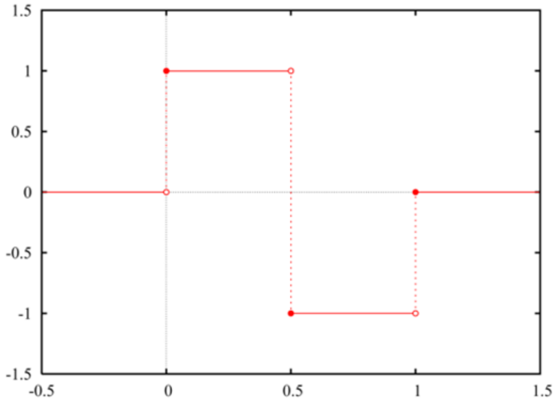

Some definitions:

The energy of a signal *x(t)* is given by :

$$E_x = \int_{-\infty}^{+\infty} |x(t)|^2 \, dt$$

with $|x(t)|$ the modulus of *x(t).*

The power of a signal *x(t)* is define by:

$$P_x = \lim_{T \to +\infty} \frac{1}{T} \int_{-\frac{T}{2}}^{+\frac{T}{2}} |x(t)|^2 \, dt$$

The Fourier transform of a signal *x(t)* with finite energy is given by:

$$X(\omega) = \int_{-\infty}^{+\infty} x(t) e^{-2\pi\omega t} dt$$

with ω the frequency.

In case of a signal with finite power (this mean that the energy of the signal is equal to 0) the definition of the Fourier transform needs the utilization of distribution (δ function) theory.

The autocorrelation of a signal *x(t)* with finite energy is given by:

$$\Gamma_{xx}(\tau) = \int_{-\infty}^{+\infty} x(t) x^*(t-\tau) dt$$

The cross correlation of a signal *x(t)* with finite energy and a signal *y(t)* is given by:

$$\Gamma_{xy}(\tau) = \int_{-\infty}^{+\infty} x(t) y^*(t-\tau) dt$$

The autocorrelation of a signal *x(t)* with finite power is given by:

$$\Gamma_{xx}(\tau) = \lim_{T \to +\infty} \frac{1}{T} \int_{-\frac{T}{2}}^{+\frac{T}{2}} x(t) x^*(t-\tau) dt$$

The cross correlation of a signal *x(t)* with finite power and a signal *y(t)* is given by:

$$\Gamma_{xy}(\tau) = \lim_{T \to +\infty} \frac{1}{T} \int_{-\frac{T}{2}}^{+\frac{T}{2}} x(t) y^*(t-\tau) dt$$

In case of finite energy signals we have:

$$\Gamma_{xx}(0) = \int_{-\infty}^{+\infty} |x(t)|^2 \, dt$$

$$\Gamma_{xy}(0) = \int_{-\infty}^{+\infty} x(t) y^*(t) dt$$

In case of finite power signals we have:

$$\Gamma_{xx}(0) = \lim_{T \to +\infty} \frac{1}{T} \int_{-\frac{T}{2}}^{+\frac{T}{2}} |x(t)|^2 \, dt$$

$$\Gamma_{xy}(0) = \lim_{T \to +\infty} \frac{1}{T} \int_{-\frac{T}{2}}^{+\frac{T}{2}} x(t) y^*(t) dt$$

The spectral densities of signals are defined as:

$$S_{xx}(\omega) = |X(\omega)|^2$$

$$S_{xy}(\omega) = X(\omega) Y^*(\omega)$$

By using the Wiener-Kinchine theorem:

$$S_{xx}(\omega) = F\left[\Gamma_{xx}(\tau)\right]$$

with $\mathrm{F}\left[\Gamma_{\mathrm{xx}}(\tau)\right]$ the Fourier transform of the autocorrelation function of the signal *x(t)*.

$$S_{xy}\left(\omega\right) = F\left[\Gamma_{xy}(\tau)\right]$$

with $\mathrm{F}\left[\Gamma_{\mathrm{xy}}(\tau)\right]$ the Fourier transform of the cross correlation function of the signal *x(t)* and the signal *y(t)*.

Parceval theorem:

$$\int_{-\infty}^{+\infty} \left|x(t)\right|^2 dt = \int_{-\infty}^{+\infty} \left|X(\nu)\right|^2 d\nu$$